



**Politecnico  
di Torino**

**ScuDo**

Scuola di Dottorato - Doctoral School  
WHAT YOU ARE, TAKES YOU FAR

Doctoral Dissertation  
Doctoral Program in Energy Engineering (35<sup>th</sup> cycle)

# **Performance evaluation of three and multi-three-phase electrical machines using off-line mapping**

By

**Ornella Stiscia**

\*\*\*\*\*

**Supervisors:**

Prof. A. Cavagnino, Supervisor

Prof. A. Tenconi, Co-Supervisor

**Doctoral Examination Committee:**

Prof. M. Mengoni, Università di Bologna (Reviewer)

Prof. G. Scelba, Università di Catania (Reviewer)

Prof. L. Ferraris, Politecnico di Torino

Prof. F. Tinazzi, Università degli Studi di Padova

Prof. S. Vaschetto, Politecnico di Torino

Politecnico di Torino  
January 19, 2023

## Abstract

A sustainable and green future requires an effective energy transition towards more efficient and carbon-free solutions. The electrification of various applications, e.g., automotive, naval, aircraft, wind energy, etc., is an effective tool for these aims. Electrified systems include different engineering areas, i.e., electrical machines, battery systems, power converters, etc. A reliable design and analysis of the system components require more efficient approaches to minimize costs and time-to-market. Nowadays, it is evident that we need new intelligent methods to emulate the whole system's behavior.

The virtualization of the electric components in an electrified system is a method with excellent potential to assess the system design goodness in terms of efficiency and operational limits. The core of electrified systems is the electrical machine, which must be designed to target the maximum possible efficiency and fault-tolerant operation. New solutions such as multiphase electrical machines fulfill these goals. The main advantage of multiphase drives consists in reducing the current per phase without increasing the phase voltage. Moreover, multiphase drives are intrinsically fault-tolerant. The latter two characteristics make multiphase machines more attractive for the future of electrified systems. Indeed, the higher number of phases improves the system reliability using redundancy from both power converter and electrical machine points of view. However, multiphase drives are still limited to high power and safety-critical application due to the historical evolution of the three-phase drives, which have reached more maturity only in the last few years.

The main goal of the dissertation is to develop a straightforward methodology for computing the efficiency and loss mapping of three-phase and multi-three-phase electrical machines. The proposed method allows a quick

and accurate energetic assessment and machine virtualization. The method does not require expensive test rigs to manage demanding speed and torque, but it is based on an equivalent circuit/analytical model accurately evaluated. Therefore, the proposed procedures represent an effective solution to avoid the burden of FEA analyses and expensive experimental mapping procedures. Moreover, the proposed method allows the reconstruction of all electrical variables of the machine (i.e., currents, voltages, fluxes), representing the first step toward accurate virtualization of electrical machines operated in wide torque-speed ranges. Last but not least, the mapping output can achieve the maximum efficiency control strategy and avoid the maximum torque per ampere that is usually implemented in machine control.

The dissertation develops as follow:

1. The procedure is developed to quickly compute the efficiency maps of three-phase induction motors (IMs) operated in wide torque-speed ranges. The efficiency, losses, currents, voltages, fluxes, maps of the machine (both in motoring and generator operation), were obtained considering different operating temperatures and dc-link voltages. All electromechanical variables are reconstructed, replacing a machine control strategy. The input of the methodology consists of the standard test procedure results like dc, no-load, and locked-rotor tests performed at different voltage and frequency levels. All machine's nonlinearities, e.g., magnetic saturation, skin effect, and iron losses, are strictly considered. The proposed methodology was validated on a 10 kW, 4 poles, 100 Hz IM prototype. Computed and experimental efficiency maps for different operating conditions are in very good agreement, confirming the validity of the proposed methodology.
2. The mapping for the three-phase synchronous internal permanent magnets (IPM) is developed based on the same methodology proposed for three-phase IMs. However, in this case, the input variables of the mapping algorithm, i.e., magnetic characterization, core, and PM losses, were not measured on a prototype but obtained by 2D Finite Element Analysis (FEA). An accurate mapping is obtained, considering all the nonlinearities of the machine. The effectiveness of the procedure was validated through a FEA comparison.

3. In the continuous need for energy saving, requiring more efficient electrical drives, the mapping for multi-three-phase IM is developed. A novel mapping algorithm is proposed considering healthy and open-winding faulty conditions. The procedure is based on the results of standard test procedures like dc, no-load, and locked-rotor tests performed at different voltage and frequency levels under sinusoidal supply. Note that the standard tests are not yet consolidated for multi-three-phase IM and are not so easy to perform due to the unavailability of sinusoidal multiphase sources. Based on the test results, performed under inverter supply, the mapping was developed using all mathematical methods available in the literature, obtaining the same results for all machine conditions and confirming the algorithm's robustness. Moreover, the simplicity of the mapping algorithm is preserved. The mapping code replaces different control strategies, i.e., maximum efficiency, minimum stator Joule losses, and minimum stator flux. The experimental validation was carried out on 12-phase asymmetrical IM 10 kW, 4 poles, 6000 rpm, implementing a sophisticated machine control, a complex test rig, and an advanced measurement system. The open-winding faulty conditions were emulated, turning off the power module, and the corresponding unit, i.e., winding set plus inverter, is disconnected from the dc-link. The experimental results demonstrate the effectiveness and feasibility of the proposed mapping algorithm, providing all necessary data for the multi-three-phase IM virtualization in both conditions and the reference values for control implementation, i.e., stator flux,  $dq$  stator currents.



# Contents

<b>List of Figures</b>	<b>ix</b>
------------------------	-----------

<b>List of Tables</b>	<b>xviii</b>
-----------------------	--------------

<b>1 Introduction</b>	<b>1</b>
1.1 Review of the previous research . . . . .	2
1.1.1 Virtualization . . . . .	2
1.1.2 Performance evaluation based on efficiency maps . . .	3
1.1.3 Multiphase machine: drive configurations, modelling and performance . . . . .	6
1.2 Research objectives . . . . .	12
1.3 Dissertation outline . . . . .	14
1.4 Conclusion . . . . .	14
<b>2 Three-phase Induction Machine Mapping</b>	<b>16</b>
2.1 Three-phase induction machine modeling . . . . .	17
2.1.1 Machine model in phase coordinates . . . . .	18
2.1.2 Machine model in stationary coordinates . . . . .	21
2.1.3 Machine in rotating coordinates . . . . .	24
2.1.4 Machine modelling for efficiency mapping . . . . .	29
2.1.5 Nonlinearities of the machine modeling . . . . .	31

2.1.6	Machine parameters . . . . .	32
2.1.7	Magnetic model manipulation . . . . .	41
2.1.8	Base region . . . . .	42
2.2	Three-phase induction machine mapping . . . . .	48
2.2.1	IM mapping algorithm . . . . .	49
2.2.2	Mapping initialization . . . . .	49
2.2.3	Mapping algorithm . . . . .	53
2.2.4	Mapping minimizing the stator Joule losses and stator flux . . . . .	62
2.3	Experimental validation . . . . .	65
2.3.1	Test rig . . . . .	65
2.3.2	Measurement system . . . . .	66
2.3.3	Validation approach . . . . .	67
2.3.4	Experimental results . . . . .	70
2.4	Conclusion . . . . .	73
<b>3</b>	<b>Three-phase Synchronous Machine Mapping</b>	<b>77</b>
3.1	eDrive Modeling . . . . .	79
3.1.1	Electromagnetic model of IPM machine . . . . .	79
3.1.2	Inverter model . . . . .	83
3.1.3	FEA flux maps . . . . .	86
3.1.4	Iron loss map . . . . .	96
3.1.5	Permanent magnets loss map . . . . .	100
3.2	Three-phase IPM machine efficiency mapping . . . . .	101
3.2.1	IPM mapping algorithm . . . . .	102
3.2.2	Mapping results for IPM e-Motor for BEV . . . . .	108
3.2.3	Multidimensional linear interpolator . . . . .	114

3.3	Conclusion . . . . .	118
<b>4</b>	<b>Multi-Three-phase Induction Machine Mapping</b>	<b>121</b>
4.1	Machine model in phase variables . . . . .	123
4.1.1	Electromagnetic model . . . . .	131
4.1.2	Mechanical model . . . . .	133
4.2	Multi-Stator (MS) modelling approach . . . . .	139
4.2.1	Electromechanical model in stationary coordinates . .	139
4.2.2	Electromechanical model in rotating coordinates . . .	148
4.3	Vector Space decomposition (VSD) modelling approach . . .	152
4.3.1	Electromechanical model in stationary coordinates . .	153
4.3.2	Electromechanical model in rotating coordinates . . .	162
4.4	Decoupling multi-stator (DMS) modelling approach . . . . .	164
4.4.1	Electromechanical model . . . . .	164
4.5	Adaptive decoupling multi-stator (A-DMS) modelling approach	170
4.6	Comparison between modeling approaches . . . . .	173
4.7	Machine investigation . . . . .	176
4.7.1	Case of study: quadruple-three-phase IM . . . . .	176
4.7.2	Measurement parameters . . . . .	178
4.7.3	Locked-rotor tests . . . . .	185
4.7.4	No-load test . . . . .	189
4.7.5	MMF Distribution in normal and faulty conditions . .	196
4.8	Magnetic model based on the flux maps . . . . .	202
4.8.1	MS approach . . . . .	202
4.8.2	VSD and DMS approaches . . . . .	217
4.8.3	A-DMS approach . . . . .	223

---

4.9	Maximum torque per speed profile (MTPS) in normal and open-winding faulty conditions . . . . .	227
4.10	Multi-Three-Phase IM mapping in normal and faulty conditions	240
4.10.1	Mapping initialization: approach and machine conditions . . . . .	240
4.10.2	Mapping algorithm: approach and machine conditions	241
4.11	Experimental validation . . . . .	259
4.11.1	Test rig . . . . .	259
4.11.2	Experimental results . . . . .	266
4.12	Conclusion . . . . .	274
<b>Bibliography</b>		<b>278</b>

# List of Figures

1.1	Multiphase drive topology with single neutral point. . . . .	7
1.2	Multiphase drive topology using multiple single-phase units. . . . .	8
1.3	Multiphase drive topology with multiple three-phase units. . . . .	8
2.1	Winding distribution of three-phase IM. . . . .	19
2.2	Stationary reference frame. . . . .	22
2.3	IM steady-state equivalent circuit in the rotating $dq$ reference frame. . . . .	28
2.4	IM steady-state equivalent circuit in the rotating $dq$ reference frame. . . . .	29
2.5	IM steady-state equivalent circuit in the rotating $dq$ reference frame used in efficiency mapping. . . . .	30
2.6	IM's equivalent circuit while performing the no-load test. . . . .	33
2.7	Mechanical losses of the IM used for the experimental validation. . . . .	35
2.8	Stator losses map (iron losses plus skin effect) of the IM used for the experimental validation. . . . .	35
2.9	Saturation profiles of three-phase IM used for the experimental validation. . . . .	37
2.10	IM's equivalent circuit while performing the locked-rotor test. . . . .	38
2.11	Rotor resistance profile due to the skin effect of the IM used for the experimental validation. . . . .	39

2.12 Steady-state torque-speed profile at the rated supply conditions of the IM used for the experimental validation. . . . .	41
2.13 MTPA and MTPV for three-phase IM in the current $dq$ plane (left) and flux plane (right), for both motoring and generating modes. . . . .	47
2.14 Saturation profile of the magnetizing and stator inductances of the IM used for the experimental validation. . . . .	50
2.15 Stator flux linkage $dq$ maps of the IM used for the experimental validation. . . . .	51
2.16 Electromagnetic torque map of the IM used for the experimental validation. . . . .	52
2.17 MTPS profiles for MUT at different dc-link voltage and machine temperature. . . . .	53
2.18 MTPS profiles of the mechanical power for MUT at different dc-link voltage and machine temperature. . . . .	53
2.19 Flow diagram of the proposed mapping procedure. . . . .	55
2.20 Computed efficiency maps at $v_{dc} = 400$ V (left) and $v_{dc} = 600$ V (right) using the maximization of the efficiency. . . . .	62
2.21 Efficiency maps at $v_{dc} = 400$ V using the minimization of the stator Joule losses (MTPA) (left) and minimum stator flux (right). . . . .	64
2.22 View of the IM under test (left), torque transducer (center), and driving machine (right). . . . .	65
2.23 Configuration of the electric drive for the experimental validation . . . . .	68
2.24 Torque control scheme of the IM under test (the superscript $\sim$ denotes an estimated parameter or variable). . . . .	68
2.25 The stator winding temperatures during the measured efficiency mapping. . . . .	71
2.26 Experimental validation of IM mapping. . . . .	72

3.1	Equivalent circuit of IPM machine in rotating reference frame without iron losses. . . . .	81
3.2	IPM equivalent circuit with iron losses (top) and equivalent Thevenin simplification (bottom). . . . .	82
3.3	Three-phase voltage source inverter. . . . .	84
3.4	$d$ -axis flux linkages at $\vartheta_{PM} = 20^\circ\text{C}$ (left, blue) and $\vartheta_{PM} = 150^\circ\text{C}$ (right, red). . . . .	89
3.5	$q$ -axis flux linkages at $\vartheta_{PM} = 20^\circ\text{C}$ (left, blue) and $\vartheta_{PM} = 150^\circ\text{C}$ (right, red). . . . .	89
3.6	Electromagnetic torque at $\vartheta_{PM} = 20^\circ\text{C}$ (left, blue) and $\vartheta_{PM} = 150^\circ\text{C}$ (right, red). . . . .	89
3.7	Flux maps: $d$ -axis flux linkage (left) and $q$ -axis flux linkage (right) at $\vartheta_{PM} = 20^\circ\text{C}$ . . . . .	91
3.8	2D flux linkage at PM temperature of $20^\circ\text{C}$ . . . . .	91
3.9	Details of 2D flux linkage at PM temperature of $20^\circ\text{C}$ for 3 different currents. . . . .	92
3.10	Flux maps: $d$ -axis flux linkage (left) and $q$ -axis flux linkage (right) at $\vartheta_{PM} = 150^\circ\text{C}$ . . . . .	92
3.11	Details of 2D flux linkage at PM temperature of $150^\circ\text{C}$ for 3 different currents. . . . .	93
3.12	PM flux at different PM temperatures. . . . .	93
3.13	Torque maps at different PM temperatures: $\vartheta_{PM}=20^\circ\text{C}$ (left) and $\vartheta_{PM}=150^\circ\text{C}$ (right). . . . .	94
3.14	MTPS profile in motoring and generating modes for different dc-link voltages: $\vartheta_{PM} = 20^\circ\text{C}$ (left) and $\vartheta_{PM} = 150^\circ\text{C}$ (right). . . . .	95
3.15	MTPS profile in motoring and generating modes for different PM temperatures at $v_{dc} = 400\text{ V}$ . . . . .	95
3.16	MTPA and MTPV locus in current and flux planes at $\vartheta_{PM} = 20^\circ\text{C}$ . . . . .	96

3.17 MTPA and MTPV locus in current and flux planes at $\vartheta_{PM} = 150^\circ\text{C}$ . . . . .	96
3.18 Iron losses for different working points evaluated with FEA simulations. . . . .	97
3.19 Stator voltage in time domain evaluated with FEA simulation: 5 Nm, 1 krpm (left) and 220 Nm, 5 krpm (right). . . . .	98
3.20 Stator voltage in $\alpha\beta$ and $dq$ reference frame: 5 Nm, 1 krpm (left) and 220 Nm, 5 krpm (right). . . . .	98
3.21 Iron losses map (@ $\vartheta_{PM} = 150^\circ\text{C}$ ) and deviation line. . . . .	99
3.22 Stator resistance map provided by the manufacturer in function of stator temperature and rotor speed. . . . .	100
3.23 Mesh of operating points in the torque-speed plane. . . . .	101
3.24 Stator Joule loss maps in kW of the IPM machine with maximum efficiency control in cold (left) and hot (right) conditions at $v_{dc} = 400\text{ V}$ . . . . .	110
3.25 Efficiency maps of the IPM machine with maximum efficiency control in cold (left) and hot (right) conditions at $v_{dc} = 400\text{ V}$ . . . . .	110
3.26 eDrive efficiency maps of the IPM machine with MTPA control (left) and efficiency difference considering maximum efficiency and MTPA control strategies (right) in cold conditions at $v_{dc} = 400\text{ V}$ . . . . .	112
3.27 Efficiency maps of the eDrive with efficiency maximization at $v_{dc} = 300\text{ V}$ (left) and $v_{dc} = 500\text{ V}$ (right). . . . .	112
3.28 Electrical loss map in kW in cold conditions at $v_{dc} = 400\text{ V}$ (left) and $v_{dc} = 500\text{ V}$ (right). . . . .	113
3.29 Stator voltage map in Volt in cold conditions at $v_{dc} = 400\text{ V}$ (left) and $v_{dc} = 500\text{ V}$ (right). . . . .	113
3.30 Stator current map in Ampere in cold conditions at $v_{dc} = 400\text{ V}$ (left) and $v_{dc} = 500\text{ V}$ (right). . . . .	113



3.31	The four $(T_m, \omega_m)$ planes selected in the first step of the 4D interpolation. . . . .	115
3.32	(Voltage, temperature) plane in the second step of the 4D interpolation. . . . .	117
4.1	Multiple three-phase squirrel cage IM. . . . .	124
4.2	Draft for the mutual inductance and magnetic flux computations. . . . .	126
4.3	Equivalent VSD magnetic scheme of a multi-three-phase squirrel cage IM: multi-three phase stator (left) and multi-three phase rotor (right). . . . .	135
4.4	Magnetic axes angle displacement of the multi-three-phase IM in one electrical revolution. . . . .	141
4.5	Equivalent MS circuit of a multi-three-phase IM in stationary $\alpha\beta 0$ coordinates. . . . .	147
4.6	Rotating $dq$ reference frame. . . . .	148
4.7	Phase magnetic axes in an asymmetrical twelve-phase machine. . . . .	155
4.8	Equivalent VSD circuit of a multi-three-phase IM in stationary components. . . . .	162
4.9	Equivalent MS circuit of a multi-three-phase IM in stationary coordinates after the application of the decoupling transformation. . . . .	170
4.10	A view of the magnetic axes of the asymmetrical 12-phase IM. . . . .	176
4.11	Conductors' distribution of the 12-phase IM. . . . .	177
4.12	Sketch of the test rig used for parameter measurement elaborated in phase-coordinates. . . . .	179
4.13	Equivalent VSD circuit of the machine in the main subspace in the stationary reference frame $\alpha\beta$ including the iron losses. . . . .	181
4.14	Sketch of the test rig used for parameter measurement elaborated using VSD approach. . . . .	183

4.15	Procedures of the standard tests elaboration. . . . .	184
4.16	The equivalent rotor resistance for different winding configurations as a function of the slip frequency. . . . .	186
4.17	The equivalent locked-rotor inductance for different winding configurations. . . . .	187
4.18	The rotor resistance as a function of the slip frequency. . . . .	188
4.19	Mechanical losses of the tested IM. . . . .	190
4.20	The equivalent magnetizing inductance for different winding configurations. . . . .	192
4.21	Iron losses for one and four active sets at different frequencies (left) and iron losses at 60 Hz (right). . . . .	193
4.22	Experimental iron losses map with 1 active set (left) and four active sets (right) in function of frequencies and stator flux linkage. . . . .	193
4.23	Multi-three-phase IM's equivalent circuit of the no-load test. . . . .	194
4.24	Magnetizing inductance vs. peak magnetizing current with MS and VSD approach. . . . .	196
4.25	Spatial vector diagrams of the air-gap MMF harmonics for the 4-three-phase winding. . . . .	198
4.26	MMF distribution for each set ( $x = 1, \dots, 4$ ) (left), the MMF distribution in the air-gap (right) with four active sets. . . . .	198
4.27	MMF distribution for each set ( $x = 1, \dots, 4$ ) (left), the MMF distribution in the air-gap (right) with three active sets. . . . .	199
4.28	MMF distribution for each set ( $x = 1, \dots, 4$ ) (left), the MMF distribution in the air-gap (right) with two active sets. . . . .	200
4.29	MMF distribution for each set ( $x = 1, \dots, 4$ ) (left), the MMF distribution in the air-gap (right) with one active sets. . . . .	201
4.30	Magnetizing inductance in both normal and faulty conditions based on MS approach. . . . .	209

4.31 Stator flux linkage $dq$ maps of the 12-phase IM in normal conditions: 4 active set (MS approach). . . . .	210
4.32 Stator flux linkage $dq$ maps of the 12-phase IM in open-winding fault conditions: 3 active sets (MS approach). . . . .	210
4.33 Stator flux linkage $dq$ maps of the 12-phase IM in open-winding fault conditions: 2 active sets (MS approach). . . . .	211
4.34 Stator flux linkage $dq$ maps of the 12-phase IM in open-winding fault conditions: 1 active set (MS approach). . . . .	211
4.35 Stator flux linkage $dq$ profiles of 12-phase IM in different machine conditions using MS approach: $I_q=0$ A (left) and $I_d=0$ A (right). . . . .	212
4.36 Electromagnetic torque maps of the 12-phase IM in both conditions: 4 active sets (a), 3 active sets (b), 2 active sets (c), 1 active set (d). . . . .	213
4.37 Stator current mapping in $dq$ rotor flux fame. . . . .	214
4.38 MTPA profile in current (left) and flux (right) planes in normal conditions: $n_{ON} = 4$ . . . . .	215
4.39 MTPA profile in current (left) and flux (right) planes in faulty conditions: $n_{ON} = 3$ . . . . .	215
4.40 MTPA profile in current (left) and flux (right) planes in faulty conditions: $n_{ON} = 2$ . . . . .	216
4.41 MTPA profile in current (left) and flux (right) planes in faulty conditions: $n_{ON} = 1$ . . . . .	216
4.42 Magnetizing inductance in all machine configurations based on VSD approach. . . . .	220
4.43 Stator flux linkage $dq$ maps of the 12-phase IM in all machine configurations (VSD approach). . . . .	220
4.44 Electromagnetic torque map of the 12-phase IM in all machine configurations (VSD approach). . . . .	221

4.45 MTPA profile in current plane in both normal and faulty conditions: $n_{ON} = 4, \dots, 1$ . . . . .	222
4.46 Magnetizing inductance in all machine configuration based on A-DMS approach. . . . .	225
4.47 Stator flux linkage $dq$ profiles of 12-phase IM in different machine conditions using A-DMS approach: $I_q=0$ A (left) and $I_d=0$ A (right). . . . .	225
4.48 A flow diagram of the MTPS computation able to handle different mathematical approaches (i.e., MS, VSD/DMS, A-DMS) for both normal and open-winding faulty conditions is reported in Fig. 4.48. . . . .	228
4.49 Multi-three-phase IM steady-state equivalent circuit in the rotating $dq$ reference frame. . . . .	234
4.50 MTPs torque, mechanical power, stator current, stator flux profiles in normal and faulty conditions. . . . .	238
4.51 MTPS torque and mechanical power profiles in faulty conditions ( $n_{ON} = 3$ ) for different dc-link voltages. . . . .	239
4.52 Flow diagram of the mapping algorithm with different approaches in both normal and open-winding faulty conditions. . . . .	242
4.53 Computed efficiency maps based on the MS approach maximizing the efficiency: $n_{ON} = 4, 3, 2, 1$ . . . . .	253
4.54 Computed efficiency maps based on the VSD/DMS approach maximizing the efficiency: $n_{ON} = 4, 3, 2, 1$ . . . . .	254
4.55 Computed efficiency maps based on the A-DMS approach maximizing the efficiency: $n_{ON} = 4, 3, 2, 1$ . . . . .	255
4.56 Computed efficiency maps based on the MS approach minimizing the stator Joule: $n_{ON} = 4, 3, 2, 1$ . . . . .	256
4.57 Computed efficiency maps based on the VSD/DMS approach minimizing the stator Joule: $n_{ON} = 4, 3, 2, 1$ . . . . .	257
4.58 Computed efficiency maps based on the A-DMS approach minimizing the stator Joule: $n_{ON} = 4, 3, 2, 1$ . . . . .	258

4.59 12-phase IM. . . . .	260
4.60 Schematic block diagram of the test rig for the experimental validation of multi-three-phase IM mapping. . . . .	260
4.61 Schematic block diagram of the test rig for the experimental validation of multi-three-phase IM mapping. . . . .	261
4.62 Rotating stator flux frame $dqs$ . . . . .	264
4.63 Drive configuration for the experimental validation of multi- three-phase IM mapping. . . . .	265
4.64 Computed and experimental efficiency maps at $v_{dc} = 150\text{ V}$ with the related percentual error map for healthy conditions ( $n_{ON} = 4$ ). . . . .	269
4.65 Computed and experimental efficiency maps at $v_{dc} = 150\text{ V}$ with the related percentual error map for faulty conditions ( $n_{ON} = 3$ ). . . . .	270
4.66 Computed and experimental efficiency maps at $v_{dc} = 150\text{ V}$ with the related percentual error map for faulty conditions ( $n_{ON} = 2$ ). . . . .	271
4.67 Computed and experimental efficiency maps at $v_{dc} = 150\text{ V}$ with the related percentual error map for faulty conditions ( $n_{ON} = 1$ ). . . . .	272
4.68 Computed and experimental efficiency maps at $v_{dc} = 100\text{ V}$ with the related percentual error map for normal conditions ( $n_{ON} = 4$ ). . . . .	273

# List of Tables

2.1	Measured parameters . . . . .	40
2.2	Machine's primary data . . . . .	66
3.1	IPM machine data . . . . .	88
3.2	Interpolation results for 3-IPM . . . . .	118
4.1	Harmonic content of the MMF with four active sets. . . . .	199
4.2	Harmonic content of the MMF with 3 active sets. . . . .	200
4.3	Harmonic content of the MMF with 2 active sets. . . . .	201
4.4	Harmonic content of the MMF with 1 active set. . . . .	202
4.5	MTPA maximum torque @ $I_{max} = 24 A$ . . . . .	216
4.6	Machine primary data . . . . .	259

# Chapter 1

## Introduction

One of the key factors in combatting climate change is electrification: transitioning from burning fossil fuels to electricity. There are more existing means to clean up electricity than combustion fuels, like geothermal, hydro, nuclear, solar, and wind [1, 2]. In this context, wind and photovoltaic energy production are undergoing impressive technological development to improve their production capability and energy efficiency. However, in parallel with the advancements in energy production, the transport sector is experiencing relevant changes. Indeed, following the future European directives [2] concerning the reduction of both global and local emissions, the leading automotive companies are moving towards the electrification of the vehicles [3]. In addition, interesting innovations are emerging in both aircraft and aerospace sectors with the current paradigm of More Electric Aircraft (MEA) and More Electric Engine (MEE) [4, 5], moving toward an electrified system [6, 7].

These ongoing changes have a fundamental impact on the electrical components, which also means new challenges for a massive redefinition of the technological development plans. This essential technological step requires intelligent and reliable solutions to replace conventional ones [8, 9] and a quick and smart simulation solutions for analyses of them. Virtualization is a new method for the simulation of the whole drive system behaviour. The main goal of virtualization is to provide a new operational environment, which is not bound to any particular computer hardware or operating system.

Virtualization allows integrated, system-wide upgrades and additional functionality without additional hardware by effectively separating functionality from hardware. Consequently, virtualization allows markedly reducing the need for expensive and time-consuming testing activities [10].

## 1.1 Review of the previous research

### 1.1.1 Virtualization

In this scenario where sustainability is top of mind, electrical drive components (eDrive), i.e., electrical machines and power converters, cover a key role, which virtualization is fundamental for system energetic assessment [6, 7, 11]. The virtualization of the eDrive components can be performed differently based on the constraints in terms of accuracy, simulation time, and detail level. In the technical literature, the following approaches are often proposed to virtualize the eDrive components:

- **Constant efficiency models:** regardless of the operating conditions in terms of speed, torque, temperature, and available supply voltage level, it is assumed that the power converter and the electrical machine perform the energy conversion with constant efficiency [12, 13]. This approach is affordable and straightforward for energetic assessments of the whole powertrain. However, it leads to low accurate results when the eDrive is not operated at a fixed working point, and it does not represent an electrical engineering point of view.
- **Efficiency map models:** different efficiency values are defined for several points in the electric machine's operative torque-speed plane and the voltage-current plane for the power electronic converter [14, 15]. This approach is particularly suitable for energetic assessments of complex systems where the Drive operates at different torque-speed working points. The method accuracy heavily depends on the map's discretization and the operative conditions to which the maps refer. Different methods for efficiency map evaluation can be adopted.



- **Computer-aided engineering (CAE) models:** the goal is to integrate all simulations and disciplinary analyses into a multidisciplinary virtual engineering environment that combines the modeling of operational scenarios with the consolidation, refinement, and integration of experimental data and operational data [16].

Detailed and accurate simulations can be performed based on CAE [17]. This approach can provide very accurate results, but it requires complete knowledge of the components, the used materials and the production technologies, and, often, the boundary conditions imposed by the surrounding ambient. Despite the accuracy of the high results, this approach requires high expertise in the model definition. It is very time-consuming both in the model setup and in its resolution.

- **Co-simulation platforms:** this approach can greatly improve the simulation accuracy by integrating the advantages of different software in a unified system [18, 19]. For instance, transient analyses based on CAE models of the electric machine are linked to numerical/analytical simulations, which define the machine's supply conditions based on the control strategy [20]. This approach often obtains accurate results, although it requires considerable computation time.

### 1.1.2 Performance evaluation based on efficiency maps

In virtualization, the efficiency map models are commonly used to illustrate and compare electric machines performance [21–25]. An efficiency map of an electrical machine is a contour plot of the machine efficiency defined in the torque-speed plane, covering all possible operating points. Also, for energetic evaluations of electrified systems, these models based on machine losses and efficiency usually represent the most convenient solution [14, 22, 15]. Many works on the applications of efficiency maps in the design and optimization of electrical machines have been published [26].

To address the efficiency mapping evaluation, in the mid-1990s, several studies were undertaken to investigate possible methods of determining motor efficiency [27]. The literature reports different solutions for computing efficiency maps of both synchronous and induction motors (IMs)

[14, 21, 28, 27, 29–31]. However, most of these solutions are based on finite element analysis (FEA) using the machine design data, thus assuming these last known inputs [24, 28, 30, 32, 33]. Although this approach sometimes requires significant computing resources and demanding calibration procedures, it still represents the most used solution to avoid the experimental measurement of efficiency maps of the motor under test, thus saving cost for expensive test rigs.

**Experimental tests** for efficiency measurement require sophisticated and accurate test facilities. It is also undoubtedly time-consuming for post-processing related to data analysis for each torque-speed point of the working area. Accurate measurements and mounting the components under test on a dedicated test rig are necessary to apply the different shaft load/speed values [34]. Moreover, measurements have to be performed when steady-state thermal conditions have been achieved, guaranteeing, as much as possible, the same components' temperature for all the tested points. Therefore, from the testing activity standpoint, the measurements of all electromechanical variables for the efficiency maps reconstruction are highly time-consuming and unquestionably impracticable.

However, in [35] an estimation method for an efficiency map based on a limited number of measured points and a simple test is presented. The proposed procedure provides two parts of experimental tests: flux-linkage map measurement and efficiency maps. This procedure is complicated because many aspects should be considered, as mentioned before [36]. But above all, the experimental investigation of the efficiency maps requires that the machine/prototype is already constructed. This aspect deviates from the virtualization concept.

**FE calculations** for efficiency mapping are also a time-consuming process. Conversely, FE simulations are a powerful tool to evaluate the electric machine losses in different working points and supply conditions [22, 37, 38]. Although this approach can get quite accurate results, mainly when three-dimensional transient simulations are performed, it requires complete knowledge of the machine design data and the detailed characteristics of the used materials; these drawbacks often limit the applicability of this method. However, the FEA results need a benchmark for comparison. The benchmark should be the efficiency and loss maps that are experimentally obtained

using a dedicated test rig, and accurate measurements [39]. Other works in literature for motor design optimization based on mapping combine FE simulations with analytical methods to reduce computational time. In [40], the FE analysis is carried out in the rotor flux reference frame so that only magnetostatic FE simulations are used, reducing the computational time for the prediction of the IM performance.

The **equivalent circuit methods** represent a good compromise between simulation time and results accuracy for performance investigation. In particular, steady-state equations are solved in closed form, and the different loss components are analytically computed for each working point [37] of the machine or modeled through an experimental lookup table [41]. The model accuracy depends on the considered nonlinearities of the equivalent machine parameters. For instance, the supply frequency and the working temperature impact the winding resistance, while the magnetic saturation phenomena on the stator and rotor cores affect the magnetizing inductance. The equivalent circuit parameters necessary for these analyses can be obtained either by the machine's design data, if available, or by standard tests at no-load and locked-rotor conditions. Some works in literature adopt the equivalent circuit methods based on the flux-linkage and iron losses, which give an estimation of efficiency maps not very thorough [39, 42, 43]. A fast method based on the theoretical approach presented in [39] has been presented for iron loss estimation for the mapping goal.

Nevertheless, it is highlighted how the literature contributions aimed at efficiency mapping are still limited despite the impressive development of know-how in recent years. The electrical machine manufacturers usually provide efficiency information only for a few working points, thus rarely providing efficiency maps. Moreover, even if efficiency maps are provided, they typically refer to a specific machine temperature and a defined supply voltage. While this level of information may be sufficient for machines operated at a fixed working point, it may not be accurate enough when variable operations in wide torque-speed ranges are considered [3, 8, 9, 37, 38]. Indeed, in these cases, the terminal voltage and the machine temperature can assume very different values in function of the required torque and speed profiles.

For this reason, the first part of the dissertation is focused on the methodology of efficiency mapping for three-phase IMs and synchronous IPM based on the equivalent circuit/analytical models, using limited input data provided by standard tests for IM and FE simulations for IMP machines. The experimental results confirmed that quick but accurate mappings have been developed.

### **1.1.3 Multiphase machine: drive configurations, modelling and performance**

Multiphase electrical machines are today a competitive solution in the electrification processes of transport and energy production for more efficient solutions [44, 45]. Nowadays, multiphase solutions can be considered a competitive alternative to the conventional three-phase ones [46] for several advantages in this green future scenario. When the power range increases to MW levels, the phase voltage must be increased to keep the phase currents at acceptable limits that can be handled with today's power electronic components, highlighting the importance of the multiphase solution. Furthermore, conventional three-phase structures are unreliable in safety-critical applications since they do not possess the fault-tolerance capability. In this context, the multiphase drives represent a good solution. They are suitable for high-reliability applications since they keep inherent fault tolerance capability from their redundant structure.

The most relevant contributions to the development of multiphase motor drives have been published in the last three decades by covering many technical aspects [44, 46–49]. The multiphase solutions have been historically employed in high power, and safety-critical applications [49], like naval and aircraft [50] applications. Currently, they represent a standard in the marine applications for both ship propulsion [50, 51] and on-board generation [52]. However, until today the multiphase application is minimally invasive for low-value power levels. The multiphase solution in automotive is used for low voltage systems fed by 48 V, keeping low current values [44].

The research on multiphase drives has been split up into subtopics, thus achieving a high level of know-how in many aspects. From the machine modeling, drive configuration up to the drive control techniques [47].

### Multiphase drive configurations

Concerning the literature, the most employed multiphase drive configurations (machine and inverter) are the following:

- Conventional multiphase with single machine neutral: it represents a standard drive having a prime number of phases, as shown in Fig. 1.1, highlighting the impossibility of a modular stator. The main disadvantage of this structure is related to the fault-tolerant operation because the power converter consists of a multiphase VSI [44].
- Multiple independent single-phase units can fulfill the requirements of fault-tolerant operation for safety-critical applications. Each machine phase is fed by a dedicated single-phase inverter, as shown in Fig. 1.2. This solution, in combination with the fractional-slot concentrated windings, gets the best fault-tolerant operation when each converter can be disconnected from the DC source. Another exciting advantage of this solution is the highest voltage utilization of the DC-link for motoring operation since the maximum peak phase voltage is the DC-link voltage.

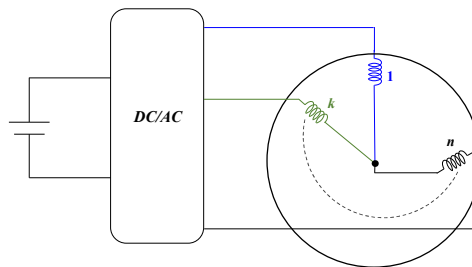


Figure 1.1 Multiphase drive topology with single neutral point.

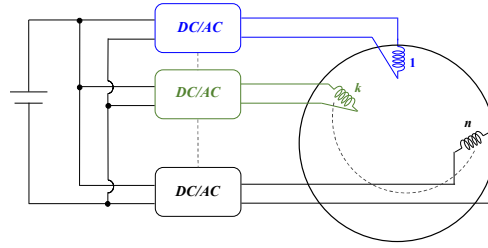


Figure 1.2 Multiphase drive topology using multiple single-phase units.

- Multiple independent three-phase units: the phase number is a multiple of three (symmetrical or asymmetrical machine), and the stator consists of separate three-phase windings with isolated neutral points (see Fig. 1.3). Each three-phase set is supplied by an independent three-phase inverter for this configuration. This topology is less attractive than the previous one from the fault-tolerant point of view. In case of fault, the faulted three-phase set (including the converter) is disconnected from the DC power supply. However, the power converter can use well-consolidated three-phase power electronics modules, reducing the converter size, cost, and design time. The main advantage of this solution is the possibility of using well-consolidated three-phase technologies, thus significantly reducing costs and design times.

Moreover, among all the possible multiphase configurations, there is a strong interest in the development of the modular ones for modeling similar to three-phase counterparts, for modular control schemes, and because they use consolidated power electronics technologies [5]. Indeed, among the modular multiphase configurations in recent years, the multiple three-phase drives have gained growing attention from industrial manufacturers [44, 53].

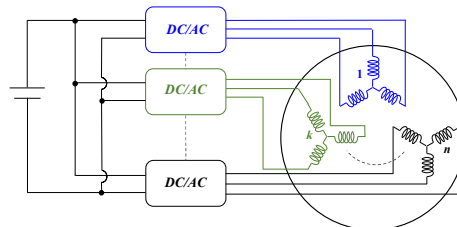


Figure 1.3 Multiphase drive topology with multiple three-phase units.

Indeed, these solutions can use well-consolidated three-phase technologies, thus leading to a significant cost reduction [5].

### **Multiphase machine configuration and modelling**

The stator winding of multiphase machine can be designed in such a way that the spatial displacement between any two consecutive stator phases equals  $\alpha = 2 \cdot \pi/n$ , obtaining a symmetrical multiphase machine. This will always be the case if the number of phases is an odd prime number. However, if the number of phases is an even number or an odd number that is not a prime number, stator winding may be realized differently. In such a case, the spatial displacement between the first phases of the two consecutive a subphase windings is  $\alpha = \pi/n$ , leading to an asymmetrical distribution of magnetic winding axes in the cross section of the machine (asymmetrical multiphase machines) [47].

### **Vector space decomposition**

According to the literature [5, 54], most of the multiphase works are based on the vector space decomposition (VSD) approach [55], allowing the use of the control algorithms defined for three-phase motor drives. The VSD decomposes the machine model into multiple orthogonal subspaces using a dedicated VSD matrix transformation. The energy conversion is performed in a single subspace, having the meaning of the machine's time-fundamental model [56], characterized by electromagnetic equations similar to the three-phase motors. The other subspaces have the meaning of the machine's harmonic patterns, highlighting possible unbalance among the stator phases in terms of currents, fluxes, and torque [57]. The VSD transformation matrix exists for multiphase machines with the stator winding in either symmetrical or asymmetrical configuration [58], thus covering most practical cases. Still, it is the first disadvantage in post-fault operation [59]. The second limitation is the lack of modularity [47], as the VSD does not emphasize the torque production of each winding set composing the stator.

### **Multi-stator**

The drawbacks of the VSD in dealing with the modular configurations can

be solved with the multistator (MS) modeling [60]. This approach models the machine as multiple winding sets operating in parallel. Each of these must consist of an  $l$ -phase configuration ( $l \geq 3$ ), having an isolated neutral point. In this way, the torque production of each set is highlighted through its own time-fundamental VSD subspace. An example is represented by the multi-three-phase machines [61], where the stator consists of multiple three-phase winding sets, allowing the use of the three-phase Clarke transformation. Therefore, if a machine having  $n$  winding sets is considered,  $n$  time-fundamental VSD subspaces are obtained. Each of the latter highlights the torque produced by the windings set of which it is representative. In summary, MS modeling can be considered as a modular application of the VSD approach to multiphase machines. In this way, the VSD constraints in symmetrical and asymmetrical configurations are restricted to the single  $l$ -phase winding set [61].

### **Decoupling multi-stator**

Recently, some attempts to combine the advantages of the VSD and MS approaches have been proposed [62]. In [63], general solutions that consider a generic number of winding sets have been developed, leading to the definition of the decoupled MS (DMS) approach. The DMS-based control scheme is structured like a VSD-based one but keeps the modularity features. Nevertheless, like the VSD-based schemes, the solution proposed in [63] requires implementing additional control modules to perform the post-fault drive operation. Indeed, if an open three-phase fault occurs, the VSD- and DMS- based control schemes need the active control of the secondary subspaces to keep the machine currents balanced and within their boundaries, as well as continuity of the torque production. In other words, implementing additional control modules with dedicated fault-tolerant strategies is necessary to manage the time-harmonic subspaces for the VSD-based solutions and the differential-mode subspaces for the DMS ones and further losses characterized by the post-fault operation. As a result, the simplicity that characterizes the VSD-based and DMS-based control schemes is lost.

### **Adaptive decoupling multi-stator**

The drawbacks highlighted can be avoided by adapting the machine mod-



eling by considering a *real* stator winding configuration considering just healthy/active winding sets. Thanks to the properties previously mentioned, the DMS-based control schemes always allow changing on-the-fly the decoupling transformation, i.e., adapting it to the post-fault configuration of the stator winding. Thus, defining a so-called adaptive DMS (A-DMS) modeling is possible. This solution is not viable for VSD-based modeling since the post-fault configuration of the stator winding hardly satisfies the constraint of being symmetrical or asymmetrical [59].

### **Multiphase performace**

A high-level investigation of electrical machines with more than three phases has been carried out in [64] by analytical means and offers some results regarding the fundamental losses and pulsating torque. In [64] the authors used a base machine design with the number of stator phases and the stator winding arrangement as variables. The possible reduction of stator copper losses was considered to be the main contribution to [65] increase the efficiency through multiphase technology. According to [64], the reduction lies within the range of 4 – 8% depending on the number of phases. The lower harmonic content in the airgap field also leads to a decrease in rotor copper losses as well, on a smaller scale. The dependency of stator and rotor copper losses on the number of phases has been verified by measurement with VSI supply in [65]. The iron losses of the fundamental are expected to be independent of the number of phases for the same airgap flux and load conditions. In [66] measurements on a high frequency three-phase and dual-three-phase IM configuration with pulse width modulation (PWM) inverter supply were performed. The measurement results for the total motor efficiency do not show a significant increase due to the low proportion of stator copper losses in the total losses for high-frequency applications. The interconnection of stator coils realized the multiphase configurations mentioned above, and the rated excitation voltage was varied in inverse proportion to the phase number. Most investigations on efficiency related topics for multiphase machines are either dedicated to respective loss components, e.g., copper losses, or the total motor and drive efficiency [67] [68].

Despite an effort in the literature, there's still more research to be done to better the performance evaluation of multiphase machines. Another fundamental aspect not investigated is the performance evaluation of the multiphase machine in open-winding faulty operating conditions. For this reason, the second part of the dissertation focuses on mapping the multi-three-phase machine in healthy and open-winding faulty conditions. Different mathematical approaches have been used, emulating different machine control strategies. The critical and expensive experimental validation confirms the effectiveness of the developed algorithm. The machine control for experimental validation is based on the reference values obtained with the offline mapping.

## 1.2 Research objectives

The thesis goal has been obtained by developing the following objectives for three-phase IMs, IPM machines, and multi-three-phase IMs:

- Development of the three-phase machine modeling of IMs and IPM machines in stationary conditions, allowing the reconstruction of all the electromechanical variables based on a few inputs.
- Development of various modeling approaches, i.e. MS, VSD, DMS, ADMS, in steady-state conditions of multiphase IMs, allowing the reconstruction of all the electromechanical variables.
- Understand how to model multiphase IMs in open-winding faulty operating conditions and the most appropriate approach for analyzing the faulty machine.
- Study the nonlinearities of machines such as saturation, iron losses, skin effect, etc., how they should be analyzed and how they should be considered in machine modeling for both three-phase and multi-three-phase machines.
- Development a general algorithm for three-phase IMs mapping, three-phase IPM machines, and multiphase IMs in steady state conditions,

which should allow the virtualization of machines for different working conditions. The mapping outputs should be organized in several matrices whose resolution depends on the torque and speed steps.

- Development multiphase IMs mapping under open-winding faulty operating conditions, considering how machine nonlinearities change under fault conditions.
- Development an interpolation method, which allows the reading of the calculated maps and, therefore, able to provide the operating conditions of the electrical machines (e.g., efficiency, current, voltage, losses, power factor, active/reactive powers) and VSI (e.g. efficiency, switching and conduction losses) for each possible working point of the eDrive and all machine conditions.

The conducted work comes from completing the objectives mentioned above. Starting with three-phase IMs and IPM machine modeling, an algorithm for the mapping has been proposed. An analytical approach is found, using a few input data provided by the standard tests for three-phase IM. In contrast, for three-phase IPMs synchronous machine, the initialization consists of the magnetic model in terms of flux and current evaluated by FEM analysis. In this way, the nonlinearities of the machines have been considered, allowing an accurate mapping.

The algorithm for multi-three-phase IMs has been developed in healthy and open-winding faulty conditions. The initialization of the proposed algorithm consists of the measured parameters, organized as a lookup table to consider the nonlinearities, evaluated in all possible machine conditions. The mapping has been developed using different mathematical machine models, giving the same results. The efficiency mapping codes have been experimentally validated.

## 1.3 Dissertation outline

The thesis is divided in 4 Chapters as follows:

**Chapter 1** provides an introduction to the importance of the electrical machines virtualization. This chapter is completed with a list of research objectives and a discussion of novelty and thesis structure.

**Chapter 2** provides the details of the mapping strategy of three-phase IMs. The algorithm is presented, demonstrating the validity of the methodology through the experimental validation.

**Chapter 3** provides the mapping of IPM machines, presenting the manipulation of the FEA results used as mapping input. The algorithm validation is provided, comparing the mapping results with the ones coming from numerical FEM analysis.

**Chapter 4** deals with the modeling of multi-three-phase IMs, the estimation of the machine parameters including the nonlinearities, and the mapping algorithm considering the healthy and open-winding faulty operating conditions. The algorithm has been developed with all approaches available in the literature, i.e., MS, VSD, DMS, ADMS. Most importantly, this chapter provides the experimental results of the proposed mapping in both operating conditions.

## 1.4 Conclusion

Electrification represents a suitable approach in the context of combatting climate change [1, 2]. New challenges for massive redefinitions of technological development plans are ongoing. However, these technical steps require intelligent and reliable solutions to replace the conventional ones [8, 9] and quick and innovative simulation solutions for analyzing the electrified system components. The virtualization of the electric components in an electrified system is a method with excellent potential to assess the system

design goodness in terms of efficiency and operational limits. Also, new solutions such as multiphase electrical machines are becoming attractive, resulting in more efficient and safer solutions [44, 45].

In this chapter, a literature survey providing state-of-the-art research in this field has been reported. The most relevant contributions to the development of performance evaluation of electrical components, i.e., electrical machines and power converters, have been published in the last four decades. The most common performance evaluation method is the torque-speed plane's efficiency map. Concerning the literature review, in the mid-1990s, several studies were undertaken to investigate possible methods of determining motor efficiency [27]. The literature reports different solutions for computing efficiency maps of both synchronous and asynchronous machines. However, most of these solutions are based on finite element analysis (FEA) using machine design data [22, 37, 38]. Although this approach sometimes requires significant computing resources and demands calibration procedures, it still represents the most used solution to avoid the experimental measurement of efficiency maps of the motor under test [34], thus saving cost for expensive test rigs. The latter approach requires sophisticated and accurate test facilities. It is also undoubtedly time-consuming for post-processing related to data analysis for each torque-speed point of the working area.

For this reason, this dissertation proposed a methodology for computing the efficiency maps of three-phase induction machines (IMs), interior permanent magnet (IPM) synchronous machines, and multi-three-phase IMs operated in wide torque-speed ranges. The main advantage of the proposed mapping approach relies on the possibility of obtaining efficiency maps, without the need for expensive test rigs or details on the machine design data, using the standard test results. Based on the efficiency, losses, etc. maps evaluated with the proposed algorithm, the electrical machines can be easily virtualized to perform energetic assessments on the final application, even if motor prototypes are not still available. The main novelty is multi-three-phase IM mapping in healthy and open-winding fault operating conditions. The developed algorithm is based on different mathematical approaches, replacing different control strategies, i.e., maximization/minimization of the efficiency/stator Joule losses.

## Chapter 2

# Three-phase Induction Machine Mapping

This chapter presents a straightforward and accurate methodology for computing the efficiency maps of induction motors (IMs) operated in wide torque-speed ranges. The proposed procedure uses the IM's equivalent circuit defined in the rotor flux  $dq$  coordinates to quickly obtain the efficiency maps of the machine both in motoring and generator operation, as well as considering the actual operating temperature and supply voltage level. Moreover, a significant advantage of the proposed methodology consists of computing the IM's efficiency maps by simply using the results of the standard test procedures like dc, no-load, and locked-rotor tests performed at different voltage and frequency levels. In this way, all machine's nonlinearities like magnetic saturation, skin effect, and iron losses are strictly considered. The proposed methodology has been validated on a 10 kW, 4 poles, 100 Hz IM prototype. Computed and experimental efficiency maps for different operating conditions are shown in this chapter, confirming the validity of the proposed methodology.

The chapter is organized as follows:

1. The steady-state model of the three-phase IM is reported in phase coordinates  $abc$ , in stationary reference frame  $\alpha\beta$ , and finally in rotating  $dq$  reference frame. The nonlinearities of the machine model as the iron losses and magnetic saturation are considered. Finally, the ma-

chine model in  $dq$  coordinates in steady-state conditions used for the mapping procedure is reported.

2. The implementation of the proposed mapping algorithm in  $dq$  coordinates is presented. Step by step, the algorithm is analyzed, describing how it has been organized. The outputs of the mapping algorithm consist of 4D matrices.
3. The experimental validation for different dc-link voltages and the machine at ambient temperature has been conducted on a 10 kW 4 pole IM prototype. The comparison between computed and measured efficiency maps shows a percentage error below 2% in most of the investigated torque-speed range, both for motoring and generator operation modes.

## 2.1 Three-phase induction machine modeling

The machine's dynamic model allows simulation of its behavior accurately, considering different working conditions in terms of the requested torque and speed at the machine shaft. Machine behavior also depends on the voltage supply and temperature. The electrical parameters shall be derived to obtain an accurate model. There are two possible approaches for knowing the machine parameters: first - design approach where all the project data are known, and second - experimental tests, as shown in the next section. However, if the machine parameters are evaluated at different voltage and/or frequency values, an accurate model can be implemented, thus providing a realistic scenario. Following from state, the variation of stator and rotor resistances, the iron losses, and magnetizing inductance, represent the model inputs. The variations of the parameters mentioned above are studied and implemented through two-dimensional lookup tables. After this, machine modeling can be implemented.

Modeling of three-phase alternating current (ac) machines usually considers the following hypotheses:

- Each machine phase is identical to the others.

- The machine windings are distributed across the stator's circumference and are designed to generate a sinusoidal magnetomotive force.
- The air gap is constant.
- The impact of the stator slots is neglected.
- Full decoupling between the leakage fluxes of the machine phases.

Note that the machine modeling obtained in the first section is ideal for computing the electromagnetic equations necessary for building an accurate model. After this, the iron losses and the magnetic saturation are added.

### 2.1.1 Machine model in phase coordinates

IMA are often called "asynchronous machines" since they operate below the synchronous speed in the motor operation, and above the synchronous speed in that of generation. A balanced set of three-phase currents flowing in a symmetrical set of three-phase windings produce a rotating magnetomotive force (*mmf*) given by:

$$F(\theta, t) = \frac{3}{2} \cdot \frac{4}{\pi} \cdot \frac{N}{2 \cdot p} \cdot I_m \cdot \cos(\theta - \omega \cdot t) \quad (2.1)$$

where  $\theta$  is the electrical angle measured from the magnetic axis of phase  $a$ ,  $\omega$  is the angular speed (rad/s) of the stator *mmf*, which depends on the electrical frequency  $f$  of the excitation currents  $I_m$ ,  $p$  is the number of the pole pairs, and  $N$  is the number of turns. The synchronous speed (rad/s) is computed as:

$$\omega_s = \frac{\omega}{p} \quad (2.2)$$

When the rotor is rotating at a constant speed of  $\omega_r$  (rad/s), the slip  $s$  between the rotor speed and that synchronous of the rotating magnetic field is defined as:

$$\omega_{sl} = \omega_s - \omega_r \quad (2.3)$$

The slip speed can be expressed in unit values as:

$$s = \frac{\omega_s - \omega_r}{\omega_s} \quad (2.4)$$



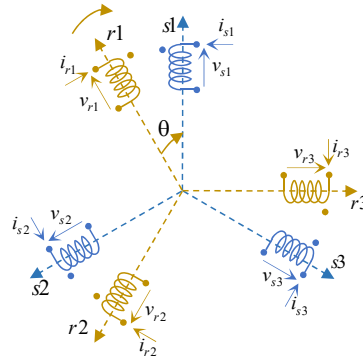


Figure 2.1 Winding distribution of three-phase IM.

Magnetically-coupled stator- and rotor- circuits are considered, as shown in Fig. 2.1. The passive sign convention is adopted. In the following, the electromagnetic equations associated with such circuits are reported [69, 70].

#### Stator electric model

The stator electric model in time-phase domain is expressed as [71]:

$$\bar{v}_{s123} = R_s \cdot \bar{i}_{s123} + \frac{d\bar{\lambda}_{s123}}{dt} \quad (2.5)$$

where  $R_s$  stands for the stator resistance (assumed equal for each stator winding),  $\bar{i}_{s123} = (i_{s1}, i_{s2}, i_{s3})^T$  represents the stator current vector,  $\bar{\lambda}_{s123} = (\lambda_{s1}, \lambda_{s2}, \lambda_{s3})^T$  stands for stator flux linkage vector, while  $\bar{v}_{s123} = (v_{s1}, v_{s2}, v_{s3})^T$  represents the stator voltage vector. The superscript  $T$  denotes the transposition of the considered array. All vectors are defined in phase coordinates 123.

#### Rotor electric model

$$\bar{v}_{r123} = \bar{0} = R_r \cdot \bar{i}_{r123} + \frac{d\bar{\lambda}_{r123}}{dt} \quad (2.6)$$

where  $R_r$  stands for rotor resistance (assumed equal for each rotor winding),  $\bar{i}_{r123} = (i_{r1}, i_{r2}, i_{r3})^T$  represents the rotor current vector while  $\bar{\lambda}_{r123} = (\lambda_{r1}, \lambda_{r2}, \lambda_{r3})^T$  stands for rotor flux linkage vector. Note that the rotor voltage vector  $\bar{v}_{r123} = (v_{r1}, v_{r2}, v_{r3})^T$  has an amplitude equal to zero  $\bar{v}_{r123} = (0, 0, 0)^T$  since a squirrel cage machine is considered.

#### Stator magnetic model

In terms of currents-to flux relationships, the flux linkage of the stator and

rotor windings can be written as:

$$\bar{\lambda}_{s123} = L_{l,s} \cdot \bar{i}_{s123} + M_{123}^{ss} \cdot \bar{i}_{s123} + M_{123}^{sr} \cdot \bar{i}_{r123} \quad (2.7)$$

### Rotor magnetic model

$$\bar{\lambda}_{r123} = L_{l,r} \cdot \bar{i}_{r123} + M_{123}^{rs} \cdot \bar{i}_{s123} + M_{123}^{rr} \cdot \bar{i}_{r123} \quad (2.8)$$

where  $L_{l,s}$  and  $L_{l,r}$  represent the per phase stator and rotor leakage inductances, while  $M$  is the mutual inductance between the phase windings. The submatrices of the stator-to-stator and rotor-to-rotor winding inductances are defined as:

$$M_{123}^{ss} = M \cdot \begin{bmatrix} 1 & -1/2 & -1/2 \\ -1/2 & 1 & -1/2 \\ -1/2 & -1/2 & 1 \end{bmatrix}; \quad M_{123}^{rr} = M \cdot \begin{bmatrix} 1 & -1/2 & -1/2 \\ -1/2 & 1 & -1/2 \\ -1/2 & -1/2 & 1 \end{bmatrix} \quad (2.9)$$

Regarding the stator-to-rotor mutual inductances, these depend on the rotor electric angle as:

$$M_{123}^{sr} = (M_{123}^{rs})^T = M \cdot \begin{bmatrix} \cos(\theta_r) & \cos\left(\theta_r + \frac{2\pi}{3}\right) & \cos\left(\theta_r - \frac{2\pi}{3}\right) \\ \cos\left(\theta_r - \frac{2\pi}{3}\right) & \cos(\theta_r) & \cos\left(\theta_r + \frac{2\pi}{3}\right) \\ \cos\left(\theta_r + \frac{2\pi}{3}\right) & \cos\left(\theta_r - \frac{2\pi}{3}\right) & \cos(\theta_r) \end{bmatrix} \quad (2.10)$$

Finally, the magnetizing inductance is defined as:

$$M = \frac{N_s \cdot N_r}{\mathcal{R}_t} \quad (2.11)$$

where  $N_s$  and  $N_r$  stand for the number of equivalent turns, considering a sinusoidal distribution of both stator and rotor windings. Lastly,  $\mathcal{R}_t$  represents the air gap reluctance [72, 73].

Note that the idealized machine is described by six first-order time-differential equations, one for each winding. Such equations are coupled through the mutual inductances between the windings. In detail, the stator-to-rotor

coupling terms depend on the rotor position, thus changing in time if the rotor speed is different from zero.

Mathematical transformations like the Clarke (123 to  $\alpha\beta$ ) and the rotational ( $\alpha\beta$  to  $dq$ ) facilitate the machine model, transforming the time-differential equations as in the following.

### 2.1.2 Machine model in stationary coordinates

A two-phase equivalent machine is considered. The new fictitious machine is characterized by two couple of orthogonal windings, one for the stator and the other for the rotor. Both the frames of the stator  $s - \alpha\beta$  and rotor  $r - \alpha\beta$  are shown in Fig. 2.2. The three-phase IM model in the new frames  $\alpha\beta$  is obtained by applying the Clarke matrix to the variables expressed in phase coordinates, as reported in Eq. (2.12) for a generic variable  $f$ :

$$\begin{bmatrix} f_\alpha \\ f_\beta \\ f_0 \end{bmatrix} = [C] \cdot \begin{bmatrix} f_1 \\ f_2 \\ f_3 \end{bmatrix} = \frac{2}{3} \begin{bmatrix} 1 & -\frac{1}{2} & -\frac{1}{2} \\ 0 & \frac{\sqrt{3}}{2} & -\frac{\sqrt{3}}{2} \\ 1 & 1 & 1 \end{bmatrix} \cdot \begin{bmatrix} f_1 \\ f_2 \\ f_3 \end{bmatrix} \quad (2.12)$$

The coefficient in the matrix front defines the proprieties of the transformation. If the machine power is kept invariant, the coefficient in front of the matrix is equal to  $\sqrt{2/3}$ . If the amplitude of the vectors is kept invariant (from 123 to  $\alpha\beta$ ), the coefficient is  $2/3$ , as in Eq. (2.12). In this work, the amplitude invariant transformation  $\alpha\beta$  is used Eq. (2.12), making necessary the use of corrective coefficients for performing the power assessments of the machine. Based on Eq. (2.12), both the stator- and rotor- electrical equations can be written as in the following.

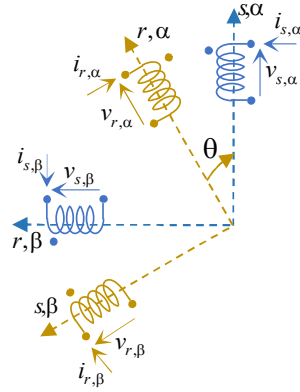


Figure 2.2 Stationary reference frame.

**Stator electric model**

$$\begin{aligned}
 [C] \cdot \bar{v}_{s123} &= [C] \cdot R_s \cdot \bar{i}_{s123} + [C] \cdot \frac{d\bar{\lambda}_{s123}}{dt} \Rightarrow \\
 \Rightarrow \bar{v}_{s\alpha\beta 0} &= R_s \cdot \bar{i}_{s\alpha\beta 0} + \frac{d\bar{\lambda}_{s\alpha\beta 0}}{dt}
 \end{aligned} \tag{2.13}$$

**Rotor electric model**

$$\begin{aligned}
 [C] \cdot \bar{v}_{r123} &= [C] \cdot R_r \cdot \bar{i}_{r123} + [C] \cdot \frac{d\bar{\lambda}_{r123}}{dt} \Rightarrow \\
 \Rightarrow \bar{v}_{r\alpha\beta 0} &= R_r \cdot \bar{i}_{r\alpha\beta 0} + \frac{d\bar{\lambda}_{r\alpha\beta 0}}{dt}
 \end{aligned} \tag{2.14}$$

**Stator magnetic model**

$$\begin{aligned}
 [C] \cdot \bar{\lambda}_{s123} &= [C] \cdot L_{l,s} \cdot \bar{i}_{s123} + [C] \cdot M_{123}^{ss} \cdot \bar{i}_{s123} + [C] \cdot M_{123}^{sr} \cdot \bar{i}_{r123} \Rightarrow \\
 \Rightarrow \bar{\lambda}_{s\alpha\beta 0} &= L_{l,s} \cdot \bar{i}_{s\alpha\beta 0} + M_{\alpha\beta 0}^{ss} \cdot \bar{i}_{s\alpha\beta 0} + M_{\alpha\beta 0}^{sr} \cdot \bar{i}_{r\alpha\beta 0}
 \end{aligned} \tag{2.15}$$

**Rotor magnetic model**

$$\begin{aligned}
 [C] \cdot \bar{\lambda}_{r123} &= [C] \cdot L_{l,r} \cdot \bar{i}_{r123} + [C] \cdot M_{123}^{rs} \cdot \bar{i}_{s123} + [C] \cdot M_{123}^{rr} \cdot \bar{i}_{r123} \Rightarrow \\
 \Rightarrow \bar{\lambda}_{r\alpha\beta 0} &= L_{l,r} \cdot \bar{i}_{r\alpha\beta 0} + M_{\alpha\beta 0}^{rs} \cdot \bar{i}_{s\alpha\beta 0} + M_{\alpha\beta 0}^{rr} \cdot \bar{i}_{r\alpha\beta 0}
 \end{aligned} \tag{2.16}$$

where the new matrices are defined as:

$$\begin{aligned} M_{\alpha\beta 0}^{ss} &= [C] \cdot M_{123}^{ss} \cdot [C]^{-1}, & M_{\alpha\beta 0}^{sr} &= [C] \cdot M_{123}^{sr} \cdot [C]^{-1} \\ M_{\alpha\beta 0}^{rs} &= [C] \cdot M_{123}^{rs} \cdot [C]^{-1}, & M_{\alpha\beta 0}^{rr} &= [C] \cdot M_{123}^{rr} \cdot [C]^{-1} \end{aligned} \quad (2.17)$$

The matrices in Eq. (2.17) are characterized by the following properties:

$$M_{\alpha\beta 0}^{ss} = M_{\alpha\beta 0}^{rr} \quad M_{\alpha\beta 0}^{rs} = \left(M_{\alpha\beta 0}^{sr}\right)^T \quad (2.18)$$

and they assume the following forms:

$$M_{\alpha\beta 0}^{ss} = M_{\alpha\beta 0}^{rr} = \frac{3}{2} \cdot M \cdot \begin{bmatrix} 1 & 0 & 0 \\ 0 & 1 & 0 \\ 0 & 0 & 0 \end{bmatrix}; \quad M_{\alpha\beta 0}^{sr} = \left(M_{\alpha\beta 0}^{rs}\right)^T = \frac{3}{2} \cdot M \cdot \begin{bmatrix} \cos(\theta) & \sin(\theta) & 0 \\ -\sin(\theta) & \cos(\theta) & 0 \\ 0 & 0 & 0 \end{bmatrix} \quad (2.19)$$

For a compact form, the electromagnetic model in the stationary reference frame is expressed as:

$$\begin{cases} \bar{v}_{s\alpha\beta 0} = R_s \cdot \bar{i}_{s\alpha\beta 0} + \frac{d\bar{\lambda}_{s\alpha\beta 0}}{dt} \\ \bar{v}_{r\alpha\beta 0} = R_r \cdot \bar{i}_{r\alpha\beta 0} + \frac{d\bar{\lambda}_{r\alpha\beta 0}}{dt} \end{cases} \quad \begin{cases} \bar{\lambda}_{s\alpha\beta 0} = L_{l,s} \cdot \bar{i}_{s\alpha\beta 0} + M_{\alpha\beta 0}^{ss} \cdot \bar{i}_{s\alpha\beta 0} + M_{\alpha\beta 0}^{sr} \cdot \bar{i}_{r\alpha\beta 0} \\ \bar{\lambda}_{r\alpha\beta 0} = L_{l,r} \cdot \bar{i}_{r\alpha\beta 0} + M_{\alpha\beta 0}^{rs} \cdot \bar{i}_{s\alpha\beta 0} + M_{\alpha\beta 0}^{rr} \cdot \bar{i}_{r\alpha\beta 0} \end{cases} \quad (2.20)$$

Regarding the stator and rotor zero sequence components 0, until now neglected, they are decoupled from the  $\alpha\beta$  axes as follows:

$$\begin{aligned} \begin{cases} v_{s0} = R_s \cdot i_{s0} + \frac{d\lambda_{s0}}{dt} \\ v_{r0} = R_r \cdot i_{r0} + \frac{d\lambda_{r0}}{dt} \end{cases} & \quad \begin{cases} \lambda_{s0} = L_{l,s} \cdot i_{s0} \\ \lambda_{r0} = L_{l,r} \cdot i_{r0} \end{cases} \Rightarrow \\ \Rightarrow & \quad \begin{cases} v_{s0} = R_s \cdot i_{s0} + L_{l,s} \cdot \frac{di_{s0}}{dt} \\ v_{r0} = R_r \cdot i_{r0} + L_{l,r} \cdot \frac{di_{r0}}{dt} \end{cases} \end{aligned} \quad (2.21)$$

### 2.1.3 Machine in rotating coordinates

The inductance matrices in Eq. (2.19) depend on the rotor position  $\theta$ . Therefore, the adoption of a rotating frame can be useful to avoid this drawback. Besides, from the machine modelling and control points of view, the use of rotating frames is useful. The electromagnetic model in a generic reference frame rotating at speed  $\omega_k$  is computed using the rotational matrix shown in Eq. (2.22).

$$R(\theta_k) = \begin{bmatrix} \cos(\theta_k) & -\sin(\theta_k) \\ \sin(\theta_k) & \cos(\theta_k) \end{bmatrix} \quad (2.22)$$

where  $\theta_k$  stands for the position of the frame, leading to as follows:

$$\omega_k = \frac{d\theta_k}{dt} \quad (2.23)$$

Considering the stator- and rotor- equations in stationary coordinates in Eq. (2.20), the rotational transformation in Eq. (2.22) is applied only to the  $\alpha\beta$  components. The  $0$ -sequence one is already decoupled, as shown in Eq. (2.21). Since the rotor position depends on the time, the rotational matrix cannot be included in the time derivative. The following artifice is performed for a generic variable  $f$ , i.e., current, voltage, flux:

$$\begin{bmatrix} f_{k1} \\ f_{k2} \end{bmatrix} = [R(\theta_k)] \cdot \begin{bmatrix} f_\alpha \\ f_\beta \end{bmatrix} \Rightarrow \begin{bmatrix} f_\alpha \\ f_\beta \end{bmatrix} = [R(\theta_k)]^{-1} \cdot \begin{bmatrix} f_{k1} \\ f_{k2} \end{bmatrix} \quad (2.24)$$

Applying Eq. (2.22) and Eq. (2.24) on the  $\alpha\beta$  components of Eq. (2.20), avoiding the subscript  $k$  on the electromagnetic variables (the reference frame is deductible by the motional terms in the electric equations), the equations in a generic rotating reference frame can be written as reported in the following.  $\omega_k$  and  $\omega_r$  are electrical values. Note that, the magnetic equations are computed by considering magnetic linearity.

**Stator electric model**

$$\begin{aligned}
[R(\theta_k)] \cdot \bar{v}_{s\alpha\beta} &= [R(\theta_k)] \cdot R_s \cdot \bar{i}_{s\alpha\beta} + [R(\theta_k)] \cdot \frac{d\bar{\lambda}_{s\alpha\beta}}{dt} \Rightarrow \\
\Rightarrow \bar{v}_s &= R_s \cdot \bar{i}_s + \frac{d\bar{\lambda}_s}{dt} + j \cdot \omega_k \cdot \bar{\lambda}_s
\end{aligned} \tag{2.25}$$

**Rotor electric model**

$$\begin{aligned}
[R(\theta_k)] \cdot \bar{v}_{r\alpha\beta} &= [R(\theta_k)] \cdot R_r \cdot \bar{i}_{r\alpha\beta} + [R(\theta_k)] \cdot \frac{d\bar{\lambda}_{r\alpha\beta}}{dt} \Rightarrow \\
\Rightarrow \bar{v}_r &= R_r \cdot \bar{i}_r + \frac{d\bar{\lambda}_r}{dt} + j \cdot (\omega_k - \omega_r) \cdot \bar{\lambda}_r
\end{aligned} \tag{2.26}$$

**Stator magnetic model**

$$\begin{aligned}
[R(\theta_k)] \cdot \bar{\lambda}_{s\alpha\beta} &= [R(\theta_k)] \cdot L_{l,s} \cdot \bar{i}_{s\alpha\beta} + [R(\theta_k)] \cdot M_{\alpha\beta}^{ss} \cdot \bar{i}_{s\alpha\beta} + [R(\theta_k)] \cdot M_{\alpha\beta}^{sr} \cdot \bar{i}_{r\alpha\beta} \Rightarrow \\
\bar{\lambda}_s &= L_s \cdot \bar{i}_s + L_m \cdot \bar{i}_r, \quad L_s = L_{l,s} + L_m, \quad L_m = \frac{3}{2} \cdot M
\end{aligned} \tag{2.27}$$

**Rotor magnetic model**

$$\begin{aligned}
[R(\theta_k)] \cdot \bar{\lambda}_{r\alpha\beta 0} &= [R(\theta_k)] \cdot L_{l,r} \cdot \bar{i}_{r\alpha\beta 0} + [R(\theta_k)] \cdot M_{\alpha\beta 0}^{rs} \cdot \bar{i}_{s\alpha\beta 0} + [R(\theta_k)] \cdot M_{\alpha\beta 0}^{rr} \cdot \bar{i}_{r\alpha\beta 0} \Rightarrow \\
\bar{\lambda}_r &= L_m \cdot \bar{i}_s + L_r \cdot \bar{i}_r, \quad L_r = L_{l,r} + L_m, \quad L_m = \frac{3}{2} \cdot M
\end{aligned} \tag{2.28}$$

where the product between the inductances matrices ( $M^{ss}, M^{sr}, M^{rs}, M^{rr}$ ) in Eq. (2.27, 2.28) and the rotational transformation in Eq. (2.22) have been obtained with the following manipulation:

$$M^{ss} = M^{rr} = M^{sr} = M^{rs} = \frac{3}{2} \cdot M \cdot \begin{bmatrix} 1 & 0 \\ 0 & 1 \end{bmatrix} \tag{2.29}$$

The magnetizing inductance  $L_m$  assumes the form reported in Eq. (2.27, 2.28) and the coefficient  $3/2$  is related to the Clarke transformation in Eq. (2.12).

The torque equation is computed by performing the power balance of the machine. In this way, the machine model is complete. Therefore, the electrical power in the machine is considered, as shown in Eq. (2.30).

$$\begin{aligned}
 P_e &= \bar{v}_s \cdot \bar{i}_s + \bar{v}_r \cdot \bar{i}_r = P_{Jsr} + P_m + P_{em} \Rightarrow \\
 &\Rightarrow \begin{cases} \bar{v}_s \cdot \bar{i}_s = R_s \cdot |\bar{i}_s|^2 + \frac{d\bar{\lambda}_s}{dt} \cdot \bar{i}_s + j \cdot \omega_k \cdot \bar{\lambda}_s \cdot \bar{i}_s \\ \bar{0} = \bar{v}_r \cdot \bar{i}_r = R_r \cdot |\bar{i}_r|^2 + \frac{d\bar{\lambda}_r}{dt} \cdot \bar{i}_r + j \cdot (\omega_k - \omega_r) \cdot \bar{\lambda}_r \cdot \bar{i}_r \end{cases} \quad (2.30)
 \end{aligned}$$

where the Joule-  $P_{Jsr}$ , magnetizing-  $P_m$ , and the electromagnetic-  $P_{em}$  powers are defined as:

$$\begin{aligned}
 P_{Jsr} &= R_s \cdot |\bar{i}_s|^2 + R_r \cdot |\bar{i}_r|^2 \\
 P_m &= \frac{d\bar{\lambda}_s}{dt} \cdot \bar{i}_s + \frac{d\bar{\lambda}_r}{dt} \cdot \bar{i}_r \\
 P_{em} &= (j \cdot \omega_k \cdot \bar{\lambda}_s) \cdot \bar{i}_s + (j \cdot \omega_k \cdot \bar{\lambda}_r) \cdot \bar{i}_r - (j \cdot \omega_r \cdot \bar{\lambda}_r) \cdot \bar{i}_r
 \end{aligned} \quad (2.31)$$

Introducing the number of pole pairs  $p$  and the power coefficient related to the Clarke transformation (3/2), the torque equation based on 2.31 becomes:

$$T_{em} = \frac{3}{2} \cdot p \cdot (\bar{i}_r \wedge \bar{\lambda}_r) \quad (2.32)$$

where the  $\wedge$  stands for cross product.

Finally, by combining rotor magnetic model Eq. (2.28) with Eq. (2.32), the electromagnetic torque can be expressed as:

$$T_{em} = \frac{3}{2} \cdot p \cdot (\bar{i}_r \wedge M \cdot \bar{i}_s) = \frac{3}{2} \cdot p \cdot (\bar{\lambda}_s \wedge \bar{i}_s) \quad (2.33)$$

that corresponds to the torque formulation of a generic three-phase ac machine.



### IM model in rotor flux reference frame

The equivalent circuit of the machine in rotating rotor flux reference frame rotating coordinates is provided. The steady-state conditions are considered, resulting in useful to perform energy assessments.

Starting from Eq. (2.25, 2.28), the following settings are applied: 1.  $\omega_k = \omega$ ; 2. all the time-derivatives equal to zero (steady-state conditions denoted by the capital letters). Therefore, the electromagnetic equations are expressed in rotating  $dq$  coordinates as:

$$\begin{aligned}\bar{V}_{s,dq} &= R_s \cdot \bar{I}_{s,dq} + j \cdot \omega \cdot \bar{\Lambda}_{s,dq} \\ \bar{V}_{r,dq} &= R_r \cdot \bar{I}_{r,dq} + j \cdot (\omega - \omega_r) \cdot \bar{\Lambda}_{r,dq} \\ \bar{\Lambda}_{s,dq} &= L_s \cdot \bar{I}_{s,dq} + L_m \cdot \bar{I}_{r,dq} \\ \bar{\Lambda}_{r,dq} &= L_m \cdot \bar{I}_{s,dq} + L_r \cdot \bar{I}_{r,dq}\end{aligned}\tag{2.34}$$

The IM machine model presented until now has not considered the iron losses. However, an equivalent iron resistance is introduced to consider this loss's contributions for an accurate mapping, as shown in Fig. 2.3. In Fig. 2.3 the iron resistance is not modeled in parallel with the magnetizing inductance, as usually reported in technical literature. Indeed, the iron losses equivalent resistance is placed between  $R_s$  and  $L_{l,s}$ , considering the contribution of the stator leakage fluxes. Hereafter others loss's contribution and machine nonlinearities will be presented.

The stator and rotor electric models, considering the iron losses, are expressed as:

$$\begin{aligned}\bar{V}_s &= R_s \cdot \bar{I}_s + j \cdot \omega \cdot L_{l,s} \cdot (\bar{I}_s - \bar{I}_{Fe}) + j \cdot \omega \cdot L_m \cdot (\bar{I}_s - \bar{I}_{Fe} + \bar{I}_r) \\ 0 &= -R_{Fe} \cdot \bar{I}_{Fe} + j \cdot \omega \cdot L_{l,s} \cdot (\bar{I}_s - \bar{I}_{Fe}) + j \cdot \omega \cdot L_m \cdot (\bar{I}_s - \bar{I}_{Fe} + \bar{I}_r)\end{aligned}\tag{2.35}$$

The Thevenin equivalent circuit is performed from the AB terminals, thus simplifying the model. An equivalent voltage  $\bar{V}_{eq}$ , equivalent resistance  $R_{eq}$ , and equivalent current  $\bar{I}_{eq}$  are introduced, simplifying the machine model.

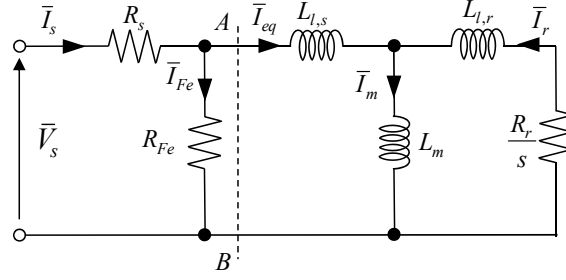


Figure 2.3 IM steady-state equivalent circuit in the rotating  $dq$  reference frame.

In detail, according to the equivalent circuit, the equation system Eq. (2.34) becomes:

#### Stator electric model

$$\bar{V}_{eq} = R_{eq} \cdot \bar{I}_{eq} + j \cdot \omega \cdot \bar{\Lambda}_s \quad (2.36)$$

#### Rotor electric model

$$0 = \frac{R_r}{s} \cdot \bar{I}_r + j \cdot (\omega - \omega_r) \cdot \bar{\Lambda}_r \quad (2.37)$$

#### Stator magnetic model

$$\bar{\Lambda}_s = L_s \cdot \bar{I}_{eq} + L_m \cdot \bar{I}_r \quad (2.38)$$

#### Rotor magnetic model

$$\bar{\Lambda}_r = L_r \cdot \bar{I}_r + L_m \cdot \bar{I}_{eq} \quad (2.39)$$

where the equivalent variables and equivalent parameters are computed as:

$$R_{eq} = \frac{R_s \cdot R_{Fe}}{R_s + R_{Fe}}; \quad \bar{V}_{eq} = \bar{V}_s \cdot \frac{R_{Fe}}{R_s + R_{Fe}}; \quad \bar{I}_{eq} = \bar{I}_s - \bar{I}_{Fe} \quad (2.40)$$

Finally, the iron losses equivalent current is computed using the superposition principle as:

$$\bar{I}_{Fe} = -\bar{I}_{eq} \cdot \frac{R_s}{R_s + R_{Fe}} + \bar{V}_s \cdot \frac{1}{R_s + R_{Fe}} \quad (2.41)$$

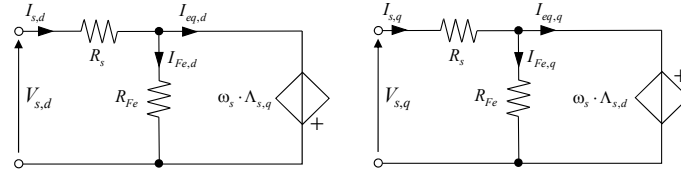


Figure 2.4 IM steady-state equivalent circuit in the rotating  $dq$  reference frame.

The  $dq$  components of flux- and torque-producing currents ( $I_{eq,d}$ ,  $I_{eq,q}$ ) differ from the stator absorbed  $dq$  currents by the corresponding iron losses current components ( $I_{Fe,d}$ ,  $I_{Fe,q}$ ).

### 2.1.4 Machine modelling for efficiency mapping

The proposed mapping procedure uses the electromagnetic model of the IM defined in the rotating  $dq$  reference frame, where the  $d$ -axis is assumed coincident with the position of the rotor flux linkage vector [71], reported in Eq. (2.36, 2.39). The steady-state equivalent circuit of the IM using the  $dq$  components in the rotor flux reference frame is shown in Fig. 2.4, and the related equivalent circuit after the Thevenin simplification is overwritten in Fig. 2.5. The voltage components referred to the Fig. 2.5 are expressed as:

$$\begin{cases} V_{eq,d} = R_s \cdot I_{eq,d} + E_{s,d} \\ V_{eq,q} = R_s \cdot I_{eq,q} + E_{s,q} \end{cases}, \quad \begin{cases} E_{s,d} = -\omega_s \cdot \Lambda_{s,q} \\ E_{s,q} = \omega_s \cdot \Lambda_{s,d} \end{cases} \quad (2.42)$$

All symbols are consistent with the previous definitions. The  $dq$  components of voltage, back-emf, current, and flux linkage stator vectors are denoted with  $(V_{eq,d}$ ,  $V_{eq,q})$ ,  $(E_{s,d}$ ,  $E_{s,q})$ ,  $(I_{s,d}$ ,  $I_{s,q})$ , and  $(\Lambda_{s,d}$ ,  $\Lambda_{s,q})$ , respectively. The synchronous speed is denoted with  $\omega_s$ .

The magnetic model, that consists of the current-to-flux relationships, is computed based on the stator and rotor magnetic models listed in Eq. (2.38, 2.39). By replacing rotor currents ( $I_{r,d}$ ,  $I_{r,q}$ ) and flux linkage  $\Lambda_r$  in steady-state conditions reported in Eq. (2.43) into the stator magnetic model, the stator flux

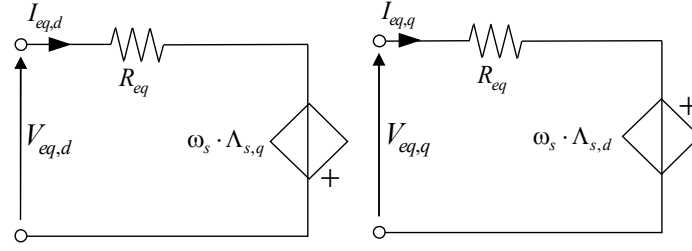


Figure 2.5 IM steady-state equivalent circuit in the rotating  $dq$  reference frame used in efficiency mapping.

components can be expressed as reported in Eq. (2.44).

$$\begin{cases} I_{r,d} = 0 \\ I_{r,q} = \frac{L_m}{L_r} \cdot I_{eq,q} \end{cases}, \quad \Lambda_r = L_m \cdot I_{eq,d} \quad (2.43)$$

$$\begin{cases} \Lambda_{s,d} = L_s \cdot I_{eq,d} = L_d \cdot I_{eq,d} \\ \Lambda_{s,q} = \sigma \cdot L_s \cdot I_{eq,q} = L_q \cdot I_{eq,q} \end{cases} \quad (2.44)$$

In Eq. (2.43)  $L_m$  and  $L_r$  stand for the magnetizing and the total rotor inductance, respectively, while in Eq. (2.44)  $L_s$  is the total stator inductance and  $\sigma$  is the overall leakage factor ( $\sigma = 1 - k_r \cdot k_s$ ,  $k_s = L_m / (L_m + L_{l,s})$  and  $k_r = L_m / (L_m + L_{l,r})$ ).

Using the variable components, the electromagnetic torque  $T_{em}$  is calculated as:

$$T_{em} = \frac{3}{2} \cdot p \cdot (\Lambda_{s,d} \cdot I_{eq,q} - \Lambda_{s,q} \cdot I_{eq,d}) \quad (2.45)$$

Finally, the rotational speed  $\omega_m$  is computed according to the slip speed  $\omega_{sl}$  based on Eq. (2.46), where  $R_r$  is the rotor resistance.

$$\omega_m = \frac{1}{p} \cdot (\omega_s - \omega_{sl}) \quad \omega_{sl} = \frac{R_r}{L_r} \cdot \frac{I_{eq,q}}{I_{eq,d}} \quad (2.46)$$

Note that in 2.46 the speed unit is rad/s. Otherwise, if the unit conversion is applied getting the rotor speed  $\omega_m$  in rpm, the name is invariant, but it is highlighted by the unit.

### 2.1.5 Nonlinearities of the machine modeling

The variations of all parameters are considered for an accurate machine model and mapping. This issue is highlighted in some applications where the components upstream (i.e., battery pack impacts on voltage supply for a traction applications) and downstream (i.e., thermal circuit impacts on machine temperature) involve the variations of the working conditions. The following nonlinearities need to be considered for accurately computing the IM maps:

1. the stator resistance  $R_s$  depends on the average temperature of the stator winding  $\vartheta_s$ , as well as on the frequency of the stator currents  $f_s$ , due to the skin effect [74–76];
2. the magnetizing inductance  $L_m$  is affected by magnetic saturation, whose extent depends on the amplitude of the magnetizing current  $I_m$  as [77]:

$$L_m = f(I_m) , \quad I_m = \sqrt{I_{eq,d}^2 + (I_{eq,q} + I_{r,q})^2} \quad (2.47)$$

3. the iron losses depend on the frequency of the stator currents  $f_s$  and the flux density values in the stator lamination or, in other words, by the stator back-electromotive force (back-emf) [78];
4. the rotor resistance  $R_r$  depends on the average temperature of the rotor cage  $\vartheta_r$ , as well as on the slip frequency  $f_{sl}$  because of the significant impact of skin effect in bar conductors in squirrel caged rotors [79, 80];
5. the IM mechanical torque  $T_m$  differs from the electromagnetic one reported in Eq. (2.45) by the torque  $T_{fv}$  necessary to sustain the friction and ventilation losses [81, 82]:

$$T_m = T_{em} - T_{fv} \quad (2.48)$$

Along with the above-mentioned nonlinearities, potential saturation effects of the total inductances should also be considered because of their impact on the inductances, as expressed in Eq. (2.49).

$$L_s = L_m + L_{l,s} , \quad L_r = L_m + L_{l,r} \quad (2.49)$$

In Eq. (2.49)  $L_{l,s}$  and  $L_{l,r}$  (stator and rotor leakage inductances) are assumed not saturable and not influenced by the skin effect phenomena.

Below more details regarding the iron losses and the magnetic saturation are reported.

### 2.1.6 Machine parameters

An accurate mapping of the machine requires knowing the parameters of this latter and their dependency on the previously reported nonlinearities. The literature reports several solutions to identify the three-phase IM's parameters, e.g., the execution of FEA analyses based on the machine design data [83] or using calibrated loss functions [82, 81]. This work proposes identifying the IM's parameters by executing standard test procedures like dc test plus no-load and locked-rotor tests [82] performed at different supply voltage and frequency levels. In this way, most of the nonlinearities affecting the IM's parameters can be directly identified, allowing an accurate mapping under different operating conditions.

The standard tests have been carried out on a 10 kW, 4 poles, 100 Hz three-phase IM, called machine under test (MUT), to validate the proposed efficiency methodology.

#### DC test

Two of three machine terminals are supplied with a dc source. By measuring the dc quantities of voltage and currents, the line-to-line stator resistance is thus obtained. Also, to compensate for any imbalance between the stator phases, the dc test is performed three times, and changing the supply terminals cyclically. In this way, all the three values of the line-to-line stator resistances are measured, allowing to get the average value that is representative of the machine. Finally, the stator phase resistance in dc conditions is obtained by considering half of the average line-to-line resistance value. It is highlighted that this test must be performed at a known temperature  $\vartheta_0$  to allow the accurate rescaling of the stator phase resistance for different operating temperatures [82].

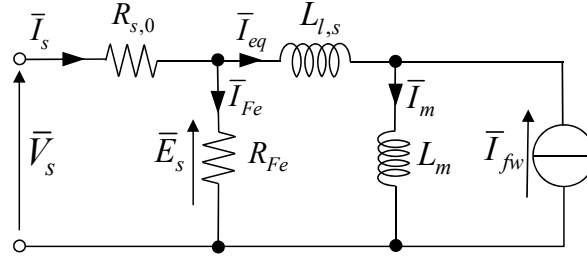


Figure 2.6 IM's equivalent circuit while performing the no-load test.

The value of stator phase resistance obtained by performing the dc test is denoted with  $R_{s,dc}^0$ . Considering the MUT, the value of  $R_{s,dc}^0 = 634 \text{ m}\Omega$  at  $\vartheta_0 = 25^\circ \text{ C}$  has been obtained.

### No-load Test

The execution of the no-load test at different supply voltage and frequency levels allows identifying the following parameters and losses sources:

- Mechanical losses caused by friction and ventilation as a function of the mechanical speed  $\omega_m$ .
- Overall losses  $P_{Fe}$  due to the stator iron and stator windings (skin effect) as a function of the supply frequency  $f_s$  and machine's back-emf  $E_s$ .
- Stator inductance  $L_s$  and its saturation as a function of the magnetizing current  $I_m$ .

The equivalent circuit of the machine when performing the no-load test is shown in Fig. 2.6. The current generator  $\bar{I}_{fw}$  models the torque-producing rotor current, thus compensating for the mechanical losses. For each supply frequency, the no-load test is performed at different supply voltage levels. However, the supply voltage must be limited according to the following constraints: *i*) voltage limit imposed by the insulation system of the stator windings (e.g., 110 - 125 % of the machine's rated voltage), and *ii*) the no-load current should be kept within the limit imposed of the machine's rated

current, avoiding useless winding's heating. Moreover, it is highlighted that all no-load tests must be performed at the same operating temperature of the dc test  $\vartheta_0$ .

In the following, the step-by-step procedure to identify the parameters and loss sources above-mentioned regardless of the supply frequency and voltage levels is reported.

### Identification of the mechanical losses

For a given supply frequency  $f_s$ , the machine's active power  $P_{elt}$  is first measured for different supply voltage levels. Secondly, the Joule losses are removed in each test point according to the measured value of the RMS no-load current  $I_{s,rms}$  and the stator phase resistance value obtained from the dc test  $R_{s,dc}^0$ :

$$P_{Fe} + P_{fw} = P_{elt} - 3 \cdot R_{s,dc}^0 \cdot I_{s,rms}^2 \quad (2.50)$$

The mechanical losses  $P_{fw}$  are computed by extrapolating the intercept of Eq. (2.50) for a supply voltage equal to zero. Moreover, since the slip speed is negligible in no-load conditions, the mechanical speed  $\omega_m$  is assumed to be identical to the synchronous one, i.e.,  $60 \cdot f_s / p$  (rpm). Finally, the ratio between the mechanical losses  $P_{fw}$  and the mechanical speed  $\omega_m$  provides the value of the torque loss  $T_{fw}$ . Other minor details are not reported since identifying the IM's mechanical losses is a well-known procedure in the literature [82].

The standard tests have been performed at different supply voltages and frequencies to identify the machine nonlinearities accurately. The experimental results for the identification of the mechanical losses obtained for the IM used to validate the proposed procedure are reported in Fig. 2.7, based on the procedure reported in 2.1.6.

### Identification of the stator losses

Once the mechanical losses  $P_{fw}$  are computed, the overall stator losses  $P_{Fe}$  due to the iron losses and skin effect are obtained from Eq. (2.50) as:

$$P_{Fe} = P_{elt} - 3 \cdot R_{s,dc}^0 \cdot I_{s,rms}^2 - P_{fw} \quad (2.51)$$

Unfortunately, separating the iron losses from those due to the skin effect of the stator winding is not possible by performing only the standard test



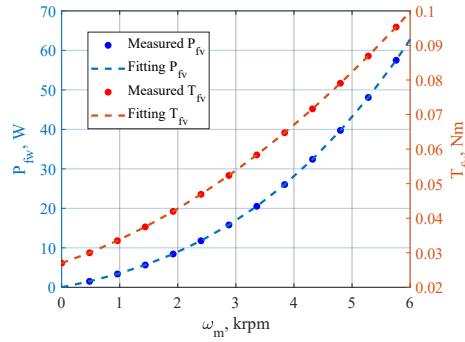


Figure 2.7 Mechanical losses of the IM used for the experimental validation.

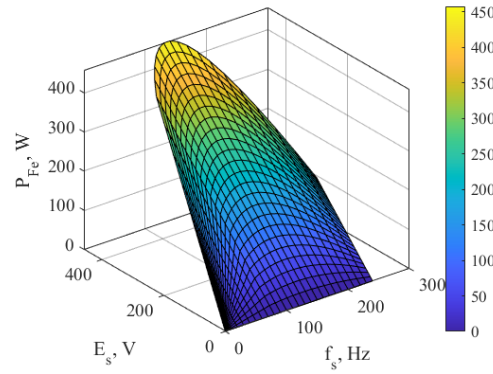


Figure 2.8 Stator losses map (iron losses plus skin effect) of the IM used for the experimental validation.

procedures. Indeed, the profile of stator resistance as a function of the supply frequency for a given temperature can be somewhat obtained if FEA analyses based on machine design data are performed, thus going beyond the goal of this work. For this reason, in this work, the skin effect losses of the stator winding are merged with the iron losses, simplifying the analysis. On the one hand, this operation represents an approximation that slightly reduces the accuracy of the input data for the mapping procedure. On the other hand, this simplification allows easily accounting for the skin effect losses avoiding neglect of the impact in the efficiency maps.

However, as well-known in the literature, the iron losses depend on the stator frequency and the magnetic induction in the iron [84, 85]. For this reason, the overall stator losses need to be expressed as a function of the stator frequency but also from the machine's back-emf. Indeed, the latter

provides a direct indication of the level of magnetic induction in the iron. In other words, the machine's back-emf is proportional to the stator flux linkage and thus directly related to the magnetic induction in the iron.

According to Fig. 2.6, the machine back-emf (peak value) is computed as follows. The no-load reactive power  $Q_{elt}$  is first calculated as:

$$Q_{elt} = \sqrt{(3 \cdot V_{s,rms} \cdot I_{s,rms})^2 - P_{el}^2} \quad (2.52)$$

where  $V_{s,rms}$  is the measured value of the RMS phase voltage. Later, the machine's back-emf  $E_s$  (peak value) is obtained as:

$$E_s = \sqrt{2} \cdot \frac{\sqrt{P_{Fe}^2 + Q_{el}^2}}{3 \cdot I_{s,rms}} \quad (2.53)$$

Therefore, the map of stator losses (iron plus skin effect ones) expressed as a function of the supply frequency and machine's back-emf is obtained by performing the no-load tests at all operative levels of supply voltage and frequency of the IM under test. The stator losses map of IM used to validate the proposed mapping procedure is shown in Fig. 2.8.

#### Identification of the stator inductance

The stator inductance  $L_s$  and its saturation profile are identified by considering the results of the no-load test at a low supply frequency. Indeed, in this condition, it is possible to inject a value of no-load current up to the machine's rated one without applying a supply voltage that overcomes the limits imposed by the insulation system of the stator windings. It is reasonable to assume that the rotor currents due to the mechanical losses give a negligible contribution to the magnetizing current. Therefore, the stator inductance  $L_s$  is computed considering the equivalent circuit of the machine (see Fig. 2.6), but neglecting the current generator modeling the mechanical losses. The RMS magnetizing current  $I_{m,rms}$  is thus calculated as:

$$I_{m,rms} = \sqrt{2} \cdot \frac{Q_{elt}}{3 \cdot E_s} \quad (2.54)$$

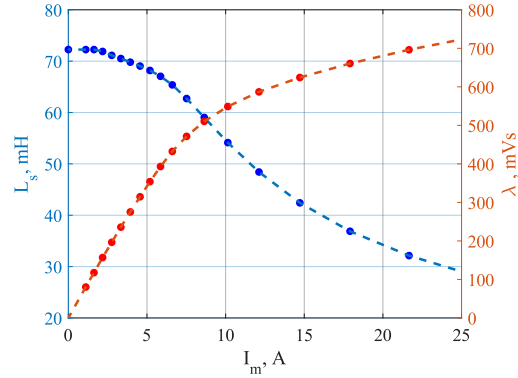


Figure 2.9 Saturation profiles of three-phase IM used for the experimental validation.

Finally, the stator inductance is computed as:

$$L_s = \frac{1}{2\pi \cdot f_s} \cdot \frac{Q_{elt}}{3 \cdot I_{m,rms}^2} \quad (2.55)$$

Therefore, by evaluating the stator inductance for different values of the magnetizing current, i.e., by performing the no-load test at different supply voltages for the selected supply frequency, the saturation profile of the stator inductance is thus obtained. The identification of the stator inductance including the related profile of the no-load stator flux linkage of the IM used to validate the proposed mapping procedure is shown in Fig.2.9. The results of the no-load test obtained at a supply frequency of 20 Hz have been considered, assuming that the magnetic model does not depend on it.

### Locked-rotor test

The locked-rotor test is performed by imposing the machine's rated current at different supply frequencies. In this way, the following parameters are identified:

- Rotor resistance  $R_r$  as a function of the slip frequency  $f_r$  to consider the skin effect in the rotor cage.
- Stator-  $L_{l,s}$  and rotor-  $L_{l,r}$  leakage inductances.

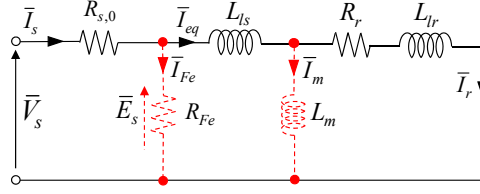


Figure 2.10 IM's equivalent circuit while performing the locked-rotor test.

The equivalent circuit of the machine when performing the locked-rotor test is shown in Fig. 2.10. As with the no-load test, the locked rotor one must be performed at the same operating temperature of the dc test  $\vartheta_0$ .

### Identification of the rotor resistance

According to the previous considerations, the stator resistance is assumed constant to the value obtained from the dc test. Therefore, by performing the locked-rotor test at different supply frequencies, the overall ac resistance  $R_{cc}$  variations correspond to ones of the rotor resistance  $R_r$  due to the skin effect. This assumption is an approximation since the variations of the stator resistance due to the skin effect are neglected. However, it must be considered that the skin effect is much more significant on the rotor cage than the stator winding, well justifying the assumption above. Obviously, an accurate separation between stator- and rotor- resistance can be obtained by performing calibrated FEA analyses supported by machine design data, however, going beyond the goal of this work. In summary, for each supply frequency, the overall ac resistance  $R_{cc}$  is computed according to Fig. 2.10 as:

$$R_{cc} = R_s + R_r = \frac{P_{elt}}{3 \cdot I_{s,rms}^2} \quad (2.56)$$

Therefore, based on the previous considerations, the rotor resistance at the tested supply frequency is computed as:

$$R_r = R_{cc} - R_{s,dc}^0 \quad (2.57)$$

Finally, the rotor resistance and its variations with the slip frequency are identified by performing the locked-rotor test for different supply frequencies.

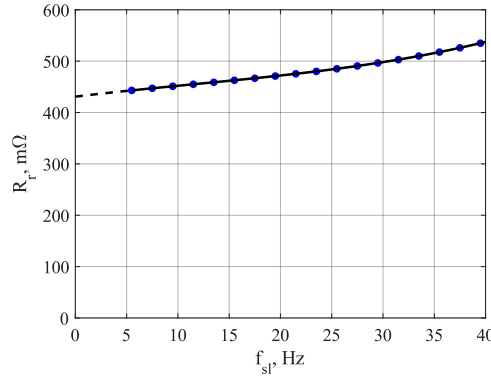


Figure 2.11 Rotor resistance profile due to the skin effect of the IM used for the experimental validation.

The profile of the rotor resistance, evaluated with locked-rotor tests of the MUT is shown in in Fig. 2.11. It is noted that the dc value of the rotor resistance is computed by extrapolating the experimental profile obtained at very low supply frequencies. Moreover, the maximum rotor frequency has been limited to 40 Hz since the operative slip frequency  $f_{sl}$ , corresponding to the rotor one, reaches a value at most equal to 15 Hz.

#### Identification of the leakage inductances

According to Fig. 2.10, the locked-rotor test allows getting the overall leakage inductance  $L_{cc}$  computed as:

$$L_{cc} = L_{l,s} + L_{l,r} = \frac{1}{2\pi \cdot f_s} \cdot \frac{Q_{elt}}{3 \cdot I_{s,rms}^2} \quad (2.58)$$

The overall leakage inductance  $L_{cc}$  should be computed at different supply frequencies to get a reliable value of this parameter, but without considering the results obtained at very low supply frequencies (e.g., 1-10 Hz). Indeed, in these last conditions, the magnetizing current is not negligible, making the equivalent circuit of Fig. 2.10 no more valid. Finally, the regulatory standard has been considered to get the single values of stator and rotor leakage inductances.

Regarding the overall leakage inductance of the MUT has been computed as the average of all measurements performed in the range 40 Hz - 200 Hz, getting a value of  $L_{cc} = 7.63$  mH. Finally, based on the rated frequency and voltage of the MUT, i.e., 100 Hz, 400 V, the steady-state torque-speed

Table 2.1 Measured parameters

Machine's parameters	
Stator resistance $R_{s,0}$ ( $\vartheta_0 = 25^\circ\text{C}$ )	634 m $\Omega$
Locked-rotor inductance $L_{cc}$	7.63 mH
Stator leakage inductance $L_{l,s}$	3.815 mH
Rotor leakage inductance $L_{l,r}$	3.815 mH

profile has been computed using the experimental data obtained from the standard tests ( $R_{s,dc}^0$ ,  $R_r$ ,  $L_{cc}$ ). The computed torque-speed profile is shown in Fig. 2.12. Since the rated torque of the machine is 16 Nm, the rated slip (1.51 %), starting torque (about 100 % of the rated torque), and the pull-out conditions (overload torque of about 280 % of the rated value with a pull-out slip of 9.33 %) have been evaluated. The IM under test has been thus classified as NEMA Class A [86] based on these data. Therefore, according to the regulatory standard [82], the following ratio between stator and rotor leakage inductances has been considered:

$$\text{NEMA Class A} \rightarrow \frac{L_{l,s}}{L_{l,r}} = 1 \Rightarrow L_{l,s} = L_{l,r} = \frac{L_{cc}}{2} \quad (2.59)$$

In summary, by applying Eq. (2.59), the leakage inductances have been computed, leading to  $L_{l,s} = L_{l,r} = 3.815$  mH.

The machine parameters of the MUT used for the mapping validations, which were considered constant, are listed in Table 2.1. Instead, the profiles presented before of mechanical losses, stator losses, rotor resistance, saturation profile, were organized as a lookup table (LUT) and opportunely interpolated to use in the mapping procedure.

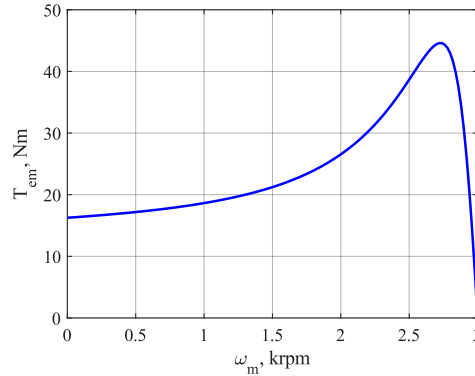


Figure 2.12 Steady-state torque-speed profile at the rated supply conditions of the IM used for the experimental validation.

### 2.1.7 Magnetic model manipulation

Note that the profiles hereafter analyzed are not necessary for the proposed mapping procedure, thus representing a magnetic model manipulation. However, the torque capability and the maximum value on the whole torque-speed range must be confirmed by the mapping algorithm presented in the next section.

After a brief discussion about the methodology to identify some control trajectories, the profiles carried out on the three-phase IM used for mapping validation are shown.

Based on the magnetic model just presented, this section investigates some control trajectory identification. This is done using the magnetic model of the machine, i.e. magnetizing and leakage inductances, maximum magnetizing current value during the no-load tests, to investigate the most considered trajectories as the maximum torque per ampere (MTPA) and the maximum torque per volt (MTPV) laws. The method to identify one locus is general and it is usually defined as the maximization or minimization of the ratio across the  $(I_{eq,d}, I_{eq,q})$  domain. For example, the MTPA consists of the maximization of the average torque for a given current amplitude. The maximum torque at  $(I_{eq,d}, I_{eq,q})$  combination is found and stored as one MTPA element. The process is repeated for the next current amplitude, ranging from zero to the maximum allowed by the maps current domain, which depends on the current limit of the machine. The MTPV is computed using

the same algorithm but moving on constant flux linkage curves instead of the current ones.

The first step is to identify the MTPS profile, which delimits the region beyond which the current and voltage limits are not respected. In detail, three operating regions are identified: base, FW I, FW II, corresponding to the constant torque-, quasi-constant power-, and pull-out- operations of the machine, respectively. The MTPA locus is related to the constant torque region of the MTPS profile, while the MTPV corresponds to FW II.

### 2.1.8 Base region

The drive voltage limit delimits the base region's speed range. The maximum stator voltage  $V_{s,\max}$  depends on the available dc-link voltage  $V_{dc}$  and the adopted pulse-width modulation (PWM) technique, as shown in Eq. (2.60). Considering the components of the stator voltage vector in  $dq$  reference frame, they should satisfy the relationship in Eq. 2.60, where *MinMax Modulations* represents different PWM techniques, as space vector modulation (SVM).

$$V_{s,d}^2 + V_{s,q}^2 \leq V_{s,\max}^2, \quad V_{s,\max} = \begin{cases} \frac{V_{dc}}{2} & \text{Sine Modulation} \\ \frac{V_{dc}}{\sqrt{3}} & \text{MinMax Modulation} \end{cases} \quad (2.60)$$

The components of the equivalent voltage vector are computed in steady-state condition as:

$$\begin{aligned} V_{eq,d} &= R_{eq} \cdot I_{eq,d} - \omega \cdot \Lambda_{s,q} \\ V_{eq,q} &= R_{eq} \cdot I_{eq,q} + \omega \cdot \Lambda_{s,d} \end{aligned} \quad (2.61)$$

Introducing Eq. (2.44) and by neglecting the stator resistance effect, the voltage limitation can be expressed as a function of the stator  $dq$  currents as:

$$\left( \omega \cdot L_q \cdot I_{eq,q} \right)^2 + \left( \omega \cdot L_d \cdot I_{eq,d} \right)^2 \leq V_{s,\max}^2 \quad (2.62)$$

where the  $dq$  inductances are defined as:  $dq$  ax  $L_d = L_s$  and  $L_q = \sigma \cdot L_s$ .

The voltage-limit in Eq. (2.62) corresponds to an ellipse that depends on the operating frequency/pulsation  $\omega$ . Therefore, the reference currents ( $I_{eq,d}$ ,



$I_{eq,q}$ ) should satisfy Eq. (2.62) for every operating frequency. It is noted how the ellipse size radii become smaller as the operating frequency increases. In other words, under a given voltage limit, the range of controllable currents ( $I_{eq,d}$ ,  $I_{eq,q}$ ) becomes smaller as the operating frequency increases. Besides, the leakage factor of the machine affects the area of the ellipse since its eccentricity is computed as:

$$e = \sqrt{1 - \sigma^2} \quad (2.63)$$

Below the voltage limit Eq. (2.62), the stator current vector  $\bar{I}_s$  follows the MTPA profile of the machine. The MTPA is the locus of the points that maximize the machine torque for a given amplitude of the current vector [87]. It leads to maximum machine efficiency if the iron losses are neglected. In  $dq$  reference frame, the torque is computed as:

$$T_{em} = \frac{3}{2} \cdot p \cdot k_r \cdot \Lambda_r \cdot I_{eq,q} = \frac{3}{2} \cdot p \cdot k_r \cdot L_m \cdot I_{eq,d} \cdot I_{eq,q} \quad (2.64)$$

where the rotor coupling factor is defined as:  $k_r = L_m / (L_m + L_{l,r})$ .

The amplitude of the stator current vector is assumed to equal to the maximum value  $I_{s,\max}$ , corresponding to the base region of the MTPS. According to the amplitude limit of the stator current vector  $I_{s,\max}$ , the  $dq$  components of the latter must satisfy the following relationship:

$$I_{eq,d}^2 + I_{eq,q}^2 \leq I_{s,\max}^2 \quad (2.65)$$

Therefore, the current-limit is a circle whose radius corresponds to  $I_{s,\max}$ . To satisfy the current constraint in Eq. (2.65), the reference currents must be inside this circle. According to Eq. (2.65), the  $d$ -axis component can be written as [88]:

$$I_{eq,d} = \sqrt{I_{s,\max}^2 - I_{eq,q}^2} \quad (2.66)$$

Combining Eq. (2.64) and Eq. (2.66), the torque is computed as:

$$T_{em} = \frac{3}{2} \cdot p \cdot k_r \cdot L_m \cdot \sqrt{I_{s,\max}^2 - I_{eq,q}^2} \cdot I_{eq,q} \quad (2.67)$$

Based on Eq. (2.67), the MTPA is computed as:

$$\begin{aligned} \frac{\partial T_{em}}{\partial I_{eq,q}} = 0, \quad \frac{\partial T_{em}}{\partial I_{eq,q}} &\propto \sqrt{I_{s,\max}^2 - I_{eq,q}^2} - \frac{I_{eq,q}^2}{\sqrt{I_{s,\max}^2 - I_{eq,q}^2}} \Rightarrow \\ \Rightarrow I_{s,\max}^2 - I_{eq,q}^2 &= I_{eq,q}^2 \Rightarrow I_{eq,q}^2 = I_{eq,d}^2 = \frac{I_{s,\max}^2}{2} \end{aligned} \quad (2.68)$$

The result of Eq. (2.68) consists of the following:

$$MTPA: I_{eq,d} = I_{eq,q} \quad (2.69)$$

where it is noted how the MTPA corresponds to the bisector of the  $(I_{eq,d}, I_{eq,q})$  plane. It is highlighted how magnetic saturation has been neglected for MTPA computation. Otherwise, the MTPA profile would start as the bisector of the  $(I_{eq,d}, I_{eq,q})$  plane and would become gradually more vertical.

### Flux weakening I (FWI)

The flux-weakening region can be divided into two subregions: *I* - it corresponds to the quasi-constant power operation of the machine; *II* - it corresponds to the pull-out operation of the machine in which the mechanical power is reduced as the speed increases. In this subsection, the first subregion is considered. The maximum torque production under the voltage constraint is performed by keeping the amplitude of the current vector to the maximum value  $I_{s,\max}$ . However, the MTPA profile cannot be followed anymore. Indeed, the *d*-axis current component must be set to satisfy the voltage constraint Eq. (2.62) for each operating frequency/pulsation  $\omega$ , leading to as follows:

$$\left\{ \begin{aligned} I_{eq,d} &= \frac{1}{\omega} \cdot \sqrt{\frac{V_{s,\max}^2 - (\omega \cdot L_q \cdot I_{s,\max})^2}{L_d^2 - L_q^2}} \\ I_{eq,q} &= \sqrt{I_{s,\max}^2 - I_{eq,d}^2} \end{aligned} \right. \Leftrightarrow \omega_b < \omega < \omega_1 \quad (2.70)$$

where  $\omega_b$  and  $\omega_1$  represent the frequency/pulsation limits of the base and FWI regions, respectively. Such limits are computed as:

$$\omega_b \simeq \frac{\sqrt{2} \cdot V_{s,\max}}{I_{s,\max} \cdot \sqrt{L_d^2 + L_q^2}} \quad \omega_1 = \frac{V_{s,\max}}{\sqrt{2} \cdot I_{s,\max}} \cdot \sqrt{\frac{L_d^2 + L_q^2}{L_d^2 \cdot L_q^2}} \quad (2.71)$$

Applying Eq. (2.70), the stator current vector follows a circular trajectory having a radius equal to  $I_{s,\max}$ . However, by expressing the stator  $dq$  currents as a function of the stator  $dq$  fluxes linkages, the following is obtained:

$$\begin{cases} \begin{cases} \Lambda_{s,d} = L_s \cdot I_{eq,d} & \Rightarrow & I_{eq,d} = \frac{\Lambda_{s,d}}{L_s} \\ \Lambda_{s,q} = \sigma \cdot L_s \cdot I_{eq,q} & \Rightarrow & I_{eq,q} = \frac{\Lambda_{s,q}}{\sigma \cdot L_s} \end{cases} \\ I_{eq,d}^2 + I_{eq,q}^2 = I_{s,\max}^2 \end{cases} \Rightarrow \left( \frac{\Lambda_{s,d}}{L_s} \right)^2 + \left( \frac{\Lambda_{s,q}}{\sigma \cdot L_s} \right)^2 = I_{s,\max}^2 \quad (2.72)$$

Therefore, in the FW I region the stator flux linkage vector moves along an ellipse having major and minor axes radii corresponding to the  $dq$  inducances. Regarding the torque in the FW I region, according to Eq. (2.67), it depends on the product between the stator  $dq$  currents. Approximately, in the FW I region, the torque depends on the inverse of the speed, leading to the quasi-constant power operation (mechanical) of the machine. This condition satisfies the goal of the flux-weakening operation. However, when the frequency/pulsation reaches  $\omega_1$ , the FW II region starts, in which the mechanical power is reduced as the speed increases. Therefore, it would be better to design the machine/converter such that the speed range is within the FW I region. In other words, it is necessary to maximize the ratio between  $\omega_1$  and  $\omega_b$ , corresponding to as follows [88]:

$$\frac{\omega_1}{\omega_b} \simeq \frac{\sqrt{1 + \sigma^2}}{2 \cdot \sigma} \simeq \frac{\sigma^{-1}}{2} \quad (2.73)$$

According to Eq. (2.73), the quasi-constant constant power region of an three-phase IM depends on the overall leakage coefficients. Therefore, an IM for spindle drives (e.g., traction) must be designed to minimize its leakage inductances (stator and rotor). In other words, the eccentricity of Eq. (2.63) of the ellipse that is followed by the stator flux linkage vector must be maximized.

### Flux weakening II (FWII)

When the pulsation/frequency reaches the  $\omega_1$  value, the position of the stator flux linkage vector to the  $dq$  reference frame is  $45^\circ$  electrical degrees. In such a condition, it is not convenient to apply the  $dq$  stator reference currents in Eq. (2.70). Indeed, starting from the torque equation in Eq. (2.45) and by expressing the stator  $dq$  currents as a function of the stator  $dq$  fluxes linkages, the following torque formulation is obtained:

$$T_{em} = \frac{3}{2} \cdot p \cdot \left( \frac{1}{\sigma \cdot L_s} - \frac{1}{L_s} \right) \cdot \Lambda_{s,d} \cdot \Lambda_{s,q} = \frac{3}{2} \cdot p \cdot \left( \frac{1}{\sigma \cdot L_s} - \frac{1}{L_s} \right) \cdot \frac{\Lambda_s^2}{2} \sin(2\delta) \quad (2.74)$$

Therefore, for a given amplitude of the stator flux linkage, the maximum obtainable torque corresponds to the following conditions:

$$T_{em} \propto \Lambda_s^2 \cdot \sin(2\delta) \propto \sin(2\delta) \Rightarrow \frac{\partial T_{em}}{\partial \delta} = 0 \Rightarrow \delta \pm \frac{\pi}{4} \quad (2.75)$$

The work points corresponding to the condition in Eq. (2.75) represent the maximum torque per speed (MTPV) profiles of the machine. For frequency/pulsation higher than  $\omega_1$ , the application of the  $dq$  stator reference currents as in Eq. (2.70) leads to overcome the MTPV, thus resulting in not convenient. For this reason, the FW II region is introduced, corresponding to the machine operation on the MTPV profiles. After performing some mathematical manipulations, the  $dq$  stator currents corresponding to the

MTPV operation are computed as [88]:

$$\begin{cases} I_{eq,d} = \frac{V_{s,\max}}{\sqrt{2} \cdot \omega \cdot L_d} = \frac{V_{s,\max}}{\sqrt{2} \cdot \omega \cdot L_s} \\ I_{eq,q} = \frac{V_{s,\max}}{\sqrt{2} \cdot \omega \cdot L_q} = \frac{V_{s,\max}}{\sqrt{2} \cdot \omega \cdot \sigma \cdot L_s} \end{cases} \Leftrightarrow \omega > \omega_1 \quad (2.76)$$

Therefore, on the MTPV profiles, the voltage and load-angle constraints  $\delta$  are applied. Regarding the amplitude of the currents, this is reduced as the speed increases. Finally, in the FW II region, the torque is computed as:

$$T_{em} = \frac{3}{2} p \cdot (\Lambda_d \cdot I_{eq,q} - \Lambda_q \cdot I_{eq,d}) = \frac{3}{4} \cdot p \cdot \frac{1 - \sigma}{\sigma \cdot L_s} \cdot \frac{V_{s,\max}}{\omega^2} \quad (2.77)$$

It is noted how the torque is reduced as the speed increases, following a quadratic law. Therefore, in the FW II region, the power is reduced as the speed increases. Finally, like the FW I region, it is convenient to minimize the leakage inductances of the machine. In this way, the MTPV torque in Eq. (2.77) is maximized.

In Fig. 2.21 the MTPA and MTPV profiles of the three-phase IM used for mapping experimental validation in the current  $dq$  plane and flux plane for both motoring and generating modes are shown. Note that the MTPA, MTPV profiles are not necessary for the mapping procedure developed in this work.

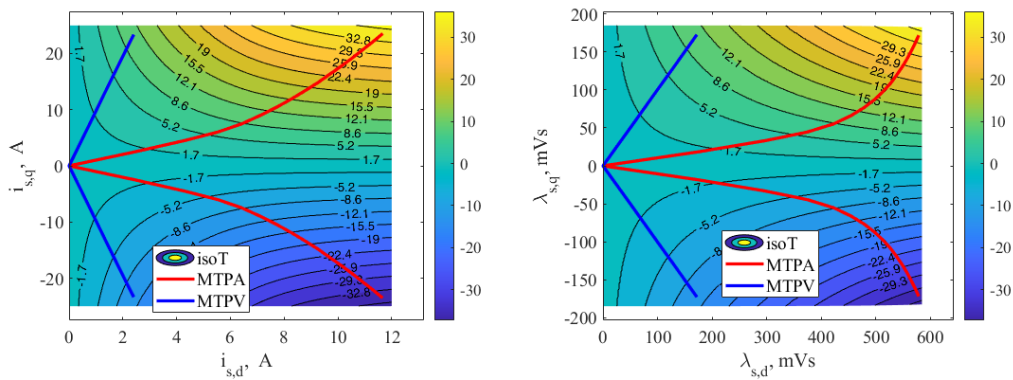


Figure 2.13 MTPA and MTPV for three-phase IM in the current  $dq$  plane (left) and flux plane (right), for both motoring and generating modes.

## 2.2 Three-phase induction machine mapping

This section describes the algorithm to perform the off-line mapping of three-phase IM. The maps are computed in steady-state conditions, thus neglecting the dynamic operation of the machine control. The mapping algorithm is based on the machine model in  $dq$  coordinates, which parameters can be easily obtained by performing the conventional no-load and locked rotor tests. The temperature, frequency, and supply voltage effects on electrical machine parameters are included, as well as the available MTPS profile for each considered dc-link voltage and machine temperature value. The proposed approach allows quickly obtaining the efficiency maps of IMs without performing any load tests in a climatic chamber, saving the time required for thermal stabilization.

Finally, the proposed algorithm also computes the maps of all electromechanical variables related to those of the efficiency. These can be used for several purposes, starting from the machine simulation until their use in the drive control, thus assuming the meaning of reference variables (e.g.,  $dq$  reference currents). Since the maps are computed as a function of speed, torque, temperature, and dc-link voltage, the maps are characterized by a four-dimensional (4D) structure.

A remark about the proposed efficiency mapping concerns the sinusoidal approach. In this work, it has been chosen to focus only on the fundamental machine's efficiency since the impact of PWM significantly depends on the considered inverter, hindering the implementation of analytical losses models. Indeed, according to [89], the harmonic content introduced by the PWM modulation depends on the switching frequency, dc-link voltage level, inverter levels, modulation technique, amplitude- and frequency-modulation indexes (i.e., the amplitude and frequency of the fundamental phase voltages, respectively). Therefore, even computing the efficiency maps of the machine considering PWM modulation, this analysis cannot be generalized and must be performed again if the inverter or any of the above variables is changed. In addition, accurate analytic models of both iron and copper losses under PWM modulation are not reported in the literature, thus still representing an open research field. For these reasons, in this work, it

has been preferred to focus on an efficiency mapping algorithm for three-phase IM that considers only the time-fundamental behaviour, regardless of the inverter supplying the machine [90].

### 2.2.1 IM mapping algorithm

### 2.2.2 Mapping initialization

The results obtained from the standard test procedures are used to compute the flux and torque maps of the IM under consideration, both inputs of the proposed mapping procedure and whose step-by-step computation is reported in the following.

#### Identification of the magnetizing inductance

The saturation profile of the magnetizing inductance  $L_m$  as a function of the magnetizing current is computed by applying Eq. (2.49) in Section 2.1.5, thus directly using the saturation profile of the stator inductance obtained from the no-load tests. The saturation profile of the magnetizing inductance of the IM used for the experimental validation is reported in Fig. 2.14.

#### Identification of the $dq$ inductances

After performing some mathematical manipulations, it is easily demonstrated that the  $q$ -axis steady-state inductance of the IM can be expressed as follows:

$$\sigma \cdot L_s = L_{l,s} + L_{l,r} \cdot \frac{L_m}{L_m + L_{l,r}} \quad (2.78)$$

Therefore, for each value of the magnetizing current  $I_m$ , the  $dq$  inductances of the steady-state magnetic model reported in Eq. (2.44) are computed ( $\Lambda_{s,d} = L_s \cdot I_{eq,d}$ ,  $\Lambda_{s,q} = \sigma \cdot L_s \cdot I_{eq,q}$ ).

#### Correlation between magnetizing current with flux- and torque- producing $dq$ currents

According to the IM model defined in the rotating  $dq$  frame, the magnetizing current can be expressed as a function of the flux- and torque- producing  $dq$

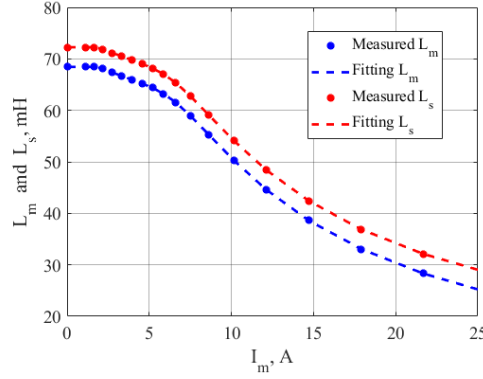


Figure 2.14 Saturation profile of the magnetizing and stator inductances of the IM used for the experimental validation.

currents as in Eq. (2.47), and whose extended-expression using Eq. (2.43) as:

$$I_m = \sqrt{I_{eq,d}^2 + I_{eq,q}^2 \cdot \left(1 - \frac{L_m}{L_m + L_{l,r}}\right)^2} \quad (2.79)$$

However, Eq. (2.79) can be reasonably simplified as  $I_m \simeq I_{eq,d}$  since the magnetizing inductance is quite higher than rotor leakage one regardless of the saturation condition.

#### Definition of the flux- and torque- producing $dq$ currents mesh grid

A regular mesh grid of flux- and torque- producing  $dq$  currents ( $I_{eq,d}, I_{eq,q}$ ) is defined, and whose limits are set as:

$$\begin{aligned} 0 &\leq I_{eq,d} \leq I_{m,max} \\ -I_{max} &\leq I_{eq,q} \leq I_{max} \end{aligned} \quad (2.80)$$

where  $I_{m,max}$  is the maximum value of magnetizing current for which the magnetizing inductance has been experimentally identified, while  $I_{max}$  is the amplitude limit of the phase currents (peak value). The latter usually consists of the maximum overload current of the IM under consideration. Alternatively, it consists of the current limit imposed by the power electronics converter feeding the machine. It is highlighted that the steps of the  $dq$  currents composing the mesh grid must be set to define the flux- and torque-maps with reasonable resolution.



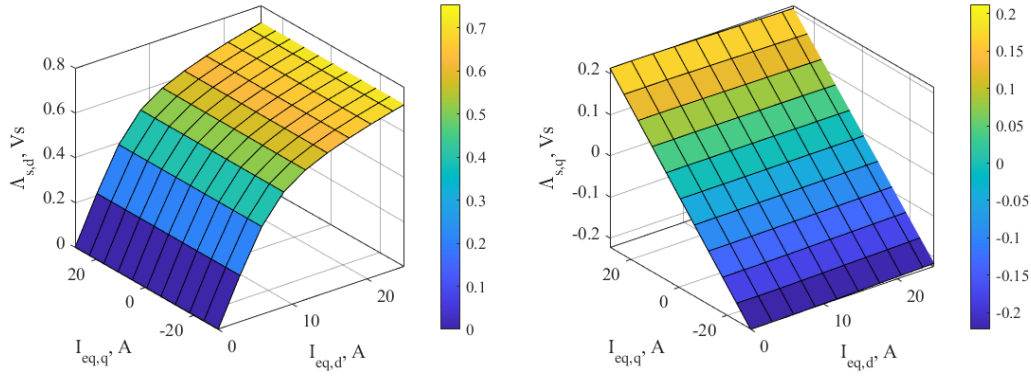


Figure 2.15 Stator flux linkage  $dq$  maps of the IM used for the experimental validation.

### Computation of the flux maps

For each  $dq$  point of the mesh grid defined at step 2.2.2, the magnetizing current is first computed using  $I_m \simeq I_{eq,d}$ . Secondly, the  $dq$  inductances of the steady-state magnetic model reported in Eq. (2.44) are calculated by using the profiles obtained at step 2.2.2 (see Fig. 2.9). Finally, the  $dq$  stator flux linkages in steady-state conditions ( $\Lambda_{s,d}, \Lambda_{s,q}$ ) are computed using Eq. (2.44). Therefore, the IM's flux maps are computed by repeating these operations for each point of the mesh grid defined at step 2.2.2. The flux maps obtained for the IM used to validate the proposed mapping procedure are reported in Fig. 2.15.

### Computation of the torque map

For each  $dq$  point of the mesh grid defined at step 2.2.2, the corresponding  $dq$  stator flux linkages are extracted from the flux maps computed at step 2.2.2. Later, the electromagnetic torque is calculated using  $I_m \simeq I_{eq,d}$ . The IM's torque map is thus obtained by repeating these operations for each  $dq$  point of the mesh grid defined at step 2.2.2. The torque map obtained for the IM used to validate the proposed mapping procedure is reported in Fig. 2.16. It is noted that the torque map reports both positive and negative torque values due to the symmetrical limits of the  $q$ -axis current in Eq. (2.80). In this way, the flux- and torque- maps can arbitrarily deal with the IM's motoring- and generator- operation.

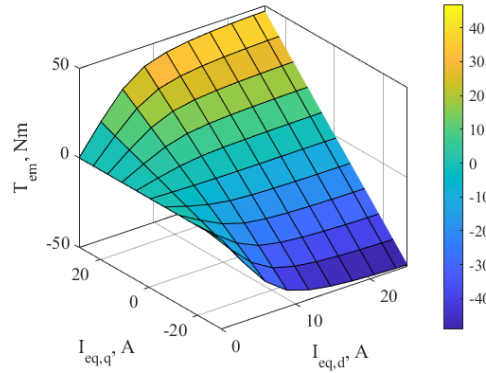


Figure 2.16 Electromagnetic torque map of the IM used for the experimental validation.

### Torque-speed working points

According to the considered speed  $\Delta\omega_n$  and torque  $\Delta T_m$  resolutions, a regular mesh grid in the torque-speed range is generated. The speed limit of the mesh grid corresponds to the maximum operative IM's speed  $\omega_{m,max}$ . Conversely, the absolute torque limit  $T_{max}$  corresponds to that of the torque map computed after elaborating the results of the standard test procedures (see Fig. 2.16). Therefore, the efficiency map is obtained by computing the efficiency of each point composing the mesh grid. It is noted how the mesh grid is composed of torque-speed points that cannot be operated since they overcome the maximum torque per speed (MTPS) profile [86].

In Fig. 2.17 the MTPS profiles for the MUT used for mapping validation for different dc-link voltages (400 V and 600 V) and machine temperatures (25 °C and 100 °C) are reported for both motoring and generating modes. Since the iron losses have been included, the maximum torque in the base region is not perfectly constant. Also, in Fig. 2.18 the corresponding profiles of the mechanical power are shown. The profiles are computed based on the machine parameters evaluated with the standard tests presented before. The base speed is strongly related to the dc-link voltage value, while the machine temperature carries very little weight. However, the proposed mapping procedure automatically rules out these points, as shown in the following. This means that the MTPS profiles are not necessary for the mapping procedure. The profiles have been computed to confirm the maximum torque achievable

with the mapping procedure.

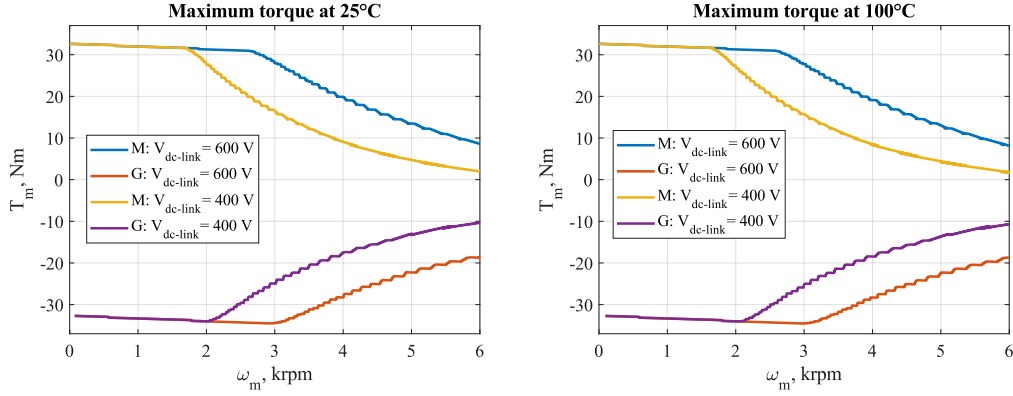


Figure 2.17 MTPS profiles for MUT at different dc-link voltage and machine temperature.

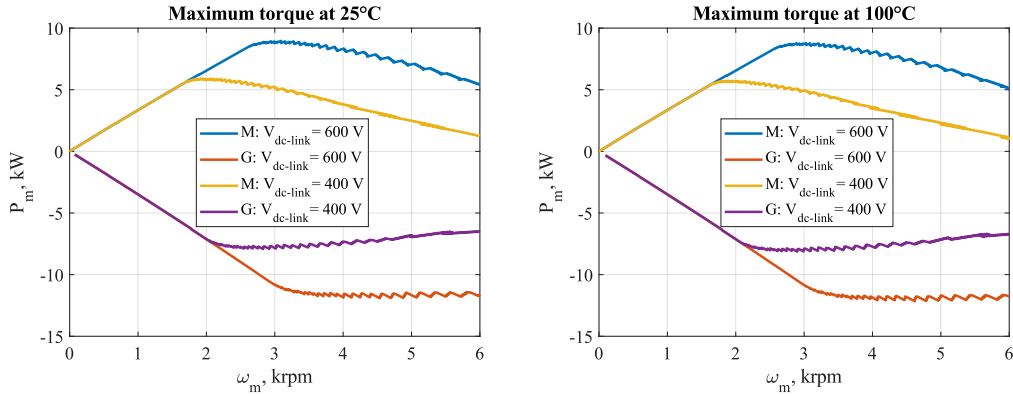


Figure 2.18 MTPS profiles of the mechanical power for MUT at different dc-link voltage and machine temperature.

### 2.2.3 Mapping algorithm

The proposed mapping procedure requires the knowledge of the following inputs to compute the efficiency map of the mesh grid:

- Amplitude limit of the phase currents  $I_{max}$ , whose meaning has been previously reported.
- Amplitude limit of the phase voltages  $V_{max}$ , whose value is computed according to the sinusoidal voltage limit of the inverter feeding the IM

as reported in 2.60:

$$V_{max} = v_{dc} / \sqrt{3} \quad (2.81)$$

where  $v_{dc}$  is the input dc voltage of the inverter. Alternatively, if considering grid-connected IMs, the amplitude limit of the phase voltages is set equal to or a bit higher than the IM's rated phase voltage (peak value).

- Stator  $\vartheta_s$  and rotor  $\vartheta_r$  operating temperatures, whose values can be chosen arbitrarily according to their operative limits.

According to the above-reported inputs and constraints, the efficiency map of the torque-speed mesh grid is computed upon base the flow diagram shown in Fig. 2.19, and whose description is reported in the following.

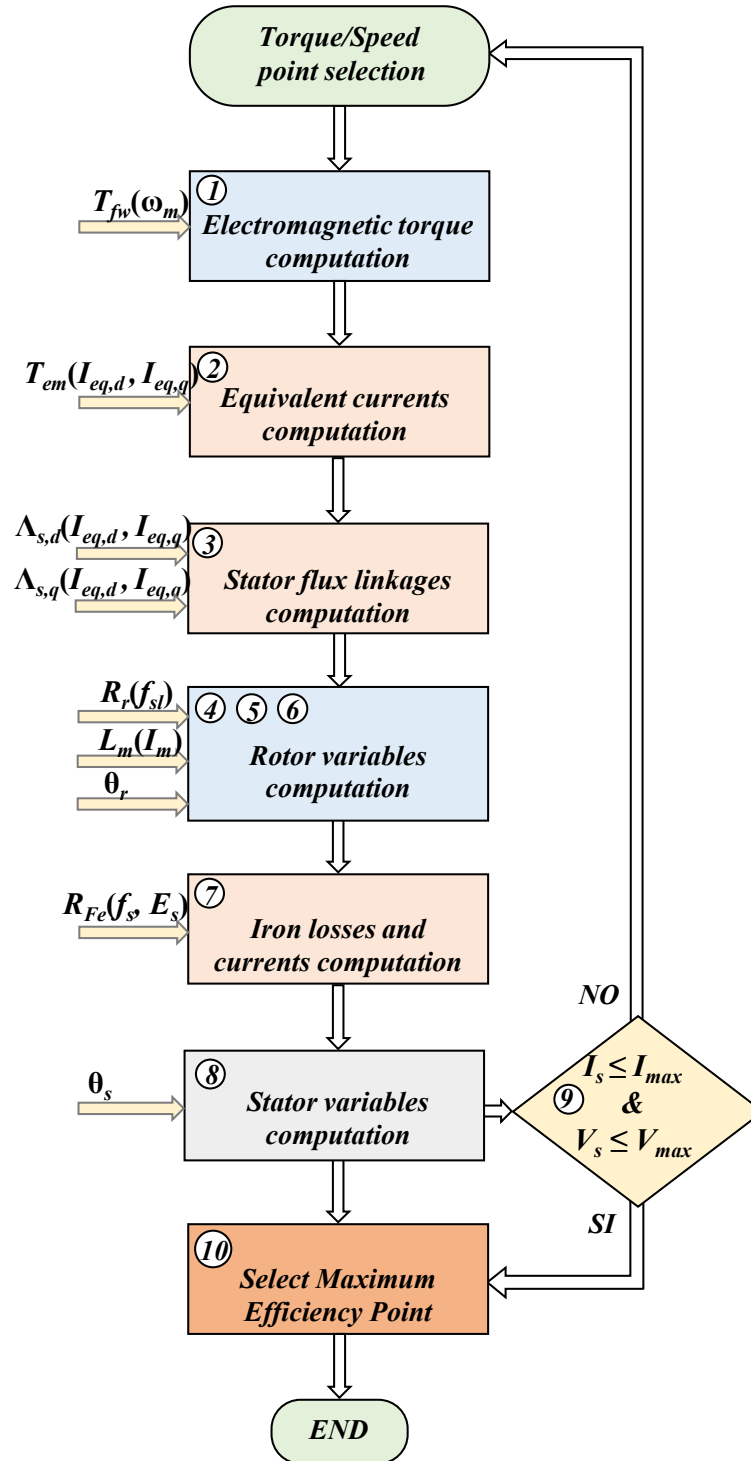


Figure 2.19 Flow diagram of the proposed mapping procedure.

### Step 1: computation of the electromagnetic torque

According to the mechanical speed  $\omega_m$  of the considered torque-speed point, the torque loss  $T_{fw}$  due to friction and ventilation is computed by interpolating the experimental profile obtained after performing the no-load tests (see Fig. 3). In this way, the electromagnetic torque  $T_{em}$  is computed from the mechanical one  $T_m$  using Eq. (2.48).

### Step 2: computation of the equivalent currents

All the combinations of flux- and torque-producing  $dq$  currents realizing the electromagnetic torque computed at *Step 1* are considered. These current components, called equivalent  $dq$  currents for simplicity, are obtained using the torque map computed after elaborating the results of the standard test procedures (see Fig.2.16). In detail, the considered combinations of equivalent  $dq$  currents correspond to those belonging to the torque map's iso contour related to the electromagnetic torque value computed at 2.2.3.

The use of the iso contour profiles of bidimensional maps is well-known in the literature [91, 92] and thus not reported here since it goes beyond the goal of this work. Let's assume that  $n_c$  -combinations of equivalent  $dq$  currents have been found; these are stored in two  $n_c$ -dimensional vectors where a generic component is denoted with  $k$  index. The current vectors are denoted as  $I_{eq,d}^{vct}$  and  $I_{eq,q}^{vct}$ .

### Step 3: computation of the stator flux linkages

For each combination of the equivalent  $dq$  currents, the  $dq$  stator flux linkages are computed by interpolating the flux maps obtained after elaborating the results of the standard test procedures (see Fig.2.15). Therefore, two  $n_c$ -dimensional stator flux linkage vectors are computed, one for each axis, and denoted as  $\Lambda_{s,d}^{vct}$  and  $\Lambda_{s,q}^{vct}$ .

**Step 4: computation of the machine's inductances**

For each combination of the equivalent  $dq$  currents, the magnetizing inductance is computed by interpolating the experimental profile obtained after elaborating the results of the standard test procedures (see Fig. 2.14). For simplicity, the magnetizing current is calculated using  $I_m \simeq I_{eq,d}$ , thus assuming its value equal to the  $d$ -axis equivalent current. Therefore, an  $n_c$ -dimensional vector of magnetizing inductance is computed and denoted as  $L_m^{vct}$ .

Finally, by considering the experimental values of leakage inductances ( $L_{l,s}$ ,  $L_{l,r}$ ) obtained after performing the locked-rotor tests, the vectors of stator-  $L_s^{vct}$  and rotor-  $L_r^{vct}$  inductances are computed from  $L_m^{vct}$  using  $L_s = L_m + L_{l,s}$ ,  $L_r = L_m + L_{l,r}$ .

**Step 5: computation of the rotor current and flux**

Based on Eq. (2.43), the  $n_c$ -dimensional vectors of  $q$ -axis rotor current  $I_{r,q}^{vct}$  and rotor flux linkage  $\Lambda_r^{vct}$  are computed as:

$$\begin{aligned} I_{r,q}^{vct}(k) &= -\frac{L_m^{vct}(k)}{L_r^{vct}(k)} \cdot I_{eq,q}^{vct}(k) \\ \Lambda_{r,q}^{vct}(k) &= L_m^{vct}(k) \cdot I_{eq,d}^{vct}(k) \end{aligned} \quad 1 \leq k \leq n_c \quad (2.82)$$

where  $k$  is a generic element of the vector composed by  $n_c$ -combinations.

**Step 6: computation of slip speed, rotor resistance, and rotor Joule losses**

The slip speed  $\omega_{sl}$  is computed using Eq. (2.46), thus noting how the rotor resistance  $R_r$  is required. However, this parameter depends on the slip frequency  $f_{sl}$  according to the experimental profile obtained from the locked-rotor tests (see Fig. 2.11). Therefore, the following implicit equation system

is solved:

$$\begin{cases} \omega_{sl}^{vct}(k) = 2 \cdot \pi \cdot f_{sl}^{vct}(k) = \frac{R_r^{vct}(k)}{L_r^{vct}(k)} \cdot \frac{I_{eq,q}^{vct}(k)}{I_{eq,d}^{vct}(k)}, & 1 \leq k \leq n_c \\ R_r^{vct}(k) = R_{r,0}^{vct}(k) \cdot K_{\vartheta}^r \end{cases} \quad (2.83)$$

where  $R_{r,0}^{vct}(j)$  at the position  $j$  stands for the experimental value of rotor resistance which depends on the slip frequency  $\omega_{sl}(j)$  (see Fig. 2.11). The coefficient  $K_{\vartheta}^r$  considers the variation of the rotor resistance to the operating rotor temperature  $r$  as:

$$K_{\vartheta}^r = \frac{k_{rt} + \vartheta_r}{k_{rt} + \vartheta_0} \quad (2.84)$$

where  $k_{rt}$  is the characteristic temperature of the conductive material of the rotor cage. According to [82],  $k_{rt} = 234$  °C for copper, while  $k_r = 225$  °C for aluminum. Finally, the  $n_c$ -dimensional vector of rotor Joule losses  $P_{jr}^{vct}$  is computed as:

$$P_{jr}^{vct}(k) = \frac{3}{2} \cdot R_r^{vct}(k) \cdot I_{r,q}^{vct}(k) \cdot I_{r,q}^{vct}(k), \quad 1 \leq k \leq n_c \quad (2.85)$$

### Step 7: computation of iron losses and iron currents

From the  $n_c$ -dimensional vector of the slip speed  $\omega_{sl}^{vct}$ , the corresponding vector of synchronous speed  $\omega_s^{vct}$  is computed using Eq. (2.46). At the same time, the  $n_c$ -dimensional vector of the stator frequency  $f_s^{vct}$  is obtained as  $f_s^{vct} = \omega_s^{vct}/2\pi$ . Therefore, the  $dq$  components ( $E_{s,d}^{vct}, E_{s,q}^{vct}$ ) and amplitude  $E_s^{vct}$  of the machine's back-emf are computed using Eq. (2.42) as:

$$\begin{aligned} E_{s,d}^{vct}(k) &= -\omega_s^{vct}(k) \cdot \Lambda_{s,q}^{vct}(k), & E_{s,q}^{vct}(k) &= \omega_s^{vct}(k) \cdot \Lambda_{s,d}^{vct}(k) \\ E_s^{vct}(k) &= \sqrt{E_{s,d}^{vct}(k) \cdot E_{s,d}^{vct}(k) + E_{s,q}^{vct}(k) \cdot E_{s,q}^{vct}(k)} \end{aligned} \quad 1 \leq k \leq n_c \quad (2.86)$$

The iron losses (including the stator skin effect) are computed from the stator frequency and amplitude of the machine's back-emf by interpolating the iron losses map obtained after performing the no-load tests (see Fig. 2.8). Therefore, the  $n_c$ -dimensional vector of iron losses  $P_{Fe}^{vct}$  is obtained, while the



corresponding current components ( $I_{Fe,d}^{vct}, I_{Fe,q}^{vct}$ ) are computed using the IM's equivalent circuit shown in Fig. 2.4 for a generic element  $j$  of the vectors as:

$$\begin{aligned} I_{Fe,d}^{vct}(k) &= \frac{2}{3} \cdot \frac{E_{s,d}^{vct}(k) \cdot P_{Fe}^{vct}(k)}{E_s^{vct}(k) \cdot E_s^{vct}(k)} \\ I_{Fe,q}^{vct}(k) &= \frac{2}{3} \cdot \frac{E_{s,q}^{vct}(k) \cdot P_{Fe}^{vct}(k)}{E_s^{vct}(k) \cdot E_s^{vct}(k)} \end{aligned}, \quad 1 \leq k \leq n_c \quad (2.87)$$

#### Step 8: computation of stator currents, stator voltages, and stator Joule losses

According to the IM's equivalent circuit shown in Fig.2.4, the  $n_c$ -dimensional vectors of  $dq$  stator currents ( $I_{s,d}^{vct}, I_{s,q}^{vct}$ ) are computed as:

$$I_{s,d}^{vct} = I_{eq,d}^{vct} + I_{Fe,d}^{vct}, \quad I_{s,q}^{vct} = I_{eq,q}^{vct} + I_{Fe,q}^{vct} \quad (2.88)$$

Using Eq. (2.42), the  $n_c$ -dimensional vectors of the  $dq$  stator voltages ( $V_{s,d}^{vct}, V_{s,q}^{vct}$ ) are instead computed as:

$$V_{s,d}^{vct} = R_s \cdot I_{s,d}^{vct} + E_{s,d}^{vct}, \quad V_{s,q}^{vct} = R_s \cdot I_{s,q}^{vct} + E_{s,q}^{vct} \quad (2.89)$$

The stator resistance  $R_s$  is computed according to the operative temperature of the stator winding  $\vartheta_s$  as:

$$R_s = R_{s,0}^{dc} \cdot \frac{k_s + \vartheta_s}{k_s + \vartheta_0} \quad (2.90)$$

where  $k_s$  is the characteristic temperature of the conductive material of the stator windings, i.e.,  $k_s = 234.5$  °C since copper is typically used to make them.

Finally, the  $n_c$ -dimensional vector of the stator Joule losses  $P_{js}^{vct}$  is computed as:

$$P_{js}^{vct}(k) = \frac{3}{2} \cdot R_s \cdot \left( I_{s,d}^{vct}(k) \cdot I_{s,d}^{vct}(k) + I_{s,q}^{vct}(k) \cdot I_{s,q}^{vct}(k) \right), \quad 1 \leq k \leq n_c \quad (2.91)$$

### Step 9: application of the voltage and current limits

The  $n_c$ -dimensional vectors reporting the amplitude of the stator phase voltages  $V_s^{vct}$  and stator phase currents  $I_s^{vct}$  are computed as:

$$\begin{aligned} V_s^{vct}(k) &= \sqrt{V_{s,d}^{vct}(k) \cdot V_{s,d}^{vct}(k) + V_{s,q}^{vct}(k) \cdot V_{s,q}^{vct}(k)} \\ I_s^{vct}(k) &= \sqrt{I_{s,d}^{vct}(k) \cdot I_{s,d}^{vct}(k) + I_{s,q}^{vct}(k) \cdot I_{s,q}^{vct}(k)} \end{aligned}, \quad 1 \leq k \leq n_c \quad (2.92)$$

Therefore, among the elements composing the  $n_c$ -dimensional vectors computed in the previous steps, the ones that break the amplitude limit of the phase currents  $I_{max}$  or the amplitude limit of the phase voltages  $V_{max}$  are ruled out. For clarity, by considering any one of the  $n_c$ -dimensional vectors computed in the previous steps and for simplicity denoted with  $X^{vct}$ , the elements of this vector that satisfy both the above-reported limits are indicated as:

$$\begin{aligned} X^{vct} \Big| \quad & V_s^{vct} \leq V_{max} \\ & I_s^{vct} \leq I_{max} \end{aligned} \quad (2.93)$$

It is highlighted that since the  $n_c$ -dimensional vectors have been computed using element-wise operators, the position indexes of the elements that satisfy the voltage and current limits are the same for all vectors.

If applying the voltage and current limits leads to ruling out all elements of the  $n_c$ -dimensional vectors, the considered torque-speed point overcomes the MTPS profile and therefore cannot be physically operated. In this case, the proposed mapping procedure rules out this torque-speed point from the efficiency computation, thus moving to consider the next one, as shown in the flow diagram of Fig. 2.19.

### Step 10: selection of the maximum efficiency point

Let's consider the elements of the  $n_c$ -dimensional vectors that satisfy both voltage and current limits. The position index of the element leading to maximizing efficiency corresponds to the one that minimizes the overall losses. For clarity, considering any one of the  $n_c$ -dimensional vectors again  $X^{vct}$ , the element of this vector that leads to maximizing efficiency is denoted

as:

$$X^{opt} = \min \left( \begin{array}{c} P_{jr}^{vct} \Big| \begin{array}{l} V_s^{vct} \leq V_{max} \\ I_s^{vct} \leq I_{max} \end{array} + P_{Fe}^{vct} \Big| \begin{array}{l} V_s^{vct} \leq V_{max} \\ I_s^{vct} \leq I_{max} \end{array} + P_{js}^{vct} \Big| \begin{array}{l} V_s^{vct} \leq V_{max} \\ I_s^{vct} \leq I_{max} \end{array} \end{array} \right) \quad (2.94)$$

The position index of the element that leads to maximizing efficiency is the same for all vectors. In other words, there is only one specific combination of  $dq$  variables (voltages, currents, flux linkages) that leads to maximizing efficiency for the considered torque-speed point.

Finally, if considering a torque-speed point in the motor operation, the machine's efficiency  $\eta^{opt}$  is computed as:

$$\eta^{opt} = \frac{T_m \cdot \omega_m}{T_m \cdot \omega_m + P_{jr}^{opt} + P_{Fe}^{opt} + P_{js}^{opt}} \quad (2.95)$$

Conversely, if considering a torque-speed point in the generation operation, the machine's efficiency is computed as:

$$\eta^{opt} = \frac{T_m \cdot \omega_m + P_{jr}^{opt} + P_{Fe}^{opt} + P_{js}^{opt}}{T_m \cdot \omega_m} \quad (2.96)$$

### Step 11: saving results

Once the IM's efficiency has been computed, the proposed mapping procedure stores it and proceeds to consider the next torque-speed point, as shown in the flow diagram of Fig. 2.19. However, other variables of interest like the stator  $dq$  currents ( $I_{s,d}^{opt}$ ,  $I_{s,q}^{opt}$ ) can be saved, thus computing the stator  $dq$  currents maps if considering this case. As reported in the next Section 2.3, the stator  $dq$  currents maps have been used to perform the experimental validation of the proposed mapping procedure. Indeed, the proposed mapping procedure can potentially map all machine's electromagnetic variables, thus representing a promising solution for accurately virtualize IMs operated in wide torque-speed ranges.

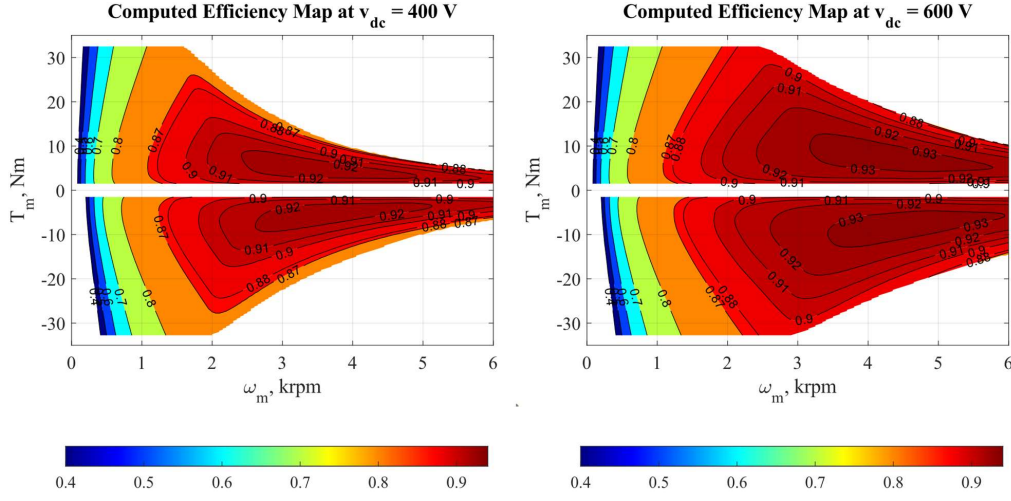


Figure 2.20 Computed efficiency maps at  $v_{dc} = 400$  V (left) and  $v_{dc} = 600$  V (right) using the maximization of the efficiency.

Fig. 2.20 shows an example of the computed efficiency maps at  $25^\circ\text{C}$  with two different dc-link voltages, implementing the maximum efficiency strategy. In the next section the experimental results are reported for mapping algorithm validation. However, based on the efficiency maps reported in Fig. 2.20 it can be highlighted how the algorithm is able to track the different working areas and base speeds, changing the dc-link voltage value. The maps shape is in agreement with the ones proposed in literature, based on experimental measurements or FEA simulations.

#### 2.2.4 Mapping minimizing the stator Joule losses and stator flux

As previously reported, the proposed mapping algorithm computes efficiency maps with the aim to minimize the overall electrical losses (see Eq. (2.94)). There is only one specific combination of  $dq$  variables (voltages, currents, fluxes) that leads to maximizing efficiency for the considered torque-speed point. However, the mapping algorithm can be modified to compute the efficiency maps to minimize the stator Joule losses, i.e., considering the machine's MTPA operation for mechanical speeds lower than the base speed (see Section 2.1.7). Otherwise, the mapping algorithm can be modified con-

sidering the minimization of the stator flux on the whole torque-speed range. For example, to consider the machine's MTPA operation, focusing on the flowchart of Fig.2.19, the block number 10 should change from "Select Maximum Efficiency Point" to "Select Minimum Stator Joule Losses". Conversely than 2.94, if the efficiency maps are computed to minimize the stator Joule losses, then the optimal element of the  $n_c$ -dimensional vectors  $X^{vct}$  is thus selected as:

$$X^{opt} = \min \left( \begin{array}{c} P_{js}^{vct} \\ V_s^{vct} \leq V_{max} \\ I_s^{vct} \leq I_{max} \end{array} \right) \quad (2.97)$$

In Fig. 2.21, the efficiency map computed using the minimization of stator Joule losses at  $v_{dc} = 400$  V is reported. Qualitatively, it is noted how the optimization strategy that maximizes the efficiency (see Fig. 2.20 - left) leads to better results as the high efficient region is wider than the one obtained if only the stator Joule losses (see Fig. 2.21 - left) are minimized. Also, in the right of Fig. 2.21 the efficiency map of the machine under test is reported, implementing the minimum stator flux control strategy, using Eq. (2.98). The high efficient region using the minimum stator flux strategy is reduced compared to other two control strategies presented (maximum efficiency - Fig. 2.20 and minimum stator Joule losses - Fig. 2.21, left). Also, the map evaluated with minimum stator flux presents the isoefficiency profiles smoother.

$$X^{opt} = \min \left( \begin{array}{c} \lambda_s^{vct} \\ V_s^{vct} \leq V_{max} \\ I_s^{vct} \leq I_{max} \end{array} \right) \quad (2.98)$$

About the MTPV operation of the machine (see Section 2.1.7), this is automatically implemented. Indeed, for mechanical speeds higher than the base speed, the working points over the MTPV profile are automatically ruled out. This confirms that the MTPS, MTPA, MTPV profiles are not necessary for the mapping procedure developed in this work.

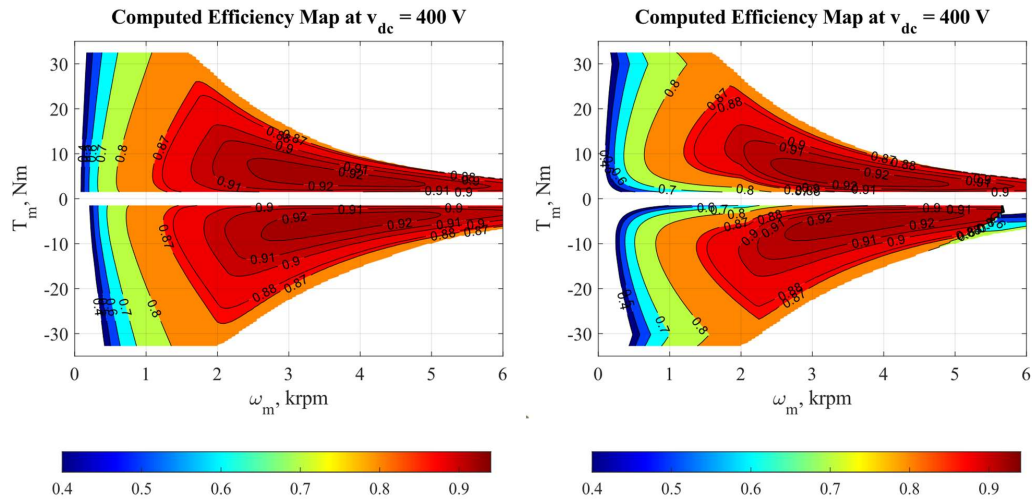


Figure 2.21 Efficiency maps at  $v_{dc} = 400 \text{ V}$  using the minimization of the stator Joule losses (MTPA) (left) and minimum stator flux (right).

## 2.3 Experimental validation

The validation of the proposed mapping procedure has been carried out on a 10 kW, 4 poles, 100 Hz IM, whose primary data are listed in Table 2.2. In detail, the IM under test consists of a reduced-scale prototype of a starter-generator for aircraft applications [93]. Therefore, efficiency maps in both motor and generator operations have been considered.

### 2.3.1 Test rig

The machine under test has been mounted on a test rig for validation purposes, as shown in Fig. 2.22. The rotor shaft has been coupled to a driving machine acting as a prime mover (speed-controlled). However, due to the limitation of the test rig, the IM's speed has been limited to 6000 rpm.

The power electronics feeding the IM consists of a three-phase inverter based on an IGBT power module, rated 50 A, 1200 V, and fed by a bidirectional programmable dc source. The switching frequency has been set at 8 kHz, with a software-implemented dead-time of 3  $\mu$ s. The digital controller consists of the fast prototyping board dSPACE MicroLabBox with the sampling frequency set at 8 kHz (single-edge PWM). Finally, the torque control algorithm of the IM has been entirely developed in C-code.

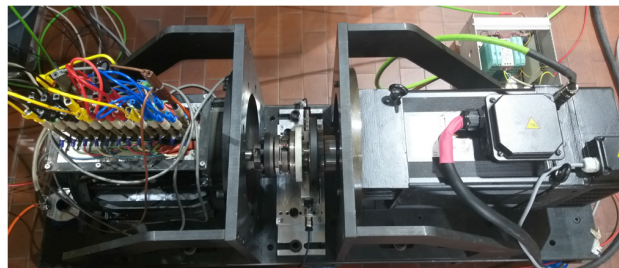


Figure 2.22 View of the IM under test (left), torque transducer (center), and driving machine (right).

Table 2.2 Machine's primary data

Rated Data	
Pole pairs	2
Rated power	10 kW
Rated speed	3000 rpm
Rated torque	16 Nm
Rated voltage (line-to-line)	400 V (RMS)
Rated current	10 A (RMS)

### 2.3.2 Measurement system

The torque transducer T40B from HBM has been mounted along with the mechanical coupling between the IM under test and the driving machine, as shown in Fig. 2.22. In this way, the mechanical quantities of torque and position have been measured. In detail, the mechanical position has been used for two purposes. On the one hand, its elaboration allowed detecting the mechanical speed for computing the IM's mechanical power. On the other hand, it has consisted as one of the feedback for the torque control algorithm thanks to its good resolution (1024 pulses/rev).

Concerning the electric measurements, the IM's phase currents have been measured using the high-performance current transducers IT 200-S Ultrastab from LEM. In parallel, the line-to-line PWM voltages have been measured using the GN610B from HBM, consisting of a voltage card equipped with high-voltage/high-speed acquisition channels (1000 V, 18 bit, 2 MS/s).

Both mechanical and electrical quantities have been sampled and stored with a sampling frequency of 2 MS/s by the data recorder GEN2tB from HBM, consisting of a high-performance transient recorder and calibrated data acquisition system. The time-fundamental components of phase voltages and phase-currents have been extracted from the sampled data using the data elaboration software integrated with the instrument. In this way, the time-fundamental electric power of the IM has been computed, thus ruling out the additional and harmonic losses introduced by the PWM modulation.

The experimental efficiency maps shown in the following subsections have been computed considering a predefined number of time-fundamental electric periods for each test point. In this time window, the average values of mechanical power and time-fundamental electric power have been



computed, allowing the evaluation of the IM's efficiency considering its time-fundamental behavior, i.e., the same one calculated by the proposed efficiency mapping procedure.

### 2.3.3 Validation approach

The proposed mapping procedure has been validated by directly comparing the experimental efficiency maps with those computed, using the maximum efficiency control strategy. Each experimental efficiency map has been evaluated by setting a reasonable resolution in speed and torque, thus leading to a predefined number of test points in the torque-speed range.

The torque of the IM under test has been controlled in each test point using a field-oriented control (FOC) scheme [94], as shown in Fig. 2.23 and Fig. 2.24. However, to correctly validate the proposed mapping procedure, the reference  $dq$  stator currents  $i_{s,dq}^*$  for the current vector control (CVC), have been generated using the following approach.

The efficiency maps have been preliminarily computed using the proposed mapping procedure and by considering the same operating conditions subsequently imposed in the experimental validation, i.e., the same working temperatures (stator  $\vartheta_s$  and rotor  $\vartheta_r$ ) and voltage  $V_{max}$  and current  $I_{max}$  limits. However, the  $dq$  stator currents maps related to each computed efficiency map have been stored and converted in lookup tables (LUTs) in order to be implemented and interpolated in the motor control algorithm. Therefore, the reference  $dq$  stator currents have been generated for each test point by first selecting the LUTs reporting the  $dq$  stator currents maps related to the actual operating temperatures (stator and rotor  $\vartheta_{s,r}^*$ ) and imposed voltage  $V_{max}$  limit (i.e., input dc voltage  $v_{dc}$  of the inverter feeding the IM). Finally, according to the reference values of torque  $T_m^*$  and speed  $\omega_m$  of the considered test point, the selected LUTs have been interpolated, getting the reference  $dq$  stator currents  $i_{s,dq}^*$  (see Fig. 2.24) evaluated with the maximum efficiency control strategy. This validation approach brings the following advantages.

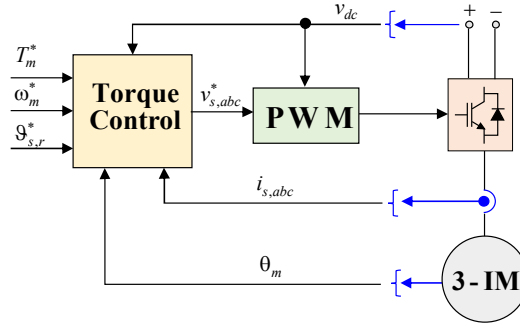


Figure 2.23 Configuration of the electric drive for the experimental validation

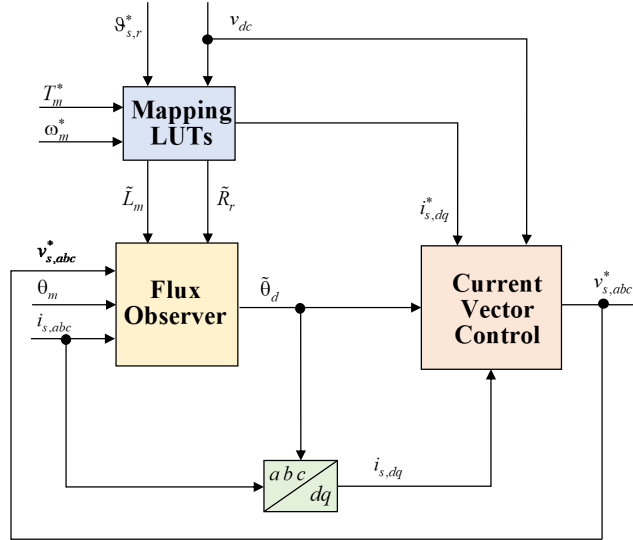


Figure 2.24 Torque control scheme of the IM under test (the superscript  $\tilde{\cdot}$  denotes an estimated parameter or variable).

- The IM's torque is controlled using the optimal references of the  $dq$  stator currents, thus maximizing the efficiency in each operating point since the proposed mapping procedure considers all the IM's losses sources. Conversely, almost all the commercial torque controllers for IM drives perform the torque regulation using control schemes that, in luckiest cases, minimize the stator Joule losses according to the voltage and current constraints imposed by the inverter feeding the machine [94, 87]. In contrast, in the worst cases, most commercial torque control solutions set the IM's rated flux below the base speed regardless of the

load torque. Above the base speed, the flux level is reduced using several strategies proposed in the literature [86, 95].

- Using a user-implemented FOC algorithm allows estimating the position of the  $d$ -axis  $\theta_d$  using a calibrated flux observer. In this way, the reference  $dq$  stator currents are imposed with a high confidence level, minimizing torque- and efficiency- steady-state errors. Conversely, most commercial IM drives often implement indirect-FOC schemes that cannot estimate the  $d$ -axis orientation accurately.

In this work, a reduced-order rotor flux observer has been implemented [96]. Therefore, the rotor flux orientation is obtained using the IM's magnetic model in the low-speed range, thus requiring the measurements of the three-phase stator currents  $i_{s,abc}$ , and rotor mechanical position  $\theta_m$ . Also, the parameters of magnetizing inductance  $L_m$  and rotor resistance  $R_r$  are required. In this work, such parameters have been directly tuned according to the off-line results obtained from the mapping procedure (see Fig. 2.24), thus improving the flux observer's performance for each test point.

In the medium- at high-speed ranges, the flux observer is instead based on the time-integration of the machine's back-emf, thus requiring the accurate reconstruction of the IM's phase voltages from the reference ones  $v_{s,abc}$  generated by the CVC. In addition, the voltage errors introduced by the inverter feeding the machine must be considered, thus requiring their identification by implementing the self-commissioning procedures reported in the literature [97]. Other details regarding the flux observer and the FOC scheme are not reported since they are beyond the goal of this work.

In summary, it is noted how the experimental mapping of IMs is more challenging than the one performed for synchronous motors. Indeed, the  $d$ -axis position can be directly measured for these last, avoiding the implementation of dedicated flux observers whose performance significantly affects the steady-state torque and efficiency. Indeed, orientation errors introduced by the flux observer lead to imposing actual  $dq$  stator currents  $i_{s,dq}$  different from the reference ones, compromising the validation. This drawback is why very few contributions concerning the experimental mapping of IMs are reported in the literature.

### 2.3.4 Experimental results

The experimental efficiency maps have been evaluated considering the following values of the inverter's dc voltage  $v_{dc} = 400 \text{ V}$  and  $v_{dc} = 600 \text{ V}$ . The amplitude limit of the phase currents has been instead kept constant to the maximum value of the IM's overload current, i.e.,  $I_{max} = 25 \text{ A}$ , leading to the maximum extension of the efficiency maps for each value of the inverter's dc voltage. To properly reconstruct the IM's efficiency maps, these have been evaluated using speed and torque resolutions of 400 rpm and 2 Nm, respectively. To guarantee that the tested IM practically operated in steady-state thermal conditions over the whole efficiency mapping procedure, an adequate pause time has waited between one test point and the next. In detail, for the case study, it has been experimentally verified that 3 s on and 60 s off was sufficient to keep reasonably constant the stator winding temperature.

Finally, all the efficiency maps have been evaluated at the same operating temperature in which the dc, no-load, and locked-rotor tests have been performed. This limitation is due to the following drawbacks.

- The IM under test is equipped with only one temperature sensor (thermistor NTC) placed on the stator winding. Therefore, even loading the IM at the rated torque and waiting for the steady-state thermal conditions, the temperature of the rotor cage would be unknown without the possibility to compute the related efficiency maps.
- Currently, the literature does not report a practice solution to keep both the temperatures of stator and rotor almost constant to the rated values while performing the mapping in a wide-torque speed range.

Therefore, the mapping has been performed under controlled ambient temperature equal to that in which the dc, no-load, and locked-rotor tests have been performed  $\vartheta_0 = 25^\circ\text{C}$ . Moreover, an adequate pause time has waited during the mapping execution between one test point and the next. In detail, considering the overall active time in which one generic test point has been operated, e.g., 3 s, the pause time has been set equal to twenty times that time, i.e., 60 s referring to the example. In addition, the stator winding

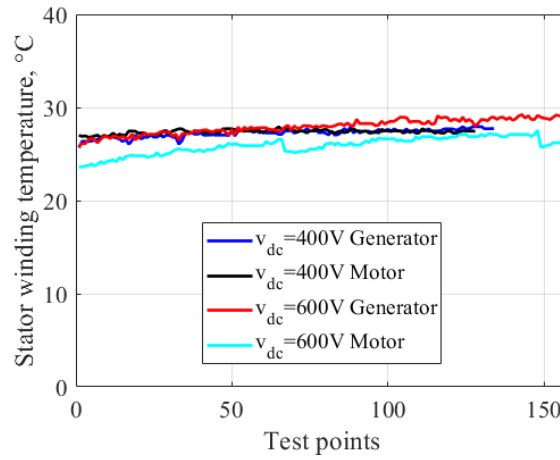


Figure 2.25 The stator winding temperatures during the measured efficiency mapping.

temperature has been monitored using the temperature sensor previously mentioned. Fig. 2.25 demonstrates that the stator winding temperature measured with the embedded NTC sensor is reasonably constant during each mapping (i.e., around 3 - 4 °C and  $\vartheta_0 = 25^\circ\text{C}$ ). The first point of each curve corresponds to that at minimum speed and torque (i.e., 400 rpm,  $\pm 2$  Nm), while the last test point corresponds to that at maximum speed (6000 rpm) and maximum torque on the MTPS profile, as confirmed Fig. 4.48.

The experimental and computed efficiency maps obtained in the above-reported test conditions are shown in Fig. 2.26, where the white markers denote the operated test points. A slight distortion characterizes experimental efficiency maps since they are affected by the uncertainty of both electric and mechanical measurements. However, the experimental results are excellent considering the complexity of both the test rig and the measurement system. It is noted that the proposed mapping procedure estimates the IM's efficiency in the whole torque-speed range with very good accuracy. Moreover, the shift of the maximum efficiency region is detected if changing the inverter's dc voltage, thus changing as well the extent of the region in which the flux-weakening is performed.

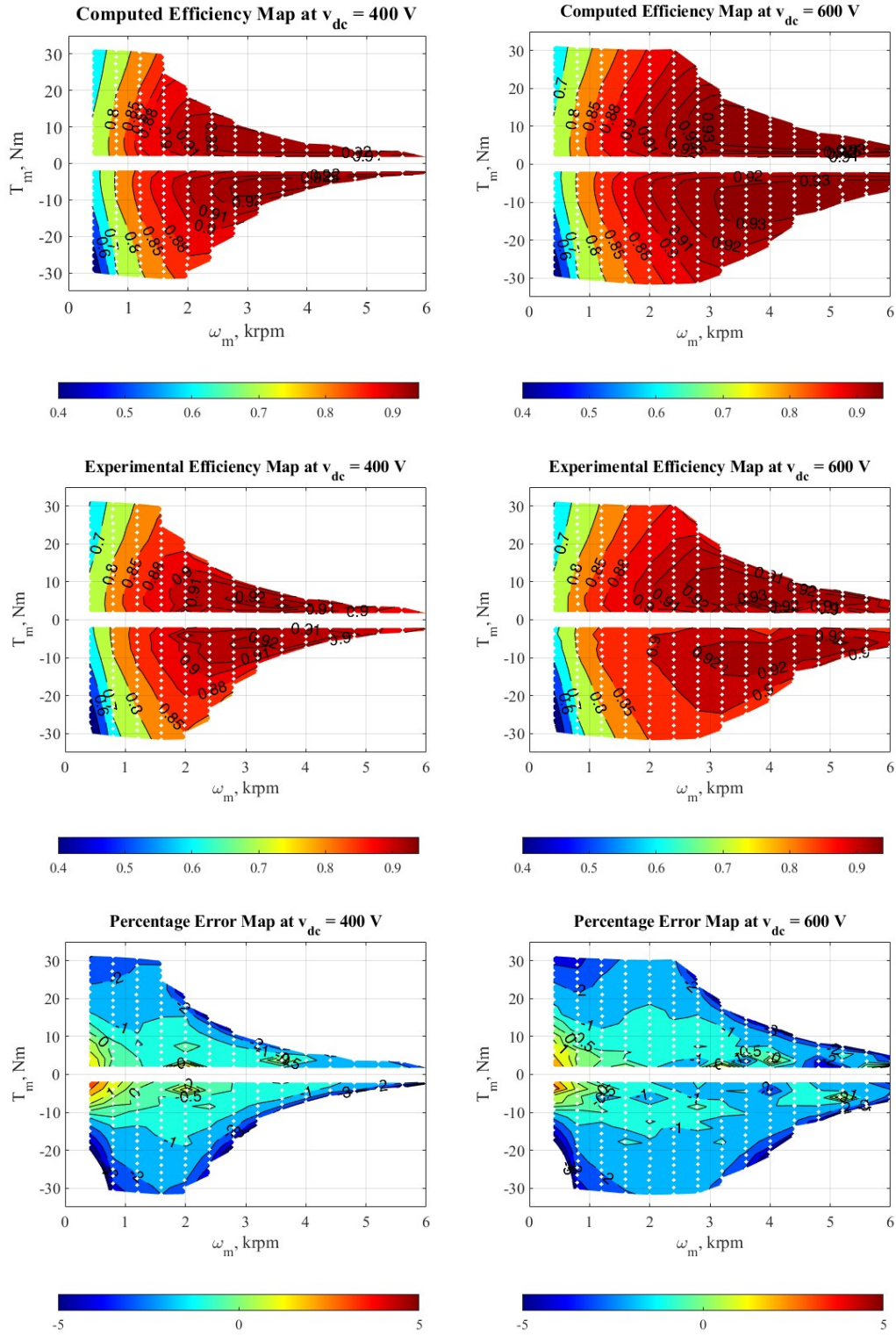
(a) Efficiency maps at  $v_{dc} = 400\text{ V}$ .(b) Efficiency maps at  $v_{dc} = 600\text{ V}$ .

Figure 2.26 Experimental validation of IM mapping.

To highlight better the accuracy of the proposed mapping procedure, the map reporting the error between the computed efficiency map and the experimental one is shown for each test condition. It is noted how the error is practically enough lower than 2 - 3 % in most of the torque-speed range, regardless of whether motoring or generator conditions are considered. In detail, it is noted how the error becomes more significant for *i*) the test points near the MTPS profile and *ii*) in the generator operation, the test points at very low speed and high braking torque.

Regarding the test points near the MTPS profile, it is highlighted that they represent the most critical ones for the torque control algorithm. Indeed, in that operating points, the performance of the flux observer in estimating the  $d$ -axis position strictly depends on that in reconstructing the machine's back-emf accurately. Thus, assessing the inverter nonlinearities and the resistive voltage drops with high accuracy. Therefore, it is most likely that in test points near the MTPS profile, the torque control algorithm has not effectively imposed the reference  $dq$  stator currents, justifying the error between computed efficiencies and measured ones. In any case, it is highlighted that the error in the test points near the MTPS profile never overcomes 4 %. Conversely, it is noted that in the generator operation, the test points at very low speed (400 rpm) and high braking torque are characterized by efficiency errors near or even higher than 5 %. This error is justified because, in this operating region, the IM's efficiency is near zero, hindering its accurate evaluation. However, the IM's efficiency assessment is low significant in that region since mechanical and electrical powers are both meager.

In summary, the comparison between computed and experimental efficiency maps confirms the accuracy of the proposed mapping procedure in estimating the IM's efficiency in wide torque-speed ranges, as well as considering very different operating conditions like a significant variation of the dc-link voltage of the inverter feeding the machine.

## 2.4 Conclusion

This chapter proposed a methodology for computing the efficiency maps of the three-phase induction motors (IMs) operated in wide torque-speed

ranges using only the results of standard test procedures like dc, no-load, and locked-rotor tests. In this way, the need for calibrating demanding finite elements analyses (FEA) requiring the machine design data is avoided [14, 21, 98, 29]. Moreover, the computed efficiency maps can be used to virtualize the machine, allowing it to perform accurate energetic assessments without needing expensive test rigs to manage demanding speed and torque [41]. The proposed efficiency mapping procedure's inputs consist of results from the standard tests performed at different supply voltage and frequency levels [82]. In this way, all the machine's nonlinearities, like magnetic saturation, iron losses, skin effect, and mechanical losses, are considered, thus accurately computing the efficiency maps. Regardless of the considered speed and torque resolutions, the proposed procedure allows computing the efficiency maps without requiring long computing times. Moreover, the efficiency maps can be calculated under different operating stator and rotor temperatures and quickly considering the voltage and current constraints introduced by the IM or the power electronics converter feeding it. Consequently, the proposed procedure has a high level of generality, which can be easily applied to grid-connected and inverter-fed IMs.

The following summarizes the advantages and strong points of the proposed methodology.

- The efficiency maps of the IM under test are computed with high accuracy since the no-load and locked-rotor tests allow considering all the machine's nonlinearities like magnetic saturation, skin effect, iron- and mechanical- losses.
- The efficiency maps of the IM under test can be computed under different operating temperatures and considering voltage and current constraints introduced by the machine or the power electronics converter feeding it.
- The different control strategies can be replaced by evaluating the impact on the efficiency values. The proposed mapping algorithm computes efficiency maps *i*) to minimize the overall electrical losses or *ii*) to minimize the stator Joule losses, i.e., considering the machine's



maximum torque per ampere (MTPA) operation for mechanical speeds lower than the base speed or *iii*) to minimize the stator flux.

Therefore, this chapter brings in added value by reporting the step-by-step procedure for performing efficiency mapping of IMs operated in wide torque-speed ranges, including the limitations introduced by the power electronics converter feeding it. However, it is highlighted that the computed efficiency maps are related to the time-fundamental components of supply voltage and currents. In this way, the calculated efficiency maps are strictly independent of the power electronics converter feeding the IM under test, thus ruling out additional- and harmonic- losses introduced by the pulse-width modulation (PWM). Indeed, according to [89], the harmonic content introduced by the PWM modulation depends on the switching frequency, dc-link voltage level, inverter levels, modulation technique, amplitude- and frequency-modulation indexes (i.e., the amplitude and frequency of the fundamental phase voltages, respectively). Therefore, even computing the efficiency maps of the machine considering PWM modulation, this analysis cannot be generalized and must be performed again if the inverter or any of the above variables is changed. In addition, accurate analytic models of both iron and copper losses under PWM modulation are not reported in the literature, thus still representing an open research field. For these reasons, in this dissertation, it has been preferred to focus on an efficiency mapping algorithm for IM that considers only the time-fundamental behavior, regardless of the inverter supplying the machine

The proposed mapping procedure has been validated on a 10 kW, 4 poles, 100 Hz IM. Efficiency maps in motor and generator operations have been evaluated, as well as considering different values of the dc-link voltage of the inverter feeding the IM. The algorithm has been validated by directly comparing the experimental efficiency maps with those computed. Each experimental efficiency map has been evaluated by setting a reasonable resolution in speed and torque, thus leading to a predefined number of test points in the torque-speed range. The torque of the IM under test has been controlled in each test point using a field-oriented control (FOC) scheme [94, 96]. However, to correctly validate the proposed mapping procedure, the reference  $dq$  stator currents for the current vector control (CVC), have

been generated using the results of the mapping algorithm. The map reports the error between the computed efficiency map and the experimental one has been shown for each test condition for highlight better the accuracy of the proposed mapping procedure. It is noted how the error is lower than 2 – 3 % in most of the torque-speed range, regardless of whether motoring or generator conditions are considered. In detail, it is noted how the error becomes more significant for *i)* the test points near the MTPS profile and *ii)* in the generator operation, the test points at very low speed and high braking torque. Regarding the test points near the MTPS profile, they represent the most critical ones for the torque control algorithm. Indeed, in that operating point, the performance of the flux observer in estimating the  $d$ -axis position strictly depends on that in accurately reconstructing the machine's back-emf. Thus, assessing the inverter nonlinearities and the resistive voltage drops with high accuracy. Therefore, it is most likely that in test points near the MTPS profile, the torque control algorithm has not effectively imposed the reference  $dq$  stator currents, justifying the error between computed efficiencies and measured ones. In any case, it is highlighted that the error in the test points near the MTPS profile never overcomes 4 %. Conversely, it is noted that in the generator operation, the test points at very low speed (400 rpm) and high braking torque are characterized by efficiency errors near or even higher than 5 %. This error is justified because, in this operating region, the IM's efficiency is near zero, hindering its accurate evaluation. However, the IM's efficiency assessment is low significant in that region since mechanical and electrical powers are both meager.

In summary, the comparison between computed and experimental efficiency maps confirms the accuracy of the proposed mapping procedure in estimating the IM's efficiency in wide torque-speed ranges and considering very different operating conditions like a significant variation of the dc-link voltage of the inverter feeding the machine.

## Chapter 3

# Three-phase Synchronous Machine Mapping

This chapter presents a possible simplified energetic modeling of the eDrive components suitable for different applications, i.e., EVs and HEVs [15, 99]. Indeed the electrical machine and power converter in energetic evaluation can be modeled using the efficiency/losses maps [100].

In this chapter, a procedure for eDrive mapping of an interior permanent magnet (IPM) synchronous machine [101] supplied by a voltage source inverter (VSI) is considered. The proposed procedure is developed in Matlab environment and linked to the 2D FEA solver FLUX. Since the computation method is based on flux maps, the proposed procedure is valid for all the machines that can be modeled in this way, and so Synchronous Reluctance (SyR), PM-assisted Synchronous Reluctance (PM-SyR) and Surface-mounted PM (SPM) [102, 103] machines.

The primary strength of the proposed approach consists of the time saving than FEA simulations for efficiency/losses maps evaluation [75] and no a dedicated test rig is required [36]. Indeed, the efficiency mapping of IPM machine could be performed with an experimental approach which requires a dedicated test rig with a prime mover or a brake, a dedicated machine control to get the desired working point, and an automatic procedure for saving the results, but above all take a lot of time [104].

For this reason, this work proposes an offline mapping developed in a Matlab environment, based on flux maps evaluated in FEA. Among the features of

the proposed approach, the limited computation time required to obtain the complete set of efficiency maps compared to fully experimental or FEM methods is also worth mentioning. The benchmark is an IPM machine for battery electric vehicle (BEV) e-Motor, provided by an automotive industry thanks to the collaboration between Politecnico di Torino and the automotive industry. The mapping approach developed in Matlab environment has been partially validated by comparing the mapping results to those obtained with FEA simulations just in some working points.

The chapter is organized as follows:

- The IPM and VSI models used in the mapping code are reported. The machine model is analyzed in rotating reference frame. The equivalent iron losses map and the magnetic model are analyzed.
- The eDrive efficiency mapping is presented, analyzing the necessary inputs, and generated outputs. The results of the mapping code on the IPM e-Motor for BEV are shown.
- A multidimensional linear interpolation is presented using the offline maps in a continuous domain. The interpolation output for a random working point is presented, using the offline maps on eDrive (IPM and VSI).

### 3.1 eDrive Modeling

The proposed efficiency mapping procedure uses the electromagnetic model of IPM synchronous machine defined in the rotating  $dq$  frame, i.e., the  $d$ -axis is assumed coincident with the PM flux. Hereafter, the used machine model is presented.

#### 3.1.1 Electromagnetic model of IPM machine

The electrical and magnetic equations regard the stator winding because the winding is not present in the rotor. The stator is composed of three sinusoidal concentrated windings. The six equations (three electrical and three magnetic equations) are obtained with these hypotheses:

- The synchronous anisotropy machine with the permanent magnets on the rotor is assumed.
- One pole pair is assumed to get a simple equation.
- The magnetic induction is assumed sinusoidal: only the first harmonic is considered.
- Magnetic linearity is considered. In the second step, saturation will be considered.
- Iron losses are neglected

In matrix form, the magnetic and electrical equations in the time phase-domain can be written as:

$$\begin{cases} \bar{v}_{123} = R_s \cdot \bar{i}_{123} + \frac{d\bar{\lambda}_{123}}{dt} \\ \bar{\lambda}_{123} = L_{ls} \cdot \bar{i}_{123} + L_{123} \cdot \bar{i}_{123} + \bar{\lambda}_{PM} \end{cases} \quad (3.1)$$

where:

- $\bar{v}_{123}$  stands for the stator voltage vector in the time phase domain;
- $\bar{i}_{123}$  stands for the stator current vector;

- $R_s$  stands for the stator resistance;
- $\bar{\lambda}_{123}$  stand for the magnetic flux vector linkage with the stator windings;
- $L_{ls}$  stand for the leakage stator inductance, equal for each phase;
- $L_{123}$  stands for stator inductance matrix;
- $\bar{\lambda}_{PM}$  stands for the flux produced by the PM.

Using The Clarke matrix  $[C]$  and the rotational matrix  $[R(\theta)]$  reported in Eq. (3.2) where the angle  $\theta$  represents the rotor position, the electromagnetic equations in  $dq$  axes, rotating at synchronous electrical speed  $p\omega_r$ , ( $p$  stands for pole pairs) can be evaluated, considering the PM flux aligned with  $d$ -axis.

$$[C] = \begin{bmatrix} 2/3 & -1/3 & -1/3 \\ 0 & 1/\sqrt{3} & -1/\sqrt{3} \\ 1 & 1 & 1 \end{bmatrix}, \quad [R(\theta)] = \begin{bmatrix} \cos(\theta) & \sin(\theta) \\ -\sin(\theta) & \cos(\theta) \end{bmatrix} \quad (3.2)$$

A new fictitious isotropic mutual inductance factor  $M_I$  and anisotropic mutual inductance factor  $M_A$  are introduced, relating to the synchronous inductance in  $d$ -axis  $L_d$  and  $q$ -axis  $L_q$  as reported in Eq. (3.3).

$$\begin{aligned} L_d &= L_{ls} + \frac{3}{2}(M_I - M_A) \\ L_q &= L_{ls} + \frac{3}{2}(M_I + M_A) \end{aligned} \quad \Rightarrow \quad L_d < L_q \quad (3.3)$$

Applying Eq. (3.2) to Eq. (3.1), the electromagnetic model is expressed as:

$$\begin{cases} \bar{V}_{dq} = R_s \cdot \bar{I}_{dq} + \frac{d\bar{\Lambda}_{dq}}{dt} + p\omega_m \cdot \begin{bmatrix} 0 & -1 \\ 1 & 0 \end{bmatrix} \cdot \bar{\Lambda}_{dq} \\ \bar{\Lambda}_{dq} = L_{ls} \cdot \bar{I}_{dq} + \frac{3}{2} \cdot M_I \bar{I}_{dq} - \frac{3}{2} \cdot \begin{bmatrix} 1 & 0 \\ 0 & -1 \end{bmatrix} \cdot M_A \bar{I}_{dq} + \begin{bmatrix} \Lambda_{PM} \\ 0 \end{bmatrix} \end{cases} \quad (3.4)$$

Performing some mathematical manipulation, the components of the electromagnetic model can be written as reported in 3.5.

$$\begin{cases} v_d = R_s \cdot i_d + L_d \cdot \frac{di_d}{dt} - p \cdot \omega_m \cdot \lambda_q \\ v_q = R_s \cdot i_q + L_q \cdot \frac{di_q}{dt} + p \cdot \omega_m \cdot \lambda_d \\ \lambda_d = L_d \cdot i_d + \Lambda_{PM} \\ \lambda_q = L_q \cdot i_q \end{cases} \quad (3.5)$$

For efficiency mapping code, the steady-state conditions are considered, overwriting Eq. (3.5) as reported in Eq. (3.6).

$$\begin{cases} V_d = R_s \cdot I_d - p \cdot \omega_m \cdot \Lambda_q \\ V_q = R_s \cdot I_q + p \cdot \omega_m \cdot \Lambda_d \\ \Lambda_d = L_d \cdot I_d + \Lambda_{PM} \\ \Lambda_q = L_q \cdot I_q \end{cases} \quad (3.6)$$

The equivalent circuit of Eq. (3.6) is shown in Fig. 3.1. However, for an accurate mapping, the iron losses and the cross saturation are considered. For this reason, an equivalent iron resistance to model the losses is introduced. A Thevenin equivalent manipulation is performed downstream of stator and equivalent iron resistances (dashed line at the top of Fig. 3.2). The equivalent circuit is shown at the bottom of Fig. 3.2, where an equivalent Thevenin simplification is performed. Thevenin simplification is helpful because the magnetic maps take into account the equivalent currents. The equivalent

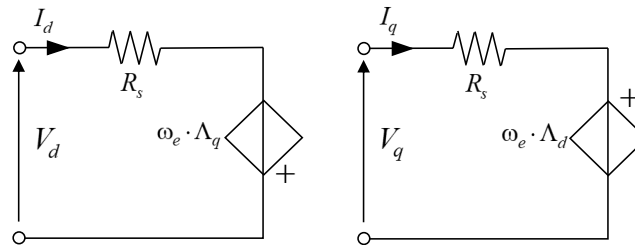


Figure 3.1 Equivalent circuit of IPM machine in rotating reference frame without iron losses.

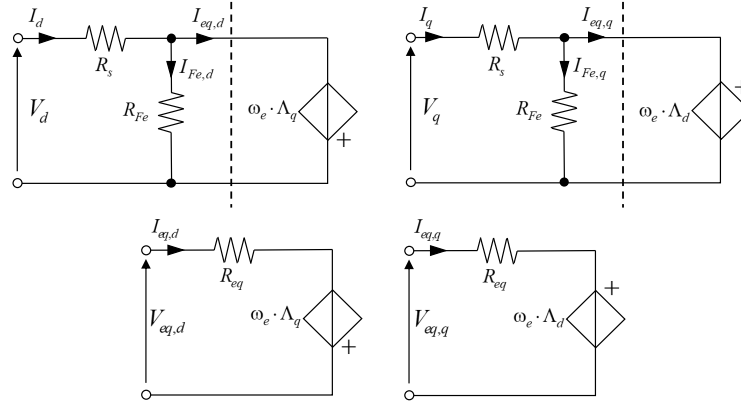


Figure 3.2 IPM equivalent circuit with iron losses (top) and equivalent Thevenin simplification (bottom).

variables and equivalent parameters are computed as:

$$R_{eq} = \frac{R_s \cdot R_{Fe}}{R_s + R_{Fe}}; \quad \bar{V}_{eq} = \bar{V}_s \cdot \frac{R_{Fe}}{R_s + R_{Fe}}; \quad \bar{I}_{eq} = \bar{I}_s - \bar{I}_{Fe} \quad (3.7)$$

Finally, the iron losses equivalent current is computed using the superposition principle as:

$$\bar{I}_{Fe} = -\bar{I}_{eq} \cdot \frac{R_s}{R_s + R_{Fe}} + \bar{V}_s \cdot \frac{1}{R_s + R_{Fe}} \quad (3.8)$$

Eq. (3.9) is overwritten following the equivalent circuit of Fig. 3.2 as:

$$\begin{cases} V_{eq,d} = R_s \cdot I_{eq,d} - p \cdot \omega_m \cdot \Lambda_q \\ V_{eq,q} = R_s \cdot I_{eq,q} + p \cdot \omega_m \cdot \Lambda_d \\ \Lambda_d = L_d \cdot I_{eq,d} + \Lambda_{PM} \\ \Lambda_q = L_q \cdot I_{eq,q} \end{cases} \quad (3.9)$$

The electromagnetic torque  $T_{em}$  is computed as in Eq. (4.23) with the  $dq$  rotor frame components, based on the  $(I_{eq,d}, I_{eq,q})$ , including the iron losses.

$$T_{em} = \frac{3}{2} \cdot p \cdot (\Lambda_d \cdot I_{eq,q} - \Lambda_q \cdot I_{eq,d}) \quad (3.10)$$

The useful torque at the machine shaft is computed based on the electromagnetic torque and mechanical losses. Mechanical power losses  $P_{fv}$  are not easy to estimate beforehand and usually are expressed as a polynomial



function of the rotor speed. The literature usually divides mechanical loss into bearing loss, proportional to the rotor speed  $\omega_r$ , and windage loss, proportional to the cubic power of the speed. In the following, mechanical loss are modeled with Eq. (3.11), where the factors  $a$  ( $nW/rpm^3$ ) is related to the bearing friction loss factor, and  $b$  ( $mW/rpm$ ) to the ventilation loss factor. The coefficient can be estimated by no load test or bearing and windage data.

$$P_{fv} = a \cdot \omega_r^3 + b \cdot n \quad (3.11)$$

After the determination of the  $P_{fv}$ , respective torque  $T_{fv}$  can be computed to evaluate the useful torque at the machine shaft as in Eq. (3.12).

$$T_m = T_{em} \mp T_{fv} \quad (3.12)$$

If the machine works in motoring mode, the friction and ventilation torques are subtracted to that electromagnetic, vice versa in generation mode. However, the mechanical losses can be evaluated with the standard tests when the prototype is available.

In the following, the procedure used in this dissertation for obtaining the iron losses map and the magnetic model based on flux maps of the IPM machine is reported. The approach presented in the following is one of the possible, based on limited data provided by the manufacturer and the impossibility of performing experimental tests.

### 3.1.2 Inverter model

For efficiency mapping of the eDrive system, the modeling of VSI is necessary. The inverter modeling used in this dissertation is based on the component's datasheet parameters. Since the primary goal for this activity is related to the energetic aspects, an ideal steady-state model is considered for the power converter. The efficiency is evaluated considering conduction and switching losses using analytical formulations for VSI [105].

In this perspective, a VSI can be considered as an ideal voltage gain in which the maximum output voltage depends on the available dc-link voltage and the modulation technique. In particular, for a defined dc-link voltage level,

the power converter can apply at the IPM terminals a maximum voltage that depends on the modulation technique used to control the inverter power switches. For instance, a linear sinusoidal modulation technique for a Pulse Width Modulation (PWM) inverter allows applying a fundamental peak phase voltage at the machine terminals approximately equal to  $V_{dc-link}/2$ . Advanced space vector modulation strategies allow increasing the maximum output voltage for a defined dc-link level. For example, the PWM balanced envelop modulation (BEM) technique (referred as *MinMax* in this dissertation) allows obtaining a fundamental peak phase output voltage up to approximately  $v_{dc}/\sqrt{3}$ . Since the inverter modulation technique markedly impacts the maximum output voltage applied to the machine terminals, the developed efficiency mapping algorithm has been conceived to consider for a PWM inverter both the linear sinusoidal and the space vector *MinMax* modulation techniques.

The power loss for a VSI are related to the conduction and switching phenomena. Fig. 3.3 shows the considered two-levels three-phase inverter, consisting of six power switches (IGBTs) and six power diodes. In the following, the losses analysis implemented in the mapping algorithm is reported.

### Conduction power loss

Due to the inverter's symmetrical structure, the power devices' current and voltage characteristics can be considered identical yet time-shifted. Hence, it is possible to compute the power loss related to one IGBT and one diode and determine the total inverter losses by multiplying for the components

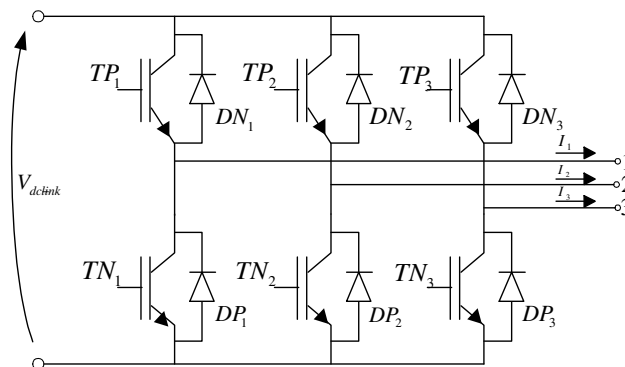


Figure 3.3 Three-phase voltage source inverter.

number. Considering the sinusoidal variation of duty cycles versus the time, the conduction power losses for an IGBT and a diode can be computed by Eq. (3.13) and Eq. (3.14), respectively. Moreover, these formulations are valid under the assumptions of a temporally constant junction temperature, linear modulation technique, and a negligible switching frequency ripple of the ac current.

$$P_{cond-1IGBT} \cong \left( \frac{1}{2\pi} + \frac{m \cdot \cos(\varphi)}{8} \right) \cdot V_{ce0} \cdot \hat{I}_s + \left( \frac{1}{8} + \frac{m \cdot \cos(\varphi)}{3\pi} \right) \cdot r_{ce0} \cdot \hat{I}_s^2 \quad (3.13)$$

$$P_{cond-1D} \cong \left( \frac{1}{2\pi} - \frac{m \cdot \cos(\varphi)}{8} \right) \cdot V_f \cdot \hat{I}_s + \left( \frac{1}{8} - \frac{m \cdot \cos(\varphi)}{3\pi} \right) \cdot r_f \cdot \hat{I}_s^2 \quad (3.14)$$

where:

- $V_{ce0}$  and  $V_f$  are the collector-emitter voltage of IGBT and the on-state forward voltage of the diode, provided by VSI datasheet;
- $r_{ce0}$  and  $r_f$  are the IGBT and diode on-state resistances, provided by VSI datasheet;
- $m$  and  $\cos(\varphi)$  are the modulation index and the power factor, respectively, computed as reported in Eq. (3.16).

$$m = \frac{V_s}{\frac{v_{dc}}{2}} \quad (3.15)$$

$$\cos(\varphi) = \cos \left( \text{tg}^{-1} \left( \frac{V_{s,q}}{V_{s,d}} \right) - \text{tg}^{-1} \left( \frac{I_{s,q}}{I_{s,d}} \right) \right) \quad (3.16)$$

### Switching power loss

The switching power losses of one IGBT and one diode for energy assessment as reported in Eq. (3.17) and Eq. (3.18), where the stator current  $I_s$  stands for the RMS value.

$$P_{sw-1D} \simeq f_{sw} \cdot E_{rr} \cdot \left( \frac{\sqrt{2}}{\pi} \cdot \frac{I_s}{I_{ref}} \right)^{0.9} \quad (3.17)$$

$$P_{sw-1IGBT} \simeq f_{sw} \cdot E_{on+off} \cdot \frac{\sqrt{2}}{\pi} \cdot \frac{I_s}{I_{ref}} \quad (3.18)$$

where  $E_{rr}$  stands for the dissipate energy during the turn off of the diode, called reverse recovery, and  $E_{on+off}$  stands for the dissipate energy of the

IGBT during the on-off of the component. The current  $I_{ref}$  is a current reference provided by the datasheet.

Merging Eq. (3.13) - (3.18) the total loss of VSI can be computed as:

$$P_{l-VSI} = 6 \cdot (P_{cond-1IGBT} + P_{cond-1D} + P_{sw-1IGBT} + P_{sw-1D}) \quad (3.19)$$

The loss matrix of inverter has been calculated with the help of MATLAB code using loss formulae discussed in this section.

### 3.1.3 FEA flux maps

Since the proposed IPM efficiency mapping is based on flux maps, the FEA flux maps computation and organization are presented in this section. Flux maps are a very general way to represent the magnetic model of a synchronous motor. The flux maps represent the fundamental  $dq$  flux linkages as a function of the  $dq$  currents of the motor: the stator flux along  $d$ - and  $q$ -axis depends on both current components due to the cross saturation. Considering the iron losses for an accurate machine model, the flux linkages must be expressed as a function of the  $dq$  flux-torque producing current ( $I_{eq,d}$ ,  $I_{eq,q}$ ), called *equivalent* currents in this dissertation (see Section 3.1.1). The average electromagnetic torque can be retrieved by cross-product of the flux linkage and current components, or by a dedicated map, function of the same current coordinates.

The flux maps can be computed through FEA simulations [106, 107] or measured with dedicated experimental procedures. The experimental approach is possible if the test bench is available and control of the machine for automating the procedure is required [108]. The experimental solution for flux linkage maps identification is performed with an inverter pulse width modulation (PWM) supply. The estimation of the flux linkage can be based on the back-emf voltages that are calculated using the measured voltages and currents [104]. Other solutions are proposed in [109–111] for flux linkage maps identification of synchronous machines.

The flux linkage maps, obtained through intensive FEA simulations, replace the experimental procedure. However, this solution can be adopted if all details related to the motor design, such as lamination, winding configu-

rations, and materials, are known. However, in many cases, these details are not available. This solution is widespread in the industry, where the drive manufacturers do not have full access to the design information for the motors their suppliers provide. This approach is used in this dissertation for the prototype lack.

The following guidelines for fast FEA computation of flux maps will be reviewed, looking at the tradeoff between accuracy and computational time. Then, the fundamental  $dq$  flux maps of the IPM machine will be presented as an example. Some tricks for fast FEA computation can be adopted for time-saving while preserving accuracy. The selection of the FEA simulated points is essential for time-saving goals and represents a tradeoff between accuracy and computational speed. To further speed up the flux maps evaluation, other techniques can be adopted as:

- 2D FEA models instead of 3D FEA. The 3D effects can be added later as end-turns inductance and resistance.
- Static models instead of transient models. This simplification stands only for the current-supplied model in steady state conditions, which are the conditions of the flux maps computation. The rotor movement is emulated by running several static simulations at different rotor positions, representing different time frames.
- Geometric symmetry: instead of simulating the entire motor, just one or two poles can be simulated, exploiting the motor's periodic or anti-periodic symmetry and reducing the problem's size.
- Electric symmetry: simulation of a fraction of the electrical period rotation of the rotor, reducing the total number of simulations [112].

IPM machine for BEV application is used as example. The cross-section of the considered machine is not reported for company privacy, while the motor ratings are reported in Table 3.1. In this work, reference is made to the 2D magnetostatic FEA simulations of the radial-flux IPM machine. Geometric and electric symmetries are utilized for fast simulation. Referring to the IPM taken as an example, the anti-periodic symmetry applies, allowing the simulation of one pole, which is  $1/8$  of the complete machine, and a rotation

Table 3.1 IPM machine data

IPM ratings	
Nominal current	450 $A_{pk}$
Max current	650 $A_{pk}$
Nominal torque	144 Nm
Max torque	350 Nm
Dc-link voltage	400 V
Nominal speed	6 krpm
Max speed	14 krpm
Nominal power	90.5 kW
Max power	220 kW
Pole pairs number	4

of 45 electrical degrees, which is again 1/8 of the electrical period. Under these assumptions, the simulation of one  $I_{eq,d}$ ,  $I_{eq,q}$  operating point with a mesh of several elements, using 90 positions over 45 electrical degrees of rotation is set, at PM temperatures of 20°C and 150°C. Different PM temperatures are considered for analyzing impacts on residual magnetic induction on the magnetic fluxes, which influence the flux weakening region. Indeed when the PM temperature is higher, the PM flux is weaker, and the flux-weakening area is reduced. This means that the base speed is higher than a base speed of a colder PM, considering the same dc-link voltage value.

Fig. 3.4 - Fig. 3.6 show a flux linkage and torque waveforms computed with  $i_{eq,d} = 195$  A and  $i_{eq,q} = 390$  A of the benchmark machine, setting two different PM temperatures: 20°C (left, blue - cold) and 150°C (right, red - hot). The dots (blue for cold and red for the hot machine) denotes the FEA simulations (90 simulations over 45 electrical degrees, in this case), while the continuous lines represent the complete waveforms over one electrical period obtained by symmetry. From FEA simulations, further manipulation gives representative values that can be saved in the flux maps, such as the average value, peak-to-peak ripple, harmonic components, and so on. As shown in Fig. 3.6, the torque value depends on the PM temperature, which will be considered in the mapping code.

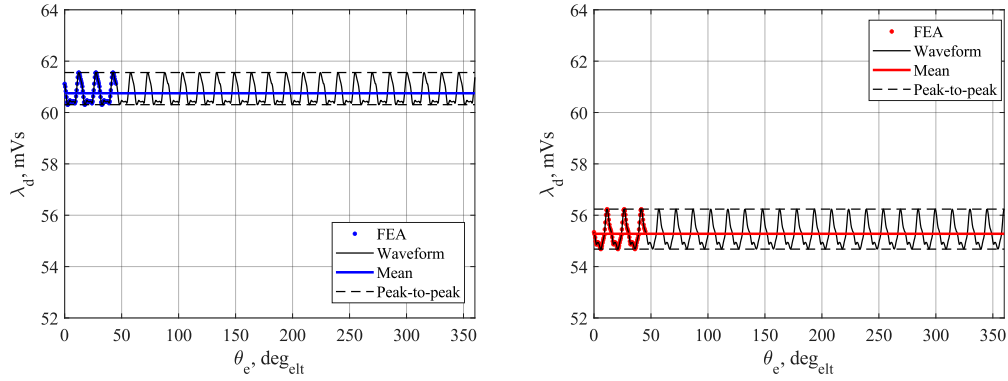


Figure 3.4  $d$ -axis flux linkages at  $\vartheta_{PM} = 20^\circ\text{C}$  (left, blue) and  $\vartheta_{PM} = 150^\circ\text{C}$  (right, red).

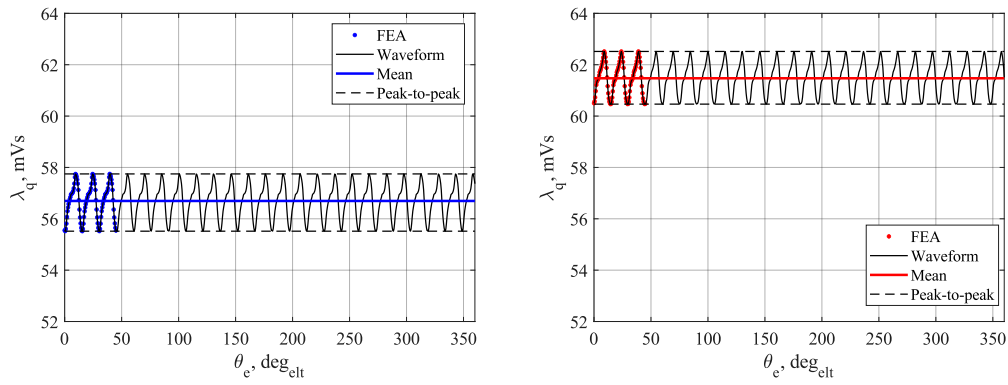


Figure 3.5  $q$ -axis flux linkages at  $\vartheta_{PM} = 20^\circ\text{C}$  (left, blue) and  $\vartheta_{PM} = 150^\circ\text{C}$  (right, red).

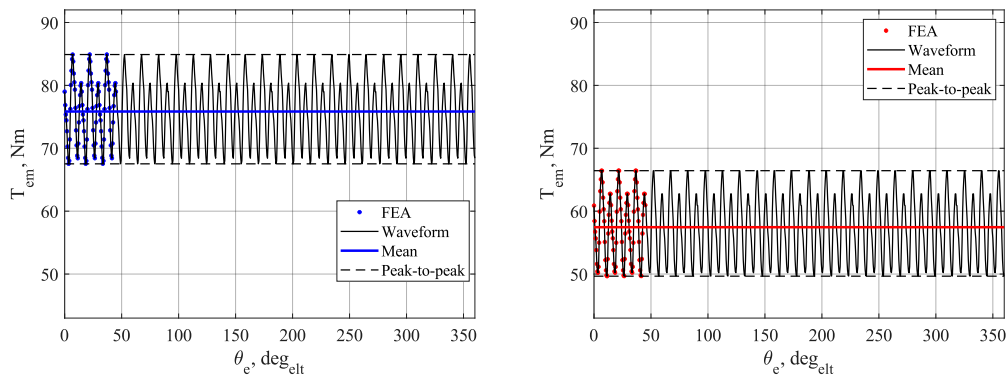


Figure 3.6 Electromagnetic torque at  $\vartheta_{PM} = 20^\circ\text{C}$  (left, blue) and  $\vartheta_{PM} = 150^\circ\text{C}$  (right, red).

### Flux maps saving

The fundamental flux maps are computed by repeating the 45-degrees simulation on a regular grid of the equivalent (stator and iron) currents  $i_{eq,d}$ ,  $i_{eq,q}$  in FLUX environment, saving the rotor position, flux and current values in time phase domain. The current combinations are organized in lookup tables after the post-process in Matlab environment, as reported in Eq. (3.20). The regular grid is composed by  $n_d$  and  $n_q$  current points, evaluated by applying the Clarke and rotational transformations to the ones in time the domain.

$$i_{eq,d}^{map} = \begin{bmatrix} i_{eq,d,1} & \dots & i_{eq,d,n_d} \\ \dots & \dots & \dots \\ i_{eq,d,1} & \dots & i_{eq,d,n_d} \end{bmatrix}, \quad i_{eq,q}^{map} = \begin{bmatrix} i_{eq,q,1} & \dots & i_{eq,q,1} \\ \dots & \dots & \dots \\ i_{eq,q,n_q} & \dots & i_{eq,q,n_q} \end{bmatrix} \quad (3.20)$$

For each FEA simulation over 45 electrical degree, injecting one of possible values of  $n_d$  and  $n_q$  combinations, the average values of torque  $T_{em}$  and flux linkages  $\lambda_d$  and  $\lambda_q$  are saved in the corresponding lookup tables, called  $T_{em}^{map}$  and  $\lambda_d^{map}$  and  $\lambda_q^{map}$ , respectively, defined as in Eq. (3.21), in function of  $i_{eq,d}$ ,  $i_{eq,q}$ .

$$\lambda_d^{map} = \begin{bmatrix} \lambda_d(i_{eq,d,1}, i_{eq,q,1}) & \dots & \lambda_d(i_{eq,d,n_d}, i_{eq,q,1}) \\ \dots & \dots & \dots \\ \lambda_d(i_{eq,d,1}, i_{eq,q,n_q}) & \dots & \lambda_d(i_{eq,d,n_d}, i_{eq,q,n_q}) \end{bmatrix} \quad (3.21)$$

$$\lambda_q^{map} = \begin{bmatrix} \lambda_q(i_{eq,d,1}, i_{eq,q,1}) & \dots & \lambda_q(i_{eq,d,n_d}, i_{eq,q,1}) \\ \dots & \dots & \dots \\ \lambda_q(i_{eq,d,1}, i_{eq,q,n_q}) & \dots & \lambda_q(i_{eq,d,n_d}, i_{eq,q,n_q}) \end{bmatrix}$$

In this work the current grid used for the FEA simulations is organised with steps 65 A between -650 A to 650 A, obtaining  $n_c = n_d = 21$  and the total currents combination, with a total number combination of  $n_c \cdot n_d = 441$  combinations. The positive  $d$ -axis current can be used for sensorless control, but this topic is outside this project's scope. The positive values of  $q$ -current are used for a motoring mode of IPM machine, while the negative values for generating mode. The currents, fluxes and electromagnetic torque maps represented by the matrices are composed by 441x441 elements considering 21 current combinations along  $d$ - and  $q$ -axis. For each current combination, 91



rotor position has been evaluated, i.e., simulated rotor position highlighted by blue/red points in Fig. 3.4 - Fig. 3.6 ( $i_{eq,d} = 195$  A and  $i_{eq,q} = 390$  A). The intermediate current/flux/torque values in the maps 441x441 are evaluated by interpolation of the presented lookup tables.

Fig. 3.7 and Fig. 3.9 report an example of the flux maps in 3D dimension and 2D dimensions with a PM temperature of 20 °C, obtained as post process of FEA simulations presented before. In Fig. 3.9 the  $d$ - and  $q$ -flux linkage are reported, injecting 21 different current values, in the left and right, respectively. The cross-saturation of IPM machine is more significant along  $q$ -axis, as shown in Fig. 3.9 because the iron path along the  $q$ -axis is higher than the path along  $d$ -axis, where are located the PM. Thus, the PM presents magnetic permeability similar to air one.

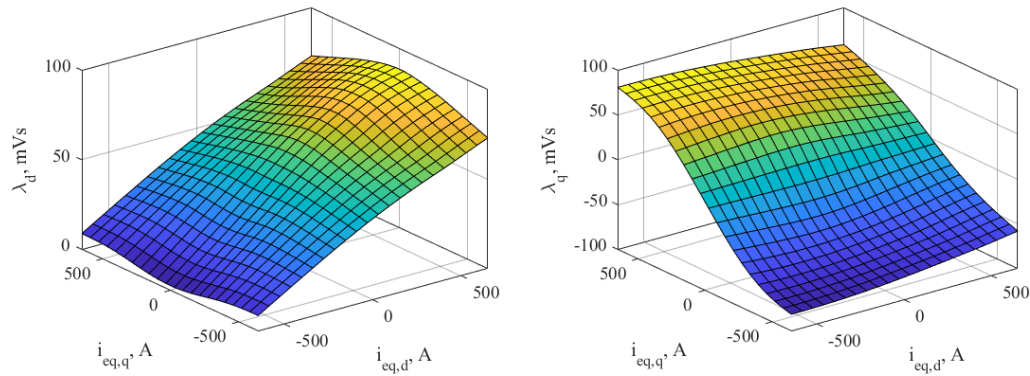


Figure 3.7 Flux maps:  $d$ -axis flux linkage (left) and  $q$ -axis flux linkage (right) at  $\vartheta_{PM} = 20^\circ\text{C}$ .

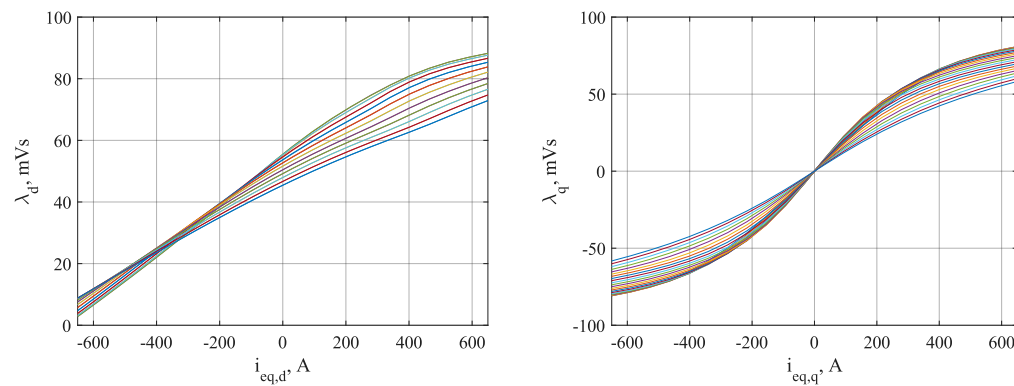


Figure 3.8 2D flux linkage at PM temperature of 20°C.

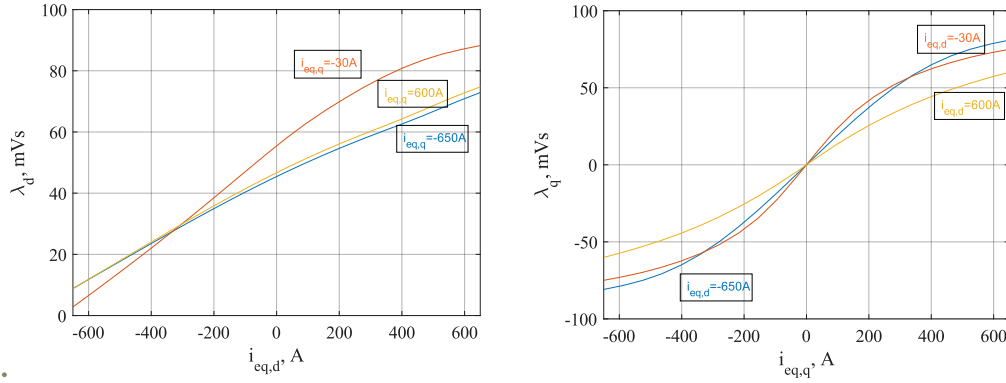


Figure 3.9 Details of 2D flux linkage at PM temperature of 20°C for 3 different currents.

To evaluate the impact of the PM temperature on flux maps, the FEA simulations are also evaluated also in hot condition at PM temperature of 150 °C. Fig. 3.10 and Fig. 3.11 show the flux maps in hotter condition obtained by FEA simulations. However, the differences are not tangible comparing Fig. 3.10 with Fig. 3.7, but is highlighted in Fig. 3.12. In this figure, the PM flux, aligned with  $d$ -axis flux, can be evaluated, setting  $I_{eq,q} = 0$  A at  $I_{eq,d} = 0$  A: for higher PM temperatures, the PM flux is lower. Indeed, at 20°C the PM flux is 56 mVs, while at 150°C decreases to 48 mVs.

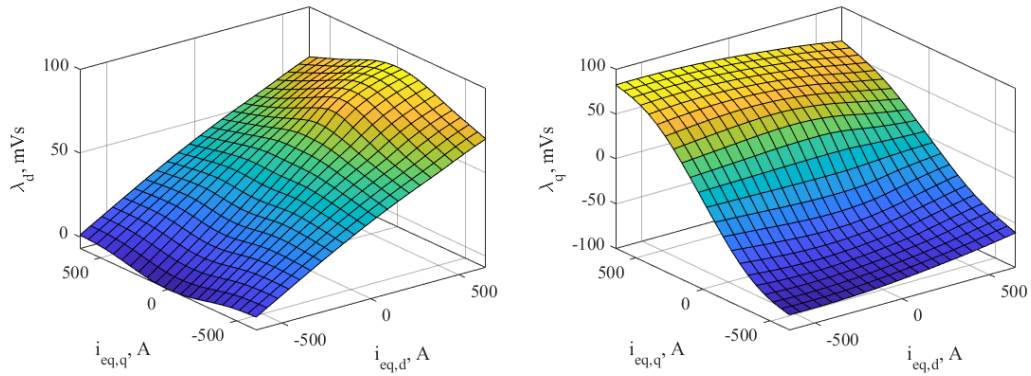


Figure 3.10 Flux maps:  $d$ -axis flux linkage (left) and  $q$ -axis flux linkage (right) at  $\vartheta_{PM} = 150^\circ\text{C}$ .

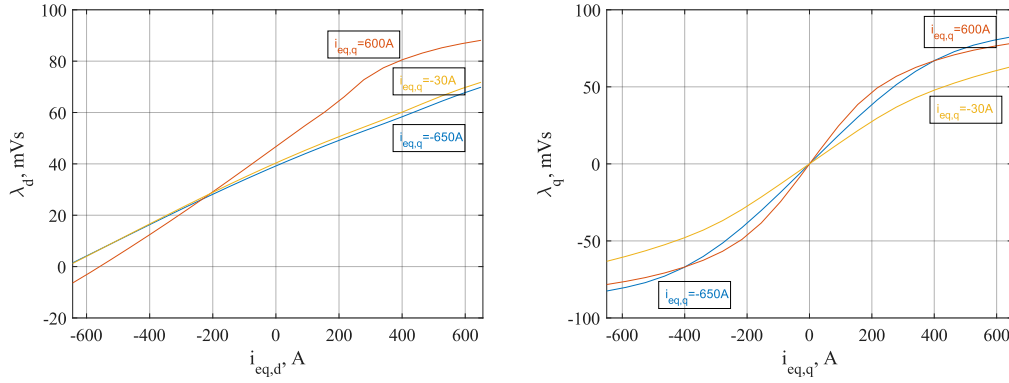


Figure 3.11 Details of 2D flux linkage at PM temperature of 150°C for 3 different currents.

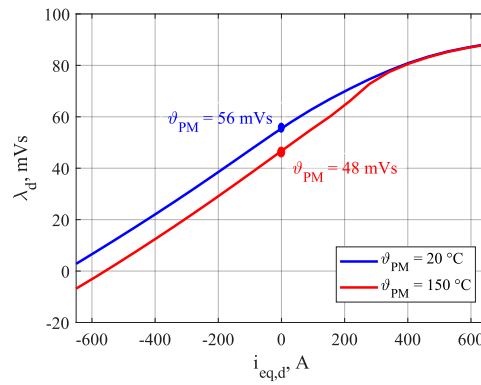


Figure 3.12 PM flux at different PM temperatures.

The torque maps of the machine under test are reported in Fig. 3.13 at different PM temperatures. On the left, the maximum value torque is higher (about 350 Nm) than one (325 Nm) that can be obtained with a higher PM temperature (left).

The intermediate values of the magnetic variables are obtained by bi-linear interpolation of the presented lookup table or by reasonable extrapolation for currents higher or lower than the regular grid evaluated with the FEA simulations.

### Flux maps manipulation

The magnetic model using the flux linkage maps (current-to-flux relationship) that are usually defined in the rotor flux frame, represent an important tool to evaluate the machine performance in terms of the torque production, MTPA (Maximum Torque per Ampere), MTPV (Maximum Torque per Voltage) operations, taking into account the cross-saturation effects [104, 109, 110]. Based on the voltage and current limits imposed by the electrical machine and/or power converter, the MTPS (Maximum Torque per Speed) profile can be defined, ruling out the working points not feasible.

An example of MTPS profiles of benchmark IPM machine is reported in Fig. 3.14 and Fig. 3.15. The profiles are evaluated at stator temperature of 100 °C, including the iron losses (see Section 3.1.4), limiting the equivalent current at 650 A for different dc-link voltages. Also, different PM temperature are considered: 20 °C (cold condition, left) and 150 °C (hot condition, right), based on the flux maps reported in Fig. 3.7 and Fig. 3.10. However, the dc-link voltage impacts base speed: a higher dc-link voltage means a base region with a constant torque larger. While the PM temperature impacts on the maximum available torque, as highlighted in Fig. 3.14 evaluated at dc-link voltage of 400 V.

The MTPA and MTPV profiles take primary importance in control trajectory identification, i.e., in the simulation system of an electrified process. The MTPA and the MTPV laws are the most considered trajectories. This is

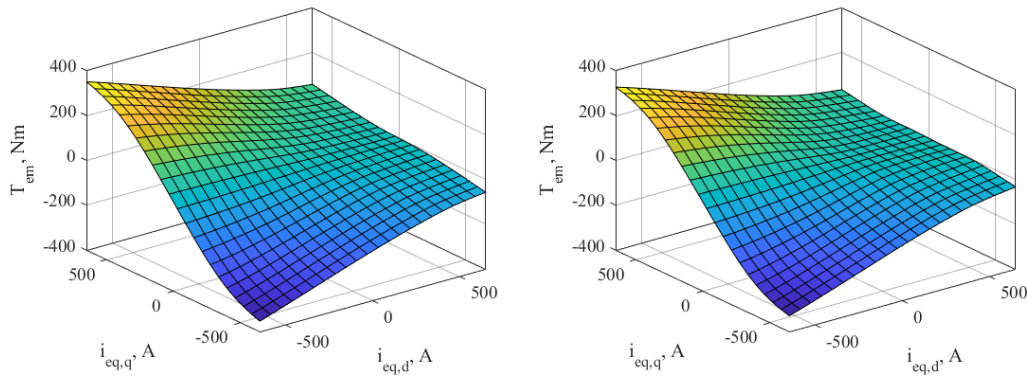


Figure 3.13 Torque maps at different PM temperatures:  $\vartheta_{PM}=20^{\circ}\text{C}$  (left) and  $\vartheta_{PM}=150^{\circ}\text{C}$  (right).

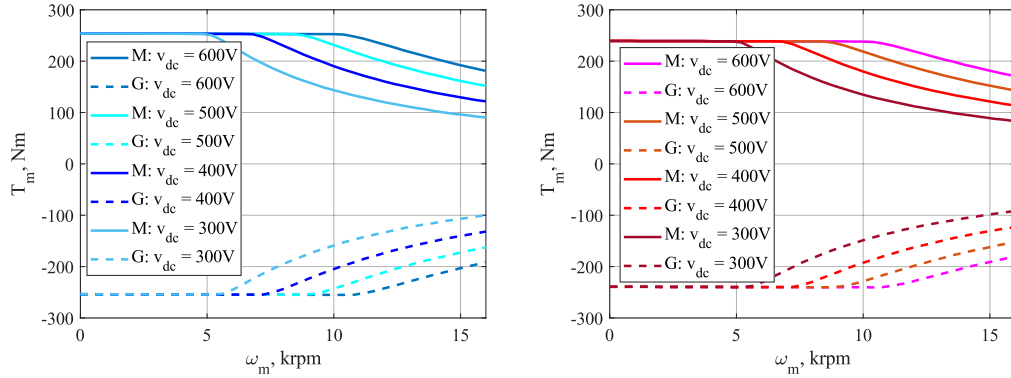


Figure 3.14 MTPS profile in motoring and generating modes for different dc-link voltages:  $\vartheta_{PM} = 20^\circ\text{C}$  (left) and  $\vartheta_{PM} = 150^\circ\text{C}$  (right).

done using the  $dq$  flux maps, referring to average values typical for control. The MTPA consists of the maximization of the average torque for a given current amplitude. In contrast, the MTPV is computed by looking at the maximization of the average torque but moving on constant flux linkage curves instead of the current ones.

The MTPA and MTPV trajectories of the IPM machine are reported in Fig. 3.16 and Fig. 3.17 in current (left) and flux (right) planes. In PM cold conditions (Fig. 3.16 - blue lines) the MTPV profile is missing due to the high value of the characteristic current over the current limit of the considered machine. The characteristic current, called short-circuit current ( $I_{sc} = \lambda_{PM}/L_d$ ), is proportionally related to the PM flux, which is higher than the one in hot

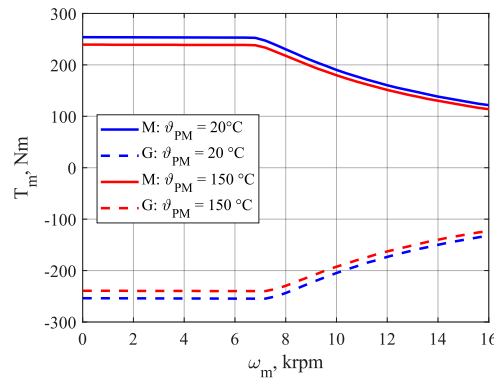


Figure 3.15 MTPS profile in motoring and generating modes for different PM temperatures at  $v_{dc} = 400\text{ V}$ .

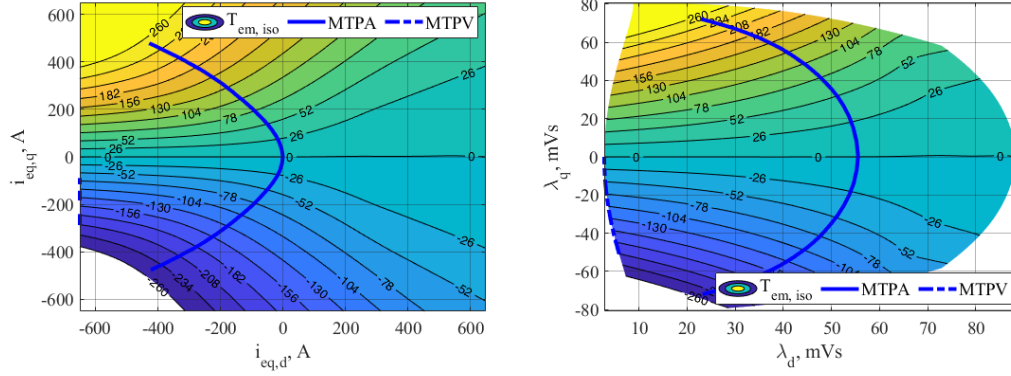


Figure 3.16 MTPA and MTPV locus in current and flux planes at  $\vartheta_{PM} = 20^\circ\text{C}$ .

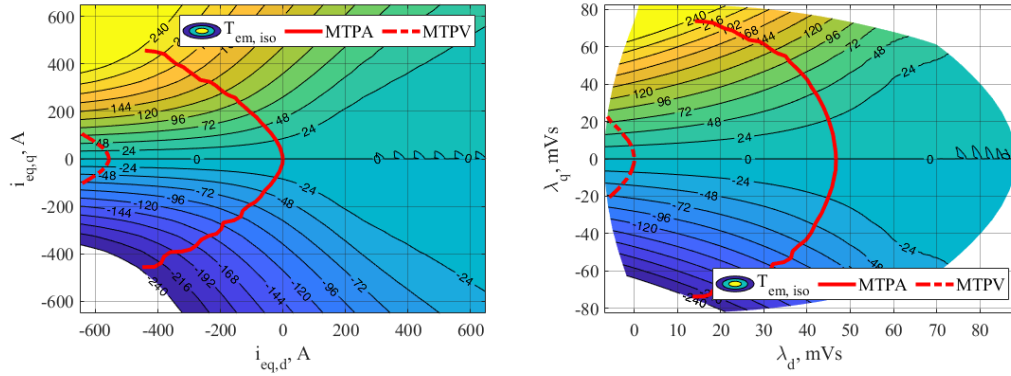


Figure 3.17 MTPA and MTPV locus in current and flux planes at  $\vartheta_{PM} = 150^\circ\text{C}$ .

condition (Fig. 3.12). Indeed, the first MTPV point match with short-circuit current, and, for this reason, the MTPV profile is not reached considering  $\vartheta_{PM} = 20^\circ\text{C}$  for the considered machine. Instead, in hot conditions, as for  $\vartheta_{PM} = 150^\circ\text{C}$ , the short-current is lower (PM flux is lower), so this value belongs to the considered current grid.

### 3.1.4 Iron loss map

In the efficiency mapping eDrive algorithm the iron losses are evaluated using a lookup table in function of the torque and rotor speed. The iron losses map represents an input of the efficiency mapping code.

There are several ways to model iron loss. In the following, the modified Steinmetz equation Eq. (3.22) is adopted [112]. In Eq. (3.22) the iron losses

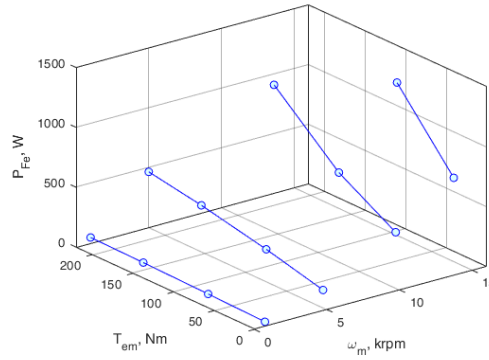


Figure 3.18 Iron losses for different working points evaluated with FEA simulations.

are evaluate at a specific frequency  $f$ : the first contribution is related to the hysteresis  $P_h$ , while the second one is related to eddy-current  $P_{ec}$  loss.

$$P_{Fe} = k_h \cdot f^\alpha \cdot B^\beta + k_e \cdot f^2 \cdot B^2 \quad (3.22)$$

In Eq. 3.22  $B$  stands for flux density in the iron section; the coefficients  $k_h$ ,  $\alpha$ ,  $\beta$ ,  $k_e$  evaluated by fitting the loss data from the manufacturer steel data. Setting opportunely the Steinmetz coefficient in the FEA simulation, the iron losses for a specific torque and rotor speed (frequency) can be evaluated.

For industrial privacy, the coefficients in Eq. (3.22) are not reported for the machine used as example. Different working points in FEA simulations are simulated to analyze the iron losses of benchmark IPM machine, saving several variables (i.e., electromagnetic torque, power, voltage, current, rotor position, etc.). In Fig. 3.18 the iron losses of benchmark machine are reported for different working conditions evaluated with FEA simulations. The iron losses are proportionally to the rotor speed (frequency) and torque. Some working point, as 220 Nm, 14 krpm, are not reported in Fig. 3.18 because are ruled out by the working area delimited by the MTPS profiles (see Fig. 3.14). Some mathematical manipulations are performed to compute the equivalent iron resistance  $R_{Fe}$  in rotating  $dq$  reference frame, based on the losses and stator voltage evaluated by FEA simulations. It is more convenient to perform these evaluations in rotating  $dq$  reference frame, and so the variables, i.e., stator voltages, are transformed. As example, in Fig. 3.19 and Fig. 3.20 the stator voltages in different reference frames are reported, starting from the

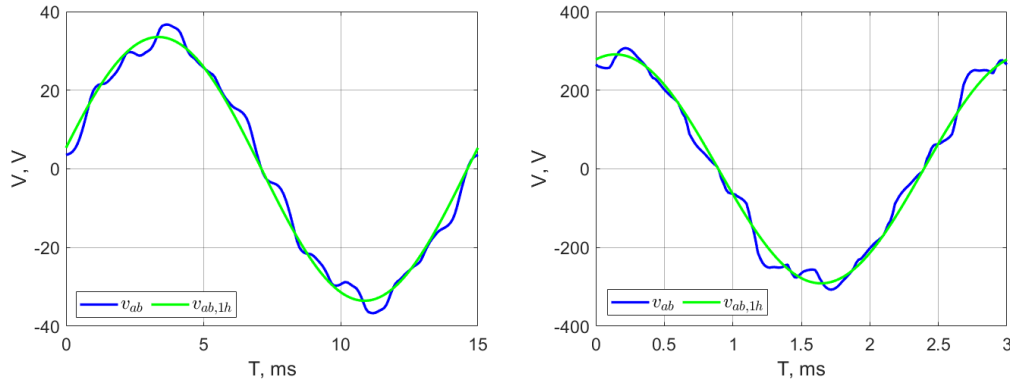


Figure 3.19 Stator voltage in time domain evaluated with FEA simulation: 5 Nm, 1 krpm (left) and 220 Nm, 5 krpm (right).

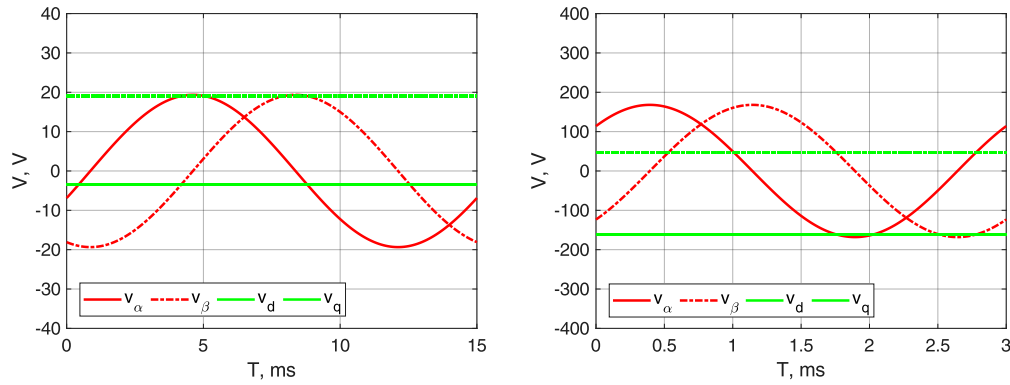


Figure 3.20 Stator voltage in  $\alpha\beta$  and  $dq$  reference frame: 5 Nm, 1 krpm (left) and 220 Nm, 5 krpm (right).

measured ones in FEA simulations in time domain (Fig. 3.19), considering 5 Nm, 1 krpm and 220 Nm, 5 krpm. The stator voltage profiles in the time domain (see Fig. 3.19) are not sinusoidal, and a fast Fourier transformer (FFT) is necessary for the evaluation of electromagnetic variables fundamental. In green, the fundamental of stator voltages is reported. Then, in the post-process, the electromagnetic variables provided in the phase time domain are computed in stationary and rotating reference frames. The stator voltages in  $\alpha\beta$  and  $dq$  reference frames are reported in Fig. 3.20 for the working points taken as example.

The equivalent iron resistance map is reported in Fig. 3.21, starting from the FEA simulations. For higher/lower torque and speed than tested points, the saturation of the parameters was taken. For example, for speeds lower



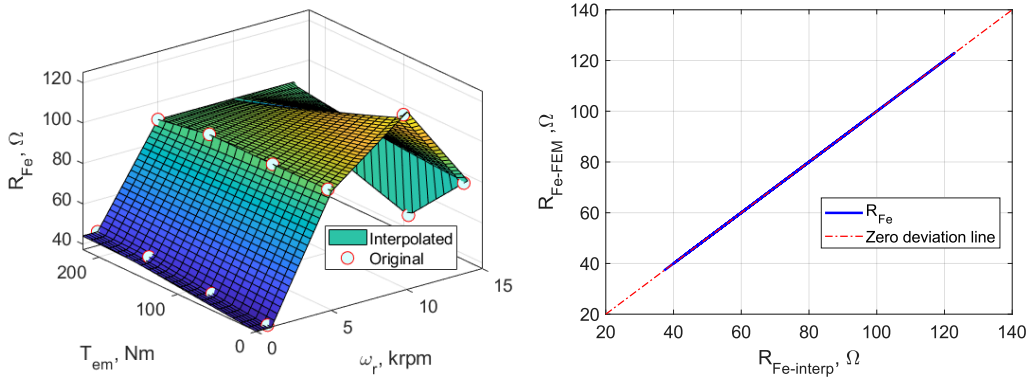


Figure 3.21 Iron losses map ( $@\vartheta_{PM} = 150^\circ\text{C}$ ) and deviation line.

than 1000 rpm, the equivalent iron resistance was taken equal to the values at 1000 rpm fixing torque value, as seen in Fig. 3.21, left. Finally, in the right, the deviation line between the computed values of equivalent iron resistance and the resistance reconstructed with the interpolation is shown: the values are perfectly in agreement. In the following, the lookup table of the equivalent iron losses will be denoted with  $\omega_{m,Fe}$ ,  $T_{em,Fe}$ ,  $R_{Fe}$  and the superscript *map* is introduced to highlighted the matrix than a vector or a constant value.

Finally, the stator resistance map provided by the manufacturer is reported in Fig. 3.22. The manufacturer also equipped the stator resistance for different stator temperatures and rotor speeds. The stator resistance variation is related to the temperature and skin effect [79, 80]. In the following, the lookup table of the stator resistance will be denoted with  $\omega_{m,R_s}$ ,  $\vartheta_{R_s}$ ,  $R_s$  and the superscript *map* is introduced to highlighted the matrix than a vector or a constant value.

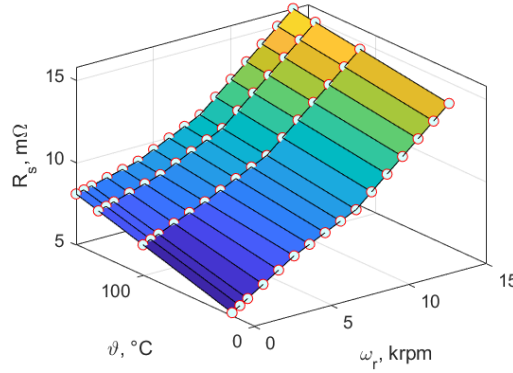


Figure 3.22 Stator resistance map provided by the manufacturer in function of stator temperature and rotor speed.

### 3.1.5 Permanent magnets loss map

Permanent magnet loss are caused by the eddy-current circulation in the PM blocks, which is minor compared to the other losses and in addition PMs are usually axially-segmented for manufacturing reason, further reducing the eddy-currents and so the PM loss. This allows to consider a simplified model of the PM loss computation. The first assumption made for the PM loss model is to neglect the effect of the eddy currents on the flux distribution. The second assumption is to consider PM loss proportional to  $f^2$ . This strongly simplifies the data manipulation, but at the cost of possible overestimation of PM loss. Thanks to these assumptions, PM loss can be computed in FEA simulation at fixed frequency/speed  $f_0/\omega_0$  [113], over a magnetizing grid current ( $I_{eq,d}, I_{eq,q}$ ) obtaining  $P_{PM,0}$  and then rescaled as:

$$P_{PM} = P_{PM,0} \cdot \left( \frac{f}{f_0} \right)^2 \quad (3.23)$$

The PM losses can be mapped at different PM temperatures and can be used in mapping code by the interpolation fixing the frequency/speed and PM temperature. In the following, the PM losses are not considered because negligible than the other losses.

## 3.2 Three-phase IPM machine efficiency mapping

The implementation of the IPM machine efficiency mapping is computed on the torque-speed domain and it is totally developed in Matlab environment. The developed mapping algorithm is able to reconstruct all electromechanical variables, saving the data into multidimensional matrices. A dense  $\Delta\omega_m$  and  $\Delta T_m$  discretization is assumed to generate a regular mesh grid. An example of the mesh grid is reported in Fig. 3.23. The speed limit of the grid is selected equal to the maximum operative speed of the machine, while the absolute torque limit corresponds to that of the torque map previously computed in the plane  $I_{eq,d}, I_{eq,q}$ , which depends on the magnetic model of the machine and PM temperature (see Section 3.1.3). Therefore, the efficiency map is obtained computing the efficiency in all the torque-speed points of the grid, even if some points can overcome the maximum torque per speed (MTPS) profile. However, the proposed efficiency mapping procedure automatically rules out these points applying the voltage and current limits.

Three other dimensions are added to the matrices: the dc-link voltage, the stator and PM temperatures. The mapping algorithm is organized with five nested loops: the outer ranging on the PM temperature, inside this stator temperature loop, is the nest, that in turn implements the dc-link voltage loop, speed loop, and torque loop.

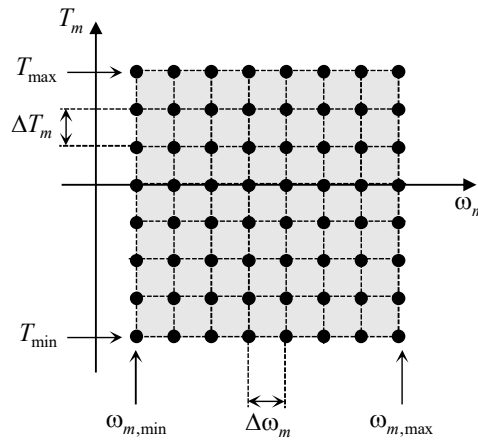


Figure 3.23 Mesh of operating points in the torque-speed plane.

Besides the flux and loss maps introduced in the previous sections, the additional data needed for the evaluation are:

1. Amplitude limit of the phase currents  $I_{max}$ : it usually consists of the minimum value between the overload motor current and the current limit of the inverter.
2. Limit of the phase voltage  $V_{max}$ : this value is the maximum amplitude of the fundamental voltage component provided by the PWM inverter. For the case study, a space vector modulation has been considered. Thus the input dc voltage of the inverter  $v_{dc}$  can be computed.
3. The machine and PM operating temperatures  $\vartheta, \vartheta_{PM}$ : the temperatures are chosen according to the thermal limits of the machine and PM or directly by the temperature load tests if available and PM datasheet.
4. The control strategy i.e., efficiency maximization, stator Joule losses minimization, stator flux minimization.

Note that the maps are computed for all electromechanical variables, which can be used for other purposes than energy assessment. The outputs of the mapping algorithm are adequately discretized and an interpolator is needed for their use in a continuous domain, as in a system simulation. For example, the eDrive thermal behaviour can be evaluated using a proper thermal machine model, based on machine losses evaluated by the interpolation of the computed offline maps.

### 3.2.1 IPM mapping algorithm

For each element of the torque-speed matrices discretized with  $\Delta\omega_m$  and  $\Delta T_m$  as explained before, fixing the dc-link voltage, stator and PM temperatures, different steps are performed, as explained hereafter.

1. For a given PM temperature  $\vartheta_{PM,z}$ , stator temperature  $\vartheta_k$ , dc-link voltage  $v_{dc,l}$ , rotor speed  $\omega_m, i$  on vectors defined in Eq. (3.24) (minimum and maximum values are based on the eDrive data) the mechanical

losses  $T_{fv}$  are computed interpolating the mechanical losses map, based on the rotor speed value  $\omega_{m,i}$  fixed at the speed loop  $i$ . Note that the map  $T_{fv}$  is repmat for all considered dc-link voltage and temperatures.

$$\begin{aligned} \vartheta_{PM}^{vct} &= [\vartheta_{PM,1} \quad \dots \quad \vartheta_{PM,z}]; \quad \vartheta^{vct} = [\vartheta_1 \quad \dots \quad \vartheta_k] \\ v_{dc}^{vct} &= [v_{dc,1} \quad \dots \quad v_{dc,l}]; \quad \omega_m^{vct} = [\omega_{m,1} \quad \dots \quad \omega_{m,i}] \end{aligned} \quad (3.24)$$

$$T_{fv} = \text{interp1}(\omega_{m,fv}, T_{fv}, \omega_{m,i}) \quad (3.25)$$

Since the PM, stator temperatures, and dc-link voltage are fixed, the indices  $z, k, l$  are not reported to simplify the notation.

2. Computation of electromagnetic torque with Eq. (3.12), accounting the  $T_{fv}$  computed in the previous step, adding or subtracting to the considered useful torque  $T_m$  is computed as:

$$\begin{aligned} T_{em} &= T_m + T_{fv}, & \omega_{m,i} > 0 \\ T_{em} &= T_m - T_{fv}, & \omega_{m,i} \leq 0 \end{aligned} \quad (3.26)$$

The equations are applied for all elements of torque-speed plane in Fig. 3.23.

3. Evaluation of all combinations of the magnetizing currents ( $I_{eq,d}, I_{eq,q}$ ) based on the  $T_{em}$ , using the *contourc* Matlab function is summarized as:

$$T_{iso} = \text{contourc}(I_{eq,d}^{map}(1,:), I_{eq,q}^{map}(:,1), T_{em}^{map}, T_{em}) \quad (3.27)$$

where the  $I_{eq,d}^{map}$ ,  $I_{eq,q}^{map}$ , and  $T_{em}^{map}$  are the flux maps presented in Section 3.1.3 at fixed stator and PM temperatures, organized as presented before. Selecting  $I_{eq,d}^{map}(1,:)$  all values of the currents along  $d$ -axis are explored using the first row of the matrix presented in Eq. (3.20), and vice versa for  $I_{eq,q}^{map}(:,1)$ .

The *contourc* function saves the current combinations  $n_c$ , indicated with  $c$ -index,  $1 \leq c \leq n_c$ . For all current combinations  $I_{eq,d}^{vct}$  and  $I_{eq,q}^{vct}$  organized as reported in Eq. (3.28), the fluxes linkage are evaluated

using the flux maps previously computed, selecting opportunely the maps to interpolate based on the PM temperature at the loop  $z$ . This means that this step depends on the considered PM temperature loop. In this way, the flux values  $\Lambda_d$  and  $\Lambda_q$  are represented by the vector of  $n_c$ -dimension, obtaining  $\Lambda_d^{vct}$  and  $\Lambda_q^{vct}$ .

$$I_{eq,d}^{vct} = [I_{eq,d-1}, \dots, I_{eq,d-c}, \dots, I_{eq,d-n_c}], \quad I_{eq,q}^{vct} = [I_{eq,q-1}, \dots, I_{eq,q-c}, \dots, I_{eq,q-n_c}], \quad (3.28)$$

From now until the selection of the current combination that respects the eDrive limits and makes getting the control strategy, all variables are temporary and are not saved into matrices.

4. Computation of the equivalent iron resistance or iron losses is performed by the interpolation of the lookup table presented in Section 4.7.4, knowing the rotor speed and electromagnetic torque:

$$\begin{aligned} R_{Fe} &= \text{interp2}(\omega_{m,Fe}^{map}, T_{em,Fe}^{map}, R_{Fe}^{map}, \omega_m, T_{em}) \\ P_{Fe} &= \text{interp2}(\omega_{m,Fe}^{map}, T_{em,Fe}^{map}, P_{Fe}^{map}, \omega_m, T_{em}) \end{aligned} \quad (3.29)$$

Similar approach is used for stator resistance computation based on the lookup table of Fig. 3.22, using the information of the electrical speed  $\omega_e(i)$  at this step and the stator temperature  $\vartheta(k)$ .

$$R_s = \text{interp2}(\omega_{m,R_s}^{map}, \vartheta_{R_s}^{map}, \omega_m, \vartheta) \quad (3.30)$$

At this point the equivalent resistance  $R_{eq}$  presented in Eq. (3.7) can be computed.

5. Computation of the equivalent and stator voltages is performed as:

$$\begin{aligned} V_{eq,d}^{vct}(c) &= R_{eq} \cdot I_{eq,d}^{vct}(c) - \omega_e \cdot \Lambda_q^{vct}(c) \\ V_{eq,q}^{vct}(c) &= R_{eq} \cdot I_{eq,q}^{vct}(c) + \omega_e \cdot \Lambda_d^{vct}(c) \end{aligned}, \quad 1 \leq c \leq n_c \quad (3.31)$$

where  $I_{eq,d}^{vct}(c)$  and  $I_{eq,q}^{vct}(c)$  are a generic element of the  $n_c$ -combination values identified in Eq. (3.27) and  $\omega_e$  depend on the loop  $i$ .

The stator voltage components are computed as:

$$V_d^{vct}(c) = \frac{V_{eq,d}^{vct}(c)}{k_{eq}}, \quad V_q^{vct}(c) = \frac{V_{eq,q}^{vct}(c)}{k_{eq}}, \quad 1 \leq c \leq n_c \quad (3.32)$$

where  $k_{eq}$  is based on Eq. (4.220) and Eq. (3.30), expressing as:

$$k_{eq} = \frac{\frac{1}{R_s}}{\frac{1}{R_s} + \frac{1}{R_{Fe}}} \quad (3.33)$$

6. The stator current components are computed as:

$$\begin{aligned} I_d^{vct}(c) &= k_{eq} \cdot I_{eq,d}^{vct}(c) + \frac{1}{R_{Fe}} \cdot V_{eq,d}^{vct}(c), \\ I_q^{vct}(c) &= k_{eq} \cdot I_{eq,q}^{vct}(c) + \frac{1}{R_{Fe}} \cdot V_{eq,q}^{vct}(c) \end{aligned}, \quad 1 \leq c \leq n_c \quad (3.34)$$

The iron current is computed as the difference of the total current ( $I_d^{vct}$ ,  $I_q^{vct}$ ) and the magnetizing current ( $I_{eq,d}^{vct}$ ,  $I_{eq,q}^{vct}$ ) as:

$$I_{Fe,d}^{vct}(c) = I_d^{vct}(c) - I_{eq,d}^{vct}(c), \quad I_{Fe,q}^{vct}(c) = I_q^{vct}(c) - I_{eq,q}^{vct}(c), \quad 1 \leq c \leq n_c \quad (3.35)$$

Based on the current components the phase-peak values can be computed as in Eq. (4.139) for the losses computation.

$$\begin{aligned} I^{vct}(c) &= \sqrt{(I_d^{vct}(c))^2 + (I_q^{vct}(c))^2}, \\ I_{Fe}^{vct}(c) &= \sqrt{(I_{Fe,d}^{vct}(c))^2 + (I_{Fe,q}^{vct}(c))^2} \end{aligned}, \quad 1 \leq c \leq n_c \quad (3.36)$$

7. Computation of PM losses is performed by the interpolation of PM loss map evaluated at the frequency  $f$  of the loop  $i$  and PM temperature  $\vartheta_{PM}$  of the loop  $z$  as:

$$P_{PM} = \text{interp2}(f_{PM}^{map}, \vartheta_{PM}^{map}, P_{PM}^{map}, f, \vartheta_{PM}) \quad (3.37)$$

8. Computation of the losses is performed as:

$$\begin{aligned}
 P_J^{vct}(c) &= \frac{3}{2} \cdot R_s \cdot (I^{vct}(c) \cdot I^{vct}(c)) \\
 P_{Fe}^{vct}(c) &= \frac{3}{2} \cdot R_{Fe} \cdot (I_{Fe}^{vct}(c) \cdot I_{Fe}^{vct}(c)) \\
 P_{PM} &= P_{PM,0} \cdot \left( \frac{f}{f_0} \right)^2 \\
 P_{fv} &= T_{fv} \cdot \omega_m
 \end{aligned}
 , \quad 1 \leq c \leq n_c \quad (3.38)$$

The total losses considered in this case can be computed as:

$$P_l^{vct}(c) = P_j^{vct}(c) + P_{Fe}^{vct}(c) + P_{PM} + P_{fv}, \quad 1 \leq c \leq n_c \quad (3.39)$$

9. Finally, the electrical power is computed as:

$$\begin{aligned}
 P_e^{vct}(c) &= T_m \cdot \omega_m + P_l^{vct}(c), \quad T_m > 0 \\
 P_e^{vct}(c) &= T_m \cdot \omega_m - P_l^{vct}(c), \quad T_m \leq 0
 \end{aligned}
 , \quad 1 \leq c \leq n_c \quad (3.40)$$

10. Elimination of all the points in the maps that violate the current and voltage limits defined based on the dc-link voltage loop  $l$  and machine thermal limit. Among the elements composing the  $n_c$ -dimensional vectors computed in the previous steps, the ones that break the amplitude limit of the phase currents  $I_{max}$  or the amplitude limit of the phase voltages  $V_{max}$  are ruled out. For clarity, by considering any one of the  $n_c$ -dimensional vectors computed in the previous steps, called generically  $X^{vct}$ , the elements of this vector must satisfy both the above-reported limits:

$$\begin{aligned}
 X^{vct} | \quad V &\leq V^{max} \\
 I &\leq I^{max}
 \end{aligned} \quad (3.41)$$

where the maximum stator voltage  $V_{max}$  depend on the dc-link voltage  $v_{dc,l}$  based on the dc-link voltage loop. The loop  $l$  impacts on this limits. If the MinMax modulation is adopted the relation between the dc-link



voltage and stator voltage is:

$$V_{max} = \frac{v_{dc}}{\sqrt{3}} \quad (3.42)$$

The position indexes of the elements that satisfy the voltage and current limits are the same for all vectors. If applying the voltage and current limits leads to ruling out all elements of the  $n_c$ -dimensional vectors, the considered torque-speed point overcomes the MTPS profile and therefore cannot be physically operated. In this case, the proposed mapping procedure rules out this torque-speed point and the NaN operator is saved.

11. Let's consider the elements of the  $n_c$ -dimensional vectors that satisfy both voltage and current limits. The position index of the element leading to maximizing efficiency corresponds to the one that minimizes the overall losses. Otherwise, if the control strategy includes the minimization of the stator losses another index will be detected. For clarity, considering any one of the  $n_c$ -dimensional vectors called  $X^{vct}$ , the element of this vector that leads to maximizing efficiency is denoted as:

$$X^{opt} = (P_j^{vct} + P_{Fe}^{vct} + P_{PM}) \left| \begin{array}{l} V_s^{vct} \leq V_{max} \\ I_s^{vct} \leq I_{max} \end{array} \right. \quad (3.43)$$

Note that there is only one specific combination of  $dq$  variables (voltages, currents, flux linkages) that leads to maximizing efficiency for the considered torque-speed point.

Finally, if considering a torque-speed point in the motor operation, the machine's efficiency  $\eta^{opt}$  is computed as:

$$\eta^{opt} = \frac{T_m \cdot \omega_m}{T_m \cdot \omega_m + P_j^{opt} + P_{Fe}^{opt} + P_{PM}^{opt} + P_{fv}^{opt}} \quad (3.44)$$

Conversely, if considering a torque-speed point in the generation operation, the machine's efficiency is computed as:

$$\eta^{opt} = \frac{T_m \cdot \omega_m + P_j^{opt} + P_{Fe}^{opt} + P_{PM}^{opt} + P_{fv}^{opt}}{T_m \cdot \omega_m} \quad (3.45)$$

12. Computation of VSI efficiency is obtained as:

$$\eta_{VSI} = \frac{P_m + P_l}{V_{dc} \cdot I_{dc}} = \frac{P_m + P_l}{P_m + P_l + P_{l-VSI}} \quad (3.46)$$

where the VSI losses  $P_{l-VSI}$  are computed as in Eq. (3.19) and  $i_{dc}$  stands for the dc-current.

Finally, the computation of eDrive efficiency is performed as product between IPM and VSI efficiencies.

13. Saving variables reconstructed with the offline mapping in multidimensional matrices represents the last step. The discretization depends on the torque, speed steps, dc-link voltage, stator and PM temperatures evaluated in the mapping code. Details about the mapping structure, and the use in a continuous domain is reported below.

All formulations are extended for all working points of the whole torque-speed range, obtained a multidimensional maps in according to the voltage and current limits.

### 3.2.2 Mapping results for IPM e-Motor for BEV

An example of the mapping results of IPM e-Motor for BEV is reported below. The machine used for the mapping validation is provided by automotive industry for a commercial EV, as mentioned before. The comparison between the outputs of the mapping code and FEA simulations has been performed. The experimental validation has not been made because the prototype was not available.

In the following, the procedure presented in the previous section is adopted to compute the efficiency maps and make some comparisons on the base inputs. Assuming that the current and voltage limits are imposed by the

inverter, the two parameters that can affect efficiency are temperature and control strategy. The former affects both winding and PMs, increasing stator Joule losses and reducing the PM remanence (and hence, the PMs strength), while the latter is more critical, since the maximum efficiency control is not possible if the machine is not completely identified. Subsequently, the dc-link voltage variation is considered to analyze the difference in terms of working area.

### Temperature effects

The effects on the efficiency maps related to the winding and PM temperatures are analyzed, fixing the dc-link voltage at 400 V and the maximum efficiency control strategy is adopted. Consider that the mechanical and PM losses are not included because it was not possible the evaluation for industrial privacy of the benchmark IPM machine.

Two conditions are considered:

- cold condition: winding temperature  $\vartheta = 30^{\circ}\text{C}$  and PM temperature  $\vartheta_{PM} = 20^{\circ}\text{C}$ ;
- hot condition: winding temperature  $\vartheta = 170^{\circ}\text{C}$  and PM temperature  $\vartheta_{PM} = 150^{\circ}\text{C}$ ;

The winding temperature affects the stator Joule loss: higher the temperature, higher the phase resistance, and so, the higher the loss for the same current. This is confirmed by the maps reported in Fig. 3.24, where the colorbar is reported in kW. Dealing with the PM temperature affects the PM remanence, and, in general, an increase in PM temperature reduces the output torque for a given current. This effect is more evident in the machines with a high PM flux linkage and that use PMs having a high-temperature coefficient.

Fig. 3.25 compares the efficiency maps for benchmark IPM machine in motoring and generation modes in the two thermal conditions. As expected, the efficiency is higher in the cold scenario, thanks to the lower phase resistance and the higher PM remanence. The PM temperature also affects the maximum torque (low-speed region): the torque produced in the hot conditions is lower than that generated in cold conditions: 250 Nm in cold conditions than 235 Nm in hot conditions. The maximum efficiency is slightly affected by temperature: in the left is 98.3% in cold conditions than 97.9 % in

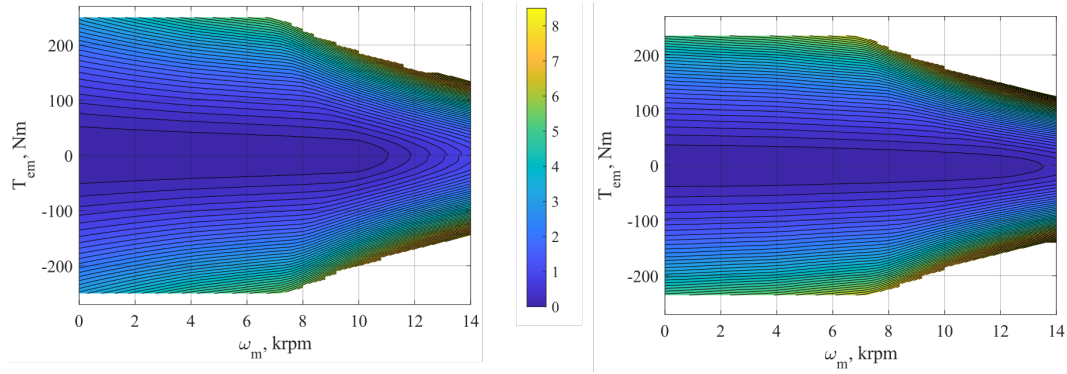


Figure 3.24 Stator Joule loss maps in kW of the IPM machine with maximum efficiency control in cold (left) and hot (right) conditions at  $v_{dc} = 400$  V.

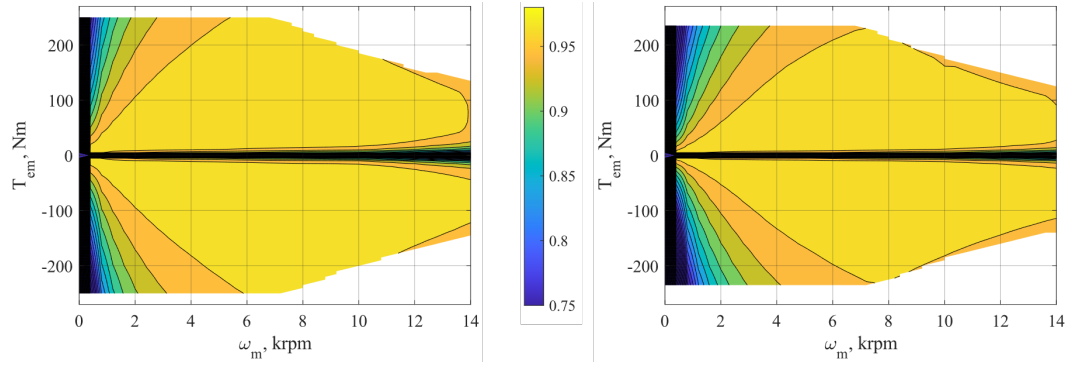


Figure 3.25 Efficiency maps of the IPM machine with maximum efficiency control in cold (left) and hot (right) conditions at  $v_{dc} = 400$  V.

hot conditions. Also, just as an example fixing the electromagnetic torque  $T_{em} = 200$  Nm and the rotor speed  $\omega_m = 4$  krpm the efficiency is increased at 1% in cold conditions than the hot one. Finally, it can be observed that the maximum efficiency locus is moved at higher torque in hot conditions than in cold ones.

### Control strategy effects

The effects on the efficiency maps related to the winding and PM temperatures is analyzed, fixing the dc-link voltage at 400 V and the maximum efficiency control strategy is adopted. Another important variable that should always be declared with an efficiency map is the control strategy. The procedure presented in the previous section relies on maximum efficiency control, which ensures the best efficiency that the machine can express. The method developed in this dissertation assumes that the iron loss map is known prior.

In practice, this is not feasible, so other controls are implemented. One of the most common control is the MTPA control. It consists of minimizing the current for a given torque reference and is based on the simple knowledge of the flux maps (and not the loss maps). At low speed, the MTPA trajectory on the  $dq$  plane is followed. Then, as the speed exceeds the base speed, the current vector is rotated towards the  $q$ -axis until the MTPV locus is reached. From this speed on, the current is decreased, according to the MTPV trajectory. The MTPA control can be easily implemented in the efficiency map computation flowchart by selecting the optimal value of  $n_c$ -combination that ensures the procedure's minimum stator current. The efficiency maps considering the MTPA control in cold condition is reported in Fig. 3.26 - left, which can be compared with Fig. 3.25 - left, considering different control strategies. This means that considering the MTPA control strategy, Eq. (3.47) is modified as:

$$X^{opt} = P_j^{vct} \left| \begin{array}{l} V_s^{vct} \leq V_{max} \\ I_s^{vct} \leq I_{max} \end{array} \right. \quad (3.47)$$

Fig. 3.26 - right reports the efficiency difference obtained with the two control strategies. The analysis shows that the difference is generally small, and the maximum penalization of the MTPA control (about 0.8 % of efficiency which significantly not impact on system efficiency, e.g., hybrid vehicle) is where iron is more important than stator Joule loss: for mid-high speed and low torque. Also, in the low-speed area, a small difference is noticeable thanks to the reduction of the iron loss of the maximum efficiency control. Nevertheless, the two control strategies in the high-speed region are the same since the voltage ( $v_{dc} = 400$  V), and current limits narrow the feasible operating region in the  $dq$  plane.

### Dc-link voltage effects

In Fig. 3.27, an example of the efficiency maps of eDrive (IPM + VSI) obtained with the proposed procedure, fixing the temperatures  $\vartheta = 30^\circ\text{C}$  and  $\vartheta_{PM} = 20^\circ\text{C}$  with different dc-link voltages are shown. On the left, the dc-link voltage is 300 V, while on the right 500 V. The figure highlights how the dc-link voltage value impacts the boundary between the base and flux weakening regions; consequently, the efficiency values are different. The

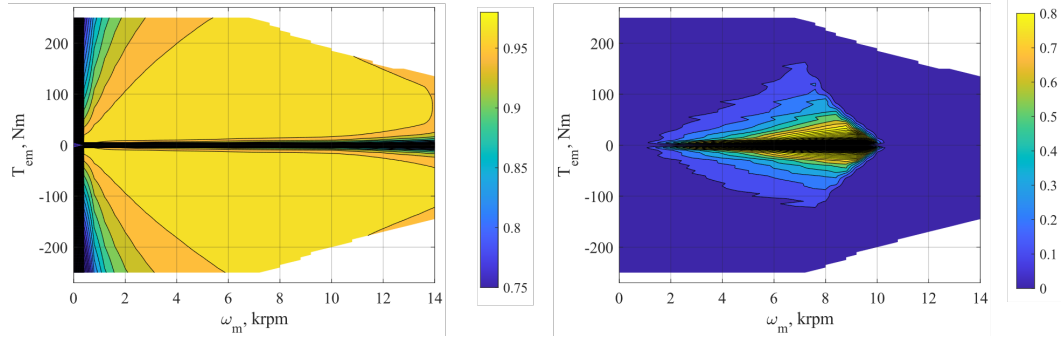


Figure 3.26 eDrive efficiency maps of the IPM machine with MTPA control (left) and efficiency difference considering maximum efficiency and MTPA control strategies (right) in cold conditions at  $v_{dc} = 400$  V.

base speed at 300 V dc-link voltage is about 5600 rpm, then 8500 rpm at 500 V.

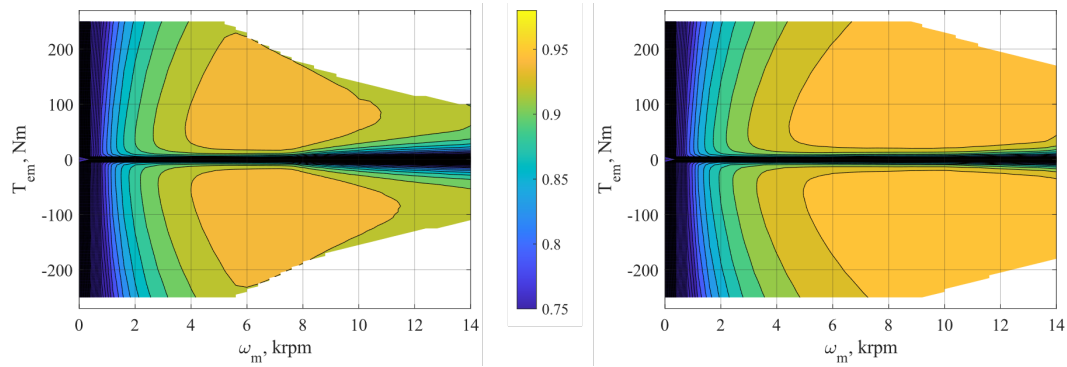


Figure 3.27 Efficiency maps of the eDrive with efficiency maximization at  $v_{dc} = 300$  V (left) and  $v_{dc} = 500$  V (right).

The electrical loss map (stator Joule + iron) evaluated with the mapping code is reported in Fig. 3.28 for different dc-link voltages. The losses increase with the speed and torque, following the stator voltage and current maps reported in Fig. 3.29 and Fig. 3.30. In Fig. 3.29 the voltage limit related to the dc-link one is highlighted: the maximum value in the left is about 220 V, while in the right is 275 V.

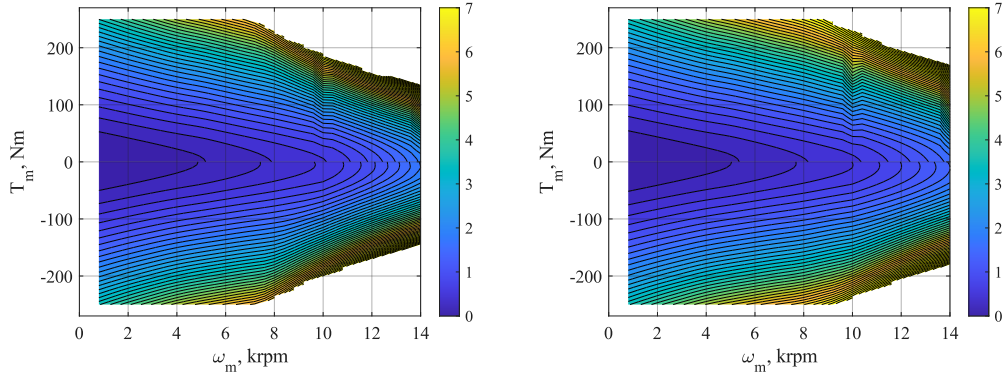


Figure 3.28 Electrical loss map in kW in cold conditions at  $v_{dc} = 400$  V (left) and  $v_{dc} = 500$  V (right).

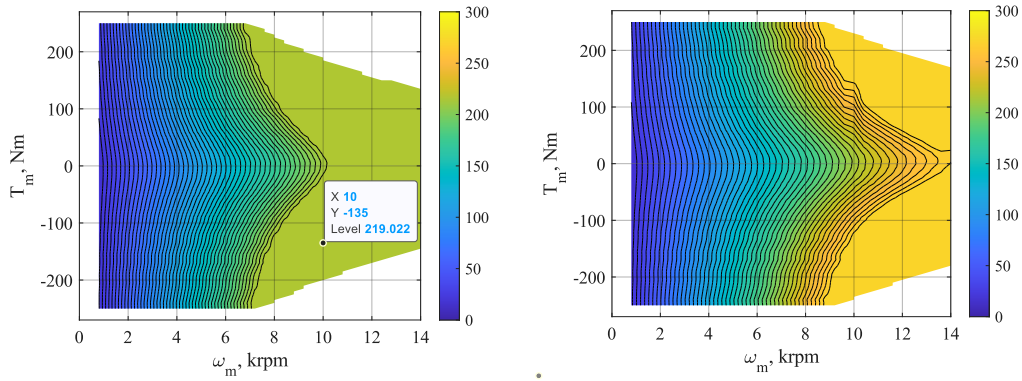


Figure 3.29 Stator voltage map in Volt in cold conditions at  $v_{dc} = 400$  V (left) and  $v_{dc} = 500$  V (right).

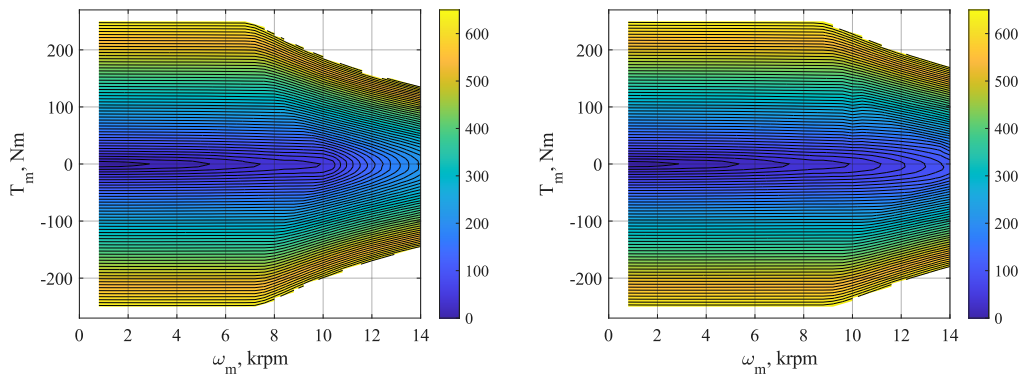


Figure 3.30 Stator current map in Ampere in cold conditions at  $v_{dc} = 400$  V (left) and  $v_{dc} = 500$  V (right).

### 3.2.3 Multidimensional linear interpolator

The maps computed with the proposed algorithm are discrete since they are defined for specific steps of torque  $\Delta T_m$ , speed  $\Delta \omega_m$ , dc-link voltage  $v_{dc}$ , and machine  $\vartheta$  and PM  $\vartheta_{PM}$  temperatures. Therefore, the evaluation of a generic variable in an arbitrary working point of the machine needs an interpolator. The 4D maps computed with the mapping algorithm are organized as reported hereafter, selecting the PM temperature to avoid an interpolation on 5 dimensions. The fifth dimension represents the PM temperature, in which values are sorted in ascending order using a predefined temperature step.

1. The first dimension represents the torque in both motoring and generating modes. The torque values are sorted in descending order, from the maximum torque value in motoring mode to the minimum in generating mode. The torque step is univocal for all maps.
2. The second dimension represents the motor speed. The speed values are sorted in ascending order, from zero to the maximum motor speed for both generating and motoring modes. The speed step is univocal for all maps.
3. The third dimension represents the dc-link voltage, in which values are sorted in ascending order using a predefined voltage step.
4. The fourth dimension represents the machine temperature, in which values are sorted in ascending order using a predefined temperature step.

Therefore, each electromechanical variable is evaluated in an arbitrary working point of the machine through a 4D interpolation, fixing the PM temperature. The mathematical relationships used in the interpolation algorithm are summarized in the following. The interpolation is presented for a generic variable  $f$ . However, the interpolation should be performed only for the equivalent  $dq$  currents of the machine since all the other variables can be reconstructed by them. The proposed interpolation algorithm is organized in two consecutive steps.



### First step

The first step consists of four interpolations performed in as many torque-speed planes. These planes correspond to the four combinations of dc-link voltage and machine's temperature that are closer to those of the considered working point. Therefore, based on such combinations, the following maps are selected:

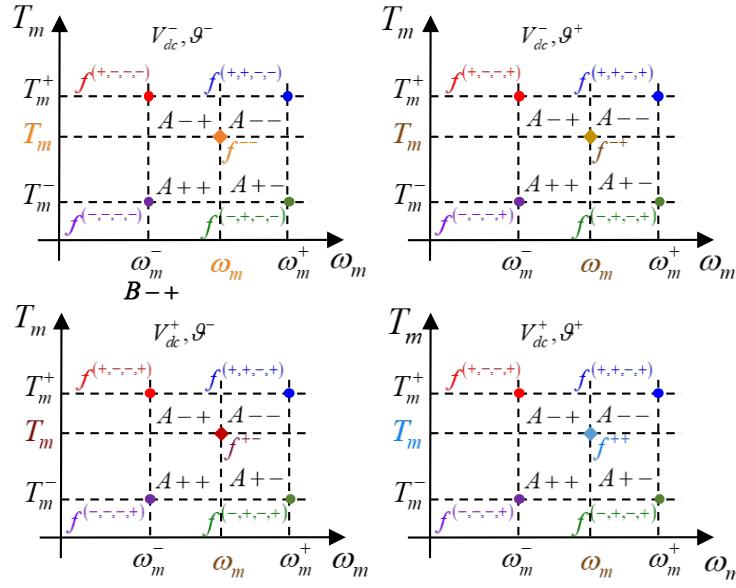


Figure 3.31 The four  $(T_m, \omega_m)$  planes selected in the first step of the 4D interpolation.

1.  $f(T, \omega, V_{dc-}, \vartheta-)$  stands for the map defined for the values of dc-link voltage and machine temperature that are both lower than those of the considered working point;
2.  $f(T, \omega, V_{dc-}, \vartheta+)$  stands for the map defined for the value of the dc-link voltage that is lower than that of the considered working point, and for the value of machine temperature that is higher than that of the considered working point;
3.  $f(T, \omega, V_{dc+}, \vartheta-)$  stands for the map defined for the value of the dc-link voltage that is higher than that of the considered working point, and for the value of machine temperature that is lower than that of the considered working point;

4.  $f^{(T, \omega, V_{dc+}, \vartheta+)}$  stands for the map defined for the values of dc-link voltage and machine temperature that are both higher than those of the considered working point.

In the  $(T_m, \omega_m)$  plane, each of the presented maps is restricted at the four  $(T_m, \omega_m)$  values that are closer to those of the considered working point, as reported in Fig. 3.31. The interpolated points  $f^{\pm\pm}$  in Fig. 3.31 are computed as weighted-average of the areas of each plane as:

$$\begin{aligned}
 f^{--} &= \frac{f^{(+,+, -, -)} \cdot A^{--} + f^{(+, -, -, -)} \cdot A^{-+} + f^{(-, +, -, -)} \cdot A^{+-} + f^{(-, -, -, -)} \cdot A^{++}}{A^{--} + A^{-+} + A^{+-} + A^{++}} \\
 f^{-+} &= \frac{f^{(+, +, -, +)} \cdot A^{--} + f^{(+, -, -, +)} \cdot A^{-+} + f^{(-, +, -, +)} \cdot A^{+-} + f^{(-, -, -, +)} \cdot A^{++}}{A^{--} + A^{-+} + A^{+-} + A^{++}} \\
 f^{+-} &= \frac{f^{(+, +, +, -)} \cdot A^{--} + f^{(+, -, +, -)} \cdot A^{-+} + f^{(-, +, +, -)} \cdot A^{+-} + f^{(-, -, +, -)} \cdot A^{++}}{A^{--} + A^{-+} + A^{+-} + A^{++}} \\
 f^{++} &= \frac{f^{(+, +, +, +)} \cdot A^{--} + f^{(+, -, +, +)} \cdot A^{-+} + f^{(-, +, +, +)} \cdot A^{+-} + f^{(-, -, +, +)} \cdot A^{++}}{A^{--} + A^{-+} + A^{+-} + A^{++}}
 \end{aligned} \tag{3.48}$$

where the areas of each plane are computed as:

$$\begin{aligned}
 A^{--} &= (\omega_m^+ - \omega_m) \cdot (T_m^+ - T_m) \\
 A^{-+} &= (\omega_m - \omega_m^-) \cdot (T_m^+ - T_m) \\
 A^{+-} &= (\omega_m^+ - \omega_m) \cdot (T_m - T_m^-) \\
 A^{++} &= (\omega_m - \omega_m^-) \cdot (T_m - T_m^-)
 \end{aligned} \tag{3.49}$$

Therefore, the results of the first step are four interpolated values of the considered variable  $f$ , related to the values of dc-link voltage and machine temperature that are closer to those of the considered working point.

### Second step

It consists of the two-dimensional interpolation of the considered variable  $f$  among the four points obtained in the previous step, as shown in Fig. 3.32.

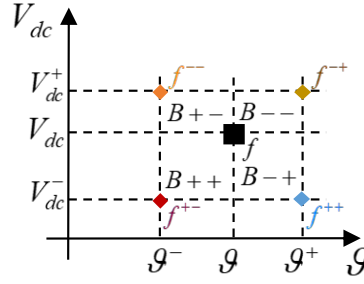


Figure 3.32 (Voltage, temperature) plane in the second step of the 4D interpolation.

Therefore, the final value of the considered variable  $f$  is computed as weighted-average of the areas of the plane as:

$$f = \frac{f^{++} \cdot B^{--} + f^{+-} \cdot B^{-+} + f^{-+} \cdot B^{+-} + f^{--} \cdot B^{++}}{B^{--} + B^{-+} + B^{+-} + B^{++}} \quad (3.50)$$

where the areas of the plane are computed as:

$$\begin{aligned} B^{--} &= (\theta^+ - \theta) \cdot (V_{dc}^+ - V_{dc}) \\ B^{-+} &= (\theta^+ - \theta) \cdot (V_{dc} - V_{dc}^-) \\ B^{+-} &= (\theta - \theta^-) \cdot (V_{dc}^+ - V_{dc}) \\ B^{++} &= (\theta - \theta^-) \cdot (V_{dc} - V_{dc}^-) \end{aligned} \quad (3.51)$$

By combining Eq. (3.48) and Eq. (3.50), the interpolation between the sixteen points that are closer to the considered working point can be computed as:

$$f = \frac{1}{B} \cdot \frac{1}{A} \cdot \left[ \begin{aligned} &\left( f^{(+,+,+,+)} \cdot A^{--} + f^{(+,-,+,+)} \cdot A^{-+} + f^{(-,+,+,+)} \cdot A^{+-} + f^{(-,-,+,+)} \cdot A^{++} \right) \cdot B^{--} + \\ &+ \left( f^{(+,+,+,-)} \cdot A^{--} + f^{(+,-,+, -)} \cdot A^{-+} + f^{(-,+,+,-)} \cdot A^{+-} + f^{(-,-,+, -)} \cdot A^{++} \right) \cdot B^{-+} + \\ &+ \left( f^{(+,+, -, +)} \cdot A^{--} + f^{(+,-, -, +)} \cdot A^{-+} + f^{(-,+, -, +)} \cdot A^{+-} + f^{(-,-, -, +)} \cdot A^{++} \right) \cdot B^{+-} + \\ &+ \left( f^{(+,+, -, -)} \cdot A^{--} + f^{(+,-, -, -)} \cdot A^{-+} + f^{(-,+, -, -)} \cdot A^{+-} + f^{(-,-, -, -)} \cdot A^{++} \right) \cdot B^{++} \end{aligned} \right] \quad (3.52)$$

where areas  $A$  and  $B$  are computed as:

$$A = A^{--} + A^{-+} + A^{+-} + A^{++}; \quad B = B^{--} + B^{-+} + B^{+-} + B^{++} \quad (3.53)$$

An example of an interpolation result for IPM used for mapping validation is reported in Table 3.2. The mechanical torque, rotor speed, dc-link voltage, and machine temperature represent the inputs of the interpolator. All electromechanical variables are interpolated based on the input variables. If the input torque cannot be obtained at the considered dc-link voltage and/or machine temperature, a warning is given. In this case, the closest possible torque value is provided.

Table 3.2 Interpolation results for 3-IPM

Interpolator output	
Elapsed time	24 ms
Winding temperature	100 °C
PM temperature	20 °C
Dc-link voltage	350 V
Speed	5000 rpm
Mechanical torque	233.2 Nm
Electromagnetic torque	234.1 6Nm
<i>d</i> -axis stator current	-440.1 A
<i>q</i> -axis stator current	461.2 A
<i>d</i> -axis stator voltage	-159.6 V
<i>q</i> -axis stator voltage	34 V
Mechanical power	122.1 kW
Power losses	9.2 kW
Electric power	131.3 kW
IPM efficiency	0.93
VSI efficiency	0.95
eD efficiency	0.88

### 3.3 Conclusion

This chapter proposed a mapping algorithm to compute the efficiency map of interior permanent magnet (IPM) synchronous machines based on the flux maps at different PM temperatures to consider most synchronous machines' nonlinear behaviors [106, 107]. Since the computation method is based on

flux maps, the proposed procedure is valid for all the machines that can be modeled in this way, and so Surface-mounted PM (SPM) machines, to the PM-assisted Synchronous Reluctance (PM-SyR) machines.

The benchmark in this study is 90.5 kW, 14 krpm, 8 poles IPM machine provided by the automotive company. The procedure is developed in Matlab implementing the steady-state IPM model in rotating  $dq$  reference frame, starting from the 2D FEA simulation results. The initialization of the proposed procedure consists of, in addition to flux maps, the iron, and PM losses [112, 32]. After briefly introducing the flux maps and losses contribution, this chapter analyzed the methodologies to compute them through simple 2D FEA simulations [112] and the implemented post-process. In addition, the proposed procedure requires the knowledge of the following inputs to compute the efficiency map of the mesh grid:

- Amplitude limit of the phase currents  $I_{max}$ .
- Amplitude limit of the phase voltages  $V_{max}$ , whose value is computed according to the dc-link voltage and modulation technique.
- Stator  $\vartheta$  and PM  $\vartheta_{PM}$  operating temperatures, whose values can be chosen arbitrarily according to their operative limits.
- Control strategy: maximum efficiency control, which ensures the best efficiency that the motor can express. Still, it assumes that the loss maps and the exact temperature of the motor are known a priori. Otherwise, the Maximum Torque per Ampere (MTPA) control strategy is presented [87]. It minimizes the current for a given torque reference and is based on the simple knowledge of the flux maps (not the loss maps).

According to the above-reported inputs and constraints, the torque-speed mesh grid's efficiency and losses maps are computed upon all electromechanical variables reconstruction on the torque-speed domain. The evaluation algorithm is organized with many nested for loops: *i*) the outer ranging loop on the PM temperature levels, *ii*) internally the stator temperature loop, *iii*) even more internally the dc-link voltage loop, *iv*) the ranging on the speed levels, and *v*) the inner ranging loop on the torque levels.

Assuming that the inverter imposes the current and voltage limits, three parameters affecting efficiency are analyzed in the chapter, i.e., temperature, control strategy, and dc-link voltage. The former affects both winding and PMs, increasing stator Joule losses and reducing the PM remanence (and hence, the PMs strength), while the control strategy is more critical since the maximum efficiency control is impossible if the motor is not completely identified. The analysis shows that the difference is generally slight in implementing the proposed control strategies. The maximum penalization of the MTPA control is where iron and PM losses are higher than stator Joule loss: for mid-high speed and low torque. Also, in the low-speed area, a slight difference is noticeable thanks to the reduction of the iron loss of the maximum efficiency control. Nevertheless, the two control strategies in the high-speed region are the same since the voltage, and current limits narrow the feasible operating region in the  $dq$  plane. Finally, the dc-link voltage impact on the flux-weakening region and the working area is shown.

In addition, the chapter deals with the efficiency mapping of the voltage source inverter (VSI). The VSI modeling used in this dissertation is based on the component's datasheet parameters. Since the primary goal for this activity is related to the energetic aspects, an ideal steady-state model is considered for the power converter. The efficiency is evaluated considering conduction and switching losses using analytical formulations for VSI. Details are provided in the chapter.

This chapter ends with a linear interpolator for evaluating a generic variable in an arbitrary working point. Indeed, maps computed with the proposed algorithm are discrete since they are defined for specific steps of torque, speed, dc-link voltage, and machine and PM temperatures.

## Chapter 4

# Multi-Three-phase Induction Machine Mapping

The objective of this chapter is to develop generalised mathematical models of an multi-three-phase induction machine (IM) for performance evaluation in healthy and open-winding faulty conditions.

Four different modelling approaches will be considered: multi-stator (MS) [60], vector space decomposition (VSD), decoupling MS (DMS), and adaptive multi-stator (AD-MS) modelling approaches. A comparison of the models will be carried out with the emphasis on their utilisation in mapping algorithm to evaluate the machine performance.

After this, the magnetic model based on the flux maps will be presented, showing how the different mathematical modelling give the same results in terms of current-to-flux relationships.

For a complete machine characterization, the iron losses and parameters will be investigated, considering both normal (healthy) and open-three-phase faulty conditions.

The flux maps manipulation allows the computation of the maximum torque per speed (MTPS) and the maximum torque per ampere (MTPA) profiles. This analysis defines the operating limits of the machine in different conditions (normal or faulty) and a possible machine control, following the MTPA trajectory, minimizing the stator joule losses.

Based on the presented machine modelling and identification, the performance evaluation of multi-three-phase IM is presented in detail for all

possible machine configurations. The proposed mapping is able to reconstruct all electromechanical variables at different machine temperatures and dc-link voltages, replacing the machine operation. Also, the proposed mapping is able to reply different control strategies: the efficiency maximization, stator Joule losses minimization (MTPA), and stator flux minimization. The efficiency mapping has been developed with different machine modeling, presented before: MS [114], VSD [115], DMS [116, 117], and AD-MS approaches, demonstrating the robustness of the algorithm.

The proposed method has been validated on 12-phase asymmetrical IM in quadruple three-phase configuration (10 kW, 6000 rpm). The experimental validation was carried out using a direct flux vector control (DFVC) scheme based on AD-MS approach.

The chapter is organized as follow:

- The first section presents a machine model of the multi-three-phase IM in phase coordinates  $abc, \dots, m$ , in stationary reference frame  $\alpha\beta$ , and finally in rotating  $dq$  reference frame using the MS, VSD, DMS, and AD-MS approaches.
- Second section deals with the machine parameters identification, carrying out on 12-phase IM in both healthy and open-winding faulty operating conditions.
- The magnetic model based on flux maps is presented. The manipulation of the flux maps and machine parameters identification allowed to define the MTPA trajectories and MTPS profiles in all operative conditions.
- The efficiency mapping algorithm has been developed using the different presented mathematical approaches, giving the same results. Details about the developed methodology are provided.
- The experimental validation for different machine conditions, i.e., healthy and faulty, has been conducted on asymmetrical 12-phase, 10 kW, 6000 rpm. The experimental validation was carried out excellent results.



## 4.1 Machine model in phase variables

A multiphase machine with  $m$ -phase machine has  $n$  windings composed of three-phase takes the name of multi-three-phase machine. Depending on the phase propagation between the winding sets, a machine can be symmetrical ( $2\pi/m$ ) or asymmetrical ( $\pi/m$ ). The assumptions in machine modelling are taken into account:

- The stator is composed by  $n$  three-phase windings.
- Each three-phase winding set is composed by identical single-phase windings with sinusoidal distribution and with a reciprocal angle displacement of  $120^\circ$  electrical degrees.
- Squirrel cage rotor modelled as an equivalent three-phase winding composed by identical single-phase windings with sinusoidal distribution and with a reciprocal angle displacement of  $120^\circ$  electrical degrees.
- The magneto-motive force is sinusoidally distributed along the air gap circumference.
- Magnetic core is linear and so the flux saturation can be neglected.
- Magnetic core losses are neglected.
- Machine is balanced with uniform air gap, neglecting the presence of both stator and rotor cage.
- The stator and rotor resistances are constant.

Each three-phase winding is identified by the first phase  $a$  belonging the magnetic axis of the considered three-phase winding. The displacement between the magnetic axis and a stationary reference frame  $(\alpha, \beta)$  is denoted  $\theta_k$ , as shown in Fig. 4.1. Finally,  $\theta_r$  stands for the position of the magnetic axis belonging to the first phase of the rotor winding than the stationary  $\alpha$ -axis, which corresponds with the real electrical rotor position. Looking Fig. 4.1, the alignment of the magnetic axis of the first set with the position of the stationary  $\alpha$ -axis is assumed. In time domain the electromagnetic

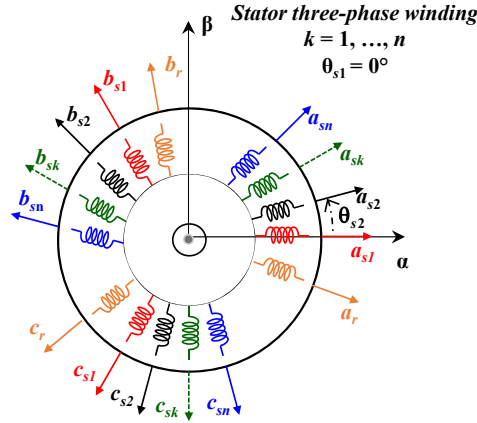


Figure 4.1 Multiple three-phase squirrel cage IM.

model is described by the stator magnetic model, rotor magnetic model, stator electrical model, and rotor electrical model [118].

### Stator magnetic model

The magnetic model represents the relationships between the current and flux. The number of equations for stator magnetic model is equal to the phases of the machine, relating the flux linkage of each phase with all machine currents. Considering the linearity assumption and decoupling leakage fluxes between the stator phases, for each three-phase winding  $k=1, \dots, n$  the stator magnetic model can be written as:

$$\bar{\lambda}_{abc,sk} = L_{l,s} \cdot \bar{i}_{abc,sk} + \sum_{z=1}^n ([M_{sk-sz}] \cdot \bar{i}_{abc,sz}) + [M_{sk-r}] \cdot \bar{i}_{abc,r} \quad (4.1)$$

where:

- $\bar{\lambda}_{abc,sk}$  stands for the stator fluxes vector of a generic three-phase winding  $k$ -set;
- $\bar{i}_{abc,sk}$  stands for the stator currents vector of a generic three-phase winding  $k$ -set;

- $\bar{i}_{abc,sz}$  stands for the stator currents vector of a generic three-phase winding  $z$ -set;
- $\bar{i}_{abc,r}$  stands for the rotor currents vector of three-phase winding;
- $L_{l,s}$  is the self-leakage phase inductance for the three-phase  $k$ -set;
- $[M_{sk-sz}]$  is the  $3 \times 3$  mutual magnetizing inductance matrix between the stator phase windings of  $k$ -set and the stator phase windings of the  $z$ -set;
- $[M_{sk-r}]$  is the  $3 \times 3$  mutual magnetizing inductance matrix between the stator phase windings of  $k$ -set and the rotor phase windings.

The matrices  $[M_{sk-sz}]$  and  $[M_{sk-r}]$  are defined based on mutual magnetizing inductance between two generic phase windings  $x$  and  $y$  of the machine as [118]:

$$M_{y-x} = \left. \frac{\lambda_{y-x}}{i_x} \right|_{i_y=0} = M_{x-y} = \left. \frac{\lambda_{x-y}}{i_y} \right|_{i_x=0} \quad (4.2)$$

This equation represents the mutual magnetizing inductance  $M_{y-x}$  related to the flux linkage  $\lambda_{y-x}$  of the  $y$  phase winding caused by the current injection  $i_x$  in the  $x$  phase-winding (see Fig. 4.2), and vice versa for  $M_{x-y}$ . The flux linkage  $\lambda_{y-x}$  depends on the magnetomotive force vector  $F_{y-x}$ , the number of turns and air gap magnetic reluctance  $\mathcal{R}_{eq}$ . Based on Fig. 4.2 and performing some mathematical manipulation reported in Eq. (4.3), and considering that the mutual magnetizing inductance  $M_{y-x}$  does not depend by the phase winding in which the current injection  $i_x$ , the flux linkage can be computed as:

$$\begin{aligned} \lambda_{x-y} &= N_y \cdot \phi_{y-x} = N_y \cdot \frac{F_{y-x}}{\mathcal{R}_{eq}} \\ F_{y-x} &= N_x \cdot i_x \cos(\delta_y - \delta_x) \implies \\ \implies \lambda_{y-x} &= \frac{N_x \cdot N_y}{\mathcal{R}_{eq}} \cdot i_x \cdot \cos(\delta_y - \delta_x) \\ M_{y-x} &= \left. \frac{\lambda_{y-x}}{i_x} \right|_{i_y=0} = \frac{N_x \cdot N_y}{\mathcal{R}_{eq}} \cdot \cos(\delta_y - \delta_x) \end{aligned} \quad (4.3)$$

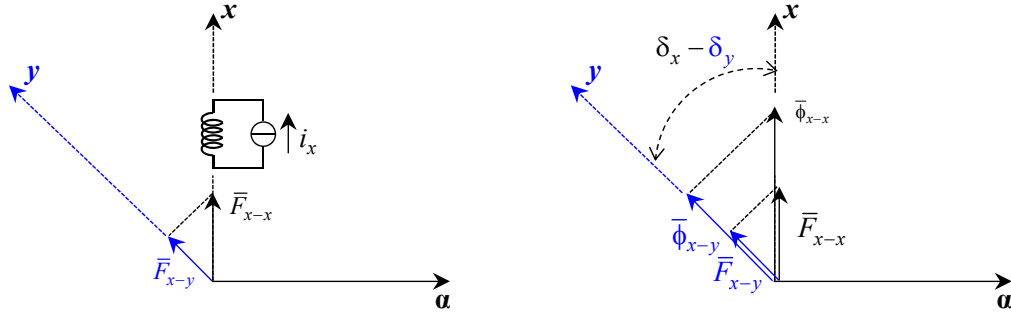


Figure 4.2 Draft for the mutual inductance and magnetic flux computations.

where:

- $N_x$  and  $N_y$  represent the number of turns of the windings  $x$  and  $y$ ;
- $\delta_x$  and  $\delta_y$  denote the position of the magnetic axis belonging to the  $x$  and  $y$  phase windings (see Fig. 4.2).

Based on Eq. (4.3) the matrix components of  $[M_{sk-sz}]$  and  $[M_{sk-r}]$  can be computed.

Regarding the mutual inductance between two generic three-phase windings the same approach used for the computation of the mutual inductance between two generic phase windings can be used. Considering that each three-phase winding set is characterized by a unique number of turns the number turns  $N_x$  characterizes the winding  $x$ , while  $N_y$  is the turns number of the winding  $y$ . Introducing the displacement  $\theta_{sk-sz}$  between the stator phase windings of  $k$ -set and the stator phase windings of  $z$ -set with an angular difference  $\Delta\theta_{sk-sz} = \theta_{sk} - \theta_{sz}$ , the mutual magnetizing matrix inductance between two generic three-phase windings is computed as:

$$[M_{sk-sz}] = \frac{N_{sk} \cdot N_{sz}}{\mathcal{R}_{eq}} \cdot \begin{bmatrix} \cos(\Delta\theta_{sk-sz}) & \cos\left(\Delta\theta_{sk-sz} - \frac{2}{3}\pi\right) & \cos\left(\Delta\theta_{sk-sz} - \frac{4}{3}\pi\right) \\ \cos\left(\Delta\theta_{sk-sz} + \frac{2}{3}\pi\right) & \cos(\Delta\theta_{sk-sz}) & \cos\left(\Delta\theta_{sk-sz} - \frac{2}{3}\pi\right) \\ \cos\left(\Delta\theta_{sk-sz} - \frac{2}{3}\pi\right) & \cos\left(\Delta\theta_{sk-sz} + \frac{2}{3}\pi\right) & \cos(\Delta\theta_{sk-sz}) \end{bmatrix} \quad (4.4)$$

Regarding the matrix  $[M_{sk-r}]$ , similarly to Eq. (4.4) and defining the angular difference  $\Delta\theta_{sk-r} = \theta_{sk} - \theta_r$  and the rotor turn number  $N_r$ , can be computed as:

$$[M_{sk-r}] = \frac{N_{sk} \cdot N_r}{\mathcal{R}_{eq}} \cdot \begin{bmatrix} \cos(\Delta\theta_{sk-r}) & \cos\left(\Delta\theta_{sk-r} - \frac{2}{3}\pi\right) & \cos\left(\Delta\theta_{sk-r} - \frac{4}{3}\pi\right) \\ \cos\left(\Delta\theta_{sk-r} + \frac{2}{3}\pi\right) & \cos(\Delta\theta_{sk-r}) & \cos\left(\Delta\theta_{sk-r} - \frac{2}{3}\pi\right) \\ \cos\left(\Delta\theta_{sk-r} - \frac{2}{3}\pi\right) & \cos\left(\Delta\theta_{sk-r} + \frac{2}{3}\pi\right) & \cos(\Delta\theta_{sk-r}) \end{bmatrix} \quad (4.5)$$

At this point, all matrices in Eq. (4.1) are defined for the stator magnetic model.

### Rotor magnetic model

The rotor magnetic model is a relationships between the current and flux of the rotor cage. Based on the hypothesis, the rotor magnetic model consists of three equations. The magnetic model of the rotor winding is written as:

$$\bar{\lambda}_{abc,r} = L_{l,r}^s \cdot \bar{i}_{abc,r} + \sum_{z=1}^n \left( [M_{r-sz}] \cdot \bar{i}_{abc,sz} + [M_{r-r}] \cdot \bar{i}_{abc,r} \right) \quad (4.6)$$

where:

- $\bar{\lambda}_{abc,r}$  stands for the rotor fluxes linkage for the three-phase rotor set in rotor phase coordinates;
- $L_{l,r}^s$  is the self-leakage phase inductance of the equivalent rotor winding;
- $[M_{r-sz}]$  is the  $3 \times 3$  mutual magnetizing inductance matrix between the rotor phase windings and the stator phase windings of the  $z$ -set;
- $[M_{r-r}]$  is the  $3 \times 3$  self-mutual magnetizing inductance matrix of the rotor phase windings.

Following Eq. (4.3), the mutual magnetizing inductance  $[M_{r-sz}]$  and self-mutual magnetizing inductance  $[M_{r-r}]$  matrices can be defined as:

$$[M_{r-sz}] = \frac{N_r \cdot N_{sz}}{\mathcal{R}_{eq}} \cdot \begin{bmatrix} \cos(\Delta\theta_{r-sz}) & \cos\left(\Delta\theta_{r-sz} - \frac{2}{3}\pi\right) & \cos\left(\Delta\theta_{r-sz} - \frac{4}{3}\pi\right) \\ \cos\left(\Delta\theta_{r-sz} + \frac{2}{3}\pi\right) & \cos(\Delta\theta_{r-sz}) & \cos\left(\Delta\theta_{r-sz} - \frac{2}{3}\pi\right) \\ \cos\left(\Delta\theta_{r-sz} - \frac{2}{3}\pi\right) & \cos\left(\Delta\theta_{r-sz} + \frac{2}{3}\pi\right) & \cos(\Delta\theta_{r-sz}) \end{bmatrix}$$

$$[M_{r-r}] = \frac{N_r \cdot N_r}{\mathcal{R}_{eq}} \cdot \begin{bmatrix} \cos(\Delta\theta_{r-r}) & \cos\left(\Delta\theta_{r-r} - \frac{2}{3}\pi\right) & \cos\left(\Delta\theta_{r-r} - \frac{4}{3}\pi\right) \\ \cos\left(\Delta\theta_{r-r} + \frac{2}{3}\pi\right) & \cos(\Delta\theta_{r-r}) & \cos\left(\Delta\theta_{r-r} - \frac{2}{3}\pi\right) \\ \cos\left(\Delta\theta_{r-r} - \frac{2}{3}\pi\right) & \cos\left(\Delta\theta_{r-r} + \frac{2}{3}\pi\right) & \cos(\Delta\theta_{r-r}) \end{bmatrix} \quad (4.7)$$

where:

- $\Delta\theta_{r-sz} = \theta_r - \theta_{sz}$  is the angular difference among the magnetic axes of the first phases belonging to the rotor winding and the stator **z**-set;
- $\Delta\theta_{r-r} = \theta_r - \theta_r = 0$ .

At this point the magnetic model of a multiple three-phase IM machine is completely defined by  $3 \cdot (n + 1)$  equations (i.e. 12-phase IM in quadruple configuration is described by 15 equations for the magnetic model).

### Stator electric model

The stator electric model consists of the equation system with the relationship of the stator phases, composed by  $3 \cdot n$  equations. Using the passive sign convention, the stator electric model for a generic set  $k$  can be expressed as:

$$\bar{v}_{abc,sk} = R_{sk} \cdot \bar{i}_{abc,sk} + \frac{d}{dt} \bar{\lambda}_{abc,sk} \quad (4.8)$$

where:

- $\bar{v}_{abc,sk}$  stands for the vector of the stator voltages for the three-phase set  $k$  defined in the stator phase coordinates  $(abc)_k$ ;
- $R_{sk}$  stands for the phase resistance for the three-phase set  $k$ .

### Rotor electric model

The rotor electric model consists of the relationships between flux and voltage of the rotor cage, modelled as an equivalent three-phase winding. Using the passive sign convention, the rotor magnetic model, composed by 3 equations, is written as:

$$\bar{v}_{abc,r} = R_r \cdot \bar{i}_{abc,r} + \frac{d}{dt} \bar{\lambda}_{abc,r} \quad (4.9)$$

where:

- $\bar{v}_{abc,r}$  stands for the the rotor voltages vector for the three-phase rotor squirrel cage, which are equal to zero  $\bar{v}_{abc,r} = \bar{0}$  considering the equivalent rotor winding in short-circuit;
- $R_r$  stands for the phase resistance of three-phase rotor.

As for magnetic equations, the electrical system equation of multi-three-phase IM consists of  $3 \cdot (n + 1)$  equations.

### Electromagnetic model

The merge of stator Eq. (4.1) and rotor Eq. (4.180) magnetic models allows to write the complete magnetic model as:

$$\begin{Bmatrix} \bar{\lambda}_{abc,s1} \\ \dots \\ \bar{\lambda}_{abc,sk} \\ \bar{\lambda}_{abc,sn} \\ \bar{\lambda}_{abc,r} \end{Bmatrix} = [L_l] \cdot \begin{Bmatrix} \bar{i}_{abc,s1} \\ \dots \\ \bar{i}_{abc,sk} \\ \bar{i}_{abc,sn} \\ \bar{i}_{abc,r} \end{Bmatrix} + [M] \cdot \begin{Bmatrix} \bar{i}_{abc,s1} \\ \dots \\ \bar{i}_{abc,sk} \\ \bar{i}_{abc,sn} \\ \bar{i}_{abc,r} \end{Bmatrix} \quad (4.10)$$

where:

- $[L_l]$  is defined in Eq. (4.11), including the leakage stator and rotor inductances;
- $[M]$  is defined in Eq. (4.12), including the magnetizing inductances between different stator winding sets and stator-rotor coupling.

$$[L_l] = \begin{bmatrix} L_{l,s1} \cdot [I]_{3 \times 3} & [0]_{3 \times 3} & \dots & [0]_{3 \times 3} & [0]_{3 \times 3} \\ [0]_{3 \times 3} & L_{l,s2} \cdot [I]_{3 \times 3} & \dots & [0]_{3 \times 3} & [0]_{3 \times 3} \\ \dots & \dots & \dots & \dots & \dots \\ [0]_{3 \times 3} & [0]_{3 \times 3} & \dots & L_{l,sn} \cdot [I]_{3 \times 3} & [0]_{3 \times 3} \\ [0]_{3 \times 3} & [0]_{3 \times 3} & \dots & [0]_{3 \times 3} & L_{l,r} \cdot [I]_{3 \times 3} \end{bmatrix} \quad (4.11)$$

$$[M] = \begin{bmatrix} [M_{s1-s1}] & [M_{s1-s2}] & \dots & [M_{s1-sn}] & [M_{s1-r}] \\ [M_{s2-s1}] & [M_{s2-s2}] & \dots & [M_{s2-sn}] & [M_{s2-r}] \\ \dots & \dots & \dots & \dots & \dots \\ [M_{s3-s1}] & [M_{s3-s2}] & \dots & [M_{s3-sn}] & [M_{sn-r}] \\ [M_{r-s1}] & [M_{r-s2}] & \dots & [M_{r-sn}] & [M_{r-r}] \end{bmatrix} \quad (4.12)$$

The matrices  $[I]_{3 \times 3}$  and  $[0]_{3 \times 3}$  are defined as:

$$[I]_{3 \times 3} = \begin{bmatrix} 1 & 0 & 0 \\ 0 & 1 & 0 \\ 0 & 0 & 1 \end{bmatrix}, \quad [0]_{3 \times 3} = \begin{bmatrix} 0 & 0 & 0 \\ 0 & 0 & 0 \\ 0 & 0 & 0 \end{bmatrix} \quad (4.13)$$

The stator and rotor electric model, merging Eq. (4.8) and Eq. (4.9), is written as:

$$\begin{Bmatrix} \bar{v}_{abc,s1} \\ \dots \\ \bar{v}_{abc,sk} \\ \bar{v}_{abc,sn} \\ \bar{v}_{abc,r} \end{Bmatrix} = [R] \cdot \begin{Bmatrix} \bar{i}_{abc,s1} \\ \dots \\ \bar{i}_{abc,sk} \\ \bar{i}_{abc,sn} \\ \bar{i}_{abc,r} \end{Bmatrix} + \frac{d}{dt} \cdot \begin{Bmatrix} \bar{\lambda}_{abc,s1} \\ \dots \\ \bar{\lambda}_{abc,sk} \\ \bar{\lambda}_{abc,sn} \\ \bar{\lambda}_{abc,r} \end{Bmatrix} \quad (4.14)$$

The  $[R]$  matrix is defined as:

$$[R] = \begin{bmatrix} R_{s1} \cdot [I]_{3 \times 3} & [0]_{3 \times 3} & \dots & [0]_{3 \times 3} & [0]_{3 \times 3} \\ [0]_{3 \times 3} & R_{s2} \cdot [I]_{3 \times 3} & \dots & [0]_{3 \times 3} & [0]_{3 \times 3} \\ \dots & \dots & \dots & \dots & \dots \\ [0]_{3 \times 3} & [0]_{3 \times 3} & \dots & R_{sn} \cdot [I]_{3 \times 3} & [0]_{3 \times 3} \\ [0]_{3 \times 3} & [0]_{3 \times 3} & \dots & [0]_{3 \times 3} & R_r \cdot [I]_{3 \times 3} \end{bmatrix} \quad (4.15)$$



Finally for a compact form, the following variables  $\{\bar{V}\}$ ,  $\{\bar{I}\}$ , and  $\{\bar{\Lambda}\}$  are introduced and the compact form of electromagnetic model of multi-three-phase IM is reported:

$$\begin{aligned} \{\bar{V}\} &= \begin{Bmatrix} \bar{v}_{abc,s1} \\ \dots \\ \bar{v}_{abc,sk} \\ \bar{v}_{abc,sn} \\ \bar{v}_{abc,r} \end{Bmatrix}; \quad \{\bar{I}\} = \begin{Bmatrix} \bar{i}_{abc,s1} \\ \dots \\ \bar{i}_{abc,sk} \\ \bar{i}_{abc,sn} \\ \bar{i}_{abc,r} \end{Bmatrix}; \quad \{\bar{\Lambda}\} = \begin{Bmatrix} \bar{\lambda}_{abc,s1} \\ \dots \\ \bar{\lambda}_{abc,sk} \\ \bar{\lambda}_{abc,sn} \\ \bar{\lambda}_{abc,r} \end{Bmatrix} \Rightarrow \\ &\Rightarrow \begin{cases} \{\bar{V}\} = [R] \cdot \{\bar{I}\} + \frac{d}{dt} \{\bar{\Lambda}\} \\ \{\bar{\Lambda}\} = [L_l] \cdot \{\bar{I}\} + [M] \cdot \{\bar{I}\} \end{cases} \end{aligned} \quad (4.16)$$

#### 4.1.1 Electromagnetic model

The electromagnetic torque generated by the the machine can be computed with different approach. A straightforward method consists to energetic balance. For each differential time  $dt$  the energetic balance is written as [119]:

$$dE = dE_M + dE_T + dE_W, \quad \forall dt \quad (4.17)$$

where:

- $dE$  stands for electrical energy infinitesimal variation;
- $dE_M$  stands for mechanical energy infinitesimal variation;
- $dE_T$  stands for thermal energy infinitesimal variation;
- $dE_W$  stands for magnetic field energy infinitesimal variation;

The infinitesimal variations of electrical energy can be computed as in Eq. (4.18), introducing the compact form of Eq. (4.16).

$$dE = \{\bar{I}\}^T \cdot \{\bar{V}\} \cdot dt \quad (4.18)$$

The infinitesimal variations of mechanical energy can be computed as in Eq. (4.19), using the temporal integration of the mechanical power generated

by the machine electromagnetic torque  $T_{em}$ :

$$dE_M = T_{em} \cdot d\theta_m, \quad d\theta_m = \frac{d\theta}{p} \quad (4.19)$$

where:

- $\theta_m$  is the mechanical rotor position;
- $\theta$  is the electrical rotor position;
- $p$  is the number of the machine pole pairs.

About the thermal energy it is generated by the Joule losses of the machine due to the ideal iron for initial assumption (absence of losses and magnetic saturation phenomena) and  $dE_T$  can be computed as:

$$dE_T = \{\bar{I}\}^T \cdot [R] \cdot \{\bar{I}\} \cdot dt \quad (4.20)$$

Finally the infinitesimal variations of the magnetic field energy is computed as temporal derivation of the power stored in the machine magnetic field:

$$dE_W = d\left(\frac{1}{2} \cdot \{\bar{I}\}^T \cdot ([L_l] + [M]) \cdot \{\bar{I}\}\right) \quad (4.21)$$

By replacing the Eq. (4.18) - Eq. (4.21) in Eq. (4.17) the energetic balance is expressed as:

$$\{\bar{I}\}^T \cdot \{\bar{V}\} \cdot dt = \frac{T_{em}}{p} \cdot \frac{d\theta_r}{dt} + \{\bar{I}\}^T \cdot [R] \cdot \{\bar{I}\} \cdot dt + d\left(\frac{1}{2} \cdot \{\bar{I}\}^T \cdot ([L_l] + [M]) \cdot \{\bar{I}\}\right) \quad (4.22)$$

where all symbols are consistent with the previous definition and the matrices  $[L_l]$  and  $[M]$  are defined in Eq. (4.11) and Eq. (4.62). Using some mathematical manipulations and Eq. (4.16), the electromagnetic torque is expressed as:

$$T_{em} = \frac{1}{2} \cdot p \cdot \{\bar{I}\}^T \cdot \frac{d}{dt} ([L_l] + [M]) \cdot \{\bar{I}\} \quad (4.23)$$

Based on the matrices in Eq. (4.11) and Eq. (4.12) and considering the magnetic linearity as initial assumption, the electromagnetic torque of multi-

three-phase machine is expressed as:

$$T_{em} = p \cdot \sum_{k=1}^n \left( \left( \bar{i}_{abc,sk} \right)^T \cdot \frac{d}{dt} [M_{sk-r}] \cdot \bar{i}_{abc,r} \right) \quad (4.24)$$

The electromagnetic torque is the sum of the contributions of the  $n=1, \dots, k$  stator sets interacting with the three-phase rotor.

### 4.1.2 Mechanical model

The mechanical model of an electrical machine is expressed by the torque balance on the mechanical shaft Eq. (4.25) and temporal integration of the mechanical speed  $\omega_m$  to get the mechanical rotor position  $\theta_m$  Eq. (4.223).

$$T_{em} - T_L = \frac{J_{eq}}{p} \cdot \frac{d\omega_m}{dt} \quad (4.25)$$

where:

- $T_L$  is the overall load torque, including eventual friction contributions;
- $J_{eq}$  is the overall momentum of inertia around the axis of rotation, considering both the machine's rotor and mechanical load;
- $\omega_m$  is the mechanical speed of the rotor shaft;
- $\omega_r$  is the electrical speed of the rotor shaft.

The temporal integration of the mechanical speed to get the mechanical rotor position  $\theta_r$  is written as:

$$\omega_m = \frac{1}{p} \cdot \frac{d\theta_r}{dt}, \quad \left\{ \begin{array}{l} \omega = \frac{d\theta_r}{dt} \\ d\theta_m = \frac{d\theta_r}{p} \end{array} \right. \quad (4.26)$$

The computation of the electromagnetic and mechanical models allows to define the electromechanical machine model for the energy conversion processes. The energy conversion model in phase coordinates is composed as:

$$\left\{ \begin{array}{l} \{\bar{V}\} = [R] \cdot \{\bar{I}\} + \frac{d}{dt} \{\bar{\Lambda}\} \\ \{\bar{\Lambda}\} = [L_l] \cdot \{\bar{I}\} + [M] \cdot \{\bar{I}\} \\ T_{em} = p \cdot \sum_{k=1}^n \left( \left( \bar{i}_{abc,sk} \right)^T \cdot \frac{d}{dt} [M_{sk-r}] \cdot \bar{i}_{abc,r} \right) \\ T_{em} - T_L = \frac{J_{eq}}{p} \cdot \frac{d\omega_r}{dt} \\ \omega = \frac{d\theta_r}{dt} \end{array} \right. \quad (4.27)$$

The equation system Eq. (4.27) represents the complete electromechanical model of a multi-three-phase IM in phase coordinates. It is described as follows:

- $3 \cdot n$  stator magnetic equations;
- 3 rotor magnetic equations;
- $3 \cdot n$  stator electrical equations;
- 3 rotor electrical equations;
- 1 electromagnetic torque equation;
- 2 mechanical equations .

### Squirrel cage rotor model in phase coordinates with MS and VSD approaches

The electromechanical model in phase coordinates can be manipulated using the reference transformations, similarly to the three-phase counterparts. This model in phase variables can be used for MS and VSD model approaches [115]. However, the procedure for the computation of the electromagnetic model in phase coordinates using the VSD approach is similar to the one presented before, which is typical for MS approach.

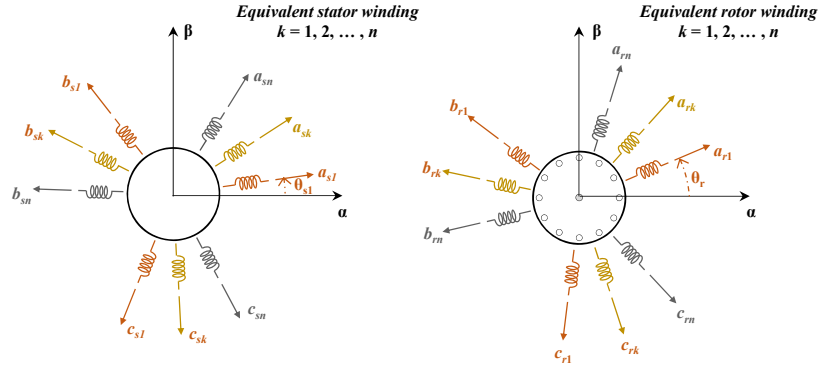


Figure 4.3 Equivalent VSD magnetic scheme of a multi-three-phase squirrel cage IM: multi-three phase stator (left) and multi-three phase rotor (right).

In VSD approach the squirrel cage rotor is modelled as an equivalent multi-three-phase winding, thus emulating the stator winding configuration, as shown in Fig. 4.3 [120]. Instead, using the MS approach the rotor winding is modelled as a three-phase winding, as presented before [60]. By doing so, the VSD magnetic model of a multi-three-phase IM machine in phase coordinates is composed by  $3 \cdot (2n)$  algebraic equations, containing the relationships between the current and flux of the phase windings. The same consideration can be done for the electric model of a multi-three-phase IM machine:  $3 \cdot (2n)$  differential equations, containing all the flux-to-voltage relationships of the phase windings with VSD approach. However, based on the assumption of multi-three-phase rotor windings, which is a virtual definition of the three-phase rotor, an equivalent number of turns of each virtual rotor phase winding must be introduced as [59]:

$$N_r^{VSD} = \frac{N_r}{\sqrt{3}} \quad (4.28)$$

The definition of  $N_r^{VSD}$  allows the computation of:

- The matrix  $[M_{sk-rz}]$  in Eq. (4.29) useful for the stator and rotor magnetic models (see Eq. (4.30)) which is the  $3 \times 3$  mutual magnetizing inductance matrix between the stator phase windings of  $k$ -set and the rotor phase windings of the  $z$ -rotor winding;

- The matrix  $[M_{rk-sz}]$  is defined as the  $3 \times 3$  mutual magnetizing inductance matrix between the rotor phase windings of  $k$ -set and the stator phase windings of the  $z$ -set, reported in Eq. (4.29);
- The matrix  $[M_{rkrz}]$  is the  $3 \times 3$  mutual magnetizing inductance matrix between the rotor phase windings of  $k$ -set and the rotor phase windings of the  $z$ -set.

Just to clarify the difference between rotor model with two different approaches, the stator magnetic equation using the VSD approach, introducing Eq. (4.28) is expressed as the first equation in Eq. (4.30). As example, the matrix  $[M_{sk-rz}]$  is computed as:

$$[M_{sk-rz}] = \frac{N_{sk} \cdot N_r^{VSD}}{\mathcal{R}_{eq}} \cdot \begin{bmatrix} \cos(\Delta\theta_{sk-rz}) & \cos\left(\Delta\theta_{sk-rz} - \frac{2}{3}\pi\right) & \cos\left(\Delta\theta_{sk-rz} - \frac{4}{3}\pi\right) \\ \cos\left(\Delta\theta_{sk-rz} + \frac{2}{3}\pi\right) & \cos(\Delta\theta_{sk-rz}) & \cos\left(\Delta\theta_{sk-rz} - \frac{2}{3}\pi\right) \\ \cos\left(\Delta\theta_{sk-rz} - \frac{2}{3}\pi\right) & \cos\left(\Delta\theta_{sk-rz} + \frac{2}{3}\pi\right) & \cos(\Delta\theta_{sk-rz}) \end{bmatrix} \quad (4.29)$$

where  $\Delta\theta_{sk-rk} = \theta_{sk} - \theta_{rk}$  is the angular difference among the magnetic axes of the first phases belonging to the stator  $k$ -set and the rotor  $z$ -set.

An overall electromagnetic model of the machine using the VSD approach in phase-coordinates is expressed as in Eq. (4.30), where the generic variables  $(v, i, \lambda)$  is a vector having a dimension equal to the total number of phases  $m = 3 \cdot n$ .

$$\left\{ \begin{array}{l} s - \lambda i : \quad \bar{\lambda}_s = L_{l,s} \cdot \bar{i}_s + [L_{ss}] \cdot \bar{i}_s + [L_{sr}] \cdot \bar{i}_r^r \\ r - \lambda i : \quad \bar{\lambda}_r^r = L_{l,r}^r \cdot \bar{i}_r^r + [L_{rs}] \cdot \bar{i}_s + [L_{rr}] \cdot \bar{i}_r^r \\ s - vi : \quad \bar{v}_s = R_s \cdot \bar{i}_s + \frac{d}{dt} \bar{\lambda}_s \\ r - vi : \quad \bar{v}_r^r = R_r \cdot \bar{i}_r^r + \frac{d}{dt} \bar{\lambda}_r^r \end{array} \right. \quad (4.30)$$

The matrices in Eq. (4.30) are defined as in Eq. (4.31) and the matrices  $[M_{sk/rk-sk/rk}]$  are computed as reported for example in Eq. (4.29) for  $sk - rk$ .

$$\begin{aligned}
 [L_{ss}] &= \begin{bmatrix} [M_{s1-s1}] & [M_{s1-s2}] & \dots & [M_{s1-sn}] \\ [M_{s2-s1}] & [M_{s2-s2}] & \dots & [M_{s2-sn}] \\ \dots & \dots & \dots & \dots \\ [M_{sn-s1}] & [M_{sn-s1}] & \dots & [M_{sn-sn}] \end{bmatrix} \\
 [L_{sr}] &= \begin{bmatrix} [M_{s1-r1}] & [M_{s1-r2}] & \dots & [M_{s1-rn}] \\ [M_{s2-r1}] & [M_{s2-r2}] & \dots & [M_{s2-rn}] \\ \dots & \dots & \dots & \dots \\ [M_{sn-r1}] & [M_{sn-r1}] & \dots & [M_{sn-rn}] \end{bmatrix} \\
 [L_{rr}] &= \begin{bmatrix} [M_{r1-r1}] & [M_{r1-r2}] & \dots & [M_{r1-rn}] \\ [M_{r2-r1}] & [M_{r2-r2}] & \dots & [M_{r2-rn}] \\ \dots & \dots & \dots & \dots \\ [M_{rn-r1}] & [M_{rn-r1}] & \dots & [M_{rn-rn}] \end{bmatrix}
 \end{aligned} \tag{4.31}$$

Finally, in Eq. (4.32) a compact a compact is introduced for stator and rotor variables:

$$\left\{ \begin{array}{l} \bar{V}_s = \begin{Bmatrix} \bar{v}_{abc,s1} \\ \dots \\ \bar{v}_{abc,sk} \\ \bar{v}_{abc,sm} \end{Bmatrix} \\ \bar{V}_r = \begin{Bmatrix} \bar{v}_{abc,r1} \\ \dots \\ \bar{v}_{abc,rk} \\ \bar{v}_{abc,rm} \end{Bmatrix} \end{array} \right\} \Rightarrow \{\bar{V}\} = \begin{Bmatrix} \bar{V}_s \\ \bar{V}_r \end{Bmatrix} \quad (4.32)$$

$$\bar{I} = \begin{Bmatrix} \bar{I}_s \\ \bar{I}_r \end{Bmatrix}; \quad \bar{\Lambda} = \begin{Bmatrix} \bar{\Lambda}_s \\ \bar{\Lambda}_s \end{Bmatrix}$$

The total machine model includes also the mechanical model which is not affected by the employed modelling approach. Therefore, the electromechanical VSD model of the machine in phase coordinates is defined as:

$$\left\{ \begin{array}{l} \{\bar{V}\} = [R] \cdot \{\bar{I}\} + \frac{d}{dt} \{\bar{\Lambda}\} \\ \{\bar{\Lambda}\} = [L] \cdot \{\bar{I}\} \\ T_{em} = p \cdot \{\bar{I}_s\}^T \cdot \frac{d[L_{SR}]}{dt} \cdot \{\bar{I}_r\} \\ T_{em} - T_L = \frac{J_{eq}}{p} \cdot \frac{d\omega_r}{dt} \\ \omega_r = \frac{d\theta_r}{dt} \end{array} \right. \quad (4.33)$$

The new matrix  $[L]$  in Eq. (4.33) is defined as:

$$[L] = \begin{bmatrix} L_{l,s} \cdot [I]_{3n \times 3n} + [L_{ss}] & [L_{sr}] \\ [L_{rs}] & L_{l,r} \cdot [I]_{3n \times 3n} + [L_{rr}] \end{bmatrix} \quad (4.34)$$



## 4.2 Multi-Stator (MS) modelling approach

The MS modeling aims at computing the state-space model of each machine set, which is essential for the decoupling model. Like for the three-phase machines, the computation of the electromechanical model in the stationary  $\alpha\beta$  frame allows for reducing the equation system complexity with more manageable formulations. It requires the application of the general three-phase Clarke transformation to get the machine model in the stationary  $\alpha\beta$  frame, starting from the electromechanical model in phase-coordinates, reported in Eq. (4.27). Indeed, the formulation given in Eq. (4.10) is valid for both MS and VSD model approaches, except the squirrel cage rotor model reported in Section 4.1.2.

### 4.2.1 Electromechanical model in stationary coordinates

The electromechanical model in stationary coordinates  $\alpha\beta$  is defined in this section, considering the number of turns characterizing the three-phase stator sets identical to each other, as reported in Eq. (4.35). This condition is typical for the multiple three-phase machines as a uniform design of the three-phase winding sets is performed [47].

$$N_{sk} = N_{sn} = N_s, \quad k = 1, \dots, n \quad (4.35)$$

The rotor variables are redefined to the stator, introducing a transformation ratio between the stator and rotor windings:

$$t_{sr} = \frac{N_s}{N_r} \quad (4.36)$$

Based on Eq. (4.37), the new rotor variables can be defined to the  $k$ -set stator as:

$$\begin{aligned} \bar{i}_{abc,r}^s &= \frac{1}{t_{sr}} \cdot \bar{i}_{abc,r} \\ \bar{v}_{abc,r}^s &= \frac{1}{t_{sr}} \cdot \bar{v}_{abc,r} \\ \bar{\lambda}_{abc,r}^s &= \frac{1}{t_{sr}} \cdot \bar{\lambda}_{abc,r} \end{aligned} \quad (4.37)$$

For each generic stator set  $k$  ( $k = 1, 2, \dots, n$ ), the general Clarke transformation (see Eq. (4.38)) is applied as in Eq. (4.39): each variable defined in the  $k$ -set phase coordinates  $abc_k$  is computed in stationary  $\alpha\beta 0$  components using Eq. (4.38) with amplitude-invariant transformation for the stator  $k$ -set.

$$[C_{sk}] = \begin{bmatrix} \cos(\theta_{sk}) & \cos\left(\theta_{sk} + \frac{2}{3}\pi\right) & \cos\left(\theta_{sk} + \frac{4}{3}\pi\right) \\ \sin(\theta_{sk}) & \sin\left(\theta_{sk} + \frac{2}{3}\pi\right) & \sin\left(\theta_{sk} + \frac{4}{3}\pi\right) \\ 1/2 & 1/2 & 1/2 \end{bmatrix} \quad (4.38)$$

The angle  $\theta_{sk}$  is defined as the position of the  $k$ -set first phase  $a_{sk}$  to the  $\alpha$ -axis, assumed coincident with the first phase of the first set  $a_{s1}$ , as shown in Fig. 4.4.

Using the rotor position  $\theta_r$  the transformation from  $abc_r$  to  $\alpha\beta 0_r$  can be applied to evaluate the rotor variables in stationary coordinates, as reported in Eq. (4.39).

Consider a generic stator or rotor variable, called  $\bar{z}$  (i.e.  $v, i, \lambda$ ) in  $\alpha\beta 0$  coordinates is evaluated by applying Eq. (4.39) as:

$$\begin{aligned} \bar{z}_{\alpha\beta 0,sk} &= [C_{sk}] \cdot \bar{z}_{abc,sk}; & \bar{z}_{\alpha\beta 0,r}^s &= [C_r] \cdot \bar{z}_{abc,r}; \\ \bar{z}_{abc,sk} &= [C_{sk}]^{-1} \cdot \bar{z}_{\alpha\beta 0,sk}; & \bar{z}_{abc,r}^s &= [C_r]^{-1} \cdot \bar{z}_{\alpha\beta 0,r}; \end{aligned} \quad (4.39)$$

### Stator magnetic model

The magnetic model of the stator  $k$ -set having rotor variables defined in the  $k$ -set stator coordinates by replacing Eq. (4.37) in Eq. (4.1) is obtained as:

$$\begin{aligned} \bar{\lambda}_{abc,sk} &= L_{l,s} \cdot \bar{i}_{abc,sk} + \sum_{z=1}^n \left( [M_{sk-sz}] \cdot \bar{i}_{abc,sz} \right) + [M_{sk-r}] \cdot \bar{i}_{abc,r}, \quad t_{sr} = \frac{N_s}{N_r} \Rightarrow \\ \Rightarrow \bar{\lambda}_{abc,sk} &= L_{l,s} \cdot \bar{i}_{abc,sk} + \sum_{z=1}^n \left( [M_{sk-sz}] \cdot \bar{i}_{abc,sz} \right) + [M_{sk-r}] \cdot \left( t_{sr} \cdot \bar{i}_{abc,r}^s \right) \end{aligned} \quad (4.40)$$

The computation of the  $k$ -set stator magnetic model in terms of stationary  $\alpha\beta 0$  variables is obtained by applying the three-phase Clarke transformation

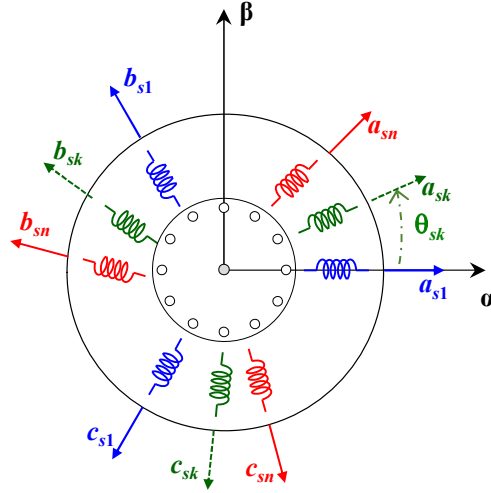


Figure 4.4 Magnetic axes angle displacement of the multi-three-phase IM in one electrical revolution.

in Eq. (4.38) or the stator  $k$ -set and for the rotor set as:

$$\begin{aligned}
 [C_{sk}] \cdot \bar{\lambda}_{abc,sk} &= [C_{sk}] \cdot (L_{l,s} \cdot \bar{i}_{abc,sk}) + \left( \sum_{z=1}^n [C_{sk}] \cdot ([M_{sk-sz}] \cdot \bar{i}_{abc,sz}) \right) + \dots \\
 &\quad \dots + [C_{sk}] \cdot ([M_{sk-r}] \cdot (t_{sr} \cdot \bar{i}_{abc,r}^s)) \Rightarrow \\
 \Rightarrow \bar{\lambda}_{\alpha\beta 0,sk} &= L_{l,s} \cdot \bar{i}_{\alpha\beta 0,sk} + \left( \sum_{z=1}^n [C_{sk}] \cdot ([M_{sk-sz}] \cdot [C_{sk}]^{-1} \cdot \bar{i}_{\alpha\beta 0,sz}) \right) + \dots \\
 &\quad \dots + [C_{sk}] \cdot ([M_{sk-r}] \cdot (t_{sr} \cdot [C_r]^{-1} \cdot \bar{i}_{\alpha\beta 0,r}^s)) \Rightarrow \\
 \Rightarrow \bar{\lambda}_{\alpha\beta 0,sk} &= L_{l,s} \cdot \bar{i}_{\alpha\beta 0,sk} + \left( \sum_{z=1}^n ([M_{\alpha\beta 0,sk-sz}] \cdot \bar{i}_{\alpha\beta 0,sz}) \right) + ([M_{\alpha\beta 0,sk-r}] \cdot (t_{sr} \cdot \bar{i}_{\alpha\beta 0,r}^s)) \\
 &\quad (4.41)
 \end{aligned}$$

where:

- $[C_{sk}]$  is the three-phase Clarke transformation for the stator  $k$ -set based on the position angle  $\theta_{sk}$ ;
- $[C_r]$  is the three-phase Clarke transformation for the rotor set based on the rotor position angle  $\theta_r$ .

The new matrices  $[M_{\alpha\beta 0,sk-sz}]$  and  $[M_{\alpha\beta 0,sk-r}]$  are defined as:

$$\begin{aligned} [M_{\alpha\beta 0,sk-sz}] &= [C_{sk}] \cdot ([M_{sk-sz}] \cdot [C_{sk}]^{-1} \cdot \bar{i}_{\alpha\beta 0,sk}) = \frac{3}{2} \cdot \frac{N_s \cdot N_s}{\mathcal{R}_{eq}} \cdot \begin{bmatrix} 1 & 0 & 0 \\ 0 & 1 & 0 \\ 0 & 0 & 1 \end{bmatrix} \\ [M_{\alpha\beta 0,sk-r}] &= [C_{sk}] \cdot ([M_{sk-r}] \cdot ([C_r]^{-1} \cdot \bar{i}_{\alpha\beta 0,r}^s)) = \frac{3}{2} \cdot \frac{N_s \cdot N_r}{\mathcal{R}_{eq}} \cdot \begin{bmatrix} 1 & 0 & 0 \\ 0 & 1 & 0 \\ 0 & 0 & 1 \end{bmatrix} \end{aligned} \quad (4.42)$$

New coefficients are introduced for a more compact form defined as:

$$m_{ss} = \frac{3}{2} \cdot \frac{N_s \cdot N_s}{\mathcal{R}_{eq}}; \quad m_{sr} = \frac{3}{2} \cdot \frac{N_s \cdot N_r}{\mathcal{R}_{eq}} \quad (4.43)$$

By separating the  $\alpha\beta$  components from the zero-sequence 0 one, the stator magnetic model is written as:

$$\begin{cases} \bar{\lambda}_{\alpha\beta,sk} = L_{l,s} \cdot \bar{i}_{\alpha\beta,sk} + \sum_{z=1}^n (m_{ss} \cdot \bar{i}_{\alpha\beta,sz}) + m_{sr} \cdot t_{sr} \cdot \bar{i}_{\alpha\beta,r}^s \\ \lambda_{0,sk} = L_{l,s} \cdot i_{0,sk} \end{cases} \quad (4.44)$$

### Rotor magnetic model

Using the same procedure of the stator magnetic model, starting from Eq. (4.180) and by replacing Eq. (4.37), the rotor model in stationary reference frame is written as:

$$\begin{aligned} \bar{\lambda}_{abc,r}^s &= L_{l,r} \cdot t_{sr}^2 \cdot \bar{i}_{abc,r}^s + t_{sr} \cdot \sum_{z=1}^n ([M_{rs}] \cdot \bar{i}_{abc,sz}) + \dots \\ &\quad \dots + [M_{rr}] \cdot t_{sr}^2 \cdot \bar{i}_{abc,r}^s \Rightarrow \\ \Rightarrow \bar{\lambda}_{\alpha\beta 0,r}^s &= L_{l,r} \cdot t_{sr}^2 \cdot \bar{i}_{\alpha\beta 0,r}^s + t_{sr} \cdot \sum_{z=1}^n ([M_{r\alpha\beta,s0}] \cdot \bar{i}_{\alpha\beta 0,sz}) + \dots \\ &\quad \dots + [M_{r\alpha\beta,r0}] \cdot t_{sr}^2 \cdot \bar{i}_{\alpha\beta 0,r}^s \end{aligned} \quad (4.45)$$

where:

$$\begin{aligned} [M_{r\alpha\beta,s0}] &= [C_r] \cdot [M_{rs}] \cdot [C_r]^{-1} = \frac{3}{2} \cdot \frac{N_s \cdot N_r}{\mathcal{R}_{eq}} \cdot \begin{bmatrix} 1 & 0 & 0 \\ 0 & 1 & 0 \\ 0 & 0 & 0 \end{bmatrix} \\ [M_{r\alpha\beta,r0}] &= [C_r] \cdot [M_{rr}] \cdot [C_r]^{-1} = \frac{3}{2} \cdot \frac{N_r \cdot N_r}{\mathcal{R}_{eq}} \cdot \begin{bmatrix} 1 & 0 & 0 \\ 0 & 1 & 0 \\ 0 & 0 & 0 \end{bmatrix} \end{aligned} \quad (4.46)$$

By separating the  $\alpha\beta$  components from the zero-sequence 0 one, Eq. (4.47) is expressed as:

$$\begin{cases} \bar{\lambda}_{\alpha\beta,r}^s = L_{l,r}^s \cdot t_{sr}^2 \cdot \bar{i}_{\alpha\beta,r}^s + t_{sr} \cdot \sum_{z=1}^n (m_{rs} \cdot \bar{i}_{\alpha\beta,sz}) + m_{rr} \cdot t_{sr}^2 \cdot \bar{i}_{\alpha\beta,r}^s \\ \lambda_{0,r}^s = L_{l,r}^s \cdot t_{sr}^2 \cdot i_{0,r}^s \end{cases} \quad (4.47)$$

where:

$$\begin{aligned} m_{rs} &= \frac{3}{2} \cdot \frac{N_s \cdot N_r}{\mathcal{R}_{eq}} \\ m_{rr} &= \frac{3}{2} \cdot \frac{N_r \cdot N_r}{\mathcal{R}_{eq}} \end{aligned} \quad (4.48)$$

### Stator electric model

The computation in stationary reference frame  $\alpha\beta$  of the stator electric model is based on the application of the Clarke transformation in Eq. (4.38) to the Eq. (4.8), obtaining the following  $\alpha\beta$  and 0 components.

$$\begin{cases} \bar{v}_{\alpha\beta,sk} = R_s \cdot \bar{i}_{\alpha\beta,sk} + \frac{d}{dt} \bar{\lambda}_{\alpha\beta,sk} \\ v_{0,sk} = R_s \cdot i_{0,sk} + \frac{d}{dt} \lambda_{0,sk} \end{cases} \quad (4.49)$$

### Rotor electric model

The computation in stationary reference frame  $\alpha\beta 0$  of the rotor electrical model is based on the application of the Clarke transformation in Eq. (4.38) to the Eq. (4.50), using the rotor electrical position  $\theta_r$ .

$$\bar{v}_{\alpha\beta 0,r}^s = R_r^s \cdot t_{sr}^2 \cdot \bar{i}_{\alpha\beta 0,r}^s + \frac{d}{dt} \bar{\lambda}_{\alpha\beta 0,r}^s + [C_r] \cdot \left( \frac{d}{dt} [C_r]^{-1} \right) \cdot \bar{\lambda}_{\alpha\beta 0,r}^s \quad (4.50)$$

where:

$$[C_r] \cdot \left( \frac{d}{dt} [C_r]^{-1} \right) \cdot \bar{\lambda}_{\alpha\beta 0,r}^s = \frac{d\theta_r}{dt} \cdot \begin{bmatrix} 1 & 0 & 0 \\ 0 & 1 & 0 \\ 0 & 0 & 1 \end{bmatrix} \cdot \bar{\lambda}_{\alpha\beta 0,r}^s \quad (4.51)$$

By separating the  $\alpha\beta$  components from the zero-sequence 0 one, Eq. (4.50) is expressed as:

$$\begin{cases} \bar{v}_{\alpha\beta,r}^s = R_r^s \cdot t_{sr}^2 \cdot \bar{i}_{\alpha\beta,r}^s + \frac{d}{dt} \bar{\lambda}_{\alpha\beta,r}^s + \omega_r \cdot \begin{bmatrix} 0 & 1 \\ -1 & 0 \end{bmatrix} \bar{\lambda}_{\alpha\beta,r}^s \\ \bar{v}_{0,r}^s = R_r^s \cdot t_{sr}^2 \cdot \bar{i}_{0,r}^s + \frac{d}{dt} \bar{\lambda}_{0,r}^s \end{cases} \quad (4.52)$$

where the rotor electrical speed is introduced as:

$$\omega_r = \frac{d\theta_r}{dt} \quad (4.53)$$

The rotor electric model in stationary coordinates in Eq. (4.52) corresponds with the one of a conventional three-phase machine.

Finally, Eq. (4.40) - Eq. (4.52) can be further simplified by introducing the complex vector notation defined as in Eq. (4.54) for a generic variable  $i, v, \lambda$  as:

$$x_{\alpha\beta,sk} = x_{\alpha,sk} + jx_{\beta,sk}; \quad x_{\alpha\beta,r}^s = x_{\alpha,r}^s + jx_{\beta,r}^s; \quad (4.54)$$

Based on Eq. (4.54) the electromagnetic model in stationary coordinates  $\alpha\beta 0$  is summarized in Eq. (4.55) in complex vector notation, where  $s$  and  $r$  stand for stator and rotor, while  $\lambda i$  and  $v i$  stand for magnetic and electrical model, respectively.

$$\left\{ \begin{array}{l}
 s - \lambda i : \left\{ \begin{array}{l} \lambda_{\alpha\beta,sk} = L_{l,sk} \cdot i_{\alpha\beta,sk} + L_m \cdot \sum_{z=1}^n i_{\alpha\beta,sz} + L_m \cdot i_{\alpha\beta,r}^{sk} \\ \lambda_{0,sk} = L_{l,sk} \cdot i_{0,sk} \end{array} \right. \\
 r - \lambda i : \left\{ \begin{array}{l} \lambda_{\alpha\beta,r}^s = L_{l,r}^s \cdot i_{\alpha\beta,r}^s + L_m \cdot \sum_{z=1}^n i_{\alpha\beta,sz} + L_m \cdot i_{\alpha\beta,r}^s \\ \lambda_{0,r}^s = L_{l,r}^s \cdot i_{0,r}^s \end{array} \right. \\
 s - vi : \left\{ \begin{array}{l} v_{\alpha\beta,sk} = R_s \cdot i_{\alpha\beta,sk} + \frac{d}{dt} \lambda_{\alpha\beta,sk} \\ v_{0,sk} = R_s \cdot i_{0,sk} + \frac{d}{dt} \lambda_{0,sk} \end{array} \right. \\
 r - vi : \left\{ \begin{array}{l} v_{\alpha\beta,r}^s = R_r^s \cdot i_{\alpha\beta,r}^s + \frac{d}{dt} \lambda_{\alpha\beta,r}^s - j\omega_r \cdot \lambda_{\alpha\beta,r}^s \\ v_{0,r}^s = R_r^s \cdot i_{0,r}^s + \frac{d}{dt} \bar{\lambda}_{0,r}^s \end{array} \right.
 \end{array} \right. \quad (4.55)$$

where the *new* parameters are defines:

- the magnetizing inductance referred to the stator  $L_m$  is introduced as in Eq. (4.56);
- the rotor resistance and leakage inductance, referred to the stator by applying Eq. (4.35) and Eq. (4.36), reported in Eq. (4.57).

$$L_m = m_{ss} = m_{sr} = m_{ss} = m_{rr} \cdot t_{sr}^2 = \frac{3}{2} \cdot \frac{N_s^2}{\mathcal{R}_{eq}} \quad (4.56)$$

$$L_{l,r}^s = L_{l,r} \cdot t_{sr}^2; \quad R_{l,r}^s = R_{l,r} \cdot t_{sr}^2 \quad (4.57)$$

### Electromagnetic torque

The electromagnetic torque has been introduced in the previous in phase-coordinates and reported here for simplicity:

$$T_{em} = p \cdot \sum_{k=1}^n \left( \left( \bar{i}_{abc,sk} \right)^T \cdot \frac{d}{dt} [M_{sk-r}] \cdot \bar{i}_{abc,r}^r \right) \quad (4.58)$$

The rotor variables are referred to the  $k$ -set based on Eq. (4.36), obtaining the following equation:

$$T_{em} = p \cdot \sum_{k=1}^n \left( \left( \bar{i}_{abc,sk} \right)^T \cdot \frac{d}{dt} [M_{sk-r}] \cdot t_{sr} \cdot \bar{i}_{abc,r}^s \right) \quad (4.59)$$

The electromagnetic model in stationary reference frame  $\alpha\beta 0$  is evaluated by applying Eq. (4.39) as:

$$T_{em} = p \cdot \sum_{k=1}^n \left( \left( [C_{sk}]^{-1} \cdot \bar{i}_{\alpha\beta 0,sk} \right)^T \cdot \frac{d[M_{sk-r}]}{dt} \cdot t_{sr} \cdot ([C_r]^{-1} \bar{i}_{\alpha\beta 0,r}^r) \right) \quad (4.60)$$

In Eq. (4.60), the rotor current use is avoided based on Eq. (4.40), replacing as:

$$\begin{aligned} \lambda_{\alpha\beta,sk} &= m_{sr} \cdot t_{sr} \cdot i_{\alpha\beta,r}^s + L_{l,s} \cdot i_{\alpha\beta,sk} \cdot \sum_{z=1}^n (m_{ss} \cdot i_{\alpha\beta,sz}) \Rightarrow \\ &\Rightarrow m_{sr} \cdot t_{sr} \cdot i_{\alpha\beta,r}^s = \lambda_{\alpha\beta,sk} - L_{l,s} \cdot i_{\alpha\beta,sk} \cdot \sum_{z=1}^n (m_{ss} \cdot i_{\alpha\beta,sz}) \end{aligned} \quad (4.61)$$

Based on the manipulation in Eq. (4.62), the electromagnetic torque is written as in Eq. (4.63).

$$([C_{sk}]^{-1})^T \cdot \frac{d[M_{sk-r}]}{dt} \cdot [C_r]^{-1} = \frac{9}{4} \cdot \frac{N_{sk} \cdot N_r}{\mathcal{R}_{eq}} \cdot \begin{bmatrix} 0 & -1 & 0 \\ 1 & 0 & 0 \\ 0 & 0 & 0 \end{bmatrix} \quad (4.62)$$

$$\begin{aligned} T_{em} &= \frac{3}{2} \cdot p \cdot \sum_{k=1}^n \left( t_{sr} \cdot m_{sr} \cdot (i_{\alpha\beta,r}^s \times i_{\alpha\beta,sk}) \right) = \\ &= \frac{3}{2} \cdot p \cdot \sum_{k=1}^n \left( \lambda_{\alpha\beta,sk} \times i_{\alpha\beta,sk} - \sum_{z=1}^n (m_{ss} \cdot i_{\alpha\beta,sz} \times i_{\alpha\beta,sk}) \right) = \\ &= \frac{3}{2} \cdot p \cdot \sum_{k=1}^n \left( \lambda_{\alpha\beta,sk} \times i_{\alpha\beta,sk} \right) \end{aligned} \quad (4.63)$$

where  $X$  indicates the cross-product operator. The cross-product between  $i_{\alpha\beta,sz}$  and  $i_{\alpha\beta,sk}$  is equal to zero since the subspaces  $\alpha\beta$  are overlapping.

In Eq. (4.63) it is noted that the torque contribution is given by the cross-product between the stator  $k$ -set current vector and the rotor one, thus respecting the induction machine operating principle.



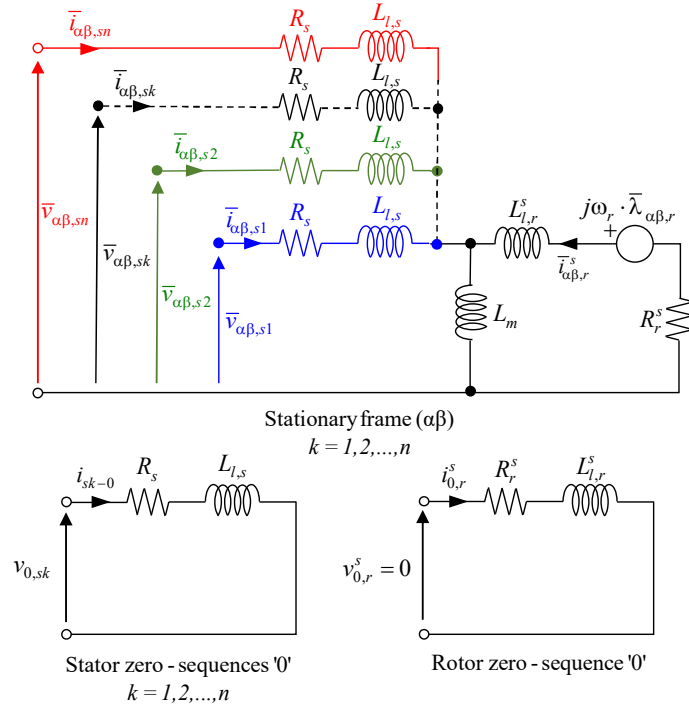


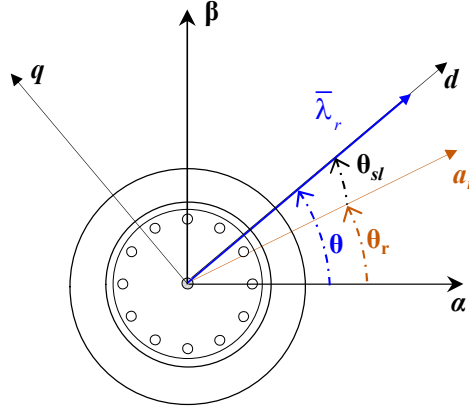
Figure 4.5 Equivalent MS circuit of a multi-three-phase IM in stationary  $\alpha\beta 0$  coordinates.

In conclusion, the electromagnetic torque in  $\alpha\beta 0$  is evaluated as:

$$T_{em} = \frac{3}{2} \cdot p \cdot \sum_{k=1}^n (\lambda_{\alpha\beta,sk} \times i_{\alpha\beta,sk}) \quad (4.64)$$

In Eq. (4.64) it is noted how the  $k$ -set torque contribution is given by the cross-product between the  $k$ -set flux-linkage vector and the  $k$ -set current vector. Using the MS approach, the modularity is preserved, as shown with the equivalent circuit in Fig. 4.5. The MS approach defines  $n$  stator flux-linkage vectors and  $n$  current vectors in  $n$  overlapped stationary  $\alpha\beta$  frame ( $n$  stands for the three-phase winding sets number). Each stator  $k$ -set interacts with the rotor, contributing to electromagnetic torque production. Instead, the zero-sequence components do not contribute to the electromechanical energy conversion, as the three-phase machine counterparts.

From now on the subscript  $s$  to identify the rotor parameters referred to the stator will be absent for manageable equations.

Figure 4.6 Rotating  $dq$  reference frame.

#### 4.2.2 Electromechanical model in rotating coordinates

The electromechanical model can be evaluated in rotating reference frame, like for three-phase counterparts, obtaining a more suitable formulations for mapping algorithm. The rotating  $d$ -axis is aligned with the rotor flux vector position  $\lambda_r$ , rotating at electrical speed  $\omega$  (different than rotor speed  $\omega_r$ ) as shown in Fig. 4.6.

The MS approach requires the application of the rotational transformation to get the machine model in the  $dq$  rotating frame, defined as:

$$[R(\theta)] = \begin{bmatrix} \cos(\theta) & \sin(\theta) \\ -\sin(\theta) & \cos(\theta) \end{bmatrix} \quad (4.65)$$

Starting from a generic variable  $z$  (i.e.,  $v$ ,  $i$ ,  $\lambda$ ) defined in the stationary  $\alpha\beta$  frame, the application of the rotational matrix allows the computation of the rotating components and vice versa as:

$$\begin{aligned} \bar{z}_{dq,sk} &= [R] \cdot \bar{z}_{\alpha\beta,sk}, & \bar{z}_{dq,r} &= [R] \cdot \bar{z}_{\alpha\beta,r} \\ \bar{z}_{\alpha\beta,sk} &= [R]^{-1} \cdot \bar{z}_{dq,sk}, & \bar{z}_{\alpha\beta,r} &= [R]^{-1} \cdot \bar{z}_{dq,r} \end{aligned} \quad (4.66)$$

### Stator magnetic equation

In Eq. (4.67) the stator magnetic model in stationary reference frame is reported for simplicity, without subscript  $s$  for the rotor variables to the stator side.

$$\lambda_{\alpha\beta,sk} = L_{l,sk} \cdot i_{\alpha\beta,sk} + L_m \cdot \sum_{z=1}^n i_{\alpha\beta,sz} + L_m \cdot i_{\alpha\beta,r} \quad (4.67)$$

Applying the rotation matrix in Eq. (4.66) to Eq. (4.67), the stator magnetic model is written as reported in Eq. (4.68). The stator electric model in rotating frame is formally identical with the one in stationary coordinates Eq. (4.67) and the zero-sequence is not involved in the rotational transformation.

$$\lambda_{dq,sk} = L_{l,s} \cdot i_{dq,sk} + L_m \cdot \sum_{z=1}^n i_{dq,sz} + L_m \cdot i_{dq,r}, \quad k = 1, \dots, n \quad (4.68)$$

### Rotor magnetic equation

The rotational matrix in Eq. (4.66) is applied to the rotor model in stationary reference frame (see Eq. (4.47)), without involving the zero sequence component to evaluate the rotor magnetic equation in rotating  $dq$  reference frame. The following equation is obtained:

$$\lambda_{dq,r} = L_{lr} \cdot i_{dq,r} + L_m \cdot \sum_{z=1}^n i_{dq,sz} + L_m \cdot i_{dq,r} \quad (4.69)$$

### Stator electric model

The stator electric model in rotating  $dq$  reference frame is obtained applying the rotational transformation in Eq. (4.66) to the one in stationary  $\alpha\beta$  components, reported in Eq. (4.70) for simplicity. The zero sequence is not involved by the rotational transformation.

$$v_{\alpha\beta,sk} = R_s \cdot i_{\alpha\beta,sk} + \frac{d}{dt} \lambda_{\alpha\beta,sk} \quad (4.70)$$

By applying Eq. (4.66) to Eq. (4.70), the stator electrical model is evaluated as:

$$\begin{aligned} v_{\alpha\beta,sk} &= R_s \cdot i_{\alpha\beta,sk} + \frac{d}{dt} \lambda_{\alpha\beta,sk} \Rightarrow \\ \Rightarrow [R(\theta)] \cdot v_{\alpha\beta,sk} &= [R(\theta)] \cdot \left( R_s \cdot i_{\alpha\beta,sk} + \frac{d}{dt} \lambda_{\alpha\beta,sk} \right) \Rightarrow \\ \Rightarrow v_{dq,sk} &= R_s \cdot i_{dq,sk} + \frac{d}{dt} \lambda_{dq,sk} + [R(\theta)] \left( \frac{d}{dt} [R(\theta)]^{-1} \right) \cdot \lambda_{dq,sk} \end{aligned} \quad (4.71)$$

where:

$$[R(\theta)] \left( \frac{d}{dt} [R(\theta)]^{-1} \right) = \frac{d\theta}{dt} \cdot \begin{bmatrix} 0 & -1 \\ 1 & 0 \end{bmatrix} = \omega \cdot \begin{bmatrix} 0 & -1 \\ 1 & 0 \end{bmatrix} \quad (4.72)$$

where  $\omega$  represents the electrical speed of the  $dq$  reference frame. Replacing Eq. (4.72) in Eq. (4.71), the stator voltage model in rotating  $dq$  reference frame is written as in Eq. (4.73), introducing the motional voltage terms in the stator electric model.

$$\begin{aligned} v_{dq,sk} &= R_s \cdot i_{dq,sk} + \frac{d}{dt} \lambda_{dq,sk} + \omega \cdot \begin{bmatrix} 0 & -1 \\ 1 & 0 \end{bmatrix} \cdot \lambda_{dq,sk} = \\ &= R_s \cdot i_{dq,sk} + \frac{d}{dt} \lambda_{dq,sk} + j \cdot \omega \cdot \lambda_{dq,sk}, \quad k = 1, \dots, n \end{aligned} \quad (4.73)$$

### Rotor voltage model

The rotor voltage model in rotating  $dq$  reference frame is evaluated by applying the rotational transformation Eq. (4.66) to the one in stationary  $\alpha\beta$  coordinates reported in Eq. (4.74), not including the zero sequence.

$$v_{\alpha\beta,r} = R_r \cdot i_{\alpha\beta,r} + \frac{d}{dt} \lambda_{\alpha\beta,r} - j\omega_r \cdot \lambda_{\alpha\beta,r} \quad (4.74)$$

The rotor electric model in rotating  $dq$  reference frame is computed as:

$$\begin{aligned}
 [R(\theta)] \cdot v_{\alpha\beta,r} &= [R(\theta)] \cdot \left( R_r \cdot i_{\alpha\beta,r} + \frac{d}{dt} \lambda_{\alpha\beta,r} - j\omega_r \cdot \lambda_{\alpha\beta,r} \right) \Rightarrow \\
 \Rightarrow v_{dq,r} &= R_r \cdot i_{dq,r} + \frac{d}{dt} \lambda_{dq,r} - j\omega_r \cdot \lambda_{dq,r} + [R(\theta)] \left( \frac{d}{dt} [R(\theta)]^{-1} \right) \cdot \lambda_{dq,r} \Rightarrow \\
 \Rightarrow v_{dq,r} &= R_r \cdot i_{dq,r} + \frac{d}{dt} \lambda_{dq,r} - j\omega_r \cdot \lambda_{dq,r} + j\omega \cdot \lambda_{dq,r} = \\
 &= R_r \cdot i_{dq,r} + \frac{d}{dt} \lambda_{dq,r} + j(\omega \cdot \lambda_{dq,r} - \omega_r \cdot \lambda_{dq,r}) = \\
 &= R_r \cdot i_{dq,r} + \frac{d}{dt} \lambda_{dq,r} + j\omega_{sl} \cdot \lambda_{dq,r}
 \end{aligned} \tag{4.75}$$

where  $\omega_{sl}$  is the slip speed of the rotating reference frame and computed as:

$$\omega_{sl} = \omega - \omega_r \tag{4.76}$$

### Electromagnetic torque

In Eq. (4.64) the torque is represented by the sum of  $n$  torque contributions computed as the cross-product between the stator flux linkage vector and stator current vector of the  $k$ -set. However, the torque does not depend on the reference frame because it is related to the position of one vector with respect to the other one. Formally the torque equation is invariant in  $dq$  reference frame than  $\alpha\beta$  one:

$$T_{em} = \frac{3}{2} \cdot p \cdot \sum_{k=1}^n (\lambda_{dq,sk} \times i_{dq,sk}) \tag{4.77}$$

The mechanical model is not affected by the application of the rotational transformation because the electrical and magnetic variables are not included.

### 4.3 Vector Space decomposition (VSD) modelling approach

The VSD approach is one possible alternative to the MS one [115]. The literature is the most employed but will prove that the mapping algorithm presents more complicated modeling and is less intuitive. However, the VSD model is investigated in this section, analyzing the difference between the other model approaches.

The multi-three-phase model in phase coordinates presented before is summarized in the system of differential equations as in Eq. (4.27). The VSD model assumes a squirrel cage rotor modeled as an equivalent multiple three-phase winding, thus emulating the stator winding configuration differently than the MS approach. Indeed, Eq. (4.28) has been introduced, keeping a general phase coordinates model.

For simplicity, the energy conversion in phase coordinates based on VSD approach is reported in Eq. (4.78).

$$\left\{ \begin{array}{l} \{\bar{V}\} = [R] \cdot \{\bar{I}\} + \frac{d}{dt} \{\bar{\Lambda}\} \\ \{\bar{\Lambda}\} = [L] \cdot \{\bar{I}\} \\ T_{em} = p \cdot \{\bar{I}_s\}^T \cdot \frac{d[L_{SR}]}{dt} \cdot \{\bar{I}_r\} \\ T_{em} - T_L = \frac{J_{eq}}{p} \cdot \frac{d\omega}{dt} \\ \omega_r = \frac{d\theta_r}{dt} \end{array} \right. \quad (4.78)$$

Compared to the general model in phase coordinates coinciding with MS approach, the electromechanical VSD model of the machine is composed as follows:

- $3 \cdot n$  stator magnetic equations;
- $3 \cdot n$  rotor magnetic equations (using the MS approach only 3 equations);
- $3 \cdot n$  stator electrical equations;

- $3 \cdot n$  rotor electrical equations (using the MS approach only 3 equations);
- 1 electromagnetic torque equation;
- 2 mechanical equations.

#### 4.3.1 Electromechanical model in stationary coordinates

VSD model approach for stationary reference frame considers the application of  $m$ -phase transformation, so all of the multiphase machines could be modeled, not only the multiple 3-phase ones. Indeed, using the MS approach, using multiple 3-phase Clarke's transformations, just multiple three-phase machines can be modeled. The VSD modeling approach is based on the symmetrical components theory. For this reason, the VSD approach is applicable for symmetrical or asymmetrical machine configurations. This is a great disadvantage, particularly for open-winding fault conditions. The machine phase variables are multiplied by VSD matrix resulting in multiple decoupled two-dimensional subspaces and zero-sequence component(s). The first subspace is a flux/torque-producing one, meaning that all electromechanical energy conversion occurs here, assuming the sinusoidal winding distribution. The other subspace variables can be used as additional degrees of freedom for some multiphase machine-specific purpose, i.e., fault tolerance, sensorless control, dc-link voltage balancing, or harmonic elimination. In summary, this approach decomposes the space of the machine variables into  $m/2$  decoupled subspaces by using  $m \times m$  transformation matrix ( $m$  stands for phases number).

However, different approaches are present in literature to get the VSD matrix transformation with some limitations (i.e., method of producing decoupling transformation only for asymmetrical machines or vice versa). However, in [59] a straightforward algorithm is presented, and it applies to any multiphase machine (symmetrical or asymmetrical) and enables relatively simple creation of the required decoupling transformation matrix in real or complex form. The application of the VSD transformation matrix obtained with the proposed procedure [59, 115] leads to the decomposition of the machine as follows:

- 1 main subspace  $\alpha\beta$ ;
- $h = 1, \dots, n_h$  harmonic subspaces ( $\mu + \mu-$  called  $xy$  and numerated with index  $h$ ):
- $z = 1, \dots, z$  homopolar subspaces ( $o + o-$  called 0 and numerated with index  $z$ ).

According to the literature, if a multi-three-phase machine having  $n$  three-phase winding sets is considered, the application of the VSD transformation leads to the definition of 1 main subspace,  $n - 1$  harmonic subspaces, and  $n$  zero-sequence components. The application of the VSD transformation on the machine's original space leads to the definition of  $(3 \cdot n)/2$  orthogonal subspaces, using a transformation matrix having a dimension equal to the total number of phases.

In this dissertation, the procedure presented in [59] has been adopted for producing decoupling transformation, focusing on the benchmark machine. Considering a twelve-phase machine configured in quadruple-three-phase winding ( $n = 4$ ) with 4 common neutral points (single neutral point), 1 main subspace,  $n_h = 3$  harmonic subspaces and  $n_o = 2$  homopolar subspaces (4 components). Just for clarity, the VSD matrix used for the machine model is expressed as:

$$[T_{S/R}^{VSD}] = \frac{2}{3 \cdot 4} \cdot \begin{bmatrix} cs(1 \cdot [\theta_{m,S/R}]) \\ cs(5 \cdot [\theta_{m,S/R}]) \\ cs(7 \cdot [\theta_{m,S/R}]) \\ cs(11 \cdot [\theta_{m,S/R}]) \\ cs(3 \cdot [\theta_{m,S/R}]) \\ cs(9 \cdot [\theta_{m,S/R}]) \end{bmatrix} \quad (4.79)$$

where:

$$cs(x \cdot [\theta_{m,S/R}])_{2 \times 12} = \begin{bmatrix} \cos(x \cdot [\theta_{m,S/R}]) \\ \sin(x \cdot [\theta_{m,S/R}]) \end{bmatrix}, \quad \begin{cases} x = 1, 5, 7, 11, 3, 9 \\ m = 1, \dots, 12 \end{cases} \quad (4.80)$$

Taking as an example the stator angle displacement of the benchmark machine (see Fig. 4.7), each row of the matrix  $[T_S^{VSD}]$  is composed by the phase propagation angles reported in Eq. (4.81). The rotor phase magnetic axes is



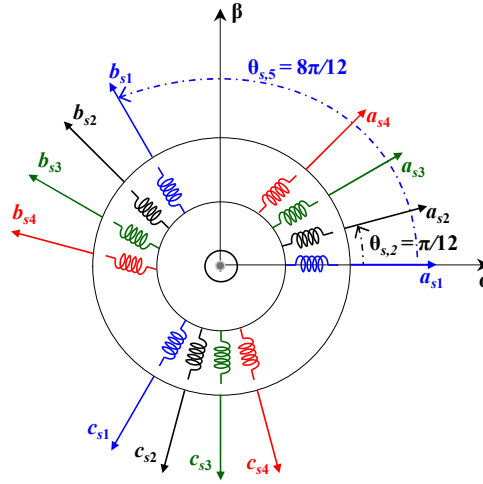


Figure 4.7 Phase magnetic axes in an asymmetrical twelve-phase machine.

the same of the stator one shown in Fig. 4.7, but shifted of  $\theta_r$  (Fig. 4.3).

$$[\theta_{m,s}] = \begin{bmatrix} 0 & \frac{\pi}{12} & \frac{2\pi}{12} & \frac{3\pi}{12} & \frac{8\pi}{12} & \frac{9\pi}{12} & \frac{10\pi}{12} & \frac{11\pi}{12} & \frac{16\pi}{12} & \frac{17\pi}{12} & \frac{18\pi}{12} & \frac{19\pi}{12} \end{bmatrix} \quad (4.81)$$

For the benchmark machine, 2 homopolar subspaces are obtained, applying the transformation in Eq. (4.79) - Eq. (4.81), while if multiple neutral points are considered (isolated neutral points), the zero sequence will be obtained. This difference is just related to mathematical manipulation.

The application of Eq. (4.80) leads to the definition of the stationary components of each variable defined in phase coordinates. In terms of mathematical formulations, this operation is obtained as:

$$\begin{aligned} \{\bar{z}_S^{VSD}\} &= [T_S^{VSD}] \cdot \{\bar{z}_S\}, & \{\bar{z}_R^{VSD}\} &= [T_R^{VSD}] \cdot \{\bar{z}_R\} \\ \{\bar{z}_S\} &= [T_S^{VSD}]^{-1} \cdot \{\bar{z}_S^{VSD}\}, & \{\bar{z}_R\} &= [T_R^{VSD}]^{-1} \cdot \{\bar{z}_R^{VSD}\} \end{aligned} \quad (4.82)$$

where  $\bar{z}_S$  and  $\bar{z}_R$  stand for a generic stator and rotor variables (i.e.,  $v, i, \lambda$ ) in phase coordinates.

### Stator magnetic model

The application of Eq. (4.82) to stator magnetic model in phase coordinates, reported in Eq. (4.83), allows to obtain the stator magnetic model in stationary ones.

$$\bar{\lambda}_s = L_{l,s} \cdot \bar{i}_s + [L_{ss}] \cdot \bar{i}_s + [L_{sr}] \cdot \bar{i}_r^r \quad (4.83)$$

The superscript  $r$  indicates that the variable is defined in the rotor coordinates, making necessary its redefinition to the stator ones. For this reason, the transformation ratio is introduced as reported in Eq. (4.84).

$$t_{sr}^{VSD} = \frac{N_s}{N_r^{VSD}} = \frac{N_s}{N_r / \sqrt{n}} = \sqrt{n} \cdot \frac{N_s}{N_r} \quad (4.84)$$

The equivalent turns number introduced in Eq. (4.84) involves a notionally increases in turns number with the consequence of reporting the variables to the stator side, reducing the voltage and flux, increasing the current as:

$$\bar{v}_r^s = t_{sr}^{VSD} \cdot \bar{v}_r; \quad \bar{i}_r^s = \frac{1}{t_{sr}^{VSD}} \cdot \bar{i}_r; \quad \bar{\lambda}_r^s = t_{sr}^{VSD} \cdot \bar{\lambda}_r \quad (4.85)$$

By replacing Eq. (4.85) in Eq. (4.83) and by applying Eq. (4.82), the stator magnet model is overwritten as:

$$\bar{\lambda}_s = L_{l,s} \cdot \bar{i}_s + [L_{ss}] \cdot \bar{i}_s + [L_{sr}] \cdot t_{sr}^{VSD} \cdot \bar{i}_r^s \quad (4.86)$$

Using the VSD transformation in Eq. (4.82), the stator magnetic model is evaluated as:

$$\begin{aligned} [T_s^{VSD}] \cdot \bar{\lambda}_s &= [T_s^{VSD}] \cdot L_{l,s} \cdot \bar{i}_s + [T_s^{VSD}] \cdot [L_{ss}] \cdot [T_s^{VSD}]^{-1} \cdot \bar{i}_s^{VSD} + \dots \\ &\dots + [T_s^{VSD}] \cdot [L_{sr}] \cdot t_{sr}^{VSD} \cdot [T_r^{VSD}]^{-1} \cdot (\bar{i}_r^s)^{VSD} \Rightarrow \\ \Rightarrow \bar{\lambda}_s^{VSD} &= L_{l,s} \cdot \bar{i}_s^{VSD} + [L_{ss}^{VSD}] \cdot \bar{i}_s^{VSD} + [L_s^{VSD}] \cdot t_{sr}^{VSD} \cdot (\bar{i}_r^s)^{VSD} \end{aligned} \quad (4.87)$$

where:

$$\left[ L_{ss}^{VSD} \right]_{3n \times 3n} = \left[ T_s^{VSD} \right] \cdot \left[ L_{ss} \right] \cdot \left[ T_s^{VSD} \right]^{-1} = \frac{3 \cdot n}{2} \cdot \frac{N_s \cdot N_s}{\mathcal{R}_{eq}} \cdot \begin{bmatrix} 1 & 0 & \dots & 0 \\ 0 & 1 & \dots & 0 \\ \dots & \dots & \dots & \dots \\ 0 & 0 & \dots & 0 \end{bmatrix} \quad (4.88)$$

$$\left[ L_{sr}^{VSD} \right]_{3n \times 3n} = \left[ T_s^{VSD} \right] \cdot \left[ L_{sr} \right] \cdot \left[ T_r^{VSD} \right]^{-1} = \frac{3 \cdot n}{2} \cdot \frac{N_s \cdot N_s}{\mathcal{R}_{eq}} \cdot \begin{bmatrix} 1 & 0 & \dots & 0 \\ 0 & 1 & \dots & 0 \\ \dots & \dots & \dots & \dots \\ 0 & 0 & \dots & 0 \end{bmatrix} \quad (4.89)$$

Isolating each subspace to highlighted the main subspace and the others subspaces and introducing Eq. (4.90), the stator magnetic model in Eq. (4.87) can be expressed as reported in Eq. (4.91).

$$n \cdot L_m^s = \frac{3 \cdot n}{2} \cdot \frac{N_s \cdot N_s}{\mathcal{R}_{eq}} \quad (4.90)$$

$$\left\{ \begin{array}{ll} \alpha\beta : & \lambda_{\alpha\beta,s} = L_{l,s} \cdot i_{\alpha\beta,s} + n \cdot L_m^s \cdot \bar{i}_{\alpha\beta,s} + n \cdot L_m^s \cdot \bar{i}_{\alpha\beta,r} \\ xy : & \lambda_{xy,sh} = L_{l,s} \cdot i_{xy,s}, \quad h = 1, \dots, n_h \\ 0 : & \lambda_{0,sz} = L_{l,s} \cdot i_{0,s}, \quad z = 1, \dots, n_0 \end{array} \right. \quad (4.91)$$

### Rotor magnetic model

The magnetic rotor model in stationary coordinates is obtained with the same procedure as the stator magnetic model. Starting from the rotor model in phase coordinates reported in Eq. (4.92), applying the Eq. (4.82), the rotor magnetic model in VSD coordinates can be evaluated.

$$\bar{\lambda}_r^r = L_{l,r}^r \cdot \bar{i}_r^r + [L_{rs}] \cdot \bar{i}_s + [L_{rr}] \cdot \bar{i}_r^r \quad (4.92)$$

The variables in Eq. (4.92) are referred to the rotor, but replacing Eq. (4.84) the following rotor magnet model is obtained:

$$\begin{aligned} \bar{\lambda}_r^s &= t_{sr}^{VSD} \cdot t_{sr}^{VSD} \cdot L_{l,r}^r \cdot \bar{i}_r^s + [L_{rs}] \cdot t_{sr}^{VSD} \cdot \bar{i}_s + t_{sr}^{VSD} \cdot [L_{rr}] \cdot t_{sr}^{VSD} \cdot \bar{i}_r^s \Rightarrow \\ \Rightarrow (\bar{\lambda}_r^s)^{VSD} &= (t_{sr}^{VSD})^2 \cdot L_{l,r}^r \cdot (\bar{i}_r^s)^{VSD} + [L_{rs}^{VSD}] \cdot t_{sr}^{VSD} \cdot \bar{i}_s + (t_{sr}^{VSD})^2 \cdot [L_{rr}^{VSD}] \cdot (\bar{i}_r^s)^{VSD} \end{aligned} \quad (4.93)$$

where the matrix  $[L_{rs}^{VSD}]$  and  $t_{sr}^{VSD} \cdot [L_{rr}^{VSD}]$  are defined as:

$$\begin{aligned} [L_{rs}^{VSD}] &= t_{sr}^{VSD} \cdot [T_s^{VSD}] \cdot [L_{rs}] \cdot [T_s^{VSD}]^{-1} = \\ &= \frac{3 \cdot n}{2} \cdot \frac{N_s \cdot N_s}{\mathcal{R}_{eq}} \cdot \begin{bmatrix} 1 & 0 & \dots & 0 \\ 0 & 1 & \dots & 0 \\ \dots & \dots & \dots & \dots \\ 0 & 0 & \dots & 0 \end{bmatrix} = n \cdot L_m^s \cdot \begin{bmatrix} 1 & 0 & \dots & 0 \\ 0 & 1 & \dots & 0 \\ \dots & \dots & \dots & \dots \\ 0 & 0 & \dots & 0 \end{bmatrix} \end{aligned} \quad (4.94)$$

$$\begin{aligned} (t_{sr}^{VSD})^2 \cdot [L_{rr}^{VSD}] &= (t_{sr}^{VSD})^2 \cdot [T_r^{VSD}] \cdot [L_{rr}] \cdot [T_r^{VSD}]^{-1} = \\ &= \frac{3 \cdot n}{2} \cdot \frac{N_s \cdot N_s}{\mathcal{R}_{eq}} \cdot \begin{bmatrix} 1 & 0 & \dots & 0 \\ 0 & 1 & \dots & 0 \\ \dots & \dots & \dots & \dots \\ 0 & 0 & \dots & 0 \end{bmatrix} = n \cdot L_m^s \cdot \begin{bmatrix} 1 & 0 & \dots & 0 \\ 0 & 1 & \dots & 0 \\ \dots & \dots & \dots & \dots \\ 0 & 0 & \dots & 0 \end{bmatrix} \end{aligned} \quad (4.95)$$

The leakage rotor inductance is defined as:

$$L_{l,r}^r \cdot (t_{sr}^{VSD})^2 = L_{l,r}^r \cdot (\sqrt{n} \cdot t_{sr})^2 = n \cdot L_{l,r}^r \cdot t_{sr}^2 = n \cdot L_{l,r}^s \quad (4.96)$$

Based on Eq. (4.93) - Eq. (4.96) the rotor magnetic model in each subspace is expressed as:

$$\left\{ \begin{array}{ll} \alpha\beta : & \lambda_{\alpha\beta,r}^s = n \cdot L_{l,r}^s \cdot i_{\alpha\beta,r}^s + n \cdot L_m^s \cdot \bar{i}_{\alpha\beta,s} + n \cdot L_m^s \cdot i_{\alpha\beta,r}^s \\ xy : & \lambda_{xy,rh} = n \cdot L_{l,r}^s \cdot i_{xy,rh}, \quad h = 1, \dots, n_h \\ 0 : & \lambda_{0,rz} = n \cdot L_{l,r}^s \cdot i_{0,rz}, \quad z = 1, \dots, n_0 \end{array} \right. \quad (4.97)$$

### Stator electric model

The stator electric model in phase coordinates using the VSD approach is expressed as:

$$\bar{v}_s = R_s \cdot \bar{i}_s + \frac{d}{dt} \bar{\lambda}_s \quad (4.98)$$

By applying Eq. (4.82) to Eq. (4.98) the stator voltage model is written in stationary coordinates as:

$$\bar{v}_s^{VSD} = R_s \cdot \bar{i}_s^{VSD} + \frac{d}{dt} \bar{\lambda}_s^{VSD} \quad (4.99)$$

For each subspace, the components are expressed as:

$$\left\{ \begin{array}{ll} \alpha\beta : & v_{\alpha\beta,s}^s = R_s \cdot i_{\alpha\beta,s} + \frac{d}{dt} \bar{\lambda}_{\alpha\beta,s} \\ xy : & v_{xy,sh} = R_s \cdot i_{xy,sh} + L_{l,s} \cdot \frac{d}{dt} i_{xy,sh}, \quad h = 1, \dots, n_h \\ 0 : & v_{0,sz} = R_s \cdot i_{0,sz} + L_{l,s} \cdot \frac{d}{dt} i_{0,sz}, \quad n_0 = 1, \dots, z \end{array} \right. \quad (4.100)$$

### Rotor electrical model

The rotor electrical model in phase coordinates is expressed as:

$$\bar{v}_r^r = R_r \cdot \bar{i}_r^r + \frac{d}{dt} \bar{\lambda}_r^r \quad (4.101)$$

Using Eq. (4.85), the model is referred to the stator as:

$$\bar{v}_r^s = n \cdot R_r^s \cdot \bar{i}_r^s + \frac{d}{dt} \bar{\lambda}_r^s \quad (4.102)$$

Finally, by applying Eq. (4.82), the model in stationary coordinates is evaluated as:

$$\begin{aligned}
 (\bar{v}_r^s)^{VSD} &= n \cdot R_r^s \cdot (\bar{i}_r^s)^{VSD} + \frac{d}{dt} (\bar{\lambda}_r^s)^{VSD} + [T_r^{VSD}] \cdot \frac{d}{dt} [T_r^{VSD}]^{-1} \cdot (\bar{\lambda}_r^s)^{VSD} = \\
 &= n \cdot R_r^s \cdot (\bar{i}_r^s)^{VSD} + \frac{d}{dt} (\bar{\lambda}_r^s)^{VSD} + \omega_r \cdot \begin{bmatrix} 0 & 1 & \dots & 0 \\ -1 & 0 & \dots & 0 \\ \dots & \dots & \dots & \dots \\ 0 & 0 & \dots & 0 \end{bmatrix}
 \end{aligned} \tag{4.103}$$

Based on Eq. (4.104) the rotor electrical model in each subspace is expressed as:

$$\left\{ \begin{array}{ll} \alpha\beta : & v_{\alpha\beta,r}^s = n \cdot R_r^s \cdot i_{\alpha\beta,r}^s + \frac{d}{dt} \bar{\lambda}_{\alpha\beta,r}^s + \omega_r \cdot \begin{bmatrix} 0 & 1 \\ -1 & 0 \end{bmatrix} \cdot \lambda_{\alpha\beta,r}^s \\ xy : & v_{xy,rh}^s = n \cdot R_r^s \cdot i_{xy,rh}^s + \frac{d}{dt} \bar{\lambda}_{xy,rh}^s, \quad h = 1, \dots, n_h \\ 0 : & v_{0,rz}^s = n \cdot R_r^s \cdot i_{0,rz}^s + \frac{d}{dt} \bar{\lambda}_{0,rz}^s, \quad z = 1, \dots, n_0 \end{array} \right. \tag{4.104}$$

### Electromagnetic torque

The electromagnetic torque in phase coordinates using the VSD approach is expressed as:

$$T_{em} = p \cdot \bar{i}_s^T \cdot \frac{d}{\lambda_r} [L_{sr}] \cdot \bar{i}_r^r \tag{4.105}$$

By applying Eq. (4.85) in Eq. (4.105) to refer the rotor variables to the stator, the electromagnetic torque is expressed as:

$$T_{em} = p \cdot \bar{i}_s^T \cdot \frac{d}{d\theta_r} [L_{sr}] \cdot t_{sr}^{VSD} \cdot \bar{i}_r^r \tag{4.106}$$

Applying the matrix transformation to Eq. (4.106), the following result is obtained:

$$\begin{aligned}
 T_{em} &= p \cdot (\bar{i}_s^{VSD})^T \cdot \left( [T_s^{VSD}]^{-1} \right)^T \cdot \frac{d[L_{sr}]}{d\theta_r} \cdot t_{sr}^{VSD} \cdot [T_r^{VSD}]^{-1} \cdot (\bar{i}_r^s)^{VSD} = \\
 &= p \cdot (\bar{i}_s^{VSD})^T \cdot \frac{9 \cdot n^2}{4} \cdot \frac{N_s \cdot N_s}{\mathcal{R}_{eq}} \cdot \begin{bmatrix} 1 & 0 & \dots & 0 \\ 0 & 1 & \dots & 0 \\ \dots & \dots & \dots & 0 \\ 0 & 0 & \dots & 0 \end{bmatrix} \cdot (\bar{i}_r^s)^{VSD} = \\
 &= p \cdot \frac{9 \cdot n^2}{4} \cdot \frac{N_s \cdot N_s}{\mathcal{R}_{eq}} \cdot (i_{\alpha,r}^s \cdot i_{\beta,s} - i_{\beta,r}^s \cdot i_{\alpha,s}) = \\
 &= p \cdot \frac{3 \cdot n}{2} \cdot L_m^s \cdot (i_{\alpha\beta,r}^s \times i_{\alpha\beta,s})
 \end{aligned} \tag{4.107}$$

Finally, replacing Eq. (4.91) to use only stator variables, the electromagnetic torque is expressed as:

$$\begin{aligned}
 T_{em} &= p \cdot \frac{3 \cdot n}{2} \cdot (\lambda_{\alpha\beta,s} \times i_{\alpha\beta,s}) = \\
 &= p \cdot \frac{3 \cdot n}{2} \cdot (\lambda_{\alpha,s} \cdot i_{\beta,s} - \lambda_{\beta,s} \cdot i_{\alpha,s})
 \end{aligned} \tag{4.108}$$

In conclusion, using the VSD approach the main subspace  $\alpha\beta$  contains the torque and flux producing current components, equal to the three-phase IM one. The others subspace do not take part to the electromechanical energy conversion because they contain only the harmonics and homopolar components. The equivalent circuit using VSD approach representative of Eq. (4.91), Eq. (4.97), Eq. (4.100), Eq. (4.104) is shown in Fig. 4.8.

Form now on the superscript  $s$  on the rotor variables is not used anymore, thus simplifying the formulation of the equation system.

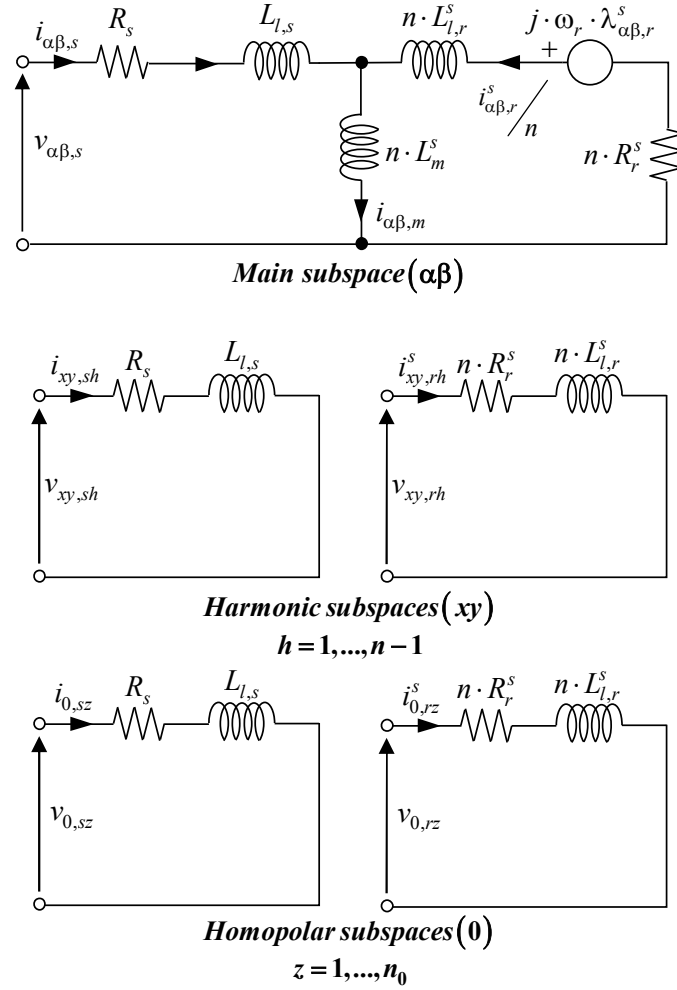


Figure 4.8 Equivalent VSD circuit of a multi-three-phase IM in stationary components.

### 4.3.2 Electromechanical model in rotating coordinates

The electromechanical model in a rotating reference frame using the VSD approach is evaluated in  $dq$  reference frame, aligning the  $d$ -axis with the rotor flux  $\lambda_r$  at the electrical speed  $\omega$ . By applying the rotational matrix of Eq. (4.66) to Eq. (4.109) referred to the main subspace, the electromagnetic



model is expressed as reported in Eq. (4.110).

$$\left\{ \begin{array}{l} s - \lambda i : \quad \lambda_{\alpha\beta,s} = L_{l,s} \cdot i_{\alpha\beta,s} + n \cdot L_m \cdot i_{\alpha\beta,s} + n \cdot L_m \cdot i_{\alpha\beta,r} \\ r - \lambda i : \quad \lambda_{\alpha\beta,r} = n \cdot L_{l,r} \cdot i_{\alpha\beta,r} + n \cdot L_m \cdot \bar{i}_{\alpha\beta,s} + n \cdot L_m \cdot i_{\alpha\beta,r} \\ s - vi : \quad v_{\alpha\beta,s} = R_s \cdot i_{\alpha\beta,s} + \frac{d}{dt} \lambda_{\alpha\beta,s} \\ r - vi : \quad v_{\alpha\beta,r} = n \cdot R_r \cdot i_{\alpha\beta,r} + \frac{d}{dt} \bar{\lambda}_{\alpha\beta,r} + \omega_r \cdot \begin{bmatrix} 0 & 1 \\ -1 & 0 \end{bmatrix} \end{array} \right. \quad (4.109)$$

Rotational transformation does not change the magnetic rotor and stator models. As for three-phase counterparts, the motional voltage terms are introduced on both stator and rotor electric models applying the rotational transformation. The harmonic and homopolar subspaces are still valid in stationary coordinates, and the vectors are referred to the stationary coordinates.

$$\left\{ \begin{array}{l} s - \lambda i : \quad \lambda_{dq,s} = L_{l,s} \cdot i_{dq,s} + n \cdot L_m \cdot i_{dq,s} + n \cdot L_m \cdot i_{dq,r} \\ r - \lambda i : \quad \lambda_{dq,r} = n \cdot L_{l,r} \cdot i_{dq,r} + n \cdot L_m \cdot i_{dq,s} + n \cdot L_m \cdot i_{dq,r} \\ s - vi : \quad v_{dq,s} = R_s \cdot i_{dq,s} + \frac{d}{dt} \lambda_{dq,s} + j\omega \cdot \lambda_{dq,s} \\ r - vi : \quad v_{dq,r} = n \cdot R_r^s \cdot i_{dq,r} + \frac{d}{dt} \lambda_{dq,r} + j\omega_{sl} \cdot \lambda_{dq,r} \end{array} \right. \quad (4.110)$$

where, as will be demonstrated, the following parameters are defined as:

$$n \cdot L_m = L_m^{VSD}, \quad n \cdot L_{l,r} = L_{l,r}^{VSD}, \quad n \cdot R_r^s = (R_r^s)^{VSD}, \quad (4.111)$$

where  $n$  stands for the three-phase winding sets number.

Finally, the electromagnetic model in rotating  $dq$  coordinates is expressed as in Eq. (4.112), while the mechanical model does not depend on the considered coordinates.

$$T_{em} = p \cdot \frac{3 \cdot n}{2} \cdot (\lambda_{d,s} \cdot i_{q,s} - \lambda_{q,s} \cdot i_{d,s}) \quad (4.112)$$

## 4.4 Decoupling multi-stator (DMS) modelling approach

The decoupling multi-stator (DMS) approach represents a competitive alternative to the VSD one for the thesis goal [116]. The DMS approach is necessary when the multi-three-phase machines are neither symmetrical or asymmetrical [59]. Compared to the MS machine model presented in Section 4.2, the DMS approach removes the magnetic couplings between the winding sets [63]. The electromagnetic model of multi-three-phase IM using the DMS approach is similar to the model obtained with VSD presented in Section 4.3. Still, the modularity of the MS approach is conserved [116].

According to the literature, the decoupling methods can be defined using several approaches [121]. In this work, the method focuses on the computation of the machine's common and differential modes. The main goal is to concentrate the energy conversion in a common-mode subspace. The unbalances between the three-phase data in flux and torque production are mapped in specific differential-mode subspaces. For a multi-three-phase machine having  $m$  winding sets, 1 common subspace and  $(n - 1)$  differential subspaces are identified. These subspaces should be defined to be independent and decoupled from each other.

### 4.4.1 Electromechanical model

The multi-three-phase machine model in stationary coordinates is evaluated by applying the transformation  $[T_D]$  to the one obtained with the MS approach. For simplicity, the electromagnetic model using MS model in

rotating coordinates at electrical speed  $\omega$  is reported:

$$\left\{ \begin{array}{l} \lambda_{dq,sk} = L_{l,s} \cdot i_{dq,sk} + L_m \cdot \sum_{k=1}^n i_{dq,sk} + L_m \cdot i_{dq,r} \\ \lambda_{dq,r} = L_{l,r} \cdot i_{dq,r} + L_m \cdot \sum_{k=1}^n i_{dq,sk} + L_m \cdot i_{dq,r} \\ v_{dq,sk} = R_s \cdot i_{dq,sk} + \frac{d}{dt} \lambda_{dq,sk} + j\omega \cdot \lambda_{dq,sk} \\ 0 = R_r \cdot i_{dq,r} + \frac{d}{dt} \lambda_{dq,r} + j\omega_{sl} \cdot \lambda_{dq,r} \end{array} \right. \quad (4.113)$$

In the following analysis, the subscript  $dq$  is not reported to simplify the notation. The stator and rotor magnetic models in Eq. (4.113) can be expressed as in Eq. (4.114) to highlight the coupling between the stator sets.

$$\left\{ \begin{array}{c} \lambda_{s1} \\ \lambda_{s2} \\ \dots \\ \lambda_{sn} \end{array} \right\} = L_{l,s} \cdot \left\{ \begin{array}{c} i_{s1} \\ i_{s2} \\ \dots \\ i_{sn} \end{array} \right\} + L_m \cdot \underbrace{\left[ \begin{array}{cccc} [I]_{2 \times 2} & [I]_{2 \times 2} & \dots & [I]_{2 \times 2} \\ [I]_{2 \times 2} & [I]_{2 \times 2} & \dots & [I]_{2 \times 2} \\ \dots & \dots & \dots & \dots \\ [I]_{2 \times 2} & [I]_{2 \times 2} & \dots & [I]_{2 \times 2} \end{array} \right]}_{[ID_{ss}]} \cdot \left\{ \begin{array}{c} i_{s1} \\ i_{s2} \\ \dots \\ i_{sn} \end{array} \right\} + L_m \cdot \left\{ \begin{array}{c} [I]_{2 \times 2} \\ [I]_{2 \times 2} \\ \dots \\ [I]_{2 \times 2} \end{array} \right\} \cdot i_r$$

$$\lambda_r = L_m \cdot \underbrace{\left[ \begin{array}{cccc} [I]_{2 \times 2} & [I]_{2 \times 2} & \dots & [I]_{2 \times 2} \end{array} \right]}_{[ID_{rs}]} \cdot \left\{ \begin{array}{c} i_{s1} \\ i_{s2} \\ \dots \\ i_{sn} \end{array} \right\} + (L_m + L_{l,r}) \cdot i_r \quad (4.114)$$

where  $n$  stands for the three-phase set number,  $[I]_{2 \times 2}$  is the identity matrix. The generic variable  $z_{s1}, \dots, z_{sn}$  is referred to the rotating coordinates  $dq$ , and so has a dimension  $2 \times 1$ . The stator flux vector has the dimension of  $2 \cdot n \times 1$ , considering a multi-three-phase machine. However, the matrices called  $[ID_{ss}]$  and  $[ID_{rs}]$  are not a identity matrices and so a decoupling matrix  $[T_D]$  must be defined. The decoupling matrix allows to define the following linear combination for a generic variable  $z$  (i.e.  $v, i, \lambda$ ) between the common and

differential modes as:

$$z_{sk} = z_{cm} + w_k \cdot z_{dmk,s} + \sum_{\substack{u=1 \\ u \neq k}}^k (q_u \cdot z_{dmu,s}) \quad (4.115)$$

where  $u$  is the index of differential modes ( $k = 1, \dots, (n-1)$ ) with one common mode of the set  $k$ . The coefficients  $w_k$  and  $q_u$  are defined as Eq. (4.116), ensuring that sum of elements for each row is equal to zero to get the decoupling. Indeed, the decoupling transformation  $[T_D]$  is computed based on this consideration.

$$w_k = \sqrt{\frac{n \cdot (n-k)}{(n-k+1)}}, \quad q_u = \sqrt{\frac{n}{(n-u+1) \cdot (n-u)}} \quad (4.116)$$

The decoupling matrix  $[T_D]$  characterized by the amplitude invariant feature with a power coefficient  $n$  is defined as:

$$[T_D] = \frac{1}{n} \cdot \begin{bmatrix} 1 & 1 & 1 & 1 & \dots & 1 & 1 & 1 & 1 \\ w_1 & q_1 & q_1 & q_1 & \dots & q_1 & q_1 & q_1 & q_1 \\ 0 & w_2 & q_2 & q_2 & \dots & q_2 & q_2 & q_2 & q_2 \\ 0 & 0 & w_3 & q_3 & \dots & q_3 & q_3 & q_3 & q_3 \\ \dots & \dots & \dots & \dots & \dots & \dots & \dots & \dots & \dots \\ 0 & 0 & 0 & 0 & \dots & 0 & w_{n-2} & q_{n-2} & q_{n-2} \\ 0 & 0 & 0 & 0 & \dots & 0 & 0 & w_{n-1} & q_{n-1} \end{bmatrix} \quad (4.117)$$

The decoupling transformation from rotating coordinates using the MS approach to the common and differential modes and vice versa is expressed as:

$$\begin{aligned} \begin{Bmatrix} z_{cm,s1} \\ z_{dm1,s} \\ \dots \\ z_{dmk,s} \end{Bmatrix} &= [T_D] \cdot \begin{Bmatrix} z_{s1} \\ z_{s2} \\ \dots \\ z_{sn} \end{Bmatrix}, \quad k = 1, \dots, (n-1) \\ \begin{Bmatrix} z_{s1} \\ z_{s2} \\ \dots \\ z_{sn} \end{Bmatrix} &= [T_D]^{-1} \cdot \begin{Bmatrix} z_{cm,s1} \\ z_{dm1,s} \\ \dots \\ z_{dmk,s} \end{Bmatrix}, \quad k = 1, \dots, (n-1) \end{aligned} \quad (4.118)$$

Note that the decoupling matrix does not depend on the angle displacement and can be applied to any multi-three-phase ac machine, regardless of the number  $n$  of three-phase winding sets and machine configuration. Indeed, then the  $[T^{VSD}]$  the  $[T_D]$  can be applied to any machine configuration, regardless of the winding, while  $[T^{VSD}]$  requires the symmetrical or asymmetrical machine configuration.

### Stator magnetic model

The decoupling transformation is applying to the stator magnetic model in rotating coordinates (the subscript  $dq$  is not reported for simplicity) obtained with the MS approach. The decoupling matrix is applied to all stator sets  $k = 1, \dots, n$  as:

$$\begin{aligned} \lambda_{sk} &= L_{l,s} \cdot i_{sk} + L_m \cdot \sum_{k=1}^n i_{sk} + L_m \cdot i_r \Rightarrow \\ \Rightarrow [T_D] \cdot \begin{Bmatrix} \lambda_{s1} \\ \lambda_{s2} \\ \dots \\ \lambda_{sn} \end{Bmatrix} &= L_{l,s} \cdot [T_D] \cdot \begin{Bmatrix} i_{s1} \\ i_{s2} \\ \dots \\ i_{sn} \end{Bmatrix} + L_m \cdot [T_D] \cdot [ID_{ss}] \cdot [T_D]^{-1} \cdot \begin{Bmatrix} i_{cm} \\ i_{dm,s1} \\ \dots \\ i_{dm,s_{n-1}} \end{Bmatrix} \Rightarrow \\ &\Rightarrow \lambda_s^{DMS} = L_{l,s} \cdot i_s^{DMS} + n \cdot L_m \cdot i_s^{DMS} + L_m \cdot i_r \end{aligned} \quad (4.119)$$

where the matrices are consistent with the previous definition. Based on Eq. (4.119), the stator magnetic model in each subspaces is expressed as:

$$\begin{cases} cm: & \lambda_{cm,s} = L_{l,s} \cdot i_{cm,s} + n \cdot L_m \cdot i_{cm,s} + L_m \cdot i_r \\ dm: & \lambda_{dm,su} = L_{l,s} \cdot i_{dm,su}, \quad u = 1, \dots, (n-1) \end{cases} \quad (4.120)$$

### Rotor magnetic model

As for the stator magnetic model, the rotor one is evaluated by applying the decoupling transformation  $[T_D]$  of Eq. (4.117) to the model in rotating

coordinates based on MS approach, obtained the following model:

$$\begin{aligned}
 \lambda_r &= L_{l,r} \cdot i_r + L_m \cdot \sum_{k=1}^n i_{sk} + L_m \cdot i_r \Rightarrow \\
 \Rightarrow \lambda_r &= L_{l,r} \cdot i_r + n \cdot L_m \cdot i_s^{DMS} + L_m \cdot i_r \Rightarrow \\
 \Rightarrow \lambda_r &= L_{l,r} \cdot i_r + n \cdot L_m \cdot i_{cm,s} + L_m \cdot i_r
 \end{aligned} \tag{4.121}$$

### Stator electrical model

The stator electrical model in rotating coordinates presents the coupling between the winding sets. by applying the decoupling transformation Eq. (4.117) the decoupled model is obtained as:

$$\begin{aligned}
 v_{sk} &= R_s \cdot i_{sk} + \frac{d}{dt} \lambda_{sk} + j\omega \cdot \lambda_{sk} \Rightarrow \\
 [T_D] \cdot \begin{Bmatrix} v_{s1} \\ v_{s2} \\ \dots \\ v_{sn} \end{Bmatrix} &= R_s \cdot [T_D] \cdot \begin{Bmatrix} i_{s1} \\ i_{s2} \\ \dots \\ i_{sn} \end{Bmatrix} + \frac{d}{dt} \left( [T_D] \cdot \begin{Bmatrix} \lambda_{s1} \\ \lambda_{s2} \\ \dots \\ \lambda_{sn} \end{Bmatrix} \right) + \omega \cdot [T_D] \cdot [J] \cdot [T_D]^{-1} \cdot \begin{Bmatrix} \lambda_{cm} \\ \lambda_{dm,s1} \\ \dots \\ \lambda_{dm,s_{n-1}} \end{Bmatrix} \Rightarrow \\
 \Rightarrow \begin{Bmatrix} v_{cm} \\ v_{dm,s1} \\ \dots \\ v_{dm,s_{n-1}} \end{Bmatrix} &= R_s \cdot \begin{Bmatrix} i_{cm} \\ i_{dm,s1} \\ \dots \\ i_{dm,s_{n-1}} \end{Bmatrix} + \frac{d}{dt} \begin{Bmatrix} \lambda_{cm} \\ \lambda_{dm,s1} \\ \dots \\ \lambda_{dm,s_{n-1}} \end{Bmatrix} + j\omega \cdot \begin{Bmatrix} \lambda_{cm} \\ \lambda_{dm,s1} \\ \dots \\ \lambda_{dm,s_{n-1}} \end{Bmatrix} \Rightarrow \\
 \Rightarrow v_s^{DMS} &= R_s \cdot i_s^{DMS} + \frac{d}{dt} \lambda_s^{DMS} + j\omega \cdot \lambda_s^{DMS}
 \end{aligned} \tag{4.122}$$

where:

$$[J] = \begin{bmatrix} [j] & [j] & \dots & [j] \\ [j] & [j] & \dots & [j] \\ \dots & \dots & \dots & \dots \\ [j] & [j] & \dots & [j] \end{bmatrix}, \quad [j] = \begin{bmatrix} 0 & -1 \\ 1 & 0 \end{bmatrix} \tag{4.123}$$

Based on Eq. (4.122), the stator electrical model in each subspaces is expressed as:

$$\left\{ \begin{array}{l} cm: \quad v_{cm,s} = R_s \cdot i_{cm,s} + \frac{d}{dt} \lambda_{cms} + j\omega \cdot \lambda_{cm,s} \\ dm: \quad v_{dm,su} = R_s \cdot i_{dm,su} + \frac{d}{dt} \lambda_{dm,su} \quad u = 1, \dots, (n-1) \end{array} \right. \quad (4.124)$$

### Rotor electrical model

The rotor electrical model is not affected by this transformation and it is written as:

$$v_r = n \cdot R_r \cdot i_r + \frac{d}{dt} \lambda_r + j\omega_{sl} \cdot \lambda_r \quad (4.125)$$

### Electromagnetic torque

The electromagnetic torque in stationary reference frame using DMS approach based on decoupling transformation of Eq. (4.117) is expressed as:

$$T_{em} = p \cdot \frac{3 \cdot n}{2} \cdot (\lambda_{cm,s} \times i_{cm,s}) \quad (4.126)$$

According to Eq. (4.126), the electromagnetic torque is given by the cross-product between the stator flux linkage vector and stator current vector, both belonging to the common-mode subspace since only there the interaction with the rotor is present. Therefore, the equivalent MS circuit of the multi-three-phase IM after applying the decoupling transformation is shown in Fig. 4.9. It can be noted that the magnetic couplings among the MS subspaces have been removed.

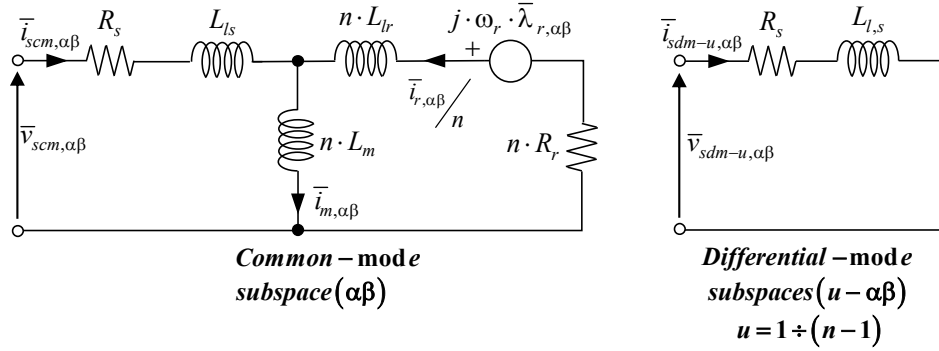


Figure 4.9 Equivalent MS circuit of a multi-three-phase IM in stationary coordinates after the application of the decoupling transformation.

## 4.5 Adaptive decoupling multi-stator (A-DMS) modelling approach

As mentioned above, some disadvantages are involved for the mapping algorithm using the VSD or DMS modelling when an open three-phase fault occurs. A solution is to adapt the machine modeling just considering the active winding sets  $n_{ON}$  than the nominal set  $n$  [63]. Consider the decoupling transformation defined in Eq. (4.117) and reported here for simplicity:

$$[T_D] = \frac{1}{n} \cdot \begin{bmatrix} [ID] & [ID] & [ID] & [ID] & \dots & [ID] & [ID] & [ID] & [ID] \\ w_1 & q_1 & q_1 & q_1 & \dots & q_1 & q_1 & q_1 & q_1 \\ 0 & w_2 & q_2 & q_2 & \dots & q_2 & q_2 & q_2 & q_2 \\ 0 & 0 & w_3 & q_3 & \dots & q_3 & q_3 & q_3 & q_3 \\ \dots & \dots & \dots & \dots & \dots & \dots & \dots & \dots & \dots \\ [0] & [0] & [0] & [0] & \dots & [0] & w_{n-2} & q_{n-2} & q_{n-2} \\ [0] & [0] & [0] & [0] & \dots & [0] & [0] & w_{n-1} & q_{n-1} \end{bmatrix}$$

$$w_k = \sqrt{\frac{n \cdot (n-k)}{(n-k+1)}}, \quad q_u = \sqrt{\frac{n}{(n-u+1) \cdot (n-u)}} \quad (4.127)$$

where  $n$  stands for the nominal winging sets (for quadruple-three-phase IM  $n = 4$ ),  $[ID]$  and  $[0]$  are the identity and zero  $2 \times 2$  submatrices. For a



quadruple-three-phase machine, Eq. (4.127) is expressed as:

$$[T_D]_{4 \times 4} = \frac{1}{4} \cdot \begin{bmatrix} [ID] & [ID] & [ID] & [ID] \\ \sqrt{3}[ID] & -\sqrt{1/3}[ID] & -\sqrt{1/3}[ID] & -\sqrt{1/3}[ID] \\ [0] & \sqrt{8/3}[ID] & -\sqrt{8/3}[ID] & -\sqrt{8/3}[ID] \\ [0] & [0] & \sqrt{2}[ID] & -\sqrt{2}[ID] \end{bmatrix} \quad (4.128)$$

However, the matrix in Eq. (4.127) can be adapted in faulty conditions, changing the decoupling transformation and adapting to the healthy windings. For example, if one three-phase winding is lost, the considered  $n$  in Eq. (4.127) becomes  $(n - 1)$  and maybe a VSD transformation cannot be defined for this faulty configuration because it is neither symmetrical nor asymmetrical. Based on the Eq. (4.118), the mathematical relation for a generic stator variable  $z(v, i, \lambda)$  is still valid. Still, the decoupling transformation must be adapted and thus applied only to the healthy/active winding sets as:

$$\begin{aligned} \begin{Bmatrix} z_{cm,s1} \\ z_{dm1,s} \\ \dots \\ z_{dmk,s} \end{Bmatrix} &= [T_D]_{n_{ON}} \cdot \begin{Bmatrix} z_{s1} \\ z_{s2} \\ \dots \\ z_{sn_{ON}} \end{Bmatrix}, \quad k = 1, \dots, (n_{ON} - 1) \\ \begin{Bmatrix} z_{s1} \\ z_{s2} \\ \dots \\ z_{sn_{ON}} \end{Bmatrix} &= [T_D]_{n_{ON}}^{-1} \cdot \begin{Bmatrix} z_{cm,s1} \\ z_{dm1,s} \\ \dots \\ z_{dmk,s} \end{Bmatrix}, \quad k = 1, \dots, (n_{ON} - 1) \end{aligned} \quad (4.129)$$

For example, considering the asymmetrical quadruple three-phase winding with stator angle displacement of  $15^\circ$  in faulty condition: the second set is fault and just 3 sets are active ( $n_{ON} = 3$ ,  $n = 4$ ). In this condition, the VSD matrix cannot be defined (symmetrical and asymmetrical neither winding

configuration), and the adaptive transformation  $[T_D]_{n_{ON}=3}$  is defined as:

$$n = n_{ON} = 4 : \begin{Bmatrix} z_{cm,s1} \\ z_{dm1,s} \\ z_{dm2,s} \\ z_{dm3,s} \end{Bmatrix} = [T_D]_{n=4} \cdot \begin{Bmatrix} z_{s1} \\ z_{s2} \\ z_{s3} \\ z_{s4} \end{Bmatrix}, \quad k = 1, \dots, 4 \quad (4.130)$$

$$n_{ON} = 3 \neq n : \begin{Bmatrix} z_{cm,s1} \\ z_{dm1,s} \\ z_{dm2,s} \end{Bmatrix} = [T_D]_{n_{ON}=3} \cdot \begin{Bmatrix} z_{s1} \\ z_{s2} \\ z_{s3} \end{Bmatrix}, \quad k = 1, \dots, 3$$

where:

$$[T_D]_{n_{ON}=3} = \frac{1}{3} \cdot \begin{bmatrix} [ID]_{2 \times 2} & [ID]_{2 \times 2} & [ID]_{2 \times 2} \\ \sqrt{2}[ID]_{2 \times 2} & -\sqrt{1/2}[ID]_{2 \times 2} & -\sqrt{1/2}[ID]_{2 \times 2} \\ [0]_{2 \times 2} & \sqrt{3/2}[ID]_{2 \times 2} & -\sqrt{3/2}[ID]_{2 \times 2} \end{bmatrix} \quad (4.131)$$

The electromagnetic model based on A-DMS approach in rotating  $dq$  rotor flux frame is expressed as:

$$\left\{ \begin{array}{l} s - \lambda i : \quad \lambda_{dq,s} = L_{l,s} \cdot i_{dq,s} + n_{ON} \cdot L_m \cdot i_{dq,s} + n_{ON} \cdot L_m \cdot i_{r,dq} \\ r - \lambda i : \quad \lambda_{r,dq} = n_{ON} \cdot L_{l,r} \cdot i_{r,dq} + n_{ON} \cdot L_m \cdot i_{dq,s} + n_{ON} \cdot L_m \cdot i_{r,dq} \\ s - v i : \quad v_{dq,s} = R_s \cdot i_{dq,s} + \frac{d}{dt} \bar{\lambda}_{dq,s} + j\omega \cdot \lambda_{dq,s} \\ r - v i : \quad v_{r,dq} = n_{ON} \cdot R_r^s \cdot i_{r,dq} + \frac{d}{dt} \lambda_{r,dq} + j\omega_{sl} \cdot \lambda_{r,dq} \end{array} \right. \quad (4.132)$$

where the rotor parameters and magnetizing inductance are rescaled by the factor  $n_{ON}$ , starting by the ones evaluated with VSD approach.

Three-phase model can be used to compute the losses of a multi-three-phase machine both in healthy and faulty operation without implementing specific equations to perform the efficiency evaluation in faulty operation, using the machine model based on A-DMS approach. Indeed, the A-DMS approach allows to keep the differential-mode quantities of currents and fluxes always equal to zero regardless of the machine operating conditions (healthy or

faulty) and consequently the losses in these subspaces are zero.

Also, the stator winding configuration can be different from the symmetrical or asymmetrical ones since all the advantages of the A-DMS modeling are preserved with the added value of keeping the machine model as simple as possible.

In summary, the common-mode torque-producing current is adapted using the A-DMS model approach in open-winding faulty conditions. The adaptive decoupling transformation (Eq. (4.127)) automatically performs some variations without implementing particular precautions. The currents of differential-mode subspaces in normal conditions are zero, and related losses are zero. According to the A-DMS approach, the decoupling transformation for the post-fault is redefined in faulty conditions, keeping only differential-mode currents of healthy windings equal to zero.

Consider the quadruple-three-phase IM in faulty conditions (i.e.,  $n_{ON} = 3$ , the second winding is lost): only two differential-mode currents are kept at zero, meaning zero losses, but in a normal condition, the common-mode torque-producing current is changed, changing the respective losses. Therefore, the fault differential-mode subspace, which does not exist anymore, is ignored after the fault event, redefining the decoupling matrix.

## 4.6 Comparison between modeling approaches

The decoupled MS model, DMS, and VSD model become formally identical after applying the decoupling transformation to the MS model. Indeed, starting from the MS machine model, the decoupling model introduces a further reference frame transformation that removes the magnetic couplings between the winding sets. The MS modularity is conserved, and decoupled MS model and the VSD model become formally identical. However, the mathematical physical meaning of VSD and DMS models is entirely different:

- The VSD modeling performs a time-harmonic decoupling of the machine space. Therefore, the energy conversion is performed by the main subspace having the meaning of the time-fundamental model of the machine. The VSD approach models the rotor cage as an equivalent

winding, emulating the stator. Consequently, the rotor harmonic and homopolar subspaces are defined (see Fig. 4.8). However, the rotor subspaces do not have physical meaning. Therefore, the limitations of the VSD are analytically overcome without using numerical workarounds: stator winding hardly satisfies the constraint of being symmetrical or asymmetrical, which is necessary for VSD application.

- The DMS subspaces, common and differential modes, are computed through linear combinations of the MS variables. Therefore, the decoupling transformation performs its action on the time-fundamental subspaces of the machine, thus preserving the modularity of the energy conversion. The harmonic and homopolar subspaces are not defined, avoiding unnecessary complications. No constraints exist on applying the decoupling transformation to machine winding configuration. However, this method can only be used for electric machines with non-prime number of phases.

In summary, the DMS differential-mode subspaces do not possess the same properties as the VSD time-harmonic ones in terms of time-harmonic decoupling. If the control scheme is based on the DMS approach for time-harmonic injection or compensation strategies, the DMS is impractical. The DMS approach removes the MS couplings among the machine's winding sets. Nevertheless, compared to VSD-based modeling, the modularity is preserved.

Nevertheless, if an open three-phase fault occurs, the VSD and DMS models involve currents in the secondary subspaces to keep the machine currents balanced and to get the torque production continuity. In other words, the computation of additional losses must be computed in the time-harmonic subspaces for the VSD approach and the differential-mode subspaces for the DMS one. In terms of the control scheme, implementing additional control modules with dedicated fault-tolerant strategies is necessary to manage the secondary subspaces for both approaches. As a result, the simplicity that characterizes the VSD and DMS approaches is lost. Therefore, the DMS approach in faulty conditions needs the active control of the secondary subspaces to keep the machine currents balanced and within their boundaries

and ensure the continuity of the torque production. The A-DMS modeling approach avoids this limitation, just adapting the decoupling matrix.

## 4.7 Machine investigation

### 4.7.1 Case of study: quadruple-three-phase IM

The benchmark machine for mapping validations is an asymmetrical 12-phase IM featuring a quadruple-three-phase (4 sets) configuration of the stator winding, rated 10 kW at 6000 rpm. The sketch of the magnetic axes of the machine windings is shown in Fig. 4.10 [93, 44]. The machine has four poles, 1 slot/pole/phase, and 19 conductors per slot. Thus, the single-layer winding is inserted in 48 stator slots. The distribution of the conductors in the stator slots is shown in Fig. 4.11. The conductors are not supplied when the machine operates in open-three-phase fault conditions.

Quadruple-three-phase machines can be modeled with different mathematical approaches presented before. For example, the MS approach decomposes the space of the machine variables in 4 parallel time-fundamental models, thus applying a dedicated Clarke transformation to each three-phase winding set. This way, the contributions to the machine flux and torque provided by each three-phase winding set are highlighted.

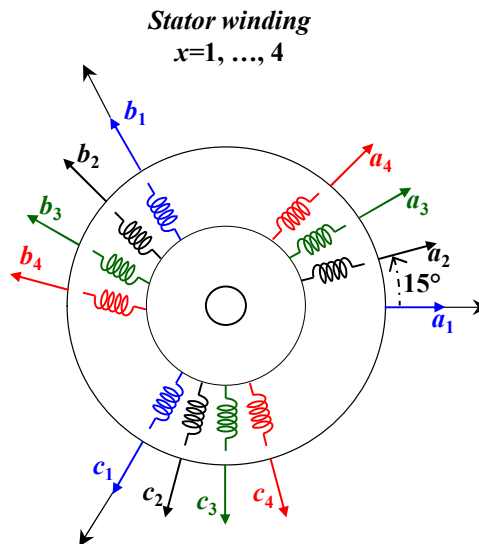


Figure 4.10 A view of the magnetic axes of the asymmetrical 12-phase IM.

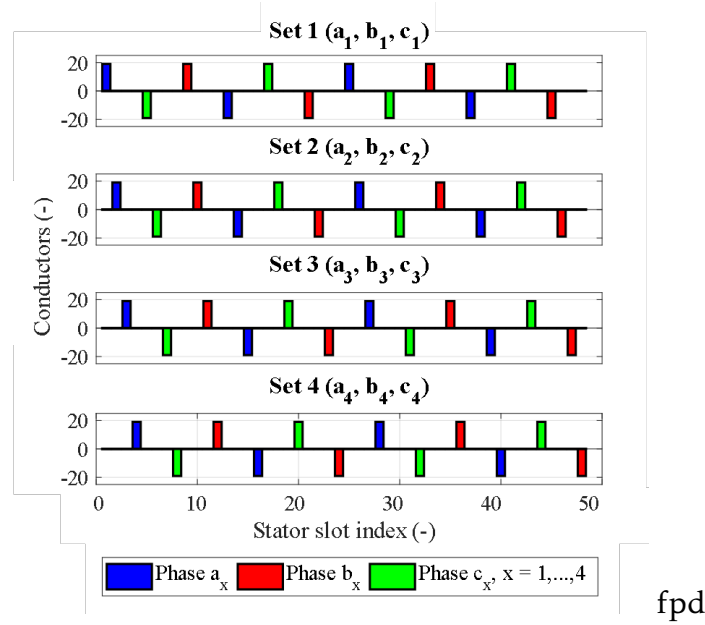


Figure 4.11 Conductors' distribution of the 12-phase IM.

4  $dq$  subspaces, 4 different stator flux linkage, and current vectors are obtained, leading to a significant cross-coupling effect among the equations of the different three-phase winding sets, as shown before. It also does not offer clear insights into the machine operation and harmonic mapping.

The VSD-model approach decomposes the space of the machine variables into 6 decoupled subspaces for twelve IM [114]. Through this approach, the flux and torque production can be modeled as an equivalent three-phase machine in the fundamental subspace  $\alpha\beta$  by using the well-known VSD transformation. Nevertheless, there is no possibility of distinguishing the contribution of each set to the total flux linkage and electromagnetic torque of the machine. Indeed, the remaining VSD subspaces represent the machine's harmonics and zero-sequence model that do not contribute to the electromechanical energy conversion. Therefore, for the machine under study ( $n_{ph} = 12$  in asymmetrical configuration with  $\pi/12$  spatial shift), it is necessary to define six subspaces: the main subspace  $\alpha\beta$ , the harmonic subspaces  $(x_5, y_5)$ ,  $(x_7, y_7)$ ,  $(x_{11}, y_{11})$ , and four zero-sequence components  $(0_1, 0_2, 0_3, 0_4)$  with isolated neutral points [60].

### 4.7.2 Measurement parameters

The no-load and locked-rotor tests are allowed to account for the following nonidealities considered in the equivalent circuit [122]:

- the saturation effect on the magnetizing inductance  $L_m$ , which profile depends on the number of active sets using the A-DMS approach and vice versa using the VSD one [123];
- the impact of the frequency and the number of active sets on the rotor resistance  $R_r$  depending by the used approach;
- the impact of the number of active sets on the equivalent locked-rotor inductance  $L_{cc}$ , i.e.,  $L_{l,s} + L_{l,r}$  (the subscript  $s$  is not reported for simplicity);
- the influence of the frequency and the stator voltage on the iron losses  $P_{Fe}$ , depending on the machine operating conditions (normal or open-winding fault).

Note that based on the data recorder, the post-process must be performed in phase coordinates or stationary reference frame. If the data recorder can register the variables' temporal trend, the post-process VSD approach can be adopted. Otherwise, if different three-phase power sources are available and the data recorder can record only the RMS values, the post-process of the standard tests is performed in phase coordinates. However, the availability of multiple three-phase power sources is complex. In the following, capital letters will be used for RMS values, while lowercase letters will be for instantaneous ones.

#### Phase-coordinates

No-load and locked-rotor tests under sinusoidal supply were performed using an open-loop voltage/frequency algorithm (V/Hz) implemented on the real-time control prototyping board PLECS RT-BOX 1 – see Fig. 4.12. The reference voltage signals were applied to four independent three-phase



power sources operated as linear power amplifiers and synchronized to each other.

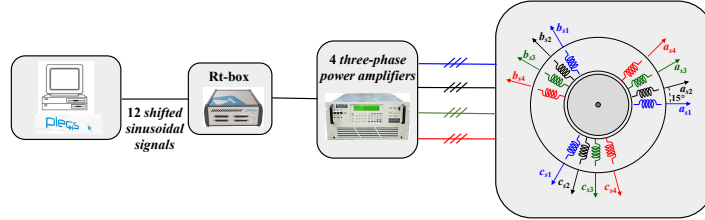


Figure 4.12 Sketch of the test rig used for parameter measurement elaborated in phase-coordinates.

The electrical quantities at the machine terminals were recorded using high-accuracy digital two wattmeter in Aron configuration for each three-phase winding set since these operate with an isolated star-point. The tests in faulty conditions have been emulated through the shut-off of the three-phase power source for all possible permutations. The data recorders were able to register the RMS values. The registered RMS values allow the definitions in Eq. (4.133). In this case, the analysis adapts the variables and parameters to the active sets number  $n_{ON}$ .

$$\begin{aligned}
 V_{eq} &= \frac{1}{n_{ON}} \cdot \sum_{k=1}^{n_{ON}} V_k, & V_k &= \frac{V_{ab,k} + V_{bc,k}}{2} \\
 I_{eq} &= \frac{1}{n_{ON}} \cdot \sum_{k=1}^{n_{ON}} I_k, & I_k &= \frac{I_{a,k} + I_{b,k}}{2} \\
 P_{eq} &= \sum_{k=1}^{n_{ON}} P_k, & P_k &= P_{ab,k} + P_{bc,k}
 \end{aligned} \tag{4.133}$$

where:

- $I_{a,k}$  and  $I_{b,k}$  are the stator RMS phase currents measured with power meters in Aron configuration located on phase  $a$  and  $b$ ;
- $P_{ac,k}$  and  $P_{bc,k}$  stand for the power measured by power meters in two wattmeter method (Aron configuration) located between the phase  $a$  and phase  $c$  and phase  $b$  and phase  $c$  for each  $k$ -three-phase winding set ;

- $P_{elt,k}$  stands for the electrical power of the  $k$ -three-phase set which is not zero if the  $k$  set is active.

An equivalent magnetizing inductance is introduced, which decreases disconnecting one or more sets. Indeed, a more magnetizing current is necessary to provide a given magnetizing flux as the number of active three-phase sets  $n_{ON}$  is reduced than the nominal sets  $n$ . For this reason, an equivalent magnetizing inductance  $L_{m,eq}$  is introduced and computed as Eq. (4.134), also suitable in saturation conditions. Eq. (4.134) is a typical concept of the A-DMS model approach, adapting the rotor parameters to the number of active sets  $n_{ON}$ .

$$L_{m-eq} = L_m \cdot \frac{n_{ON}}{n}, \quad n_{ON} \equiv n_{active} \quad (4.134)$$

$L_m$  is the magnetizing inductance measured in normal conditions (4 sets ON,  $n_{ON} = n$ ) or the VSD value, while  $n_{ON}$  is the number of active sets. The same rescaling procedure as in Eq. (4.134) can be used to calculate the equivalent rotor resistance and the equivalent rotor leakage inductance referred to the stator side as Eq. (4.135) based on the A-DMS approach presented before. Using the definition of Eq. (4.134) and Eq. (4.135) the equivalent circuit in Fig. 4.13 is not valid because the rotor parameters must be adapted with  $n_{ON}$ .

$$L_{l,r-eq}^s = L_{l,r}^s \cdot \frac{n_{ON}}{n}, \quad R_{r-eq}^s = R_r^s \cdot \frac{n_{ON}}{n} \quad (4.135)$$

The rescaling procedure described above is not valid for conventional iron losses. The no-load and locked-rotor tests performed on the benchmark machine are reported below, demonstrating the rescale of the rotor parameters, magnetizing inductance, and iron loss behavior. After this, the magnetomotive force (MMF) analysis in ideal conditions is presented to investigate the substantial increase in iron losses in faulty conditions.

## VSD

The VSD approach leads to the equivalent circuit shown in Fig. 4.13, which considers the main  $\alpha\beta$  subspace responsible for the flux and torque production in the machine. For this reason, the VSD approach was considered the most convenient for the machine parameters investigation necessary for

mapping. In Fig. 4.13 an equivalent iron resistance is reported to model the iron losses.

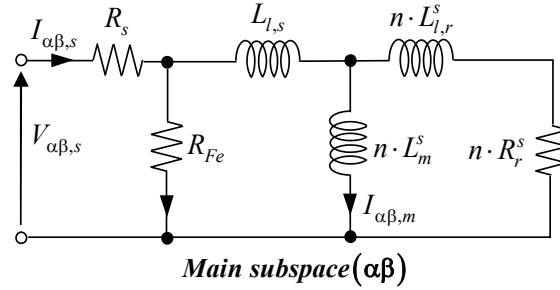


Figure 4.13 Equivalent VSD circuit of the machine in the main subspace in the stationary reference frame  $\alpha\beta$  including the iron losses.

Based on the VSD approach, the test elaboration procedure is independent of machine operation (healthy or faulty). The equivalent circuit in Fig. 4.13 is valid for all machine operations in the main  $\alpha\beta$  subspace: all symbols are consistent with the ones defined before and the components  $\alpha\beta$  stand for the equivalent defined using the VSD model approach.

The no-load and locked-rotor tests are analyzed as an equivalent three-phase machine by computing the average value of each variable from the ones of all active three-phase sets. The average of the values belonging to each of the three-phase sets allows computing the variables of the associated equivalent circuit as [93]:

$$i_\alpha = \frac{1}{n} \cdot \sum_{k=1}^n i_{\alpha,k}, \quad i_\beta = \frac{1}{n} \cdot \sum_{k=1}^n i_{\beta,k} \quad (4.136)$$

$$v_\alpha = \frac{1}{n} \cdot \sum_{k=1}^n v_{\alpha,k}, \quad v_\beta = \frac{1}{n} \cdot \sum_{k=1}^n v_{\beta,k} \quad (4.137)$$

where  $i_\alpha, i_\beta, v_\alpha, v_\beta$  are the current and voltage instantaneous components in the main subspace  $\alpha\beta$ , while  $i_{\alpha,k}, i_{\beta,k}, v_{\alpha,k}, v_{\beta,k}$  are the values of the considered variable in each  $k$ -three phase set, and  $n$  is the number of three-phase sets.

It is necessary to record the instantaneous values of the generic variables  $(\alpha\beta)_k$  because the matrix in Eq. (4.138) introduces an angle displacement between the RMS variables. The current components  $k$  is zero if the  $k$ -three-

phase set is fault, while the voltage components are equal to back-emf for the fault three-phase winding.

The components in  $\alpha\beta$  are evaluated by applying the Clarke transformation  $[C(\theta_k)]$  to the  $k$ -three-phase set as:

$$z_{\alpha\beta 0,k} = [C(\theta_k)] \cdot z_{abc,k}$$

$$[C(\theta_k)] = \frac{2}{3} \cdot \begin{bmatrix} \cos(\theta_k) & \cos(\theta_k + 2\pi/3) & \cos(\theta_k - 2\pi/3) \\ \sin(\theta_k) & \sin(\theta_k + 2\pi/3) & \sin(\theta_k - 2\pi/3) \\ 1/2 & 1/2 & 1/2 \end{bmatrix} \quad (4.138)$$

where  $z_{\alpha,i}$  and  $z_{\beta,i}$  components correspond to the first two rows (the zero-sequence component is not relevant) and the angle  $\theta_k$  is defined as the position of the first phase  $a$  of the  $k$ -three-phase set respect to the  $\alpha$ -axis.

Based on the instantaneous values, the RMS ones can be computed as in Eq. (4.139) for a generic variable  $z$  in the period  $T$ :

$$Z_{RMS} = \sqrt{\frac{1}{T} \cdot \int_0^T (z(t))^2 dt} \quad (4.139)$$

Finally, the power components in the main subspace  $P_\alpha, P_\beta$  are computed for the analysis of the standard test as:

$$P_\alpha = \frac{3}{2} \cdot n \cdot V_\alpha \cdot I_\alpha, \quad P_\beta = \frac{3}{2} \cdot n \cdot V_\beta \cdot I_\beta \quad (4.140)$$

where the capital letters stand for RMS values (i.e.  $V_\alpha$  represents the RMS value of  $v_\alpha$ ). The current, voltage and power components allow defining the phase RMS current  $I_s$ , phase RMS voltage  $E_s$ , and the input power  $P_{in}$  as:

$$I_s = \sqrt{I_\alpha^2 + I_\beta^2}$$

$$E_s = \sqrt{V_\alpha^2 + V_\beta^2} \quad (4.141)$$

$$P_{in} = P_\alpha + P_\beta$$

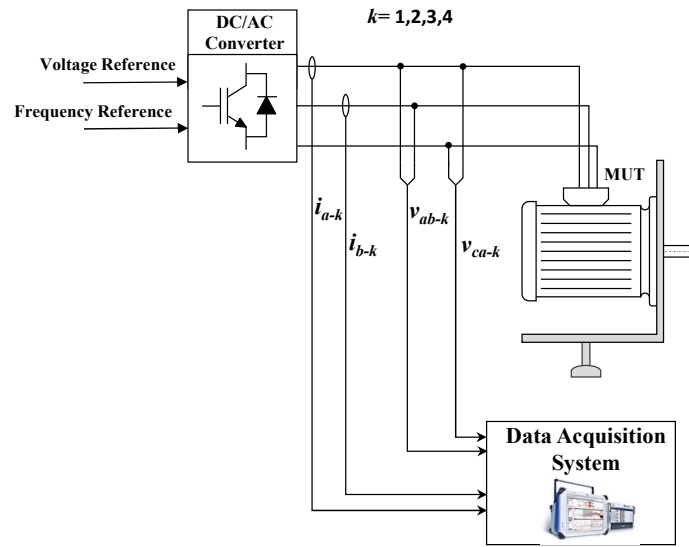


Figure 4.14 Sketch of the test rig used for parameter measurement elaborated using VSD approach.

To record the instantaneous variables, a more sophisticated test rig is necessary. A sketch of the test bench used for the machine characterization under power converter is shown in Fig. 4.14 for a generic winding set  $k^{th}$  ( $k = 1, 2, 3, 4$ ). The experimental tests have been performed using four independent three-phase inverters that are part of a modular converter to which the voltage and frequency references have been provided. A single DC power source feeds the inverter modules [124]. The inverter modules are fed by a single DC power source providing a DC link voltage of 270 V. The digital controller is the dSpace, and the sampling frequency and the inverter switching frequency have been set at 5 kHz.

Two wattmeter method configuration for electrical variables measurement has been used. The phase currents have been measured using the high-performance current transducers LEM IT 200-S Ultrastab, and line-to-line PWM voltages have been measured using the HBM, consisting of a voltage card equipped with high-voltage/high-speed acquisition channels (1000 V, 18 bit, 2 MS/s). The electrical quantities have been sampled and stored with a sampling frequency of 2 MS/s using the data recorder HBM. In this way, using the data elaboration software integrated with the instrument, the time-fundamental electric power of the IM has been computed. Open-winding

fault conditions have been emulated through the shut-off of the three-phase power converter units for all possible permutations.

A sketch of the procedures for the standard tests elaboration is reported in Fig. 4.15. It is essential to highlight that using the VSD approach, the RMS variables of the  $k$ - and  $z$ -three-phase sets cannot be summed related to the displacement angle introduced by the Clarke transformation Eq. (4.138). For this reason, the instantaneous measurements of the variables both healthy and fault sets are necessary.

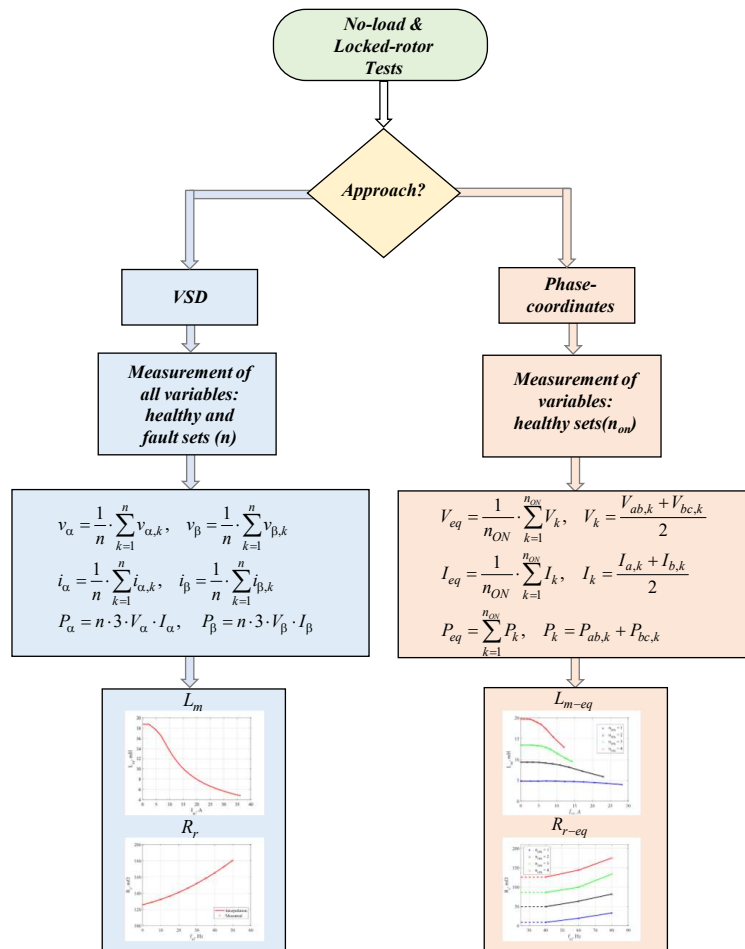


Figure 4.15 Procedures of the standard tests elaboration.

### 4.7.3 Locked-rotor tests

#### Phase-coordinates

The locked-rotor test is performed by imposing the machine-rated current at different supply frequencies [82] in different machine configurations. The locked-rotor tests have been performed to determine the rotor resistance as a function of the slip frequency (to account for the skin effect on the rotor bar), limiting the supply frequency. In this way, the skin effect on the stator resistance is practically always negligible, and the rotor resistance can be estimated by the difference of the locked-rotor resistance and  $R_{s,0}$  reported at the test temperature Eq. (4.142). In normal and faulty conditions, the measured equivalent rotor resistance as a function of the slip frequency is reported in Fig. 4.16. By extrapolating at zero frequency the trends shown in this figure, the dc values of the rotor resistance are obtained. The rotor resistances at different machine configurations were thus estimated by the difference between the locked-rotor resistance and the stator winding resistance measured by a dc test. The capital letters stand for RMS values.

$$R_{cc} = R_{s,0} + R_{r-eq} = \frac{P_{elt}}{3 \cdot n_{ON} \cdot I_s^2}, \quad R_{s,0} = R_{sk,0}, \quad \forall k = 1, \dots, n \quad (4.142)$$

where:

$$I_s = \frac{1}{n_{ON}} \cdot \sum_{k=1}^n I_{ks}, \quad I_{ks} = \frac{1}{2} \cdot (I_{a,sk} + I_{b,sk}) \quad (4.143)$$

$$P_{elt} = \sum_{i=1}^n P_{elt,i}, \quad P_{elt,k} = P_{ac,k} + P_{bc,k} \quad (4.144)$$

where:

- $I_{a,sk}$  and  $I_{b,sk}$  are the stator RMS phase currents measured with power meters in Aron configuration located on phase  $a$  and  $b$ ;
- $P_{ac,k}$  and  $P_{bc,k}$  stand for the power measured by power meters in Aron configuration located between the phase  $a$  and phase  $c$  and phase  $b$  and phase  $c$  for each  $k$ -three-phase winding set ;
- $P_{elt,k}$  stands for the electrical power of the  $k$ -three-phase set which is not zero if the  $k$  set is active.

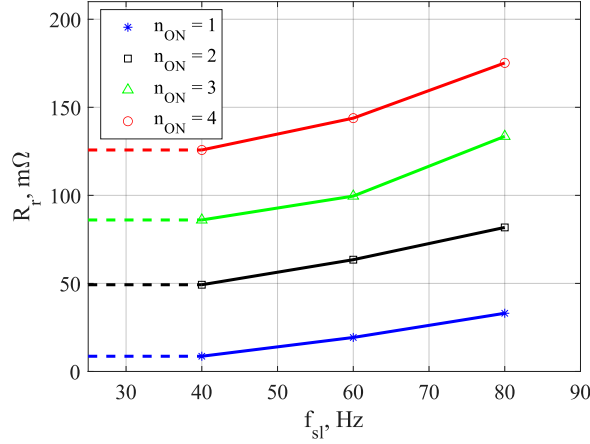


Figure 4.16 The equivalent rotor resistance for different winding configurations as a function of the slip frequency.

The equivalent locked rotor resistance depends on the active sets number, and the rescaling in Eq. (4.145) is confirmed by Fig. 4.16: the rescaling allows to evaluate of the rotor parameters just in normal conditions because applying Eq. (4.145) the profiles are overlapped.

$$R_{r-eq} = R_r \cdot \frac{n}{n_{ON}} \quad (4.145)$$

The total leakage inductance  $L_{cc}$  has been measured at different supply frequencies and machine conditions (normal and faulty). For each test, the  $L_{cc}$  has been evaluated as:

$$X_{cc} = R_{cc} \cdot tg(\varphi_{cc}), \quad L_{cc} = \frac{X_{cc}}{2 \cdot \pi \cdot f} \quad (4.146)$$

where  $R_{cc}$  is computed in Eq. (4.142). The power factor of locked-rotor test is computed as:

$$\cos(\varphi_{cc}) = \frac{P_{elt}}{n_{ON} \cdot 3 \cdot E_s \cdot I_s} \quad (4.147)$$

where  $P_{elt}$  and  $I_s$  are consistent with Eq. (4.144) and the stator RMS phase voltage  $E_s$  is computed as:

$$E_s = \frac{1}{n_{ON}} \cdot \sum_{k=1}^n E_{s,k}, \quad E_{s,k} = \frac{1}{2} \cdot (E_{a,skb} + E_{b,skc}) \quad (4.148)$$



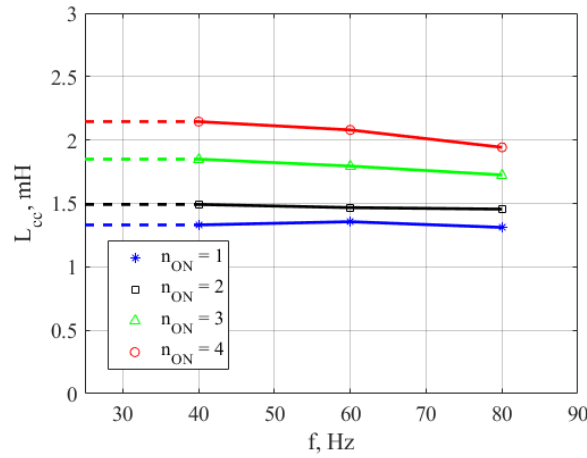


Figure 4.17 The equivalent locked-rotor inductance for different winding configurations.

Finally, the leakage rotor inductance is computed as in Eq. (4.149), assuming the  $L_{l,s} = 1 \text{ mH}$ , evaluated with another test [123]. The trends at different machine configurations are reported in Fig. 4.17.  $L_{cc}$  value decreases as the number of faulty winding sets increases, as already highlighted in Eq. (4.135). In contrast, the stator leakage inductance  $L_{l,s}$  is not influenced by the number of active sets.

$$L_{l,r-eq} = \frac{X_{cc}}{2 \cdot \pi \cdot f} - L_{l,s} \quad (4.149)$$

### VSD

The same result can be obtained by elaborating the locked-rotor test based on the VSD-based model obtaining the rotor parameters and the magnetizing inductance independent of the active sets. However, a more sophisticated data recorder is necessary for recording instantaneous values.

The rotor resistance can be expressed as:

$$R_r = \frac{P_{jr}}{n \cdot 3 \cdot I_s^2} \quad (4.150)$$

where:

$$P_{jr} = P_{elt} - n \cdot 3 \cdot R_s \cdot I_s^2, \quad (4.151)$$

$I_s$  and  $P_{elt}$  represent the RMS stator current and the input electrical power. Note that in Eq. (4.150) and Eq. (4.151) the equations depend on nominal

number sets  $n$  and not on the active number sets  $n_{ON}$  related to the VSD approach. The tests elaborated based on VSD approach confirm the trends in Fig. 4.16, overlapping the profiles based on Eq. (4.150), providing a  $R_r = 126 \text{ m}\Omega$  at lowest frequency. The rotor resistance profile in the slip frequency function is shown in Fig. 4.18.

About the stator leakage inductance, elaborating the locked-rotor test based on VSD-based model the following variables can be defined:

$$Q_{elt} = \sqrt{(3 \cdot n \cdot E_s \cdot I_s)^2 - (3 \cdot n \cdot R_s \cdot I_s^2)^2} \quad (4.152)$$

$$Q_{l,s} = 3 \cdot n \cdot 2 \cdot \pi \cdot f \cdot L_{l,s} \cdot I_s^2$$

The reactive power associated to the leakage rotor inductance is expressed as:

$$Q_{l,r} = Q_{elt} - Q_{l,s} \quad (4.153)$$

Based on  $Q_{l,r}$  the equivalent leakage rotor inductance is computed as Eq. (4.154), obtaining the profiles overlapped for all machine conditions, confirming Eq. (4.135).

$$L_{l,r} = \frac{Q_{l,r}}{2 \cdot \pi \cdot f \cdot 3 \cdot n \cdot I_s^2} \quad (4.154)$$

The value of  $L_{l,r}$  do not depend on the frequency as shown in Fig. 4.17 and it is assumed  $L_{l,r} = 1.2 \text{ mH}$ .

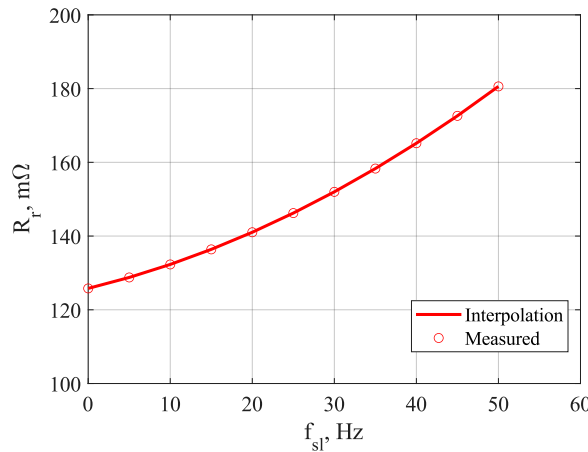


Figure 4.18 The rotor resistance as a function of the slip frequency.

#### 4.7.4 No-load test

From the no-load operation of the machine, it is possible to estimate the conventional iron losses. Here, the nomenclature *conventional* refers to the iron losses measured by the standard no-load test procedures. This contribution considers the magnetic losses in the core (i.e., hysteresis and eddy current) and the additional losses due to secondary effects, e.g., harmonic Joule losses in the rotor cage. These other harmonic losses are not load-dependent; thus, they are ‘automatically’ included in the measured conventional iron losses. In this way, they can also estimate the machine’s efficiency in different load conditions.

##### Phase-coordinates

The conventional iron losses  $P_{c,Fe}$  can be estimated from the power balance of the machine operating at no-load as:

$$P_{c,Fe} = P_{elt} - P_{js} - P_{fv} \quad (4.155)$$

where  $P_{elt}$ ,  $P_{fv}$  and  $P_{js}$  are the no-load active power, the mechanical losses (related to the friction and ventilation) and the stator Joule losses, respectively computed as Eq. (4.156). Note that the active power of  $k$ -three-phase set can be positive or negative. The total  $P_{elt}$  must be positive.

$$\begin{aligned} P_{elt} &= \sum_{k=1}^n P_{elt,k} & P_{elt,k} &= P_{k,ab} + P_{bc,k} \\ P_{js} &= \sum_{i=1}^n P_{js,k} & P_{js,k} &= 3 \cdot R_s \cdot I_{sk}^2 \end{aligned} \quad (4.156)$$

In no-load tests, the  $I_s$  has not been calculated because the three-phase sets are unbalanced in currents despite the symmetry in the supply of voltages between the sets.

Concerning the mechanical losses  $P_{fv}$  are computed by extrapolating the intercept of Eq. (4.157) for a supply voltage equal to zero. Moreover, since the slip speed is negligible in no-load conditions, the mechanical speed is assumed to be identical to the synchronous one, i.e.,  $\omega_m = 60 \cdot f_s/p$  (rpm). Finally, the ratio between the mechanical losses and the mechanical speed provides the value of the torque loss. The profile of mechanical losses of the

benchmark machine is reported in Fig. 4.19.

$$P_{c,Fe} + P_{fv} = P_{elt} - P_j \quad (4.157)$$

The following procedure has been adopted for magnetizing inductance evaluation. The no-load reactive power  $Q_{elt}$  in input to the machine is first calculated as Eq. (4.158). The reactive power of the  $i$ -three-phase set  $Q_{elt,i}$  is zero if the considered set is a fault.

$$Q_{elt} = \sum_{k=1}^n Q_{elt,k}, \quad Q_{elt,k} = \sqrt{\left(3 \cdot E_{sk} \cdot I_{sk}\right)^2 - \left(P_{elt,k} - 3 \cdot R_s \cdot I_{sk}^2\right)^2} \quad (4.158)$$

where  $E_{si}$  is the measured value of the RMS phase voltage of the  $k$ -three-phase set ( $E_{si} = 1/2 \cdot (E_{ab,sk} + E_{bc,sk})$ ). Later, the machine's back-emf  $E_{Fe}$  is obtained as:

$$E_{Fe} = \frac{V_{Fe}}{\sqrt{3}}, \quad V_{Fe} = V_s - DV \quad (4.159)$$

where  $V_s$  stands for the stator line-to-line voltage computed as Eq. (4.160), while  $DV$  represent the stator resistance drop on  $R_s$  expressed as Eq. (4.160). Note that  $V_s$  is the mathematical mean of the stator voltages of all sets; the stator voltage of the  $i$ -three-phase set is zero if the  $i$  set is fault. The no-load tests are carried out imposing the stator voltage, so the sets in terms of

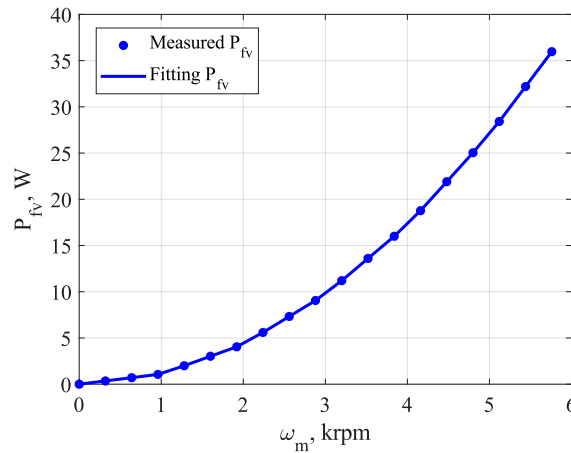


Figure 4.19 Mechanical losses of the tested IM.

voltage are symmetrical.

$$\begin{aligned} V_s &= \frac{1}{n_{ON}} \cdot \sum_{k=1}^n V_{sk}, & V_{sk} &= \frac{1}{2} \cdot (V_{ab,sk} + V_{bc,sk}) \\ DV &= \frac{1}{n_{ON}} \cdot \sum_{k=1}^n DV_k, & Dv_k &= \sqrt{3} \cdot R_s \cdot I_{sk} \cdot \cos(\varphi_{Fe,k}) \end{aligned} \quad (4.160)$$

The power factor  $\cos(\varphi_{Fe,k})$  is evaluated downstream of stator resistance as:

$$\cos(\varphi_{Fe,k}) = \frac{P_{elt,k} - P_{js,k}}{\sqrt{Q_{elt,k}^2 + (P_{elt,k} - P_{js,k})^2}} \quad (4.161)$$

Computed the back-emf  $E_{Fe}$  in Eq. (4.160), the magnetizing current can be computed as Eq. (4.162). It is reasonable to assume that the rotor currents, due to the mechanical losses, give a negligible contribution to the magnetizing current. Therefore, the stator inductance  $L_s$  is computed considering the equivalent circuit of the machine shown in Fig. 4.23, but neglecting the rotor current related to the mechanical losses.

$$I_m = \frac{\sqrt{Q_{elt}^2 + (P_{elt} - P_{js} - P_{c,Fe})^2}}{3 \cdot n_{ON} \cdot E_{Fe}}, \quad P_{js} = \sum_{k=1}^n P_{js,k} \quad (4.162)$$

Finally, the stator equivalent inductance is computed as:

$$\begin{aligned} L_s &= \frac{E_{Fe}}{2 \cdot \pi \cdot f \cdot I_m} \Rightarrow \\ &\Rightarrow L_{m-eq} = L_s - L_{l,s} \end{aligned} \quad (4.163)$$

In Fig. 4.20, the equivalent magnetizing inductance  $L_{m-eq}$  based on Eq. (4.163) is reported in all four different operating conditions, obtaining different profiles related to different active number sets  $n_{ON}$ . In Fig. 4.20, only some cases among all the permutations of the faulty three-phase windings are shown because it has been noticed that the results exclusively depend on the number of active sets. Also, the trends do not depend on the supply frequency. In saturated conditions, the no-load current measured with one active set is higher than that in normal conditions by a factor  $4/n_{ON}$ .

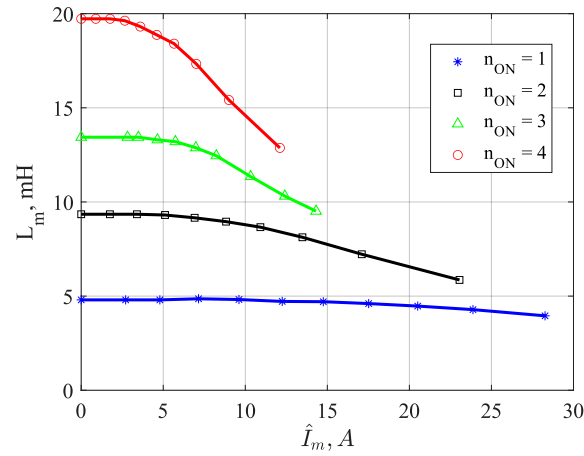


Figure 4.20 The equivalent magnetizing inductance for different winding configurations.

If the number  $n_{ON}$  of the active set decreases, the remaining active sets draw more current to produce the same flux, injecting the same equivalent current, defined as Eq. (4.136). Considering faulty conditions, i.e.,  $n_{ON} = 3$ , the respective current is zero  $i_{\alpha,s3} = i_{\beta,s3} = 0$  A. The equivalent current is decreased, but the current injected in the machine is higher at the same flux. The magnetizing profiles confirm Eq. (4.134), and applying a scaling factor  $n_{on}/4$ , the profiles are overlapped.

Based on Eq. (4.164) and Eq. (4.157), Fig. 4.21 reports the measured conventional iron loss profiles obtained. The conventional iron losses are shown at different supply frequencies only in the case of one and four active winding sets to help readability. Their value increases with the frequency for each possible machine configuration. However, according to Fig. 4.21, comparing the conventional iron loss profiles in normal conditions (4 sets ON) with those in faulty conditions (1 set ON) at the same supply frequency (60 Hz), they are not overlapped, demonstrating that the additional studies are necessary. Also, it is interesting to notice that a factor cannot scale their variation  $4/n_{on}$ , as observed for the rotor and magnetizing parameters. The complete maps of the conventional iron losses in the function of the supply frequency and stator flux linkage values are shown in Fig. 4.22.

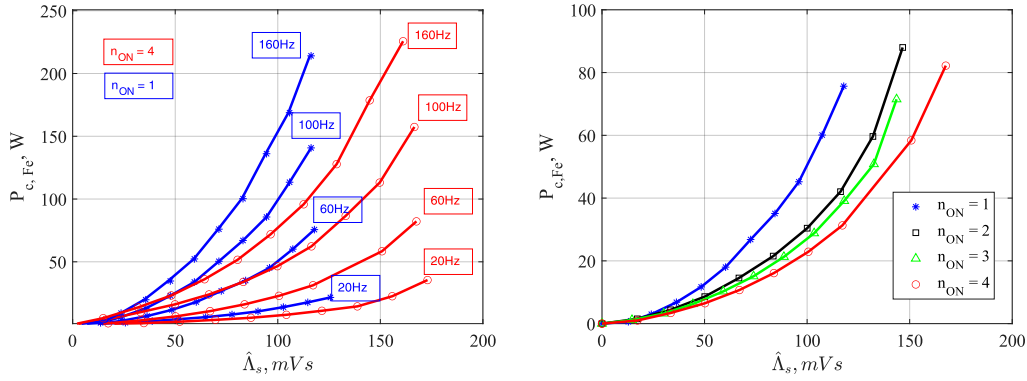


Figure 4.21 Iron losses for one and four active sets at different frequencies (left) and iron losses at 60 Hz (right).

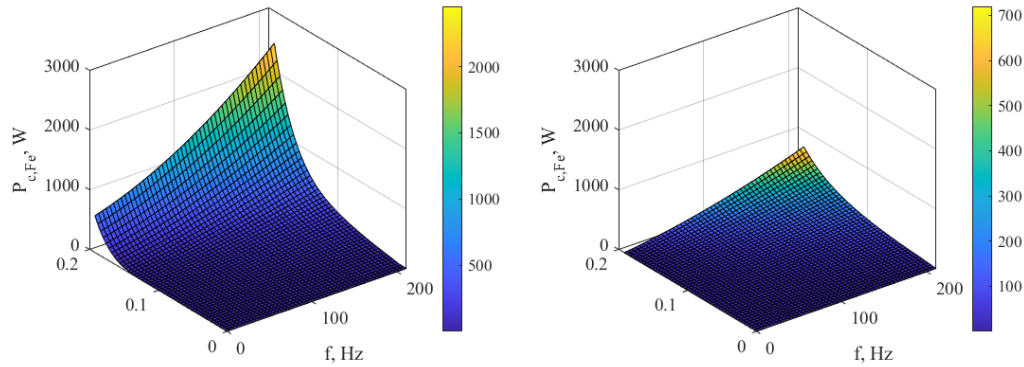


Figure 4.22 Experimental iron losses map with 1 active set (left) and four active sets (right) in function of frequencies and stator flux linkage.

It is noted how the iron losses significantly increase when the machine operates in the worst faulty condition, i.e., one active set. For comparison, it is interesting to observe their maximum value at the rated stator flux linkage of 0.15 Vs and maximum supply frequency of 200 Hz. In the case of one active set, the losses are about 650 W, while with 4 active sets, they are almost halved, i.e., 320 W. Based on the considerations reported before, confirmed by the experimental results, the conventional iron losses modeled with an equivalent iron loss resistance  $R_{Fe}$  cannot be rescaled in faulty conditions as was done for the rotor magnetizing parameters. An experimental 2D look-up table is thus necessary to accurately map the conventional iron losses for the efficiency evaluation in different load conditions. The trend of

conventional iron losses is related to the MMF in the air gap. For this reason, the following section investigates analyzing the harmonic content. Further analysis would be necessary to investigate the iron losses trend in normal and faulty conditions of multi-three-phase IM.

### VSD

The magnetizing inductance trend can be obtained by introducing the post-process of the no-load tests based on VSD modeling. The equivalent circuit valid for the no-load tests is reported in Fig. 4.23. Indeed, defining the current, voltage and power components in the main subspace  $\alpha\beta$  using Eq. (4.136) and Eq. (4.140), the conventional iron losses are expressed as:

$$P_{c,Fe} = P_{elt} - P_{js} - P_{fv} \quad (4.164)$$

where  $P_{elt}$  stands for no-load electrical power and  $P_{js}$  stands for the total stator Joule losses related to all three-phase sets  $n$  expressed as:

$$P_{elt} = P_\alpha + P_\beta, \quad P_{js} = n \cdot 3 \cdot E_s \cdot I_s \quad (4.165)$$

where:

$$E_s = \sqrt{V_\alpha^2 + V_\beta^2}, \quad I_s = \sqrt{I_\alpha^2 + I_\beta^2} \quad (4.166)$$

$$P_\alpha = n \cdot 3 \cdot V_\alpha \cdot I_\alpha, \quad P_\beta = n \cdot 3 \cdot V_\beta \cdot I_\beta$$

The back-emf on equivalent iron resistance  $E_{Fe}$  (peak value) can be computed as:

$$E_{Fe} = \frac{S_{Fe}}{n \cdot 3 \cdot I_s} \quad (4.167)$$

where:

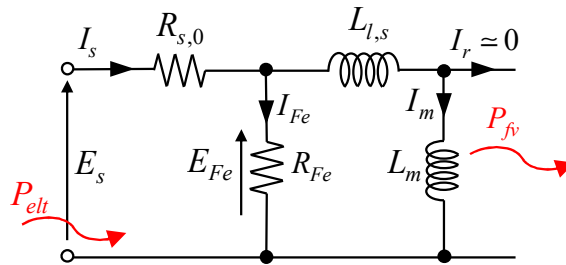


Figure 4.23 Multi-three-phase IM's equivalent circuit of the no-load test.



$$S_{Fe} = \sqrt{P_{Fe}^2 + Q_{elt}^2}, \quad Q_{elt} = \sqrt{(n \cdot 3 \cdot E_s \cdot I_{s,rms})^2 - P_{elt}^2} \quad (4.168)$$

Based on Eq. (4.168) and assuming the rotor currents due to the mechanical losses give a negligible contribution to the magnetizing current  $I_m$ , the magnetizing current  $I_m$  is thus calculated as:

$$I_m = \frac{S_{Fe}}{n \cdot 3 \cdot E_s}, \quad I_{m-eq} = I_m \cdot \frac{n}{n_{ON}} \quad (4.169)$$

Finally, the stator inductance is computed as:

$$L_s = \frac{1}{2 \cdot \pi \cdot f} \cdot \frac{Q_{elt}}{n \cdot 3 \cdot I_m^2} \quad (4.170)$$

where:

$$L_m = L_s - L_{l,s}, \quad L_{l,s} = 1 \text{ mH} \quad (4.171)$$

By applying the procedure presented in Eq. (4.164) - Eq. (4.171), the profiles of the magnetizing inductance presented in Fig. 4.20 are overlapped, confirmed Eq. (4.134).

In conclusion, the no-load and locked-rotor tests can be performed even in healthy conditions (for the benchmark machine with 4 active sets) since the rescaling of the machine parameters is confirmed by the presented experimental tests. For the considered machine prototype, the no-load and locked-rotor tests with all three-phase sets active (normal conditions) led to the following results:

$$\begin{aligned} n_{ON} = 4 : L_{m-eq} &= 18 \text{ mH}, \quad L_{l,r-eq} = 1.14 \text{ mH}, \quad R_{r-eq} = 126 \text{ m}\Omega \\ VSD : L_m^{VSD} &= 18 \text{ mH}, \quad L_{l,r}^{VSD} = 1.14 \text{ mH}, \quad R_r^{VSD} = 126 \text{ m}\Omega \Rightarrow \\ \Rightarrow MS : L_m^{MS} &= 4.5 \text{ mH}, \quad L_{l,r}^{MS} = 0.28 \text{ mH}, \quad R_r^{MS} = 31.5 \text{ m}\Omega \end{aligned} \quad (4.172)$$

The profile of the magnetizing inductance with both MS and VSD approaches is shown in Fig. 4.24, where the rescaling of the magnetizing current and inductance is percetible.

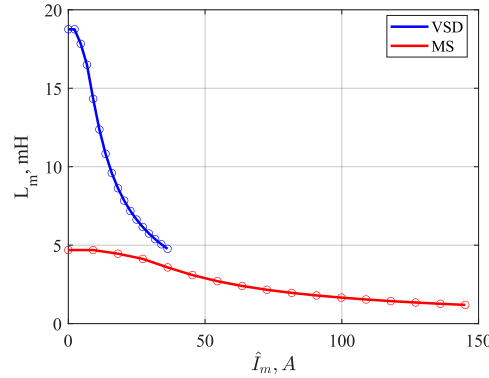


Figure 4.24 Magnetizing inductance vs. peak magnetizing current with MS and VSD approach.

However, the tests in healthy conditions are insufficient to investigate the machine's iron losses. Indeed, as shown in Fig. 4.21 and 4.22 the trend is not proportional to the active sets number, as in Eq. (4.134) and Eq. (4.135). For the thesis goal of accurately mapping multi-three-phase IM in normal and open-winding faulty conditions, the iron losses must be considered on the whole torque-speed range. Still, in particular, for high-speed applications when this loss contribution is relevant.

#### 4.7.5 MMF Distribution in normal and faulty conditions

This subsection analyses the stator magnetomotive force (MMF) distribution in normal and faulty conditions for multi-three-phase machines to investigate the iron losses trend in different machine configurations [122]. Under the assumptions of ideal magnetic cores ( $\mu_{Fe} \rightarrow \infty$ ) and an infinitesimal slot opening, it is simple to determine the air-gap MMF step-like distribution summing the contribution of each three-phase set. The MMF distribution can be computed as:

$$MMF(\alpha, t) = \sum_{x=1,2,3,4} \left[ \sum_{h=6k+1} \frac{3}{2} \cdot \hat{I}_m \cdot \frac{Z_f \cdot k_{w,h}}{hp\pi} \sin \left( h p \alpha - \omega t - (x-1) \cdot \frac{(h-1)\pi}{12} \right) \right] \quad (4.173)$$

where  $\hat{I}_m$  is the peak value of the magnetizing phase current,  $Z_f$  is the number of conductors in series per phase,  $k_{w,h}$  is the harmonic winding factor (equal

to 1 for each harmonic because the winding has been distributed using 1 slot/pole/phase),  $p$  is the pole pair number,  $h$  is the harmonic index ( $h = 1$  for the fundamental four-pole distribution),  $x$  is the set index and  $k = 0, \pm 1, \pm 2, \dots, \pm \infty$ . When all four three-phase sets are active, Eq. (4.173) can be simplified in Eq. (4.174), where it is possible to observe that only the tooth harmonics are present in the MMF harmonic spectrum.

$$MMF(\alpha, t) = 6 \cdot \hat{I}_m \cdot \sum_{h=24k+1} \frac{Z_f \cdot k_{w,h}}{hp\pi} \sin(hp\alpha - \omega t) \quad (4.174)$$

However, Eq. (4.173) is more general, and it can be used to investigate better the MMF harmonic spectrum fault conditions of one or more three-phase sets. For this purpose, it is helpful to represent each MMF harmonic of a three-phase winding as a spatial vector, where the shift angle between the vectors must be defined considering the harmonic order  $h$  with its correct sign.

The sketch of these vector diagrams is shown in Fig. 4.25: the color identifies the set, like in Fig. 4.10. In this table, the amplitude of the harmonics is not in scale for readability reasons. Looking at Fig. 4.25, it is evident that when all the three-phase sets are supplied with the same magnetizing current, all the harmonic sums are equal to zero. The exception is just for the fundamental and the tooth harmonics (i.e.,  $h = 23$  and  $h = 25$ ). For example, in the case of the faults of the second set (Set 2 in Fig. 4.10), the black dashed arrow disappears, and the harmonic sums are no longer equal to zero for all the harmonics orders. It is interesting to observe that different MMF harmonics can be present in the air gap for a fault of two sets if the two active sets are shifted by 15 or 30 electrical degrees, respectively.

The step-like MMF waveforms for selected working conditions of the quadruple-three-phase winding are reported in Fig. 4.26 - Fig. 4.29, while their harmonic contents are computed Table 4.1 to Table 4.25. The MMF harmonics have been calculated using  $\hat{I}_m = 1$  A, assuming the problem is magnetically linear. With respect to the lower order MMF harmonics (i.e. the belt harmonic  $h = 5$  and  $h = 7$ ), in absolute terms the most severe case is the considered two-sets fault (see Table 4.3), while the one-set and the three-sets faults are substantially comparable. It is also interesting to observe that the

$23^{rd}$  and  $25^{th}$  tooth harmonics decrease with the increase of the number of faulty sets. Also, the fundamental components show the same trend.

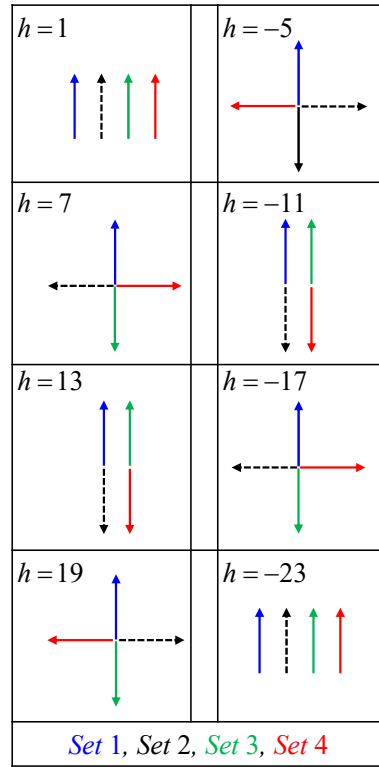


Figure 4.25 Spatial vector diagrams of the air-gap MMF harmonics for the 4-three-phase winding.

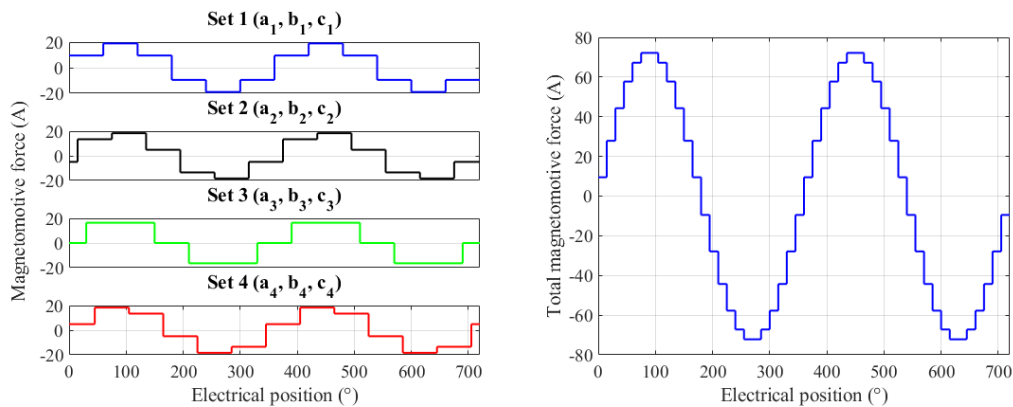


Figure 4.26 MMF distribution for each set ( $x = 1, \dots, 4$ ) (left), the MMF distribution in the air-gap (right) with four active sets.

Table 4.1 Harmonic content of the MMF with four active sets.

Harmonic spectrum	
Harmonic order(-)	Magnitude (%)
1	72.6 A (100.0%)
5	0.0%
7	0.0%
13	0.0%
17	0.0%
19	0.0%
23	31.1 A(4.3%)
25	2.9 A(4.0%)

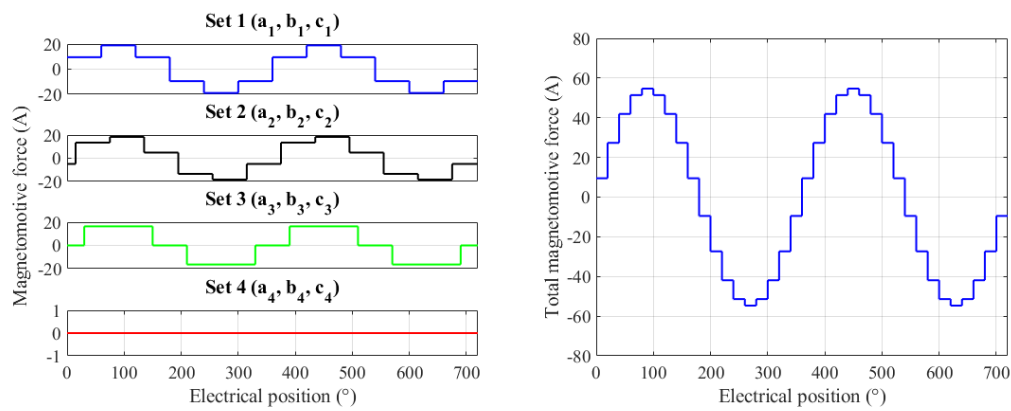
Figure 4.27 MMF distribution for each set ( $x = 1, \dots, 4$ ) (left), the MMF distribution in the air-gap (right) with three active sets.

Table 4.2 Harmonic content of the MMF with 3 active sets.

Harmonic spectrum	
Harmonic order(-)	Magnitude (%)
1	54.4 A (100.0%)
5	3.6 A (6.7%)
7	2.6A (4.8%)
11	1.6 A (3.0%)
13	1.4 A(2.6%)
17	1.1 A(2.0%)
19	1 A(1.8%)
23	2.3 A(4.3%)
25	2.2 A(4.0%)

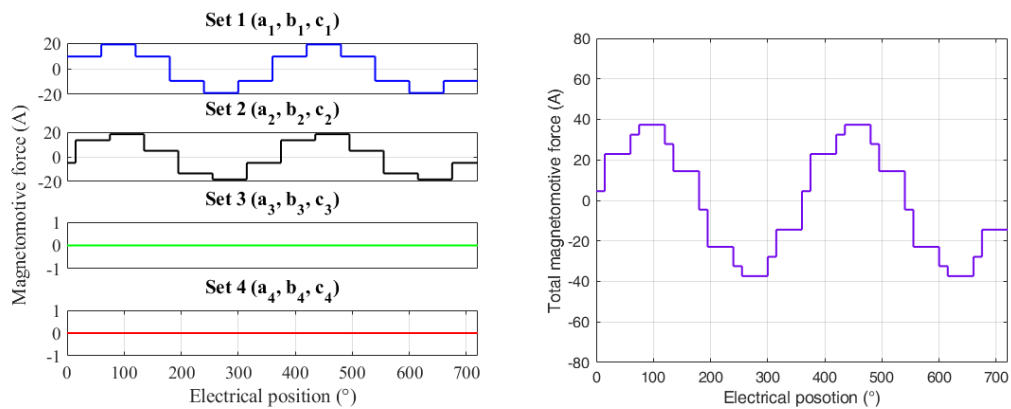


Figure 4.28 MMF distribution for each set ( $x = 1, \dots, 4$ ) (left), the MMF distribution in the air-gap (right) with two active sets.

Table 4.3 Harmonic content of the MMF with 2 active sets.

Harmonic spectrum	
Harmonic order(-)	Magnitude (%)
1	36.6 A (100%)
5	5.1 A (14.0%)
7	3.6 A (10.0%)
11	0 A (0.0%)
13	0 A (0.0%)
17	1.5 A (4.2%)
19	1.3 A (3.7%)
23	1.6 A (4.3%)
25	1.4 A (4.0%)

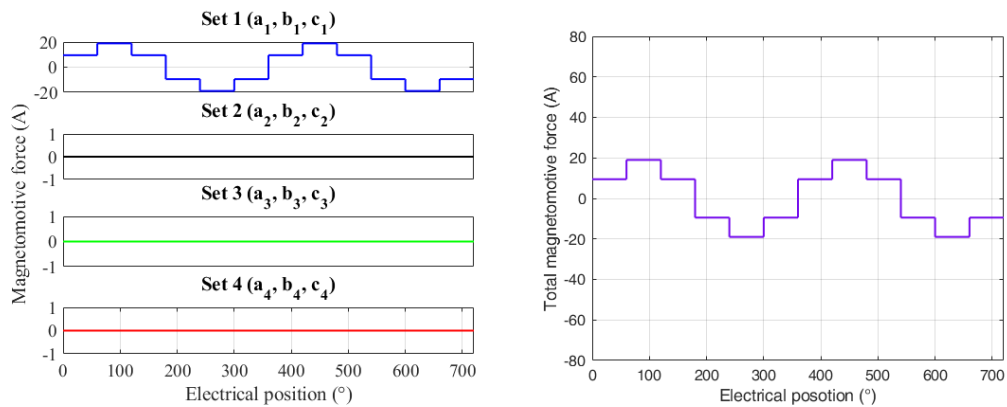


Figure 4.29 MMF distribution for each set ( $x = 1, \dots, 4$ ) (left), the MMF distribution in the air-gap (right) with one active sets.

Table 4.4 Harmonic content of the MMF with 1 active set.

Harmonic spectrum	
Harmonic order(-)	Magnitude (%)
1	18.1 A (100.0%)
5	3.6 A (20.0%)
7	2.6 A (14.3%)
11	1.6 A (9.1%)
13	1.4 A (7.7%)
17	1.1 A (5.9%)
19	1.0 A (5.3%)
23	0.8 A (4.3%)
25	0.7 A (4.0%)

## 4.8 Magnetic model based on the flux maps

The optimal operating criteria, such as maximum torque per ampere (MTPA), field-weakening (FW), and maximum torque per volt (MTPV), are often implemented to enhance the efficiency and control performance of three-phase IM. However, for the three-phase counterparts, the mentioned locus is becoming increasingly crucial in multi-three-phase IM. Indeed, an optimal flux selection represents a key factor in the multi-three-phase machine, especially in faulty conditions: a wrong selection of the flux operating point involves a lower efficiency, and the torque capability is heavily compromised. However, an optimal choice of the flux operating point can be performed following the MTPA, both normal and faulty conditions [123]. For this reason, in this section, the study to investigate the MTPA trajectory is presented, showing how the different approaches presented before provide the same results in all machine configurations ( $n_{ON} = 4$ ,  $n_{ON} = 3$ ,  $n_{ON} = 2$ ,  $n_{ON} = 1$ ).

### 4.8.1 MS approach

The manipulation of the magnetic model based on the flux maps allows the definition of the MTPA locus in both normal and faulty conditions. The



magnetic model of a multi-three-phase in rotating  $dq$  coordinates at the electrical speed  $\omega$  based on the MS approach, representing this section's starting point. All details about the MS approach are reported in Section 4.2, reporting here for simplicity the magnetic model expressed as in Eq. (4.175). The lowercase letters stand for dynamic values. The capital letter will be introduced for the model in steady-state conditions.

$$\begin{cases} s - \lambda i : & \lambda_{dq,sk} = L_{l,s} \cdot i_{dq,sk} + L_m^{MS} \cdot \sum_{k=1}^n i_{dq,sk} + L_m^{MS} \cdot i_{dq,r} \\ r - \lambda i : & \lambda_{dq,r} = L_{l,r}^{MS} \cdot i_{dq,r} + L_m^{MS} \cdot \sum_{k=1}^n i_{dq,sk} + L_m^{MS} \cdot i_{dq,r} \end{cases} \quad (4.175)$$

where:

- $\lambda_{dq,sk}$  and  $\lambda_{dq,r}$  stand for the stator flux linkage vector of the  $k$ -three-phase set ( $k = 1, \dots, n$ ) and rotor flux linkage vector (the rotor in MS approach is modelled with a three-phase winding), respectively;
- $i_{dq,sk}$  and  $i_{dq,r}$  stand for the stator current of the  $k$ -three-phase set and rotor current;
- $L_{l,s}$  and  $L_{l,r}^{MS}$  are the stator of the  $k$ -three-phase set and rotor leakage inductances, respectively;
- $L_m^{MS}$  is the magnetizing inductance.

From now on, the subscript  $MS$  will not report because, in this section, all parameters are to be understood referred to MS, otherwise specified. The rotor parameters and magnetizing inductance are referred to MS values, reported in Eq. (4.172) for the benchmark machine. The equivalent three-phase currents cannot be measured or directly controlled for a rotor cage. Therefore, the stator and rotor flux equations in Eq. (4.175) are combined in a single vector as:

$$\lambda_{dq,sk} = L_{l,s} \cdot i_{dq,sk} + L_m \cdot \sum_{k=1}^n i_{dq,sk} + \frac{L_m}{L_m + L_{l,r}} \cdot \left( \lambda_{dq,r} - L_m \cdot \sum_{k=1}^n i_{dq,sk} \right) \quad (4.176)$$

By introducing the rotor coupling factor  $k_r$  in Eq. (4.177), Eq. (4.176) is manipulated as in Eq. (4.178).

$$k_r = \frac{L_m}{L_m + L_{l,r}} \quad (4.177)$$

$$\begin{aligned} \lambda_{dq,sk} &= L_{l,s} \cdot i_{dq,sk} + L_m \cdot \sum_{k=1}^n i_{dq,sk} + k_r \cdot \lambda_{dq,r} - k_r \cdot L_m \cdot \sum_{k=1}^n i_{dq,sk} = \\ &= L_{l,s} \cdot i_{dq,sk} + L_m \cdot (1 - k_r) \cdot \sum_{k=1}^n i_{dq,sk} + k_r \cdot \lambda_{dq,r} = \\ &= L_{l,s} \cdot i_{dq,sk} + L_m \cdot \left( \frac{L_m - L_r}{L_r} \right) \cdot \sum_{k=1}^n i_{dq,sk} + k_r \cdot \lambda_{dq,r} = \\ &= L_{l,s} \cdot i_{dq,sk} + k_r \cdot L_{l,r} \cdot \sum_{k=1}^n i_{dq,sk} + k_r \cdot \lambda_{dq,r} \end{aligned} \quad (4.178)$$

The stator flux equation can be expressed in components as:

$$\begin{aligned} \lambda_{dq,sk} &= L_{l,s} \cdot i_{dq,sk} + k_r \cdot L_{l,r} \cdot \sum_{k=1}^n i_{dq,sk} + k_r \cdot \lambda_{dq,r} \Rightarrow \\ \Rightarrow \begin{cases} d: & \lambda_{d,sk} = L_{l,s} \cdot i_{d,sk} + k_r \cdot L_{l,r} \cdot \sum_{k=1}^n i_{d,sk} + k_r \cdot \lambda_{d,r} \\ q: & \lambda_{q,sk} = L_{l,s} \cdot i_{q,sk} + k_r \cdot L_{l,r} \cdot \sum_{k=1}^n i_{q,sk} + k_r \cdot \lambda_{q,r} \end{cases} \end{aligned} \quad (4.179)$$

In steady-state conditions, the rotor flux can be expressed as:

$$\begin{cases} d: & \Lambda_{d,r} = L_m \cdot \sum_{k=1}^n I_{d,sk} \\ q: & \Lambda_{q,r} = 0 \end{cases} \quad (4.180)$$

where the component  $\Lambda_{q,r}$  is zero because the considered rotating coordinates is characterized by the  $d$ -axis aligned with the rotor flux  $\lambda_r$ . By replacing Eq. (4.180) in Eq. (4.179), the stator magnetic model in components is expressed as Eq. (4.181). Please note that the parameters are intended as MS

ones, and the flux components are related to the  $k$ -three-phase set.

$$\left\{ \begin{array}{l} d: \quad \Lambda_{d,sk} = L_{l,s} \cdot I_{d,sk} + k_r \cdot L_{l,r} \cdot \sum_{k=1}^n I_{d,sk} + k_r \cdot L_m \cdot \sum_{k=1}^n I_{d,sk} \\ q: \quad \Lambda_{q,sk} = L_{l,s} \cdot I_{q,sk} + k_r \cdot L_{l,r} \cdot \sum_{k=1}^n I_{q,sk} \end{array} \right. \quad (4.181)$$

In a balanced machine the following relations are valid:

$$\left\{ \begin{array}{l} \lambda_{dq,sk} = \lambda_{dq,s} \\ \Lambda_{d,sk} = \Lambda_{d,s} \quad , \quad \forall k = 1, \dots, n_{ON} \\ \Lambda_{q,sk} = \Lambda_{q,s} \end{array} \right. \quad (4.182)$$

By opportunely adapting the rotor and magnetizing parameters in Eq. (4.181) and based on Eq. (4.182), the stator flux linkage components in Eq. (4.183) represent the machine flux of all active sets and not only the stator flux of the  $k$ -three-phase set. Indeed, the stator magnetic model equations can be expressed as in Eq. (4.183) where the rotor parameters and magnetizing inductance evaluated with MS approach are rescaled with  $n_{ON}$  as:

$$\left\{ \begin{array}{l} d: \quad \Lambda_{d,s} = L_{l,s} \cdot I_{d,s} + k_r \cdot n_{ON} \cdot L_{l,r} \cdot I_{d,s} + k_r \cdot n_{ON} \cdot L_m \cdot I_{d,s} \\ q: \quad \Lambda_{q,s} = L_{l,s} \cdot I_{q,s} + k_r \cdot n_{ON} \cdot L_{l,r} \cdot I_{d,s} \end{array} \right. \quad (4.183)$$

In conclusion, rescaling the MS parameters using the active sets number  $n_{ON}$ , the stator flux represents the machine stator flux related to all active sets. The equations of the stator flux components reported in Eq. (4.183) allow us to define the flux maps based on the MS approach for the active sets, which are equal to the machine flux maps (see Eq. (4.182)). Then the computation of the MTPA trajectory for both normal and faulty machine conditions is performed simply by changing the active sets number in Eq. (4.183). The stator flux linkage of the  $k$ -three-phase inactive/fault set ( $n - n_{ON}$ ) can be expressed as in Eq. (4.184). The subscript *OFF* stands for fault set and the flux maps are different than the ones of the active sets for the contribution

related to the leakage stator inductance.

$$\begin{cases} d: & \Lambda_{d,s-OFF} = \Lambda_{d,s} - L_{l,s} \cdot I_{d,s} \\ q: & \Lambda_{q,s-OFF} = \Lambda_{q,s} - L_{l,s} \cdot I_{q,s} \end{cases} \quad (4.184)$$

Before presenting the flux maps, and MTPA computation algorithm, a distinction is necessary. In Eq. (4.183) the stator flux linkage components depend on the stator currents. Therefore, considering the iron losses, the stator flux components depend on the flux- and torque-producing currents ( $I_{d,ft}, I_{q,ft}$ ). The iron losses are modeled using an equivalent iron resistance for each active set, assuming  $R_{Fe,k} = R_{Fe}$ . For simplicity, the subscript *ft* is removed, but where the subscript is omitted is to be understood as the flux- and torque-producing currents. The magnetic stator flux in Eq. (4.183) is replaced as:

$$\begin{cases} d: & \Lambda_{d,s} = L_{l,s} \cdot I_d + k_r \cdot n_{ON} \cdot L_{l,r} \cdot I_q + k_r \cdot n_{ON} \cdot L_m \cdot I_d \\ q: & \Lambda_{q,s} = L_{l,s} \cdot I_q + k_r \cdot L_{l,r} \cdot I_d \end{cases} \quad (4.185)$$

where  $(I_d, I_q) \equiv (I_{d,ft}, I_{q,ft})$ . Therefore, flux and torque maps of the IM are correlate the flux- and torque- producing *dq* currents  $I_d, I_q$  with the steady-state values of *dq* stator flux linkages  $\Lambda_d, \Lambda_q$  and electromagnetic torque  $T_{em}$ , which is expressed as:

$$T_{em} = \frac{3}{2} \cdot n_{ON} \cdot p \cdot (\Lambda_{d,s} \cdot I_q - \Lambda_{q,s} \cdot I_d) \quad (4.186)$$

Flux- and torque- maps are computed using the results of the no-load and locked-rotor tests and machine and/or converter limits, as reported in the following. Starting from the saturation profile of the magnetizing inductance  $L_m$  as a function of the peak magnetizing current  $\hat{I}_m$  (all variables (flux, current, etc. are peak values even if not specified ^), the MS profile is extrapolated for the active sets  $n_{ON}$ . Thus directly using the saturation profile of the MS magnetizing inductance obtained from the no-load test, shown in Fig. 4.24, the magnetizing inductance profile based on the active sets is obtained. According to the MS multi-three-phase model defined in the

rotating  $dq$  frame, the magnetizing current can be expressed as a function of the flux- and torque-producing currents as in Eq. (4.187).

$$L_m = f(I_m) , \quad I_m = \sqrt{I_d^2 + (I_q + I_{q,r})^2} \quad (4.187)$$

Please note that:

$$I_m^{MS} = n \cdot I_m, \quad L_m^{MS} = \frac{1}{n} \cdot L_m \quad (4.188)$$

Extending the expression in Eq. (4.187), using  $I_{q,r} = -(L_m/L_r) \cdot I_q$ , the magnetizing current is expressed as:

$$I_m = \sqrt{I_d^2 + I_q^2 \cdot \left(1 - \frac{L_m}{L_m + L_{l,r}}\right)^2} \quad (4.189)$$

However, Eq. (4.189) can be reasonably simplified as in Eq. (4.190) since the magnetizing inductance is relatively higher than rotor leakage one regardless of the saturation condition.

$$I_m \simeq I_d, \quad I_d \equiv I_{d,ft} \quad (4.190)$$

A regular mesh grid based on the magnetizing current  $I_m$  of flux- and torque-producing  $dq$  currents can be defined, and whose limits are set as:

$$\begin{aligned} 0 &\leq I_d \leq I_{m,max} \\ -I_{max} &\leq I_q \leq I_{max} \end{aligned} \quad (4.191)$$

where  $I_{m,max}$  is the maximum value of magnetizing current for which the magnetizing inductance has been experimentally identified. In contrast,  $I_{max}$  is the amplitude limit of the phase currents (peak value). The latter usually consists of the maximum overload current of the IM under consideration. Alternatively, it consists of the current limit imposed by the power electronics converter feeding the machine. It is highlighted that the steps of the  $dq$  currents composing the mesh grid must be set to define the flux- and torque maps with reasonable resolution. The current mesh grid, denoted with the subscript *map*, which dimension depends on the step current  $\Delta I$ , is organized

as:

$$I_d^{map} = \begin{bmatrix} 0 & 0 + \Delta I & \dots & I_{m,max} \\ 0 & 0 + \Delta I & \dots & I_{m,max} \\ \dots & \dots & \dots & \dots \\ 0 & 0 + \Delta I & \dots & I_{m,max} \end{bmatrix}, \quad I_q^{map} = \begin{bmatrix} -I_{max} & -I_{max} & \dots & I_{max} \\ -I_{max} + \Delta I & -I_{max} + \Delta I & \dots & -I_{max} + \Delta I \\ \dots & \dots & \dots & \dots \\ I_{max} & -I_{max} & \dots & I_{max} \end{bmatrix} \quad (4.192)$$

Now, to apply Eq. (4.185) the magnetizing inductance is extrapolated based on the active sets to get a mesh grid as:

$$L_m^{map} = interp1(I_m^{MS}, L_m^{MS}, n_{ON} \cdot I_d^{map}) \Rightarrow \Rightarrow L_m^{map} = \begin{bmatrix} L_m^{unsat} & \dots & \dots & L_m^{sat} \\ L_m^{unsat} & \dots & \dots & L_m^{sat} \\ \dots & \dots & \dots & \dots \\ L_m^{unsat} & \dots & \dots & L_m^{sat} \end{bmatrix} \quad (4.193)$$

where *interp1* consists of one-dimensional interpolation and  $L_m^{unsat}$  and  $L_m^{sat}$  stand for unsaturated (maximum) and saturated (minimum) magnetizing values. The product  $(n_{ON} \cdot I_d^{map})$  represents the sum of the stator currents, as visible on the equivalent circuit in Fig. 4.5.

For each  $dq$  point of the mesh grid defined in Eq. (4.192), the corresponding  $dq$  stator flux linkages are extracted based on Eq. (4.185), obtaining the 2-dimensional look-up tables of the stator flux components, defined as:

$$\Lambda_{d,s}^{map} = \begin{bmatrix} \Lambda_{d,s}(0, -I_{max}) & \dots & \dots & \Lambda_{d,s}(I_{m,max}, +I_{max}) \\ \dots & \dots & \dots & \dots \\ \dots & \dots & \dots & \dots \\ \Lambda_{d,s}(0, -I_{max}) & \dots & \dots & \Lambda_{d,s}(I_{m,max}, I_{max}) \end{bmatrix} \quad (4.194)$$

$$\Lambda_{q,s}^{map} = \begin{bmatrix} \Lambda_{q,s}(0, -I_{max}) & \dots & \dots & \Lambda_{q,s}(0, -I_{max}) \\ \dots & \dots & \dots & \dots \\ \dots & \dots & \dots & \dots \\ \Lambda_{q,s}(I_{m,max}, +I_{max}) & \dots & \dots & \Lambda_{q,s}(I_{m,max}, +I_{max}) \end{bmatrix}$$

When the above stator flux maps are known, the computation of the torque map on the selected  $I_d, I_q$  grid is straightforward: by repeating these oper-

ations for each  $dq$  point of the defined mesh grid Eq. (4.192) the torque is computed using Eq. (4.186). The torque map includes motor and generator operations due to the assumed symmetrical limits for the  $q$ -axis current in Eq. (4.191).

The profiles of the magnetizing inductance evaluated using the Eq. (4.193) of the 12-phase IM with a quadruple-three-phase configuration are reported for different machine conditions. The profiles of the magnetizing inductance do not change when the number of active three-phase sets changes. There is only a reduction in the saturated value.

The stator flux and torque maps for the tested 12-phase IM require the knowledge of the following inputs to compute the maps of the mesh grid defined in Eq. (4.192):

- Amplitude limit of the phase currents  $I_{max}$  equal to 24 A;
- The magnetizing profile reported in Fig. 4.30  $I_{m,max} = 36$  A;
- The active sets number  $n_{ON}$ .

According to the above-reported inputs and constraints, the stator flux and torque maps of the current mesh grid are computed for both normal and fault conditions. In Fig. 4.31 - Fig. 4.34 the components of the stator flux linkage

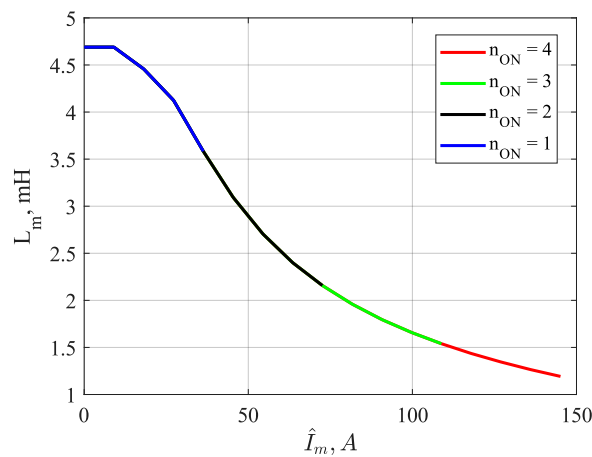


Figure 4.30 Magnetizing inductance in both normal and faulty conditions based on MS approach.

are reported, showing the same trend of the three-phase IM counterparts. The stator flux maps for each machine condition ( $n_{ON} = 4, \dots, 1$ ) represent the total machine flux and match the stator flux of each active set. Focusing on Fig. 4.31, the maps in the figure represent the machine flux and the flux of each of the four active sets (in this case, all sets are active). Focusing on Fig. 4.32: the maps in the figure represent the machine flux and the flux of each of the three active sets, while the stator flux of the inactive/fault set is different than the flux in the figure, and it can be computed as reported in Eq. (4.184). The maximum stator flux components are lower when the number of active sets decreases, and fixing the stator flux requires more current in fault conditions, as confirmed in Fig. 4.35.

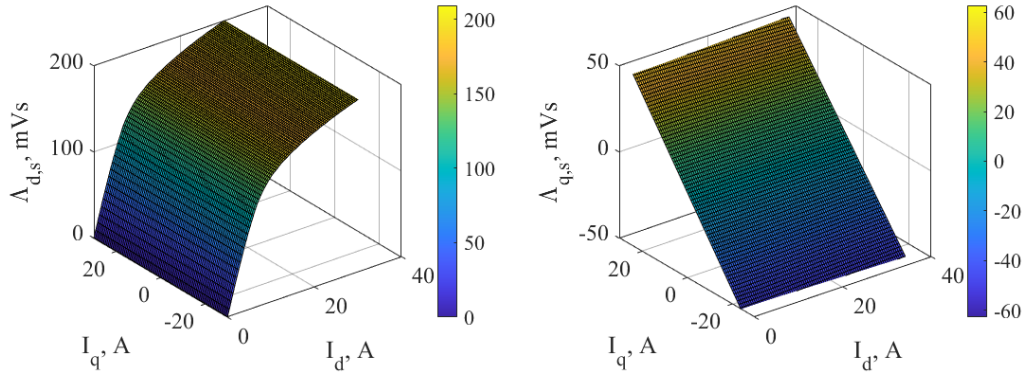


Figure 4.31 Stator flux linkage  $dq$  maps of the 12-phase IM in normal conditions: 4 active set (MS approach).

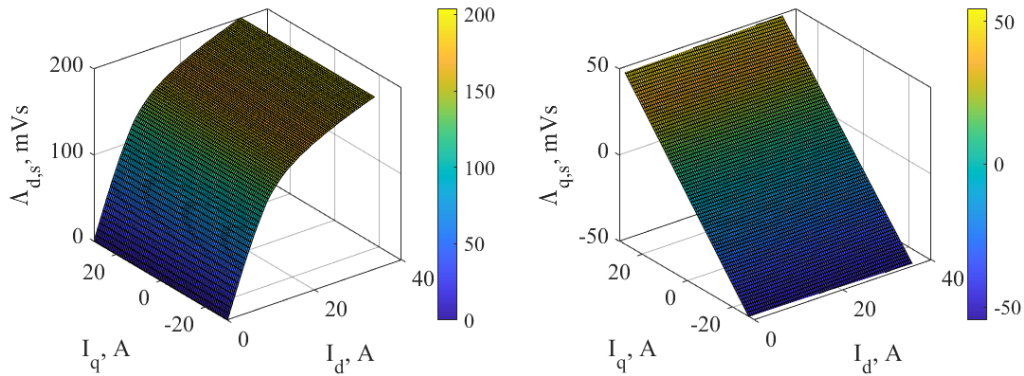


Figure 4.32 Stator flux linkage  $dq$  maps of the 12-phase IM in open-winding fault conditions: 3 active sets (MS approach).



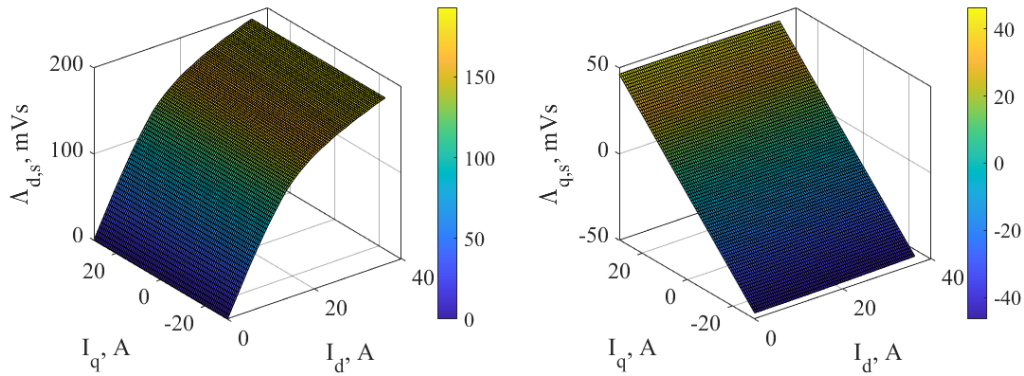


Figure 4.33 Stator flux linkage  $dq$  maps of the 12-phase IM in open-winding fault conditions: 2 active sets (MS approach).

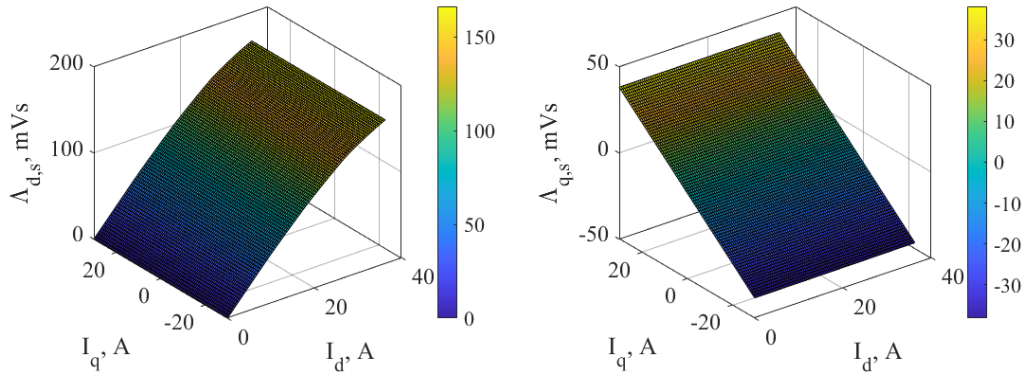


Figure 4.34 Stator flux linkage  $dq$  maps of the 12-phase IM in open-winding fault conditions: 1 active set (MS approach).

A straightforward comparison of the stator flux components in both normal and faulty conditions is shown in Fig. 4.35. On the left, the  $d$ -axis flux is shown, setting the  $q$ -current equal to zero, which is representative of the magnetization: fixing the stator flux in the machine, in fault conditions, more current is required. However, the saturation phenomena visible in this figure are analyzed in stator flux: the machine has a sufficient value to saturate, increasing the number of active sets. While in the right of the figure, both  $q$ -axis flux in motor and generator modes are reported: the saturation phenomena are not tangible. The straight profiles highlight this because the stator flux along  $q$ -axis depends only on stator and rotor leakage inductances, not affected by the saturation. By applying Eq. (4.63), the

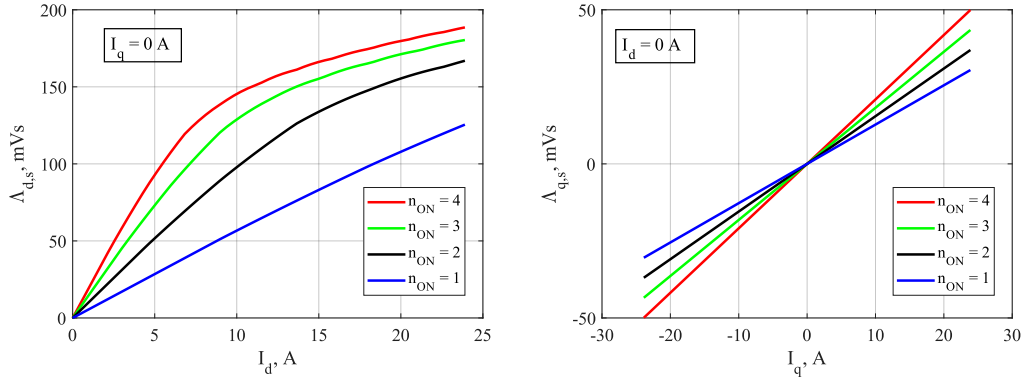


Figure 4.35 Stator flux linkage  $dq$  profiles of 12-phase IM in different machine conditions using MS approach:  $I_q=0$  A (left) and  $I_d=0$  A (right).

electromagnetic torque maps are computed for the tested 12-phase IM. The torque capability, as shown in Fig. 4.36 is heavily affected by the machine conditions. However, not to compromise even more the torque capability, the optimal flux selection is a key factor, especially in fault operations. Indeed, there is an optimal combination of  $dq$  currents, giving a working point in terms of torque and flux, following the MTPA. If the machine does not perform the MTPA operation in normal conditions involves a reduction of efficiency. While in a fault condition, in addition to the efficiency reduction related to the wrong selection of the flux, the torque capability is even more compromised (i.e.,  $q$ -current is reduced) and probably more heat on the healthy sets. For this reason, the computation of the MTPA profile assumes relevant importance in the multi-three-phase machine. The procedure is described hereafter.

### MTPA computation algorithm - MS approach

The computation of the MTPA variable is performed in a rotating  $dq$  rotor flux frame, as mentioned before. Therefore, more details are provided in this section using the MS approach. In the following, it will be shown that different approaches give the same optimal trajectories. The MTPA algorithm needs as input the maximum current  $I_{max}$ , and the first and fourth quadrant of the  $dq$  current plane is mapped for evaluating the MTPA in motor and generator modes.

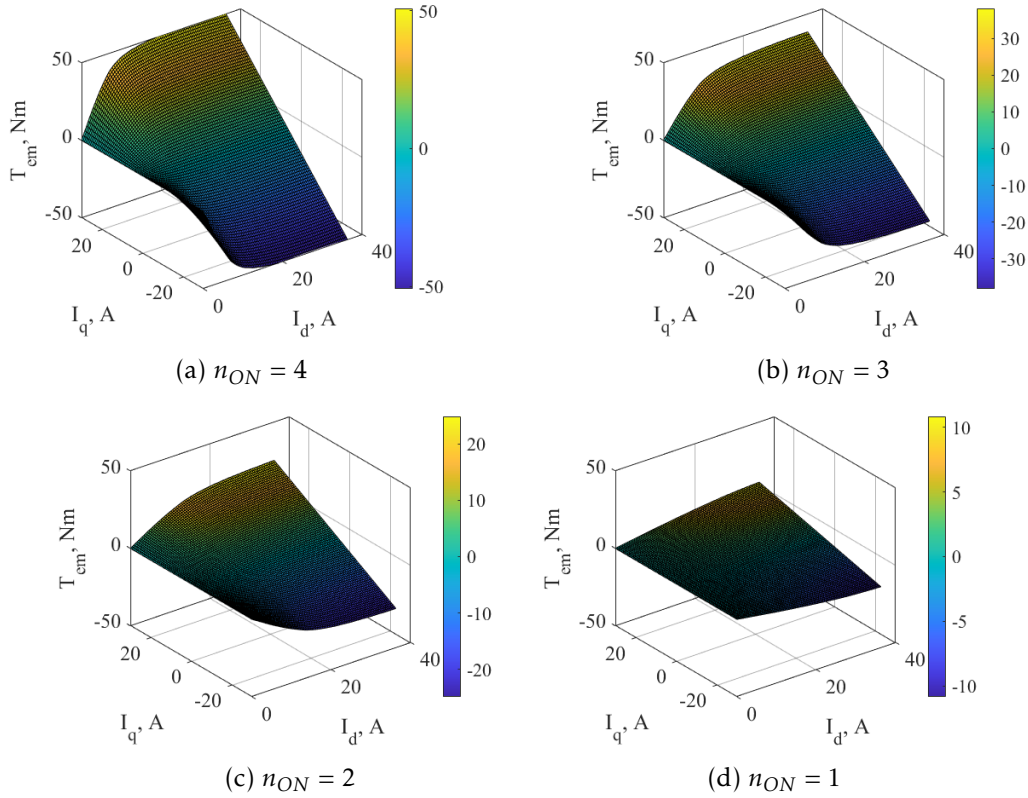


Figure 4.36 Electromagnetic torque maps of the 12-phase IM in both conditions: 4 active sets (a), 3 active sets (b), 2 active sets (c), 1 active set (d).

A current vector matrix is composed of vectors current, which is composed by the two components along  $d$ - and  $q$ -axes [87]. The stator current magnitude  $I$  spans between zero and  $I_{max}$ , while the current position spans between a minimum value and 90 electrical degrees, as for a three-phase machine (see Fig. 4.37). The minimum value of the current position span ensures that the  $d$ -axis current is lower than  $I_{d,max}$ , justifying the forbidden area in Fig. 4.37. The relation  $I_{d,max} \simeq I_{m,max}$  is still valid leads to negligible errors. For each current vector  $I$ , the stator flux, rotor flux and electromagnetic torque are computed, using Eq. (4.183) and Eq. (4.60). For each current amplitude  $I$ , the optimal MTPA is selected from all possible current positions  $\theta$  that present the maximum electromagnetic torque. In other words, given the stator current magnitude  $I$ , the stator current position  $\theta$  is varied in the mapping area (minimum value up to 90 electrical degrees). The selected MTPA flux is the value that corresponds to the maximum elec-

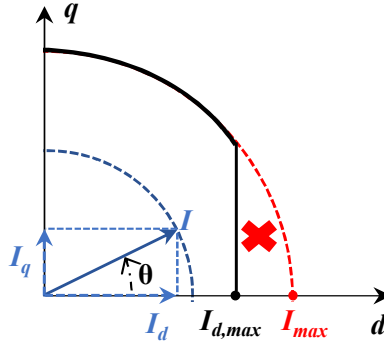


Figure 4.37 Stator current mapping in  $dq$  rotor flux fame.

tromagnetic torque. By repeating the procedure for all points between 0 and  $I_{max}$  the MTPA profile is computed. This process is automatically performed by the function *contourc* which specifies the  $d$ - and  $q$ -current coordinates for the values in torque map such as those reported in Fig. 4.36. Selected the  $dq$ -current optimal components, the stator flux components are easily evaluated based on the flux maps presented before. However, the limit of the current must be respected ( $I_{MTPA} \leq I_{max}$ ). In this way, the optimal machine command signals can be obtained in both normal and faulty conditions, suctioning opportunely the flux and torque maps based on the active sets number. Please note that, the starting point in terms of flux and torque maps changes based on the machine conditions (see Fig. 4.31 - 4.34), but the procedure for MTPA computation is invariant. The achievable MTPA maximum torque is heavily dependent on the machine conditions. For the 12-phase IM the MTPA profiles are shown: in Fig. 4.38 the MTPA in current and flux planes in normal conditions are shown, while Fig. 4.39 - 4.41 report the MTPA trajectories in faulty conditions. Looking at these figures, the torque capability reduction when the number of active sets decreases is heavily tangible. The MTPA maximum torques are reported in Table 4.5, considering the maximum current  $I_{max}$  equal to 24 A, independently by the active sets number.

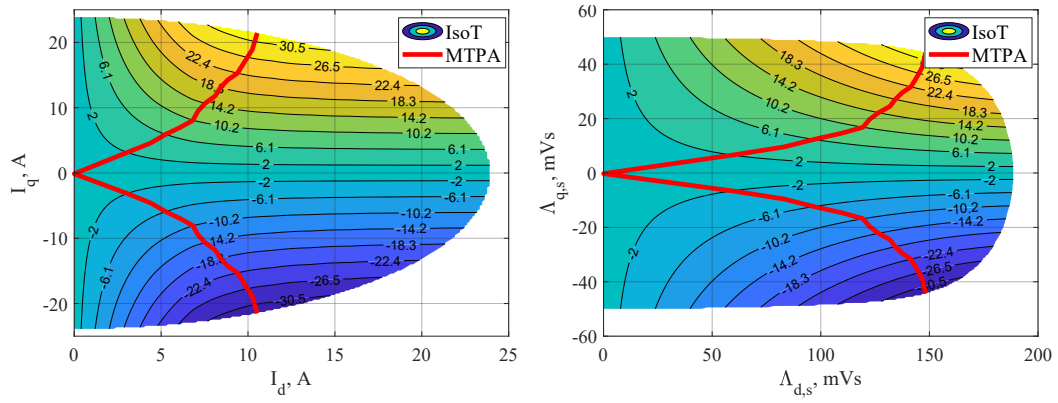


Figure 4.38 MTPA profile in current (left) and flux (right) planes in normal conditions:  $n_{ON} = 4$ .

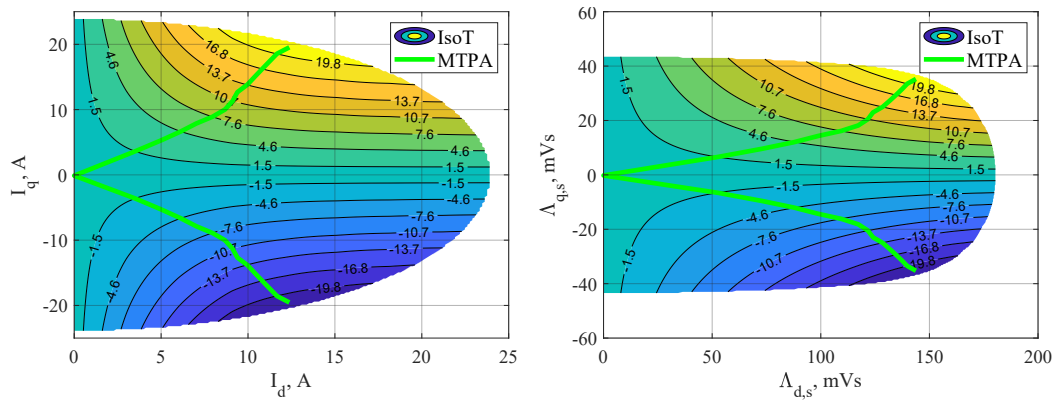


Figure 4.39 MTPA profile in current (left) and flux (right) planes in faulty conditions:  $n_{ON} = 3$ .

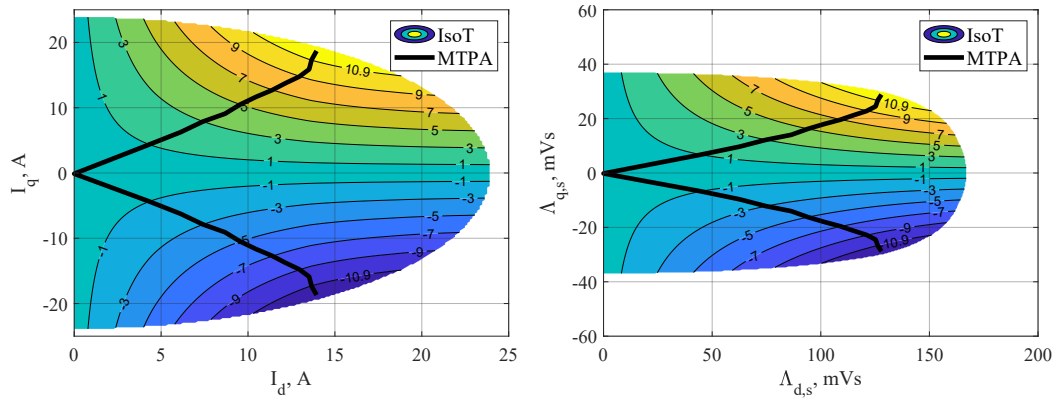


Figure 4.40 MTPA profile in current (left) and flux (right) planes in faulty conditions:  $n_{ON} = 2$ .

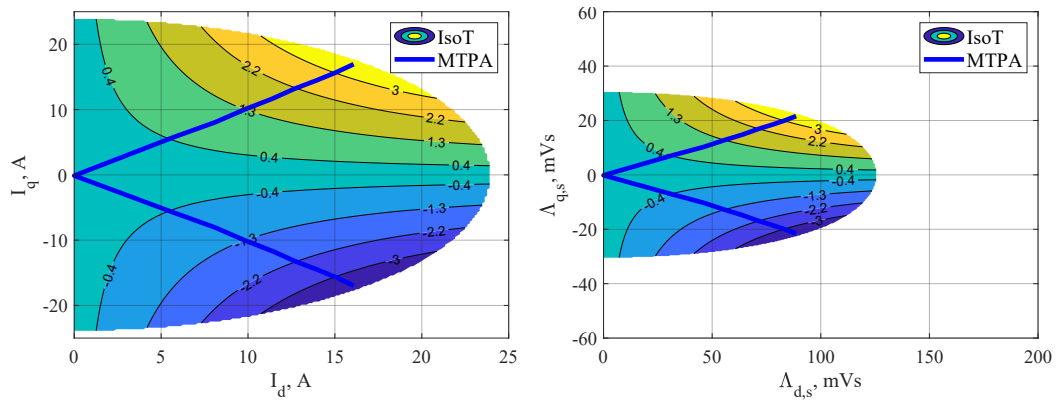


Figure 4.41 MTPA profile in current (left) and flux (right) planes in faulty conditions:  $n_{ON} = 1$ .

Table 4.5 MTPA maximum torque @  $I_{max} = 24 \text{ A}$

Torque capability	
Active sets number $n_{ON}$	$T_{em,MTPA}^{max}$
4	32.7 Nm
3	24.0 Nm
2	12.5 Nm
1	3.6 Nm

### 4.8.2 VSD and DMS approaches

As for the MS approach, the aim is to get the magnetic model based on flux maps in normal and faulty conditions. The MTPA trajectories will be defined, which must match those evaluated using the MS approach, manipulating the flux and torque maps opportunely. It is just a mathematical manipulation using different approaches, but the torque capability of the machine at the same conditions is invariant, independently of the used approach.

Starting from the stator and rotor magnetic models in rotating  $dq$  rotor flux frame evaluated in Eq. (4.110) and reported here for simplicity, the steady-state model is considered.

$$\begin{cases} s - \lambda i : & \lambda_{dq,s} = L_{l,s} \cdot i_{dq,s} + n \cdot L_m \cdot i_{dq,s} + n \cdot L_m \cdot i_{dq,r} \\ r - \lambda i : & \lambda_{dq,r} = n \cdot L_{l,r} \cdot i_{dq,r} + n \cdot L_m \cdot \bar{i}_{dq,s} + n \cdot L_m \cdot i_{dq,r} \end{cases} \quad (4.195)$$

where:

- $\lambda_{dq,s}$  and  $\lambda_{dq,r}$  stands for the stator and rotor linkage vector fluxes;
- $i_{dq,s}$  and  $i_{dq,r}$  stands for the stator and rotor current vectors;
- $n$  stands for the rated/nominal three-phase sets;
- $L_{l,s}$  and  $L_{l,r}$  stand for the stator and rotor leakage inductances, respectively;
- $L_m$  stands for the magnetizing inductance.

As demonstrated before, the parameters evaluated with the standard tests elaborated using the VSD approach do not depend on the active sets number, and so the products  $n \cdot L_m$  and  $n \cdot L_{l,r}$  are intended constant in both normal and faulty conditions. In short,  $L_m^{VSD} = n \cdot L_m$  and  $L_{l,r}^{VSD} = n \cdot L_{l,r}$ . Considering the tested 12-phase IM  $L_m^{VSD} = 18mH$  in unsaturated conditions and  $L_{l,r}^{VSD} = 1.2mH$ .

However, based on Eq. (4.8.2) and clarified that the parameters are defined in VSD approach (no subscript is reported), the magnetic stator model

is manipulated by replacing the rotor model to avoid the rotor current dependency:

$$\begin{aligned}\lambda_{dq,s} &= L_{l,s} \cdot i_{dq,s} + n \cdot L_m \cdot i_{dq,s} + n \cdot L_m \cdot \left( \frac{\lambda_{dq,r} - n \cdot L_m \cdot i_{dq,s}}{n \cdot L_r} \right) = \\ &= L_{l,s} \cdot i_{dq,s} + L_m \cdot i_{dq,s} + L_m \cdot \left( \frac{\lambda_{dq,r} - L_m \cdot i_{dq,s}}{L_r} \right)\end{aligned}\quad (4.196)$$

where the  $k_r$  stands for the rotor coupling coefficient:  $L_m/(L_m + L_{l,r})$ . The stator magnetic model components are expressed as:

$$\begin{cases} d: & \lambda_{d,s} = L_s \cdot i_{d,s} + k_r \cdot (\lambda_{d,r} - L_m \cdot i_{d,s}) \\ q: & \lambda_{q,s} = L_s \cdot i_{q,s} + k_r \cdot (\lambda_{q,r} - L_m \cdot i_{q,s}) \end{cases}\quad (4.197)$$

where  $L_s$  stands for the total stator inductance ( $L_s = L_{l,s} + L_m$ ).

In steady-state operation with constant flux and torque, the rotor flux vector components in rotor flux frame as follow:

$$\begin{cases} d: & \Lambda_{r,d} = L_m \cdot I_{d,s} \\ q: & \Lambda_{r,q} = 0 \end{cases}\quad (4.198)$$

By replacing Eq. (4.198) in Eq. (4.197) and expressing the stator magnetic model in steady-state, Eq. (4.197) is expressed as:

$$\begin{cases} d: & \Lambda_{d,s} = L_s \cdot I_{d,s} \\ q: & \Lambda_{q,s} = \sigma \cdot L_s \cdot I_{q,s} \end{cases}\quad (4.199)$$

where  $\sigma = 1 - k_r \cdot k_s$  is the total coupling factor and  $k_s$  is the stator coupling factor ( $k_s = L_m/L_s$ ).

Based on Eq. (4.199), the magnetic model of a multi-three-phase machine can be computed in both normal and faulty conditions. The stator flux represents just the flux of the main VSD subspace. However, in normal conditions, the harmonic subspaces are inactive, so the stator flux of the main subspace coincides with the machine flux. While in faulty conditions, the other harmonic subspaces became active, and the harmonic stator flux is only related to the leakage stator inductance. So in faulty conditions, the stator flux computed with Eq. (4.199) is not representative of the machine,



but just of the main subspace, but for the flux maps just the flux of the main subspace is considered because is the subspace responsible for the flux and torque producing.

As for the MS approach, iron losses are considered. In this case, equivalent iron resistance is introduced in the main subspace. Now, the stator flux components depend on the flux- and torque-producing currents ( $I_{d,ft}, I_{q,ft}$ ). For simplicity, the subscript  $ft$  is removed, but where the subscript is omitted is to be understood as the flux- and torque-producing currents. The magnetic stator flux in Eq. (4.199) is replaced as:

$$\begin{cases} d: & \Lambda_{d,s} = L_s \cdot I_d \\ q: & \Lambda_{q,s} = \sigma \cdot L_s \cdot I_q \end{cases} \quad (4.200)$$

Finally, the electromagnetic  $T_{em}$  is expressed as:

$$T_{em} = \frac{3}{2} \cdot n \cdot p (\Lambda_{d,s} \cdot I_q - \Lambda_{q,s} \cdot I_d) \quad (4.201)$$

Please, note that the electromagnetic torque in Eq. (4.201) depends on the rated three-phase sets  $n$  based on the VSD approach, while the one based on MS approach depends on the active sets number  $n_{ON}$  as reported in Eq. (4.186).

The procedure adopted for evaluating the stator flux and torque maps based on the MS approach Eq. (4.187) - Eq. (4.194), is replaced here based on VSD model. The magnetizing inductance profile of the tested 12-phase IM used for the maps evaluation is reported in Fig. 4.42, obtained by the no-load tests. The magnetizing inductance is not evaluated for different machine conditions with respect to the interpolation in MS approach reported in Eq. (4.193). Indeed, in Eq. (4.193) the function is related to the active sets number  $n_{ON}$  and the respective map is adequate, while based on the VSD approach no adjustments are necessary. The stator flux maps based on Eq. (4.199) and using the magnetizing profile in Fig. 4.42, are reported in Fig. 4.43. The maps are in agreement with the ones reported in Fig. 4.31, evaluated with the MS approach in healthy conditions. In this case, the stator maps in Fig. 4.43 are valid for all machine configurations. When the number of active sets decreases, the stator flux maps is invariant. The maps represent

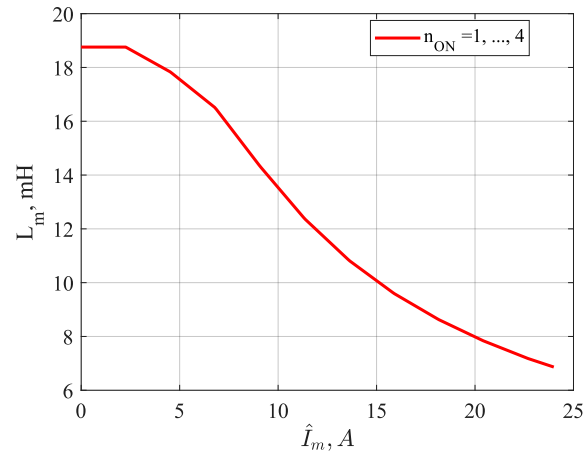


Figure 4.42 Magnetizing inductance in all machine configurations based on VSD approach.

the stator flux of the main  $\alpha\beta$  subspace in all machine configurations, but they are not representative of the all flux machine. However, this is not an approximation, since the torque and flux production is associated to the main subspace. Also, the torque map computed with Eq. (4.201) is shown in Fig. 4.44, representative of all machine conditions, in agreement with the map reported in Fig. 4.36a.

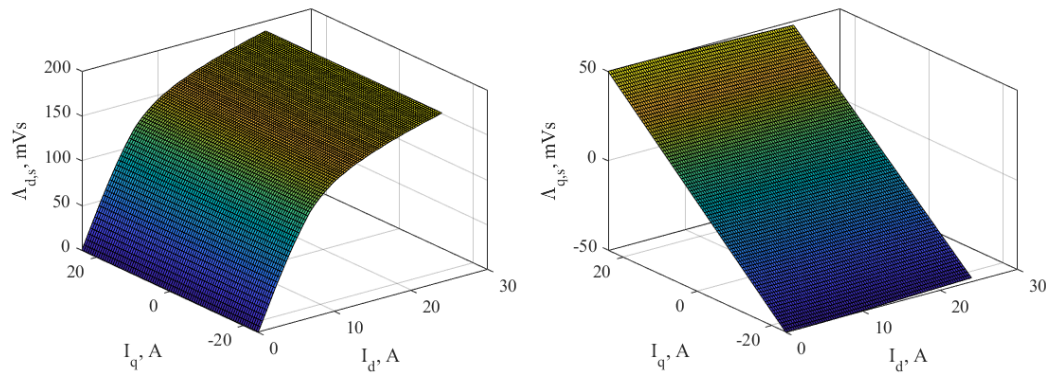


Figure 4.43 Stator flux linkage  $dq$  maps of the 12-phase IM in all machine configurations (VSD approach).

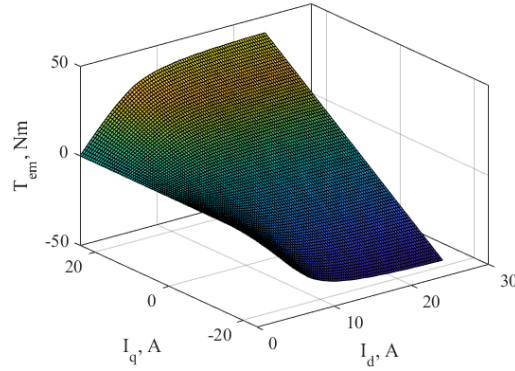


Figure 4.44 Electromagnetic torque map of the 12-phase IM in all machine configurations (VSD approach).

### MTPA computation algorithm - VSD approach

The MTPA trajectory is computed with the same approach shown in Section 4.8.1. In Section 4.8.1, the starting point for different machine conditions ( $n_{ON} = 4, \dots, 1$ ) was adapted based on the number of active sets, as reported in the stator flux and torque maps shown in Fig. 4.31 - 4.36, setting the same maximum current value to satisfy  $I_{max} = 240$  A.

However, the machine conditions (normal or faulty) must be considered independently of the approach. Using the VSD approach starting from the same stator flux and torque maps, the amplitude limit of the phase currents  $I_{max}$  is adequate. An equivalent maximum phase current  $I_{max-eq}$  is defined as reported in Eq. (4.202). This constraint is considered for MTPA trajectory computation and does not impact the maps presented before. The constrain related to the amplitude limit of the equivalent phase currents  $I_{max-eq}$  is satisfied when:

$$I_s \leq I_{max-eq}, \quad I_{max-eq} = I_{max} \cdot \frac{n_{ON}}{n} \quad (4.202)$$

When the number of active sets  $n_{ON}$  decreases, the equivalent current  $I_{max-eq}$  reduces, consequently derating torque production. This procedure allows the use of the same regular current grid Eq. (4.192) and the magnetizing profile of Fig. 4.42. Still, the maximum allowed value of the phase currents considers the opportune machine condition, impacting MTPA trajectory. The

MTPA trajectories for both normal and faulty conditions evaluated based on VSD approach are reported in Fig. 4.45: they are in agreement with the ones reported in Fig. 4.38 - 4.41. Note that the colors are in agreement: red is referred to  $n_{ON} = 4$ ; green is referred to  $n_{ON} = 3$ ; black is referred to  $n_{ON} = 4$ ; blue is referred to  $n_{ON} = 1$ . The MTPA profiles on the flux plane are not reported because they agree with the profiles in the MS approach.

Please note that the methodology developed in this section, related to the VSD approach, is identically replaced with the DMS approach to get the stator flux and torque maps and then the MTPA trajectories. Indeed, the DMS-model based, as for the VSD approach, concentrates the energy conversion in a common-mode subspace, while the other subspaces do not participate in energy conversion. These analogies commit that the procedure of this section is preserved for the DMS approach, despite the mathemati-

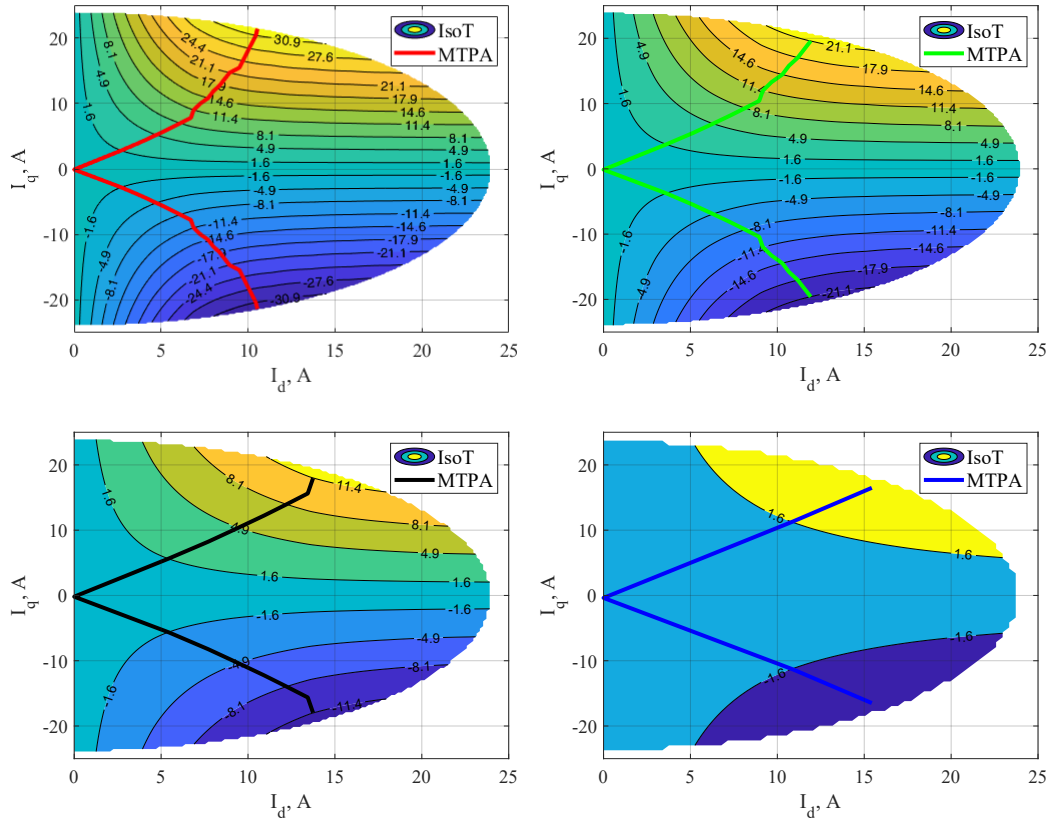


Figure 4.45 MTPA profile in current plane in both normal and faulty conditions:  $n_{ON} = 4, \dots, 1$ .

cal/physical meaning of these two models being entirely different from each other.

In summary, the procedure to get the flux and torque maps based on the MS approach depends on the active sets number  $n_{ON}$ . Conversely, using the VSD/DMS approach, the maps do not depend on the active sets, but just on the rated number sets  $n$ , rescaling the maximum stator phase current opportunely, introducing the concept of the equivalent maximum current  $I_{max-eq}$ . Indeed, about the parameters: using the MS approach, the values are rescaled by  $1/n$  than the ones evaluated with VSD; using the VSD approach, the parameters of the main subspace do not depend on the machine conditions.

### 4.8.3 A-DMS approach

The A-DMS modeling has been presented in Section 4.5, which combines the advantages of MS and VSD approaches and alleviates the disadvantages of both approaches, as mentioned before. The electromechanical model based on A-DMS model is obtained in Eq. (4.132) in a rotating  $dq$  rotor flux frame. It is similar to the VSD one Eq. (4.110), but with the characteristic of adapting the machine modeling by considering a stator winding configuration based on healthy/active winding sets. For this reason, the stator flux and torque maps require a different procedure from the previous one, as shown in the following.

The electromechanical models evaluated with VSD and A-DMS approach are formally identical, and the relation in Eq. (4.199) in steady-state conditions are still valid and reported here for simplicity:

$$\begin{cases} d: & \Lambda_{d,s} = L_s^{A-DMS} \cdot I_{d,s} \\ q: & \Lambda_{q,s} = \sigma \cdot L_s^{A-DMS} \cdot I_{q,s} \end{cases} \quad (4.203)$$

However, the parameters in Eq. (4.203) assume the same meaning. Still, their values are different: the rotor parameters and magnetizing inductance must be adapted to the number of active sets  $n_{ON}$ . Based on the mathematical model evaluated with the adaptive matrix, the magnetizing and leakage

rotor inductances are rescaled as:

$$L_m^{A-DMS} = L_m^{VSD} \cdot \frac{n_{ON}}{n}, \quad L_{l,r}^{A-DMS} = L_{l,r}^{VSD} \cdot \frac{n_{ON}}{n} \quad (4.204)$$

The total coupling factor  $\sigma$  is computed as:

$$\sigma = 1 - k_s \cdot k_r = 1 - \frac{L_m^{A-DMS}}{L_s^{A-DMS}} \cdot \frac{L_m^{A-DMS}}{L_r^{A-DMS}} \quad (4.205)$$

where:

$$L_s^{A-DMS} = L_{l,s} + L_m^{A-DMS}, \quad L_r^{A-DMS} = L_{l,r}^{A-DMS} + L_m^{A-DMS} \quad (4.206)$$

Finally, the electromagnetic torque based on A-DMS model is expressed as:

$$T_{em} = \frac{3}{2} \cdot n_{ON} \cdot p \cdot (\Lambda_{d,s} \cdot I_q - \Lambda_{q,s} \cdot I_d) \quad (4.207)$$

The torque equation Eq. (4.207) is formally the same based on MS approach Eq. (4.186), but different flux maps are used.

The regular current mesh grid is built as reported in Eq. (4.192), setting the maximum stator phase current  $I_{max}$  consistent with the machine and/or converter limits. The magnetizing inductance profile is extrapolated considering an equivalent current of the machine as:

$$L_m^{map} = \text{interp1} \left( I_m, L_m^{A-DMS}, \frac{n_{ON}}{n} \cdot I_d^{map} \right) \quad (4.208)$$

where the definition of *interp1* function is consistent with the previous,  $I_m$  is the magnetizing vector evaluated during the no-load tests, and the flux- and torque- current producing along  $d$ -axis  $I_s^{map}$  is opportunely rescaled respect with the active sets number. The magnetizing map  $L_m^{map}$  is organized as in Eq. (4.193), starting from the magnetizing inductance profiles reported in Fig. 4.46. For the tested 12-phase IM, the maximum phase current is set to 24 A, and the maximum magnetizing current during the no-load tests is 36 A.

The stator flux and torque maps based on the A-DMS approach for both normal and faulty conditions are shown according to the above-reported

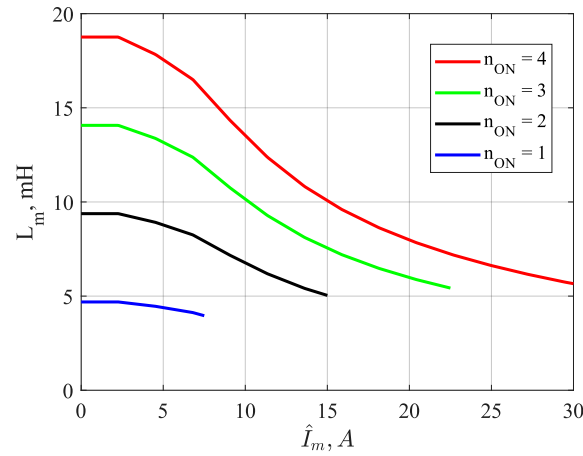


Figure 4.46 Magnetizing inductance in all machine configuration based on A-DMS approach.

inputs and constraints. The maps for each machine's conditions represent the total machine flux. Indeed, compared to the VSD approach, the differential subspaces are always inactive in both normal and faulty conditions. For this reason, the stator flux of the common subspace is evaluated by mapping the stator flux of the machine. Still, the rotor parameters and magnetizing inductance must be adapted by the factor  $n_{ON}/n$ . The stator flux of all differential subspaces ( $u = n_{ON} - 1$ ) is zero also in faulty conditions.

The stator flux profiles along  $d$ - and  $q$ -axes setting the current in quadrature to zero for both normal and faulty conditions are reported in Fig. 4.47. The profiles in the figure agree with those reported in Fig. 4.35, evaluated

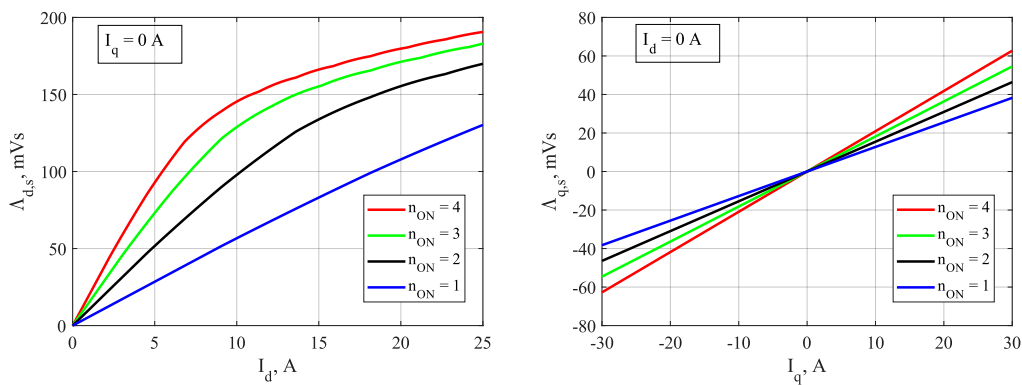


Figure 4.47 Stator flux linkage  $dq$  profiles of 12-phase IM in different machine conditions using A-DMS approach:  $I_q=0$  A (left) and  $I_d=0$  A (right).

with the MS approach. This demonstrates that, independently of the used mathematical approach, the profiles are confirmed, even if the physical interpretation must be adapted and parameters must be opportunely considered. The torque maps can only be confirmed based on the same stator flux maps. Regarding the MTPA profiles, the trajectories are confirmed as the ones reported in Fig. 4.41 - Fig. 4.38, without rescaling the maximum current, unlike the VSD approach.

In conclusion, with all approaches, MS, VSD/DMS, and A-DMS have presented the stator flux and torque maps, representing the input of the multi-three-phase IM mapping. However, depending on the approach used, rescaling the currents and parameters is required. Since the different models are just mathematical manipulations, the results are in agreement, and the physical meanings are different:

- MS approach: all rotor and magnetizing parameters are rescaled by  $1/n$  of those computed using VSD/DMS modeling, while the currents are higher in normal conditions. Also, the iron losses are related to the active sets. The whole machine is analyzed since the flux maps of the machine are representative of each active set, considering just the  $dq$  subspace. The torque map represents the machine based on active sets  $n_{ON}$ .
- VSD/DMS approach: all rotor and magnetizing parameters are constant in the main or common subspace. They do not depend on the number of active sets, but the maximum stator phase current is rescaled with the factor  $n_{ON}/n$ , introducing an equivalent current. The main/common subspace in healthy conditions is active, while the other subspaces (harmonic/differential) become active in faulty conditions. The presented flux maps represent the active sets, and in faulty conditions, the harmonic/differential subspaces must be considered for energetic balance. However, for torque and flux maps, just the main subspace is considered because it is responsible for energy conversion. The presented flux and torque maps represent the active sets, and in faulty conditions, the harmonic/differential subspaces must be considered for energetic balance. However, for torque and flux maps, just



the main subspace is considered because it is responsible for energy conversion.

- A-DMS approach: parameters of the common subspace depend on active sets number. The  $(n-1)$  differential subspaces are always inactive and in faulty conditions. The presented flux and torque maps represent the whole machine.

Based on the presented analysis, some approaches can be more convenient than another based on the work aim. Also, this section shows how different methods provide the same results in stator flux, torque capability, and MTPA profiles for both normal and open-winding faulty conditions.

## 4.9 Maximum torque per speed profile (MTPS) in normal and open-winding faulty conditions

The MTPS profile delimits the working area of the machine for given values of dc-link voltage  $V_{dc}$  and machine temperature  $\vartheta$ . Thus, in this section, the computation of the MTPS profiles based on electromagnetic variables reconstruction is presented. The analysis is carried out for both normal and open-winding faulty conditions of multi-three-phase IM. The results of the benchmark 12-phase IM are reported, showing the heavy torque capability reduction. Also, the MTPS profiles have been obtained with different mathematical approaches: MS, VSD/DMS, and A-DMS approaches deliver the same results.

The working points that satisfy the current  $I_{max}$  and voltage  $V_{max}$  limits of the machine and/or converter are considered; vice versa, the others are ruled out. Among the acceptable points, those that lead to the maximum torque are selected for each electrical pulsation. This way, the MTPS for the different dc-link voltage and temperature values are computed. In addition, the MTPS profiles are calculated for all the possible machine conditions ( $n_{ON} = 4, 3, 2, 1$ ).

A flow diagram of the MTPS computation able to handle different mathematical approaches (i.e., MS, VSD/DMS, A-DMS) for both normal and open-winding faulty conditions is reported in Fig. 4.48. The flowchart in

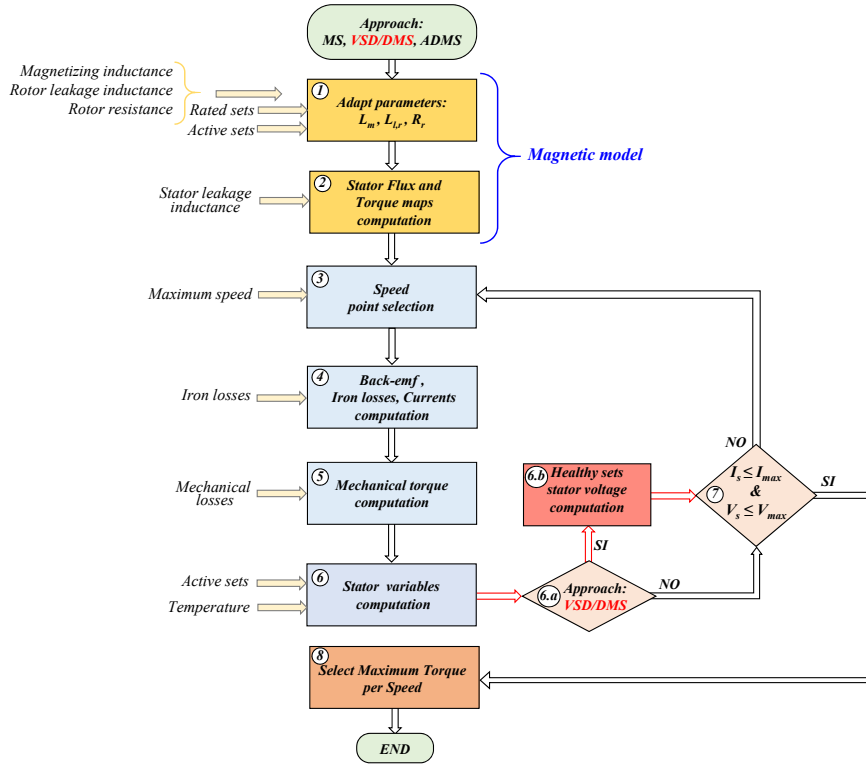


Figure 4.48 A flow diagram of the MTPS computation able to handle different mathematical approaches (i.e., MS, VSD/DMS, A-DMS) for both normal and open-winding faulty conditions is reported in Fig. 4.48.

Fig. 4.48 shows the step-by-step algorithm for any used approach to compute the MTPS profile in any machine conditions. In the figure, the numbering refers to the steps hereafter briefly described. In the flow diagram descriptive of the MTPS computation procedure, the input parameters/maps are highlighted with yellow arrows, and the already analyzed magnetic model is reported in yellow blocks. The *if* conditions are represented by pink rhombus. The flow in red between Step 6 and Step 6.b highlights an *alternative* path for the VSD-based model. Details are reported hereafter.

### Step 1 - Adapt the parameters

The rotor parameters  $L_{l,r}$ ,  $R_r$ , and the magnetizing inductance  $L_m$  are rescaled considering the used approach and machine conditions. Starting from the parameters evaluated with the VSD approach (see Fig. 4.42 and Fig. 4.18), selecting the MS approach the parameters and magnetizing current are computed in Eq. (4.209), while selecting the A-DMS approach the ones are

computed in Eq. (4.210).

$$\begin{aligned} L_m^{MS} &= \frac{1}{n} \cdot L_m, & L_{l,r}^{MS} &= \frac{1}{n} \cdot L_{l,r}, & R_r^{MS} &= \frac{1}{n} \cdot R_r \\ I_m^{MS} &= n \cdot L_m \end{aligned} \quad (4.209)$$

$$\begin{aligned} L_m^{A-DMS} &= \frac{n_{ON}}{n} \cdot L_m, & L_{l,r}^{A-DMS} &= \frac{n_{ON}}{n} \cdot L_{l,r}, & R_r^{A-DMS} &= \frac{n_{ON}}{n} \cdot R_r \\ I_m^{A-DMS} &= \frac{n_{ON}}{n} \cdot L_m \end{aligned} \quad (4.210)$$

where  $n$  and  $n_{ON}$  are the rated sets and active sets number, respectively. Please note that the parameters adaption is related to the squirrel cage model presented in Section 4.1.2.

### Step 2 - Stator Flux and Torque maps computation

The magnetic model based on flux maps is built in this step. The stator flux components in rotating  $dq$  rotor flux frame in steady-state conditions are computed, as reported in Section 4.8. In summary, the stator flux components and torque are expressed as:

**MS:**

$$\begin{cases} d : & \Lambda_{d,s} = L_{l,s} \cdot I_d + k_r \cdot n_{ON} \cdot L_{l,r} \cdot I_d + k_r \cdot n_{ON} \cdot L_m \cdot I_d \\ q : & \Lambda_{q,s} = L_{l,s} \cdot I_q + k_r \cdot L_{l,r} \cdot I_d \end{cases} \quad (4.211)$$

$$T_{em} = \frac{3}{2} \cdot n_{ON} \cdot p \cdot (\Lambda_{d,s} \cdot I_q - \Lambda_{q,s} \cdot I_d) \quad (4.212)$$

where the parameters without subscript are referred to VSD approach, following Eq. (4.209). The stator parameters  $L_{l,s}$  do not depend on the mathematical approach. The equations of the stator flux components and electromagnetic torque are applied for each point of the current mesh grid rescaled by the factor  $n_{ON}$ , presented in Eq. (4.192). Note that the stator flux components and electromagnetic torque depend on the active sets number  $n_{ON}$ . The stator flux thus calculated corresponds to the flux of the active sets.

**VSD/DMS:**

$$\begin{cases} d : & \Lambda_{d,s} = L_s \cdot I_{d,s} \\ q : & \Lambda_{q,s} = \sigma \cdot L_s \cdot I_{q,s} \end{cases} \quad (4.213)$$

$$T_{em} = \frac{3}{2} \cdot n \cdot p \cdot (\Lambda_{d,s} \cdot I_q - \Lambda_{q,s} \cdot I_d) \quad (4.214)$$

where the rotor leakage and magnetizing inductances to compute  $L_s = L_m + L_{l,s}$  and  $\sigma = 1 - k_s \cdot k_r$  are referred to the VSD approach and they do not depend on the machine conditions (healthy/faulty). The electromagnetic torque depends on rated sets number  $n$ , independently of the active sets number. Also, the equations are applied for each point of the current mesh grid in this case, obtaining the stator flux and torque maps. The stator flux corresponds to the flux of the main subspace (VSD) or common-mode subspace (DMS). The latter corresponds to the machine stator flux only in normal conditions. In contrast, in faulty conditions ( $n \neq n_{ON}$ ), the harmonic subspaces (VSD) or differential-mode subspaces (DMS) became active subspaces.

**A-DMS:**

$$\begin{cases} d: & \Lambda_{d,s} = L_s^{A-DMS} \cdot I_{d,s} \\ q: & \Lambda_{q,s} = \sigma \cdot L_s^{A-DMS} \cdot I_{q,s} \end{cases} \quad (4.215)$$

$$T_{em} = \frac{3}{2} \cdot n_{ON} \cdot p \cdot (\Lambda_{d,s} \cdot I_q - \Lambda_{q,s} \cdot I_d) \quad (4.216)$$

where the parameters  $L_s^{A-DMS}$  follows Eq. (4.210), depending on the active sets number. Obviously, the total coupling factor  $\sigma$  is computed based on  $L_m^{A-DMS}$  and  $L_{l,r}^{A-DMS}$ . The electromagnetic torque depends on active sets number  $n_{ON}$ . In this case, the equations are applied for each point of the current mesh grid, rescaled by the factor  $n_{ON}/n$ , obtaining the stator flux and torque maps. In this case, the flux of the common-mode subspace corresponds to the machine flux both in normal and open-winding faulty conditions. Indeed, the differential subspace ( $n - 1$ ) are always inactive using the A-DMS approach.

Based on Step 1 and Step 2, the magnetic model of the machine is defined. Note that the current components  $I_d, I_q$  are flux- and torque-current producing. These currents are obtained based on the current mesh grid in Eq. (4.192), based on the maximum current and maximum magnetizing current evaluated during the no-load tests.

### Step 3 - Speed point selection

Based on the maximum expected pulsation, the vector composed by  $n_{sp}$  points, having the dimension of  $1 \times n_{sp}$ , is built in according to the speed

resolution  $\Delta\omega$  as:

$$[\omega]_{1 \times n_{sp}} = 0 : \Delta\omega : \omega_{max}, \quad s = 0, \dots, n_{sp} \quad (4.217)$$

For each pulsation value,  $s^{th}$  will correspond to the rotor speed based on the reconstruction of the reporter's electromechanical variables hereafter. The maximum torque is sought for each speed point, respecting the current and voltage limits.

#### Step 4 - Back-emf, Iron losses, Currents computation

For each point of the vector  $[\omega]$  the back-emf map is computed as:

$$\begin{cases} d : & E_{d,s} = -\omega \cdot \Lambda_{q,s} \\ q : & E_{q,s} = +\omega \cdot \Lambda_{d,s} \end{cases} \quad (4.218)$$

$$E_s = \sqrt{E_{d,s}^2 + E_{q,s}^2}$$

where  $(\Lambda_{d,s}, \Lambda_{q,s})$  are the elements of the stator flux maps computed at the previous step. The equations are applied for all elements of the maps, obtaining the back-emf map. The equations in Eq. (4.218) are applied for each element of the stator flux and current maps for the selected pulsation  $s=0, \dots, N_{sp}$ , obtaining the maps of back-emf components. Obviously, since they are the maps for each pulsation, the product and the division are performed using the matrix element-wise product and division. In the following the latter consideration is assumed.

The iron losses (including the stator skin effect) are computed from the stator frequency ( $f = \omega/(2 \cdot \pi)$ ), and amplitude of the machine's back-emf  $E_s$  by interpolating the iron losses map obtained after performing the no-load tests. However, the iron losses map is an input of this step and is selected based on the active sets numbers. Indeed, Section 4.7.4 has discussed the contribution of the iron losses, which strongly depends on the machine conditions (normal/faulty). The rescaled based on the active sets number  $n_{ON}$  is not applicable as for the rotor and magnetizing parameters, involving an experimental look-up table opportunely selected, as shown in the flow

diagram of Fig. 4.48. In mathematical formulation can express as:

$$P_{Fe} = \text{interp2}(\omega^{map}, E_s^{map}, P_{Fe-n_{ON}}^{map}, \omega, E_s) \quad (4.219)$$

where the function *interp2* returns interpolated iron losses value of the iron losses map in input  $P_{Fe-n_{ON}}^{map}$  of two variables (pulsation and back-emf) at specific query points ( $p^{th}$  - pulsation using linear interpolation.  $P_{Fe-n_{ON}}^{map}$  stands for the experimental iron losses map related to the active sets number  $n_{ON}$ , while  $\omega^{map}$  and  $E_s^{map}$  stand for the respective pulsation and back-emf experimental maps (see Section 4.7.4).

Computed the iron losses related to the  $p^{th}$ -pulsation point and the back-emf value Eq. (4.218), the equivalent iron losses resistance is computed as:

$$\begin{aligned} MS : \quad R_{Fe} &= \frac{3}{2} \cdot n_{ON} \cdot \frac{E_s^2}{P_{Fe}} \\ VSD/DMS : \quad R_{Fe} &= \frac{3}{2} \cdot n \cdot \frac{E_s^2}{P_{Fe}} \\ A-DMS : \quad R_{Fe} &= \frac{3}{2} \cdot n_{ON} \cdot \frac{E_s^2}{P_{Fe}} \end{aligned} \quad (4.220)$$

Finally, the iron current components are computed as:

$$\begin{cases} d : I_{d,Fe} = \frac{E_{d,s}}{R_{Fe}} \\ q : I_{q,Fe} = \frac{E_{q,s}}{R_{Fe}} \end{cases} \quad (4.221)$$

#### Step 5 - Mechanical torque computation

For each  $p^{th}$ -pulsation and each current component of the regular mesh grid, the mechanical speed  $\omega_r$  can be computed, based on the slip speed  $\omega_{sl}$ , expressed as:

$$\omega_{sl} = \frac{1}{\tau_r} \cdot \frac{I_q}{I_d}, \quad \tau_r = \frac{L_r}{R_r(f_{sl}, K_\theta^r)} \quad (4.222)$$

In Eq. (4.222) the rotor resistance  $R_r$  is required. However, this parameter depends on the slip frequency  $f_{sl}$  according to the experimental profile obtained from the locked-rotor tests (see Fig. 4.18). Also, the rotor resistance is adapted to the operating rotor temperature  $\vartheta_r$ , including the coefficient

$K_\theta^r$  related to the characteristic temperature of the conductive material of the rotor cage.

Finally, the mechanical speed is expressed as:

$$\omega_r = \omega - \omega_{sl} \quad (4.223)$$

According to the mechanical speed,  $\omega_r$  of the considered pulsation, the torque loss  $T_{fv}$  due to the friction and ventilation is computed by interpolating the experimental profile obtained after performing the no-load tests (see Fig. 4.19). In this way, the mechanical torque  $T_m$  is computed from the electromagnetic one  $T_{em}$  as reported in Eq. (4.224). The electromagnetic torque  $T_{em}$  is evaluated in Step 2 for the magnetic model definition.

$$T_m = T_{em} - T_{fv} \quad (4.224)$$

The mechanical power is expressed as:

$$P_m = T_m \cdot \omega_m \quad (4.225)$$

#### Step 6 - Stator variables computation

According to the multi-three-phase IM's equivalent circuit reported in Fig. 4.49, the  $dq$  current components are computed as:

$$\begin{cases} d: & I_{d,s} = I_{d,Fe} + I_d \\ q: & I_{q,s} = I_{q,Fe} + I_q \end{cases} \quad (4.226)$$

$$I_s = \sqrt{I_{d,s}^2 + I_{q,s}^2}$$

The stator voltage components are computed as:

$$\begin{cases} d: & V_{d,s} = R_s \cdot I_{d,s} + E_{d,s} \\ q: & V_{q,s} = R_s \cdot I_{q,s} + E_{q,s} \end{cases} \quad (4.227)$$

$$V_s = \sqrt{V_{d,s}^2 + V_{q,s}^2}$$

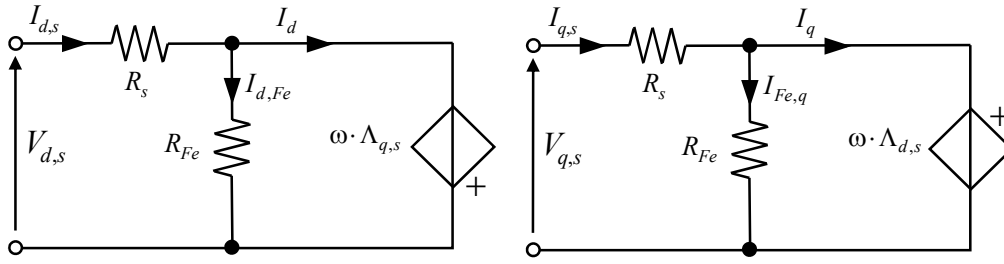


Figure 4.49 Multi-three-phase IM steady-state equivalent circuit in the rotating  $dq$  reference frame.

The stator resistance  $R_s$  is computed according to the operative temperature of the stator winding  $\vartheta$  considering the characteristic temperature of the conductive material of the stator windings. The stator voltages calculated in Eq. (4.245) assume different physical meanings based on the used approach.

- **MS:** the stator voltages in Eq. (4.245) represent the ones of active sets (Eq. (4.228)) and do not represent the whole machine (for the faulty sets the stator voltage is equal to the back-emf).

$$\begin{cases} d: & V_{d,s} = V_{d,sk} \\ q: & V_{q,s} = V_{q,sk} \end{cases}, \quad k = 1, \dots, n_{ON} \quad (4.228)$$

- **VSD:** the stator voltages in Eq. (4.245) represent the ones of the main subspace (VSD) or common-mode subspace (DMS), but they are unsuitable for defining the stator voltages of active/healthy sets of the machine. For this reason, if the selected approach is VSD, the flow diagram presents a branch line to evaluate the stator voltages of healthy sets starting from the ones of the main/common subspace computed at this step.
- **A-DMS:** the stator voltages in Eq. (4.245) represent the ones of the common-mode. However, based on A-DMS theory, they represent the whole machine because the other subspaces are always inactive, independently of machine conditions (healthy/faulty).



**Step 6 - Approach: VSD/DMS & Healthy sets stator voltage computation**

Please remember that the aim is the computation of MTPS profiles. The goal can be reached with different mathematical approaches, but the results must match. The VSD approach, until the stator flux and torque maps computation, appears as simple due to the parameters opportunely evaluated and invariant ones in the main/common subspace, independently by the active sets number  $n_{ON}$ . However, an equivalent maximum current will be introduced as for the MTPA computation. However, based on the stator voltage components in Eq. (4.245) representative of the main subspace, it is necessary the computation of the stator voltages of healthy sets. The knowledge of the latter is required to verify the voltage limit. The stator voltage of healthy sets is expressed as:

$$V_{s-ON} = \frac{\sqrt{P_e^2 + Q_e^2}}{\frac{3}{2} \cdot n_{ON} \cdot \frac{n}{n_{ON}} \cdot I_s} \quad (4.229)$$

where  $I_s$  is computed in Eq. (4.226), and  $P_e$  and  $Q_e$  stand for electrical (active) and reactive powers of the machine, respectively, computed as:

$$P_e = P_m + \underbrace{P_{js} + P_{jr} + P_{Fe}}_{P_{l-tot}} \quad (4.230)$$

$$Q_e = \underbrace{-\frac{3}{2} \cdot n \cdot (V_{d,s} \cdot I_{q,s} - V_{q,s} \cdot I_{d,s})}_{Q_{\alpha\beta/cm}} + \underbrace{\frac{3}{2} \cdot n \cdot X_s \cdot I_s^2 \cdot \left(\frac{n}{n_{ON}} - 1\right)}_{Q_{h/dm}}$$

where  $P_{js}$  and  $P_{jr}$  stand for the stator and rotor Joule losses computed in Eq. (4.231) that added to the iron losses  $P_{Fe}$  define the total losses  $P_{l-tot}$ . The stator Joule losses are computed for the main/common-mode subspace and the harmonic/differential-mode subspaces, as highlighted in Eq. (4.231). The last factor  $n/n_{ON}$  involves increased losses related to the harmonic/differential subspaces that become active in faulty conditions. In normal conditions, this factor is equal to one. For the rotor Joule losses, just the main/common-mode subspace is considered because the rotor does not involve in other subspaces. The mechanical power  $P_m$  is computed in Eq. (4.225).

Regarding the reactive power:  $Q_{\alpha\beta/cm}$  and  $Q_{h/dm}$  stand for the reactive power of the main/common-mode and harmonic/differential-mode subspaces, respectively. The sum of the reactive powers of the main/common-mode subspace and one of the harmonic/differential-mode subspaces allows computing the total reactive power of the machine  $Q_e$ .

$$\begin{aligned} P_{js} &= \frac{3}{2} \cdot n \cdot R_s \cdot I_s^2 \cdot \frac{n}{n_{ON}} \\ P_{jr} &= \frac{3}{2} \cdot n \cdot R_r \cdot I_r^2 \end{aligned} \quad (4.231)$$

where the rotor current  $I_r$  is expressed as in Eq. (4.232), as mentioned above, the rotor current along  $d$ -axis is zero. The relation in Eq. (4.231) are valid only for VSD-based model.

$$I_r = -k_r \cdot I_q, \quad k_r = \frac{L_m}{L_r} \quad (4.232)$$

Based on Eq. (4.229) - Eq. (4.232), the stator voltages of healthy sets is computed.

**Step 7 - Voltage and current limits** All equations in Step 3 - Step 6 define the maps for each pulsation of the vector  $\omega$  ( $s = 1, \dots, n_{sp}$ ) because they are computed using the stator flux and current maps defined in Step 2. For each element of the map, the current and voltage limits are verified: the ones that break the amplitude limit of the phase currents  $I_{max}$  or the amplitude limit of the phase voltages  $V_{max}$  are ruled out. The elements of the map that satisfy both the above-reported limits are indicated as follows:

$$\begin{aligned} X| \quad & V_s \leq V_{max} \\ & I_s \leq I_{max} \end{aligned} \quad (4.233)$$

where for VSD approach means  $V_{s-ON}$ .

The range of the map elements that satisfy the voltage and current limits is selected, organized the values in a vector that corresponds to the pulsation/speed. The range is the same for all maps. Note that, the voltage limit  $V_{max}$  is defined according to the converter limit and modulation technique.

#### **Step 8 - Select Maximum Torque per Speed**

Let's consider the torque vector for each pulsation value that satisfy both volt-

age and current limits. The position index of the vector leading to maximum torque corresponds to the one that maximizes the torque at the considered speed. In this way, the maximum torque per speed profile is defined for a fixed dc-link voltage and machine temperature.

### MTPS profiles of 12-phase IM

The presented procedure has been applied to the 12-phase IM. The magnetic model of the benchmark machine based on flux maps for both normal and open-winding faulty conditions has been presented in the previous section (see Section 4.8). For each point of the current, flux, and electromagnetic torque maps presented before, fixing the speed/pulsation, the maximum mechanical torque is investigated based on the electromechanical variables reconstruction, as shown in the flow diagram of Fig. 4.48. The maximum mechanical torque obtained at  $s^{th}$ -pulsation, satisfying the voltage and current limits, becoming a value of the MTPS vector at the position  $s$ .  $s$  stands for the pulsation/speed position index of the vector  $[\omega]$  defined in Eq. (4.217). The developed algorithm for the MTPS computation deals with different mathematical approaches, i.e., MS, VSD/DMS, and A-DMS for different dc-link voltages and machine temperatures. The iron losses are included, but disabling the ones, the first region of the MTPS profile coincides with the MTPA maximum torque. The difference is negligible for the tested machine.

In Fig. 4.50, the MTPS profiles of the mechanical torque, mechanical power, stator current, and stator flux for all machine conditions ( $n_{ON} = 4, 3, 2, 1$ ) are reported, selecting the MS approach in the flow diagram of Fig. 4.48. The dc-link voltage has been set at 100 V, rescaling by the factor  $1/\sqrt{3}$ , assuming the MinMax modulation technique to compute the maximum stator voltage ( $V_{max} = V_{dc}/\sqrt{3}$ ) at the stator temperature of 25°C. The maximum current has been set at 24 A. The dc-link voltage is kept low to enjoy the flux weakening: the maximum speed equal to 6 krpm has been set for experimental test limits. The continuous lines stand for the profiles in motoring mode, while the dashed line is for generating mode. The color lines are in agreement with the ones in other plots.

In the base region, the amplitude of the currents assumes the maximum value  $I_{max} = 24$  A, corresponding to the MTPA operation. Also, in the first

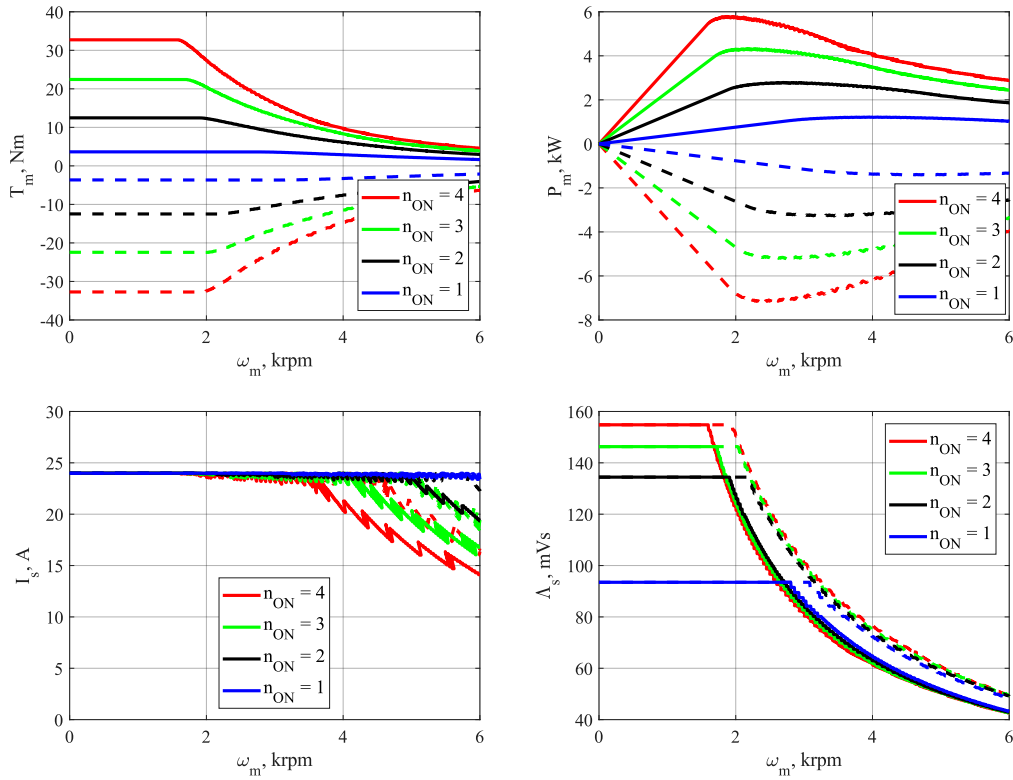


Figure 4.50 MTPs torque, mechanical power, stator current, stator flux profiles in normal and faulty conditions.

region of the flux weakening, the current is kept at the same value, later reduced in the second region of the flux weakening (MTPV).

Fig. 4.51 shows examples of MTPS profiles for 12-IM obtained by the developed MTPS algorithm (Fig. 4.48), selecting the VSD approach. Note that, selecting different approach in Fig. 4.51 (VSD) than Fig. 4.50 (MS), the profiles in green at  $V_{dc} = 100V$  are perfectly in agreement.

Focusing on Fig. 4.51: the profiles show the dc-link voltage's impact on the MTPS profiles. These plots show that regardless of the mathematical approach or machine conditions (normal/faulty), the available maximum voltage strongly affects the MTPS profiles. Lower dc-link voltage markedly reduces the base speed at which the flux weakening operation occurs, thus reducing the MTPA operation of the machine. Moreover, the flux weakening occurs in generation mode for a speed value higher than that in motoring mode at the same dc-link voltage value. This difference is related to the sign

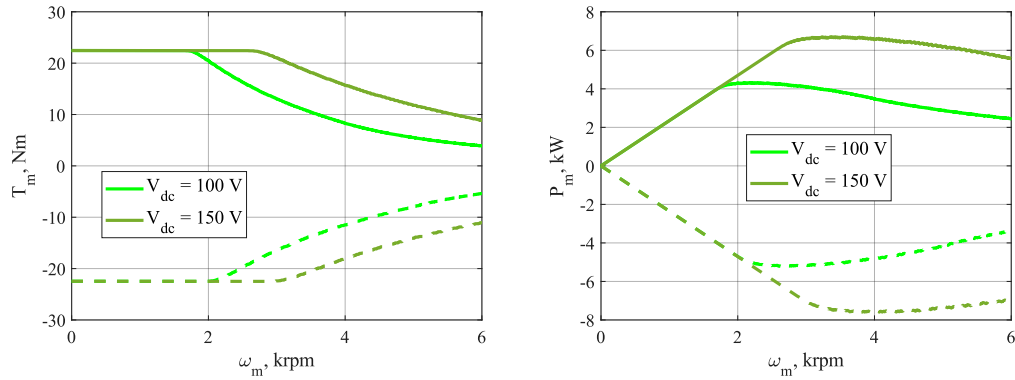


Figure 4.51 MTPS torque and mechanical power profiles in faulty conditions ( $n_{ON} = 3$ ) for different dc-link voltages.

change of both the slip speed and the voltage drops on stator resistance. In detail, the sign-changing of the slip speed has a higher impact since it leads to a lower amplitude of the stator voltages for a given amplitude of the stator flux linkage. In contrast, the effect of the winding temperatures on the MTPS profiles is marginal. In particular, the temperature impact on the base speed value is due to the increment of the voltage drop on the stator resistance.

## 4.10 Multi-Three-Phase IM mapping in normal and faulty conditions

The procedure for multi-three-phase IM mapping is formally similar to the one for three-phase IM, but after understanding the physical meaning of the variables to correspond a sort of equivalent three-phase machine. The physical meaning change based on the mathematical approach and machine conditions: the machine model must be adopted and opportunely emulated in faulty conditions. The losses for energetic balance are computed based on detailed knowledge of the machine model, and all approaches must be in agreement. The calculated results hereafter are validated experimentally on 12-phase IM.

### 4.10.1 Mapping initialization: approach and machine conditions

The proposed algorithm estimates the multi-three-phase IM efficiency maps in the operative torque-speed range. The algorithm features are the following:

- Approach: different mathematical approaches are implemented, providing the same results, demonstrating the MS or A-DMS simplicity than the VSD approach.
- Machine conditions: normal and open-winding faulty conditions are implemented for a full investigation.
- Working conditions; different dc-link voltages and machine temperatures are implemented for an impact study on the maps.

The required input data of the algorithm and preliminary computation are discussed in the previous and summarized in the following:

- Amplitude limit of the phase currents  $I_{max}$ : it usually consists of the minimum value between the overload motor current and the current limit of the inverter. Using the VSD approach, the maximum current

$I_{max}$  is rescaled by the factor  $n_{ON}/n$  for faulty conditions. Otherwise, the maximum phase currents are invariant for MS, and VSD/DMS approaches, independently of the machine conditions (normal or faulty).

- Limit of the phase voltage  $V_{max}$ : this value is the maximum amplitude of the fundamental voltage component provided by the PWM inverter. For the case study, a space vector modulation has been considered. Thus the maximum value is computed based on dc-link voltage  $V_{dc}$  as:

$$V_{max} = \frac{V_{dc}}{\sqrt{3}} \quad (4.234)$$

- The machine parameters were extracted by elaborating the no-load and locked-rotor tests. The elaboration of the standard tests performed on multi-three-phase machines depends on the available data recorder. However, the VSD elaboration results are more immediate but require sophisticated facilities. However, these tests are not easy to perform due to the availability of sinusoidal multiphase sources. Details are reported in Section 4.7.2.
- Flux and torque maps of the tested 12-phase IM: these maps correlate the flux- and torque-producing currents  $I_d, I_q$  with the steady-state values of stator flux linkages  $\Lambda_{d,s}, \Lambda_{q,s}$  and electromagnetic torque  $T_e$ . Details are reported in Section 4.8: for the multi-three-phase machine, the procedure for the map computation depends heavily on the used approach.

#### 4.10.2 Mapping algorithm: approach and machine conditions

According to the considered speed and torque steps  $\Delta\omega_m$  and  $\Delta T_m$  resolutions for a fixed dc-link voltage  $V_{dc}$  and machine temperature, a regular mesh grid in the torque-speed range is generated. The speed limit of the mesh grid corresponds to the maximum operative multi-three-phase IM's speed. Conversely, the absolute torque limit corresponds to that of the torque map, which heavily depends on the active sets number (see Table 4.5). Therefore, the efficiency map is obtained by computing the efficiency of each point

composing the mesh grid. It is noted how the mesh grid is composed of torque-speed points that cannot be operated since they overcome the MTPS profile. However, the proposed mapping procedure automatically rules out these points, as shown in the following. Please note that the mapping algorithm does not require the computation of the MTPA and MTPS profiles. They are accessories, but the results must be in agreement.

According to the above-reported inputs and constraints, the efficiency map of the torque-speed mesh grid in normal and faulty conditions with different mathematical approaches is computed based on the flow diagram shown in Fig. 4.52, and whose description is reported in the following. The input parameters/maps are highlighted with yellow arrows/blocks in the flow diagram descriptive of the mapping computation procedure. The *if* conditions are represented by pink rhombus. The flow in red between Step 6 and Step

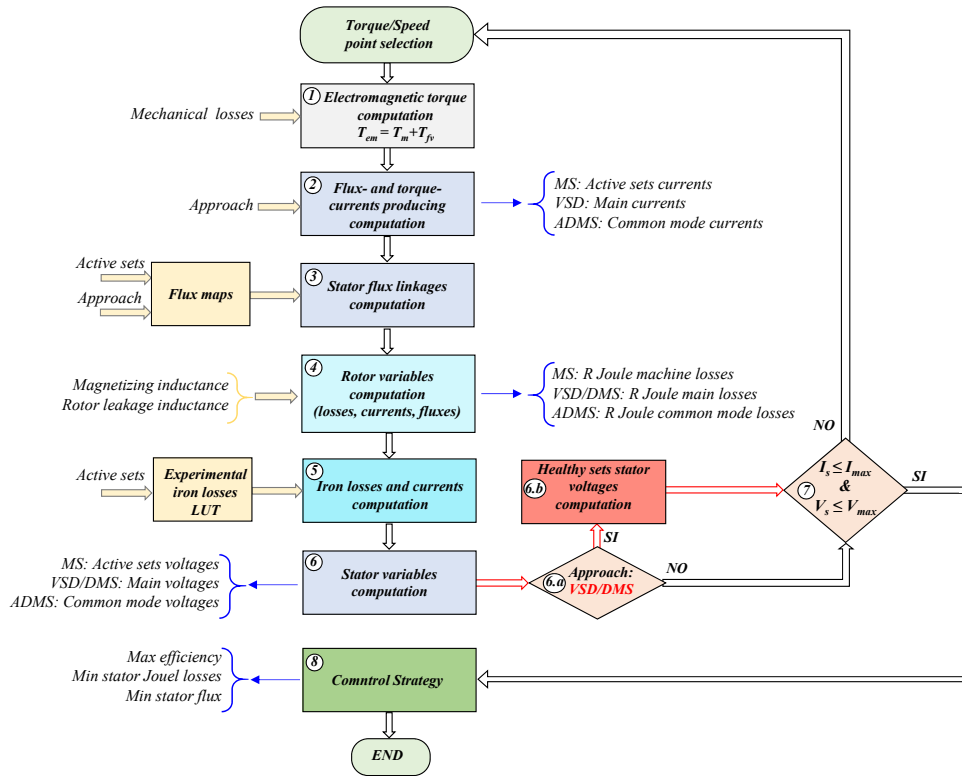


Figure 4.52 Flow diagram of the mapping algorithm with different approaches in both normal and open-winding faulty conditions.



6.b highlights the *alternative* path for the VSD-based model analyzed in the previous section. The blue arrows highlight details related to the approaches and control strategies.

### Step 1 - Electromagnetic torque computation

According to the mechanical speed  $\omega_m$  of the considered torque-speed point, the torque loss  $T_{fv}$  due to friction and ventilation is computed by interpolating the experimental profile obtained after performing the no-load tests (see Fig. 4.19). In this way, the electromagnetic torque  $T_{em}$  is computed from the mechanical one  $T_m$ .

### Step 2 - Flux- and torque- currents producing computation

The electromagnetic torque computed in Step 1 reflects in an isocontour on the surface of the torque map, which heavily depends on the active sets number. This means that infinite  $dq$  combinations generate the imposed torque at Step 1. The isocontour is discretized in  $n_c$  points and the corresponding  $I_d, I_q$  values are stored in two  $n_c$ -dimensional vectors denoted as  $I_d^{vct}$  and  $I_q^{vct}$  (superscript *vct* stands for vector variables). The number  $n_c$  is variable with the electromagnetic torque value, with the discretization assumed for the torque and obviously with the machine conditions.

As highlighted in the flow diagram in Fig. 4.52, the flux- and torque-currents producing assume a different physical meaning based on the used approach: in MS-, VSD/DMS, A-DMS-based models, these currents correspond to the ones of each active sets, to the ones in the main/common-mode subspace, to the ones in common-mode subspace, respectively.

### Step 3 - Stator flux linkages computation

For each combination of the equivalent  $dq$  currents, the  $dq$  stator flux linkages are extracted by interpolating the flux maps, obtaining the two  $n_c$ -dimensional stator flux linkage vectors  $\Lambda_{d,s}^{vct}$  and  $\Lambda_{q,s}^{vct}$ . The flux maps depend on the active sets number as shown in the flow diagram of Fig. 4.52 and as mentioned before in Section 4.8. Also, the flux maps are computed using the methodology presented before based on the mathematical approach. The flux maps are built by opportunely rescaling the magnetizing profile and selecting the current maps.

### Step 4 - Rotor variables computation

The rotor  $q$ -axis rotor current  $I_r^{vct}$  and flux linkage  $\Lambda_r^{vct}$  are computed as reported in Eq. (4.235), based on  $n_c$ -dimensional vector of magnetizing in-

ductance  $L_m^{vct}$  based on Eq. (4.236) and rotor resistance  $R_r^{vct}$ .

$$I_r^{vct} = -L_m^{vct} ./ L_r^{vct} .* I_q^{vct}, \quad \Lambda_r^{vct} = L_m^{vct} .* I_d^{vct} \quad (4.235)$$

where  $.*$  and  $./$  are the element-wise operators of product and division, respectively. The magnetizing inductance vector  $L_m^{vct}$  is evaluated differently depending on the used approach as reported in Eq. (4.236).

$$\begin{aligned} MS: \quad L_m^{vct} &= \text{interp1}\left(n \cdot I_m, \frac{L_m}{n}, I_d^{vct} \cdot n_{ON}\right) \\ VSD: \quad L_m^{vct} &= \text{interp1}\left(I_m, L_m, I_d^{vct}\right) \\ A-DMS: \quad L_m^{vct} &= \text{interp1}\left(I_m, L_m \cdot \frac{n_{ON}}{n}, I_d^{vct} \cdot \frac{n_{ON}}{n}\right) \end{aligned} \quad (4.236)$$

where  $I_m$  and  $L_m$  are the magnetizing current and inductance evaluated with the no-load tests (see Fig. 4.42) and the function *interp1* is consistent with the previous definition. In this way, the magnetizing inductance vector composed by  $n_c$  combination related to the  $n_c$  combination of  $d$ -current opportunely rescaled based on the used approach to realize the imposed electromagnetic torque at Step 1 is built.

The  $n_c$ -dimensional vector of rotor Joule losses  $P_{jr}^{vct}$  is computed based on the rotor current vector computed in Eq. (4.235) and the rotor resistance vector as:

$$\begin{aligned} MS: \quad P_{jr}^{vct} &= \frac{3}{2} \cdot R_r^{vct} .* I_r^{vct} .* I_r^{vct} \\ VSD: \quad P_{jr}^{vct} &= \frac{3}{2} \cdot n \cdot R_r^{vct} .* I_r^{vct} .* I_r^{vct} \\ A-DMS: \quad P_{jr}^{vct} &= \frac{3}{2} \cdot n_{ON} \cdot R_r^{vct} .* I_r^{vct} .* I_r^{vct} \end{aligned} \quad (4.237)$$

where the rotor resistance vector  $R_r^{vct}$  depends on the slip frequency  $f_{sl}$ , according to the experimental profile obtained from the locked-rotor tests – see Fig. 4.18. Note that the relation in Eq. (4.237) in VSD-based model is in agreement with the one in Eq. (4.231).

The rotor resistance depends on the used approach as:

$$\begin{aligned}
 MS : \quad R_r^{vct} &= \frac{1}{n} \cdot R_r^{vct} \\
 VSD : \quad R_r^{vct} &= R_r^{vct} \\
 A-DMS : \quad R_r^{vct} &= \frac{n_{ON}}{n} \cdot R_r^{vct}
 \end{aligned} \tag{4.238}$$

where  $R_r^{vct}$  is evaluated based on the profile shown in Fig. 4.18 interpolating based on the slip frequency  $f_{sl}$  computed as:

$$f_{sl}^{vct} = \frac{1}{2 \cdot \pi} \cdot R_r^{vct} \cdot \left( \frac{1}{L_r^{vct}} \cdot I_q^{vct} \cdot \frac{1}{I_d^{vct}} \right) \tag{4.239}$$

where  $L_r^{vct}$  is computed based on  $L_m^{vct}$  and  $L_{l,r}$ , which vector is built repeating the constant value of rotor leakage inductance. The computation of the variables is expressed using the same approach. The rotor resistance is correct in rotor temperature  $\vartheta_r$  considering the variation of the rotor resistance to the operating rotor temperature.

Please note that the physical meaning of the rotor Joule losses Eq. (4.237) depends on the used approach: MS-, VSD/DMS-, A-DMS-based models the ones corresponding to the rotor Joule machine losses, rotor Joule losses of the main/common-mode subspace, rotor Joule losses of the common-mode. The mathematical manipulation in Eq. (4.237) is justified as follows:

- MS: squirrel cage rotor is modeled as an equivalent three-phase winding composed of identical single-phase windings. Therefore, no rescaling of the rotor current and resistance is required.
- VSD: squirrel cage rotor is modeled as an equivalent multi-three-phase winding, thus emulating the stator winding configuration. Consequently, the adjustment of the rotor resistance by the factor  $n$  (rated sets number) is required.
- A-DMS: The squirrel cage rotor is modeled for the VSD approach but is adapted to the machine conditions. For this reason, the rotor resistance is adjusted by the factor  $n_{on}$  (active sets number).

### Step 5 - Iron losses and currents computation

From the slip frequency  $f_{sl}$  in Eq. (4.239), the corresponding vector of synchronous speed  $\omega$  is computed as:

$$\omega = \omega_m + \omega_{sl} \quad (4.240)$$

At the same time, the  $n_c$ -dimensional vector of the stator frequency  $f^{vct}$  is easily obtained as  $f^{vct} = \omega^{vct}/2\pi$ . Therefore, the  $dq$  components of the back-emf  $E_{d,s}^{vct}, E_{q,s}^{vct}$  and amplitude  $E_s^{vct}$  of the machine's back-emf are computed as:

$$\begin{aligned} E_{d,s}^{vct} &= -\omega^{vct} \cdot \Lambda_{q,s}^{vct}, & E_{q,s}^{vct} &= \omega^{vct} \cdot \Lambda_{d,s}^{vct} \\ E_s^{vct} &= \sqrt{E_{q,s}^{vct} \cdot E_{d,s}^{vct} + E_{q,s}^{vct} \cdot E_{q,s}^{vct}} \end{aligned} \quad (4.241)$$

where  $\omega^{vct}$  is computed in Eq. (4.240) based on  $\omega_{sl}^{vct}$  and the stator flux components vector are computed in Step 2. The iron losses, including the stator skin effect, are evaluated from the stator frequency  $f$  and amplitude of the machine's back-emf  $E_s$  by interpolating the corresponding map based on the active sets number. For example, considering the normal conditions, the map on the right of Fig. 4.22 is interpolated, while the map on the left is interpolated if just one set is active.

Therefore, the  $n_c$ -dimensional vector of iron losses  $P_{Fe}^{vct}$  is obtained, while the corresponding current components  $I_{d,Fe}^{vct}, I_{q,Fe}^{vct}$  are computed using the multi-three-phase IM equivalent circuit as:

$$I_{d,Fe}^{vct} = E_{d,Fe}^{vct} / R_{Fe}^{vct}, \quad I_{q,Fe}^{vct} = E_{q,Fe}^{vct} / R_{Fe}^{vct} \quad (4.242)$$

where the equivalent iron resistance vector  $R_{fe}^{vct}$  is computed according to the used approach as:

$$\begin{aligned} MS: \quad R_{Fe}^{vct} &= \frac{3}{2} \cdot n_{ON} \cdot E_s^{vct} \cdot E_s^{vct} / P_{Fe}^{vct} \\ VSD: \quad R_{Fe}^{vct} &= \frac{3}{2} \cdot n \cdot E_s^{vct} \cdot E_s^{vct} / P_{Fe}^{vct} \\ A-DMS: \quad R_{Fe}^{vct} &= \frac{3}{2} \cdot n_{ON} \cdot E_s^{vct} \cdot E_s^{vct} / P_{Fe}^{vct} \end{aligned} \quad (4.243)$$

Eq. (4.243) gives an equivalent iron resistance of the active sets, main sub-space, or common mode based on the MS-, VSD-, or A-DMS-based models, respectively.

#### Step 6 - Stator variables computation

According to the equivalent circuit shown in Fig. 4.49, the  $n_c$ -dimensional vectors of  $dq$  stator currents  $I_{d,s}^{vct}, I_{q,s}^{vct}$  are computed (see Eq. (4.244)), as well as the  $dq$  stator voltages  $V_{d,s}^{vct}, V_{q,s}^{vct}$  in Eq. (4.245), in according to Eq. (4.241). For this calculation, the stator resistance  $R_s$  is evaluated to the considered operative temperature of the stator winding  $\vartheta$ . Finally, the  $n_c$ -dimensional vector of the stator Joule losses  $P_{js}^{vct}$  can be computed.

$$I_{d,s}^{vct} = I_{d,Fe}^{vct} + I_d^{vct}, \quad I_{q,s}^{vct} = I_{q,Fe}^{vct} + I_q^{vct} \quad (4.244)$$

$$I_s^{vct} = \sqrt{I_{d,s}^{vct} \cdot I_{d,s}^{vct} + I_{q,s}^{vct} \cdot I_{q,s}^{vct}}$$

$$V_{d,s}^{vct} = R_s(\vartheta) \cdot I_{d,s}^{vct} + E_{d,s}^{vct}, \quad V_{q,s}^{vct} = R_s(\vartheta) \cdot I_{q,s}^{vct} + E_{q,s}^{vct} \quad (4.245)$$

$$V_s^{vct} = \sqrt{V_{d,s}^{vct} \cdot V_{d,s}^{vct} + V_{q,s}^{vct} \cdot V_{q,s}^{vct}}$$

The physical meaning of the  $dq$  stator current and voltage depend on the used approach, as already explained many times. However, the working point selected at the beginning of the mapping procedure in the flow diagram of Fig. 4.52, is acceptable if the current and voltage limits are satisfied. The voltage limit must be compared to the healthy sets' voltage because the voltage of other sets (inactive/faulty) is lower than that of healthy sets. Please note that inactive sets in faulty conditions are subjected to the back-emf Eq. (4.241), while the stator voltage drop is zero in open-winding faulty conditions. For this reason, knowing the physical meaning of the stator voltage in Eq. (4.245), a further step is necessary if the VSD approach is used.

The  $n_c$ -dimensional vector of the stator Joule losses  $P_{js}^{vct}$  is computed as:

$$\begin{aligned} MS : \quad P_{js}^{vct} &= \frac{3}{2} \cdot n_{ON} \cdot R_s^{vct} \cdot I_s^{vct} \cdot I_s^{vct} \\ VSD : \quad P_{js}^{vct} &= \frac{3}{2} \cdot n \cdot R_s^{vct} \cdot I_s^{vct} \cdot I_s^{vct} \cdot \frac{n}{n_{ON}} \\ A-DMS : \quad P_{js}^{vct} &= \frac{3}{2} \cdot n_{ON} \cdot R_s^{vct} \cdot I_s^{vct} \cdot I_s^{vct} \end{aligned} \quad (4.246)$$

The relation in Eq. (4.246) in VSD-based model is in agreement with Eq. (4.231).

Finally the computation of the mechanical and electrical power is performed as:

$$P_e^{vct} = P_m^{vct} + P_{l-tot}^{vct}$$

$$P_m^{vct} = T_m \cdot \omega_m^{vct} \quad (4.247)$$

$$P_{l-tot}^{vct} = P_{js}^{vct} + P_{jr}^{vct} + P_{fv}^{vct}$$

where  $P_{l-tot}^{vct}$  stands for the  $n_c$ -dimensional overall losses vector,  $T_m$  is the mechanical torque referred to the speed/torque point selection and any other are consistent with the previous definitions.

#### Step 6 - VSD: healthy sets stator voltages computation

The current and voltage limits must be verified according to the stator voltages computed in the previous step. However, a new step is added if the used approach is the VSD-based model. In Step 6.b of the flow diagram in Fig. 4.52, the computation of the stator voltages of healthy sets is performed, starting from the ones of the main/common-mode subspace for the VSD/DMS approach. The stator voltage of the healthy sets is computed with the same procedure reported in Step 6 of Section 4.9. The reconstruction of the stator voltage of the healthy sets is obtained with energetic balance because, in faulty conditions, the harmonic/differential-mode subspaces become active sets. Consequently, the main subspace is not representative of the healthy sets, and the stator voltages in Eq. (4.78) represent just the voltage of the main subspace, which is not representative of healthy sets. Also, the harmonic subspaces are not representative of the faulty sets; consequently, the reconstruction of the stator voltage of the healthy sets is required. This step is not required for other approaches (i.e. MS and A-DMS) because the stator voltages in Eq. (4.245) coincide with the ones of the active sets. Based on the above, the  $n_c$ -dimensional vectors of the stator voltage of the healthy sets, the reactive power, and electrical power are computed, using the relation in Eq. (4.230) and Eq. (4.229) as:

$$V_{s-ON}^{vct} = \frac{\sqrt{P_{e-ON}^{vct} \cdot P_{e-ON}^{vct} + Q_{e-ON}^{vct} \cdot Q_{e-ON}^{vct}}}{\frac{3}{2} \cdot n_{ON} \cdot \frac{n}{n_{ON}} \cdot I_s^{vct}} \quad (4.248)$$

**Step 7 - Current and voltage limits**

All the elements of the  $n_c$ -dimensional vectors computed in the previous steps that do not respect the  $I_{max}$  and/or  $V_{max}$  limits are ruled out, avoiding the saving. Obviously, for the grid points that overcome the MTPS profile (see Section 4.9), and therefore cannot be physically obtained, the algorithm skips the computation of the efficiency moving to consider the next torque-speed combination, as shown in Fig. 4.52. Note that the MTPS profile is implicitly computed in this step. The previous computation in Section 4.9 is not necessary for mapping algorithm. Therefore, the MTPS profiles must match independently by mathematical approach and as obtained.

For clarity, by considering any one of the  $n_c$ -dimensional vectors computed in the previous steps and for simplicity denoted with  $hX^{vct}$ , the elements of this vector that satisfy both the above-reported limits are indicated as:

$$\left. X^{vct} \right| \begin{array}{l} V_s^{vct} \leq V_{max} \\ I_s^{vct} \leq I_{max} \end{array} \quad (4.249)$$

It is highlighted that since the  $n_c$ -dimensional vectors have been computed using element-wise operators (i.e.,  $*$  and  $./$ ), the position indexes of the elements that satisfy the voltage and current limits are the same for all vectors.

**Step 8 - Control strategy**

The developed mapping algorithm, in addition, considers:

- Different mathematical approaches (MS, VSD/DMS, A-DMS),
- Different machine condition (healthy, faulty),
- Different dc-link voltage values,
- Different machine temperature values,

and it is able to consider different control strategies:

- Maximum efficiency,
- Minimum stator Joule losses.

Let's consider the elements of the  $n_c$ -dimensional vectors that satisfy both voltage and current limits. The position index of the element that emulates one of the possible control strategies corresponds to the one that minimizes the overall losses, minimizes the stator Joule losses (MTPA), and minimizes the stator flux. In other words, only one specific combination of  $dq$  variables (voltages, currents) leads to emulating the chosen strategy control. For clarity, considering any one of the  $n_c$ -dimensional vectors again  $X^{vct}$ , the element of this vector that leads to emulating the control strategy is denoted with the superscript  $opt$  as in Eq. (4.250) based on the chosen control strategy.

$$X^{opt} = \min \left( P_{jr}^{vct} + P_{js}^{vct} + P_{Fe}^{vct} \right) \Big|_{\substack{V_s^{vct} \leq V_{max} \\ I_s^{vct} \leq I_{max}}} \quad (4.250)$$

$$X^{opt} = \min \left( P_{js}^{vct} \right) \Big|_{\substack{V_s^{vct} \leq V_{max} \\ I_s^{vct} \leq I_{max}}}$$

Finally, if considering a torque-speed point in the motor operation, the machine's efficiency  $\eta^{opt}$  is computed as:

$$\eta^{opt} = \frac{T_m \cdot \omega_m}{T_{em} \cdot \omega_m + P_{jr}^{opt} + P_{Fe}^{opt} + P_{js}^{opt}} \quad (4.251)$$

Conversely, if considering a torque-speed point in the generation operation, the machine's efficiency is computed as:

$$\eta^{opt} = \frac{T_{em} \cdot \omega_m + P_{jr}^{opt} + P_{Fe}^{opt} + P_{js}^{opt}}{T_m \cdot \omega_m} \quad (4.252)$$

The mathematical equations for efficiency computation for multi-three-phase IM coincide with the one for the three-phase IM counterpart. As reported, the procedure for loss evaluation formally coincides, but the mathematical manipulations are fundamental for a correct performance evaluation.

Once the multi-three-phase IM's efficiency has been computed in all machine conditions (healthy and faulty), the proposed mapping procedure stores it and proceeds to consider the next torque-speed point, as shown in the flow diagram of Fig. 4.52. However, other variables of interest like the stator  $dq$  currents are saved, thus computing the stator  $dq$  currents maps if



considering this case. As reported in the next Section, the stator currents maps have been used to perform the experimental validation of the proposed mapping procedure. In other words, the proposed method can potentially map all machine's electromagnetic variables, thus representing a promising solution for accurately virtualizing multi-three-phase IMs operated in wide torque-speed ranges. An important feature of the mapping is the ability to virtualize the machine in open-winding faulty conditions, which is an advantage of the multi-phase machines over the three-phase counterparts. The torque capability is reduced in faulty conditions, but the machine can work, covering a key factor in safety applications.

The efficiency algorithm using MS-based model provides the same results as the algorithms based on the VSD and A-DMS approaches, showing how the difference is related to the mathematical manipulations. However, the VSD approach presents the same disadvantages, i.e., the reconstruction of the stator voltage of the active sets and the stator Joule losses related to the harmonic subspaces, which became active in faulty conditions. Indeed, using the A-DMS approach, the differential-mode subspaces are always inactive, independently of the machine conditions. The modularity of MS approach is preserved, avoiding the coupling between the active sets.

The mapping algorithm provides in output a set of efficiency maps in the torque-speed plane, computed for each combination of maximum available dc-link voltage and operating temperature considered for the analyses and the healthy and faulty conditions ( $n_{ON} = 4, 3, 2, 1$ ). In Fig. 4.53 - Fig. 4.55 are reported some examples of maps computed for the machine under test when a control strategy that maximizes the machine efficiency is considered: three different mathematical approaches are used, analyzing different machine operating conditions.

The efficiency map is insignificant when just one set is active ( $n_{On} = 1$ ): torque values are adapted than  $n_{ON} = 4, 3, 2$ , but the maximum available torque is relatively low, and the efficiency value had no great significance. The other maps confirm the maximum available torque presented in Table 4.5. In addition, in Fig. 4.53 - Fig. 4.55 can be observed the agreement between different mathematical approaches: Fig. 4.53 reports the efficiency map obtained with MS approach; Fig. 4.54 reports the efficiency map obtained with VSD/DMS approach; Fig. 4.55 reports the efficiency map ob-

tained with A-DMS approach.

The following figures are reported:

- MS: in Fig. 4.53 - Fig. 4.56 the efficiency maps of 12-phase IM calculated with proposed algorithm based on MS approach are reported, implementing the maximization of the efficiency and minimization of stator Joule losses, respectively.
- VSD/DMS: in Fig. 4.54 - Fig. 4.57 the efficiency maps of 12-phase IM calculated with proposed algorithm based on VSD/DMS approach are reported, implementing the maximization of the efficiency and minimization of stator Joule losses, respectively.
- ADMS: Fig. 4.55 - Fig. 4.58 the efficiency maps of 12-phase IM calculated with proposed algorithm based on A-DMS approach are reported, with both control strategies.

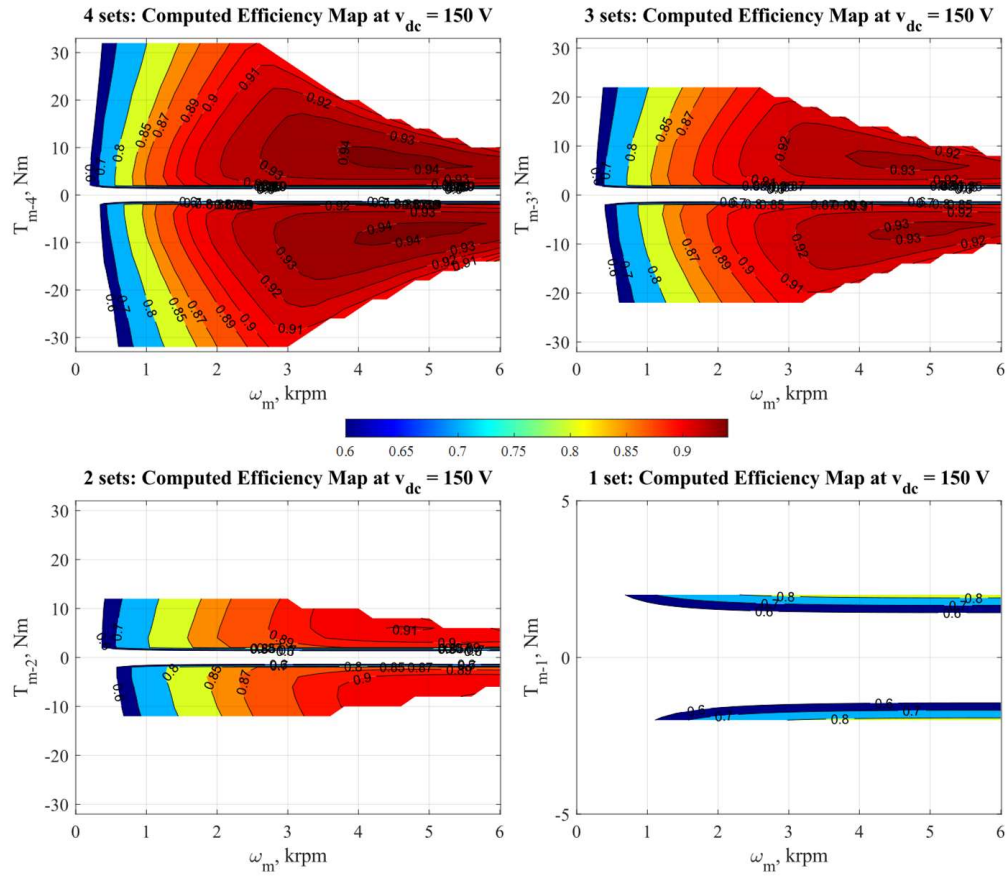


Figure 4.53 Computed efficiency maps based on the MS approach maximizing the efficiency:  $n_{ON} = 4, 3, 2, 1$ .

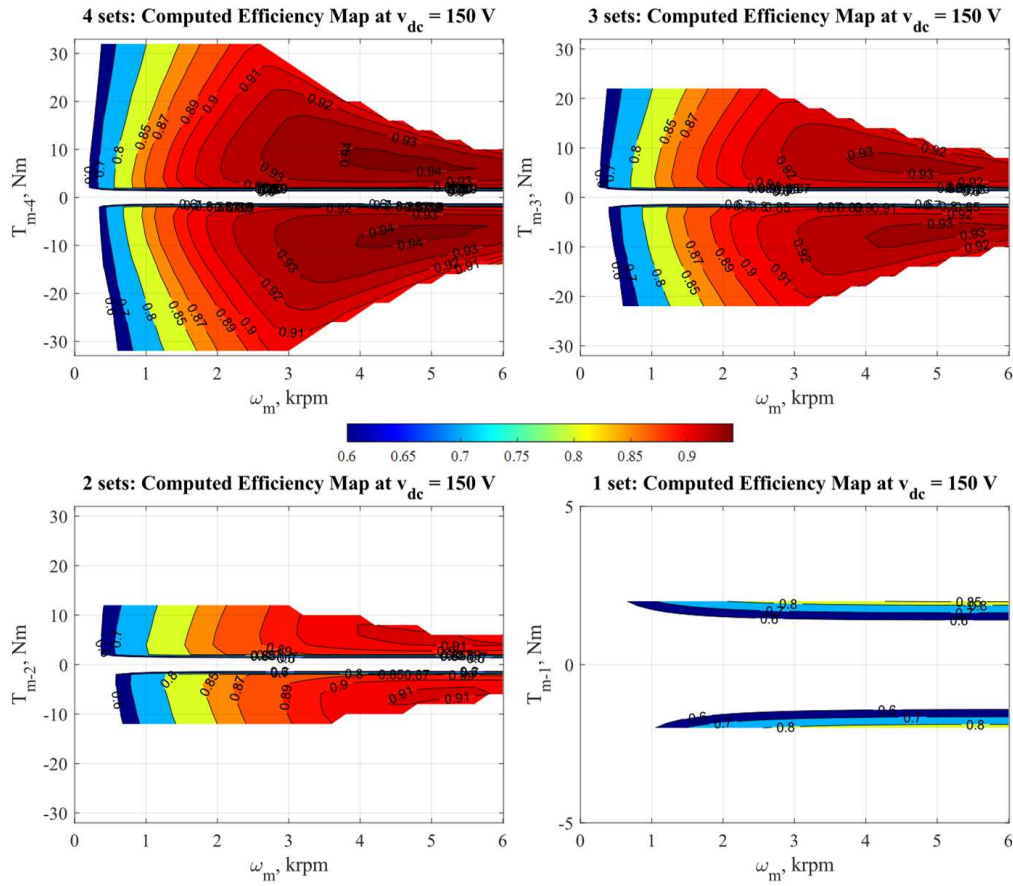


Figure 4.54 Computed efficiency maps based on the VSD/DMS approach maximizing the efficiency:  $n_{ON} = 4, 3, 2, 1$ .

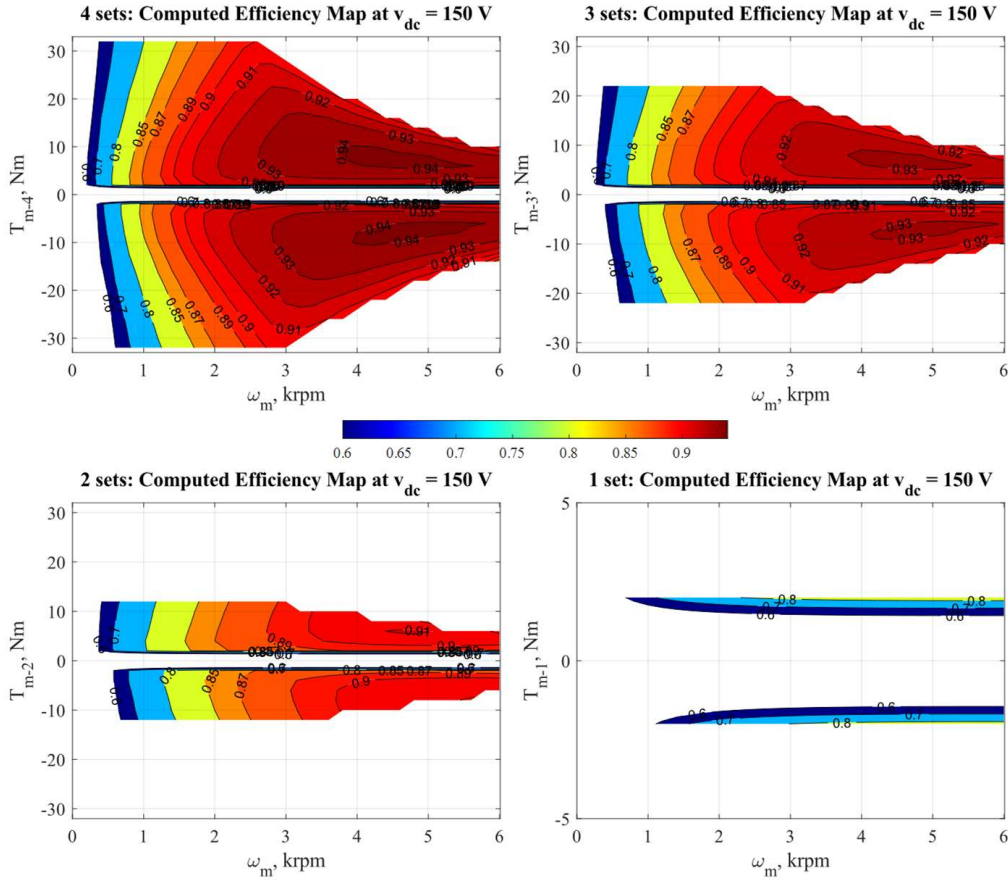


Figure 4.55 Computed efficiency maps based on the A-DMS approach maximizing the efficiency:  $n_{ON} = 4, 3, 2, 1$ .

Similarly, Fig. 4.56 - Fig. 4.58 show the efficiency maps computed assuming a control strategy that minimizes the machine stator Joule losses. It has been verified that the two considered control strategies do not present significant differences in efficiency because the IM under test is characterized by relatively low iron losses, especially in overloaded conditions. In any case, it was found that the developed algorithm can discriminate between the two control strategies. In particular, for the same operation point, the efficiency results are slightly higher in the maximum efficiency control (Fig. 4.53 - Fig. 4.55) with respect to the minimum Joule loss strategy – see Fig. 4.56 - Fig. 4.58.

As expected, the obtained maps does not depend on the mathematical approaches.

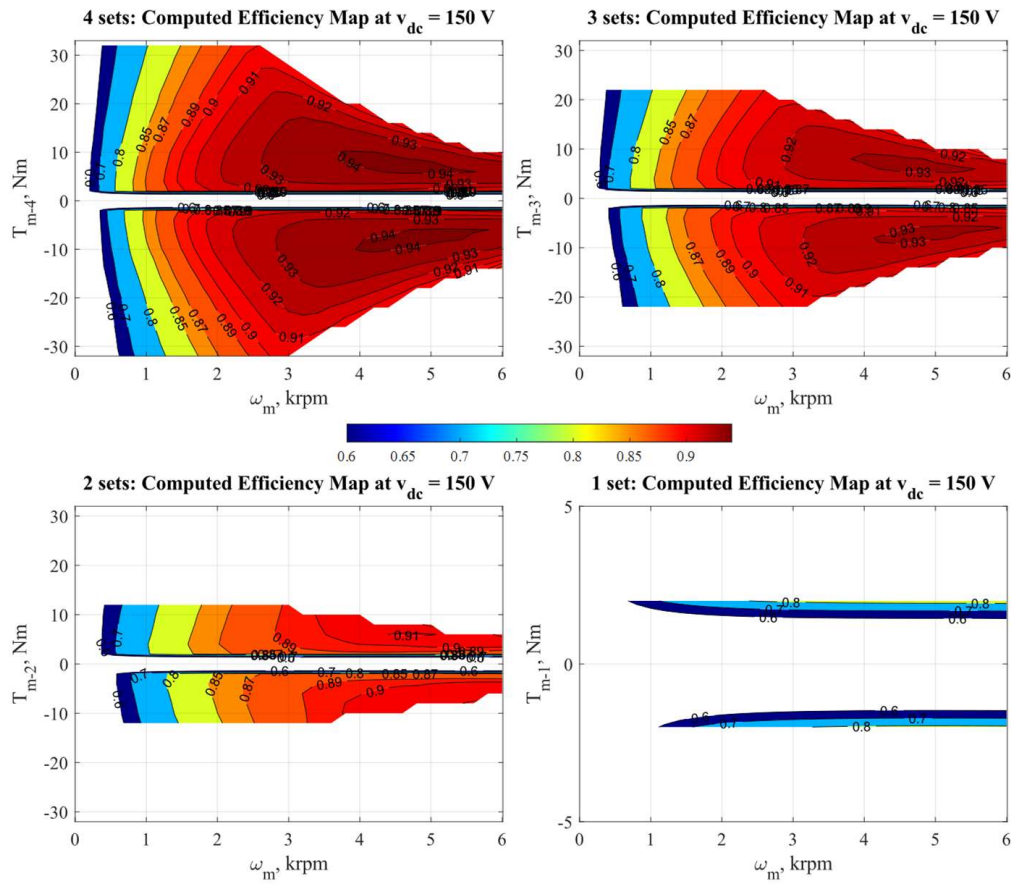


Figure 4.56 Computed efficiency maps based on the MS approach minimizing the stator Joule:  $n_{ON} = 4, 3, 2, 1$ .

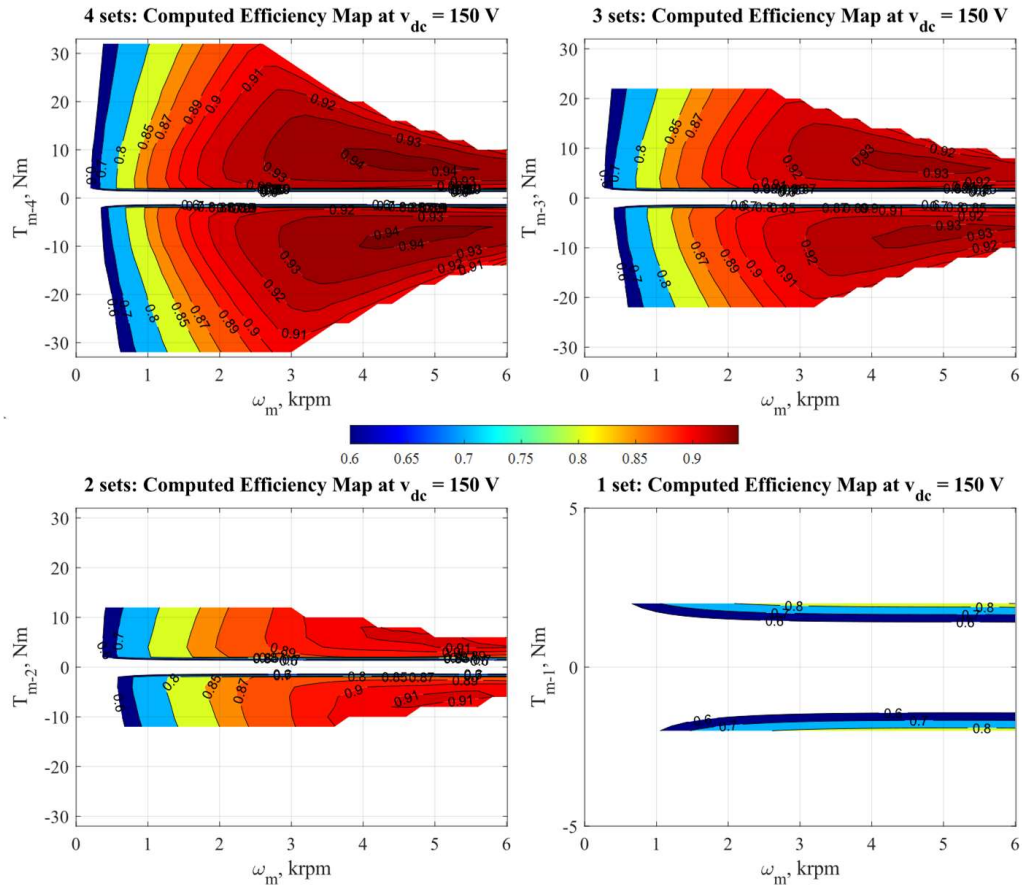


Figure 4.57 Computed efficiency maps based on the VSD/DMS approach minimizing the stator Joule:  $n_{ON} = 4, 3, 2, 1$ .

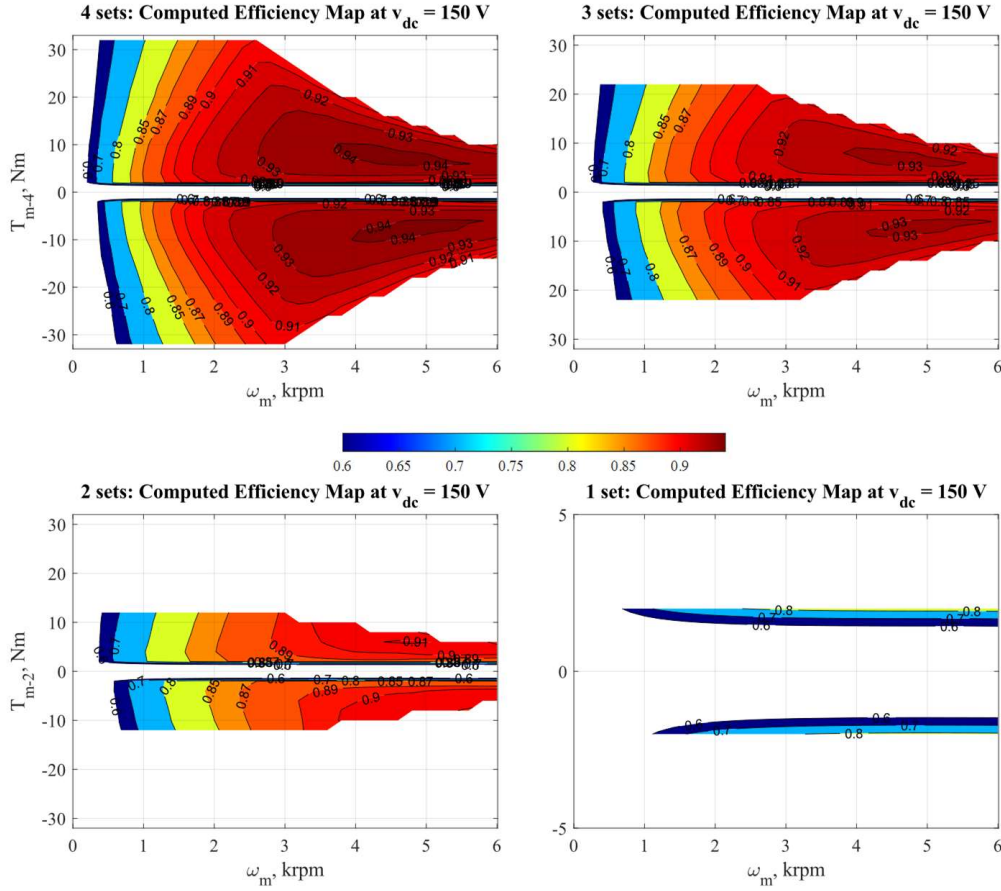


Figure 4.58 Computed efficiency maps based on the A-DMS approach minimizing the stator Joule:  $n_{ON} = 4, 3, 2, 1$ .

The developed mapping algorithm based on the MS and A-DMS approaches provides the same results (see Fig. 4.53 - Fig. 4.55 and Fig. 4.56 - Fig. 4.58). Indeed, based on the DMS/VSD approach (Fig. 4.54 - Fig. 4.57), the mapping algorithm provides minimal differences in the efficiencies in faulty conditions. One possible reason could be the flux contribution in the differential/harmonic subspaces for the iron losses computation. However, the results are pretty consistent, and the results based on VSD/DMS approaches can be considered perfectly valid and in agreement with the ones based on MS and A-DMS approaches. For simplicity, the MS and A-DMS approaches are highly recommended for mapping analysis, independently by the adapted control strategy.



## 4.11 Experimental validation

This section presents the experimental validation of the 12-phase IM mapping algorithm. The proposed mapping algorithm has been validated with a multi-modular power converter feeding a squirrel cage quadruple three-phase IM prototype, 10 kW, 4 poles, 200 Hz IM. Their primary data are listed in Table 4.6. The 12-phase IM under test consists of a reduced-scale prototype of a starter-generator for aircraft applications. The tested machine is shown in Fig. 4.59.

### 4.11.1 Test rig

The machine under test has been mounted on a test rig for validation, as shown in Fig. 4.60. The rotor shaft has been coupled to a driving machine acting as a prime mover (speed-controlled). However, due to the limitation of the test rig, the 12-phase IM's speed has been limited to 6000 rpm. The machine parameters have been evaluated based on the no-load and locked-rotor tests, as explained in Section 4.7.2. The iron losses have been investigated and integrated into the modeling through the lookup tables based on the machine conditions (healthy or faulty).

Table 4.6 Machine primary data

Electrical data	
Phase number	12 (4 x 3-phase)
Pole number	4
Rated power	10 kW
Rated speed	6 krpm
Rated phase-voltage	115 Vrms
Rated phase-current	10 Arms
Machine parameters	
Stator resistance	$R_s = 160 \text{ m}\Omega$
Stator leakage inductance	$L_{l,s} = 1 \text{ mH}$
Magnetizing inductance	$L_m = 18 \text{ mH}$
Rotor resistance	$R_r = 126 \text{ m}\Omega$
Rotor leakage inductance	$L_{l,r} = 1.14 \text{ mH}$
Rated stator flux amplitude	$\lambda_s = 115 \text{ mVs}$

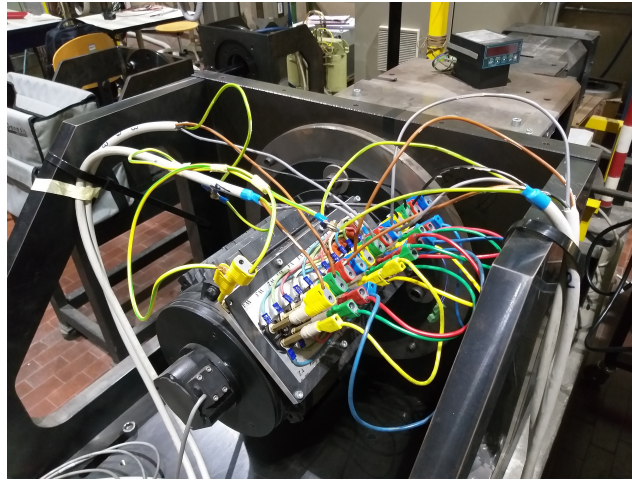


Figure 4.59 12-phase IM.

The power electronics feeding the 12-phase IM consists of four independent three-phase inverter power modules based on an IGBT power module, rated 100 A, 1200 V, and fed by a bidirectional programmable dc source. The switching and sampling frequencies have been set at 5 kHz to provide a compatible scenario with the industrial implementations. A software-implemented dead-time of  $3\mu\text{s}$  has been used. Finally, a single DC voltage source is employed according to the power converter structure. This consisted of a battery emulator.

Finally, the digital controller is the dSpace DS1103 fast prototyping board, allowing the online operations of setup and monitoring of the experimental tests, including the real-time data acquisition. The control algorithm has been developed in C-code. A schematic of the test rig is reported in Fig. 4.61.

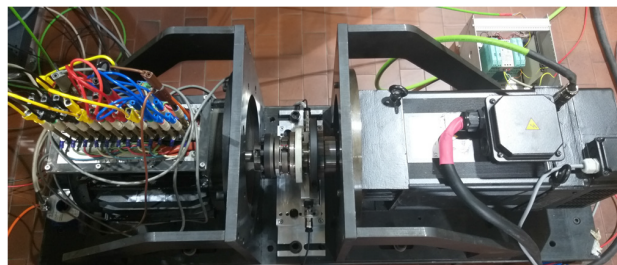


Figure 4.60 Schematic block diagram of the test rig for the experimental validation of multi-three-phase IM mapping.

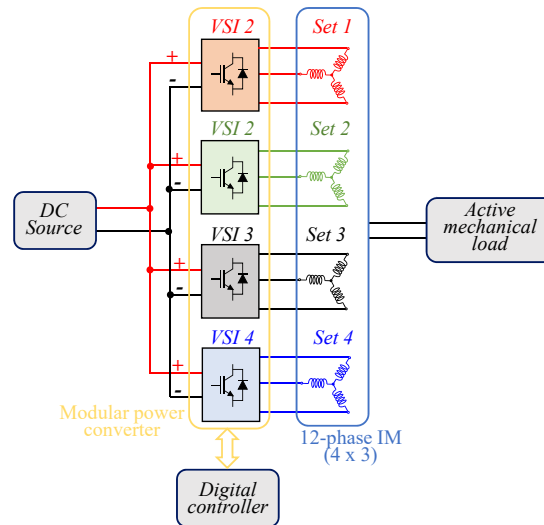


Figure 4.61 Schematic block diagram of the test rig for the experimental validation of multi-three-phase IM mapping.

### Efficiency maps measurement

The torque transducer T40B from HBM has been mounted along with the mechanical coupling between the 12-phase IM under test and the driving machine, as shown in Fig. 4.63, as for the experimental validation of three-phase IM. In this way, the mechanical quantities of torque and position have been measured. In detail, the mechanical position has been used for two purposes. On the one hand, its elaboration allowed the detection of the mechanical speed for computing the 12-phase IM's mechanical power. On the other hand, it has consisted as one of the feedback for the torque control algorithm thanks to its good resolution (1024 pulses/rev).

The electric measurements of the 12-phase IM's phase currents of all stator phases have been measured using the high-performance current transducers IT 200-S Ultrastab from LEM. In parallel, the line-to-line PWM voltages have been measured using the GN610B from HBM, consisting of a voltage card equipped with high-voltage/high-speed acquisition channels (1000 V, 18 bit, 2 MS/s). Both mechanical and electrical quantities have been sampled and stored with a sampling frequency of 212 MS/s by the data recorder GEN2tB from HBM, consisting of a high-performance transient

recorder and calibrated data acquisition system. The time-fundamental components of phase voltages and phase currents have been extracted from the sampled data using the data elaboration software integrated with the instrument. In this way, the time-fundamental electric power has been computed, thus ruling out the additional harmonic losses introduced by the PWM modulation.

In summary, the experimental efficiency maps shown in the following subsections have been computed considering a predefined number of time-fundamental electric periods for each test point. In this time window, the average values of mechanical and time-fundamental electric power have been computed, allowing the evaluation of the efficiency considering its time-fundamental behavior, i.e., the same one calculated by the proposed mapping procedure. The same procedure has been adopted to validate healthy and faulty machine conditions. All efficiency maps have been evaluated at the same operating temperature in which the no-load and locked-rotor tests have been performed (i.e.,  $\vartheta_0 = 25^\circ\text{C}$ ).

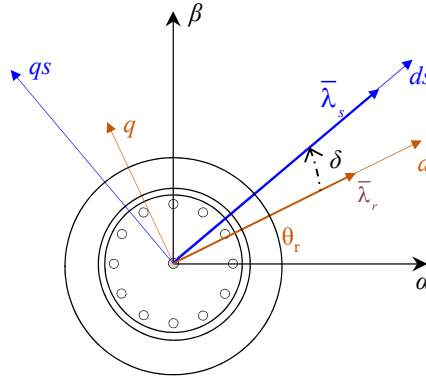
### Validation approach

The proposed mapping procedure has been validated by directly comparing the experimental efficiency maps with those computed for healthy and faulty conditions ( $n_{ON} = 4, 3, 2, 1$ ). Each experimental efficiency map has been evaluated by setting a reasonable resolution in speed and torque, thus leading to a predefined number of test points in the torque-speed range. Also, consider that the efficiency maps validated experimentally have been obtained using the mapping procedure summarized in Fig. 4.52, selecting the maximum efficiency as the control strategy based on the A-DMS-based model. The validation based on the A-DMS approach has been sufficient because the results with different approaches have perfectly agreed with the used one. Regarding the control strategy, only the maximum efficiency results are validated due to the few differences in computed results varying the control strategy (i.e., minimum Joule losses, minimum stator flux).

The stator flux and  $q$ -current torque producing of the 12-phase IM under test has been controlled in each test point using a multi-three-phase

direct flux vector control (DFVC) scheme [125] to regulate the stator flux and torque of a multi-three-phase IM. However, to correctly validate the proposed procedure, the reference stator  $q$ -current  $i_q^*$  for the torque control and the stator flux  $\lambda_s^*$  have been generated using the following approach. The efficiency maps have been preliminarily computed using the proposed procedure based on the maximum efficiency control strategy using the A-DMS mathematical approach and by considering the same operating conditions subsequently imposed in the experimental validation, i.e., the same working temperatures, voltage  $V_{max}$  and current  $I_{max}$  limits, machine conditions (healthy or faulty). However, the  $q$ -current and stator flux maps related to each computed efficiency map have been stored and converted in lookup tables (LUTs), shown in Fig. 4.63, to be implemented and interpolated in the motor control algorithm. Therefore, the reference  $q$ -current and stator flux have been generated for each test point by first selecting the LUTs reporting the reference maps to the same experimental conditions (actual operating temperatures, dc-link voltage value  $v_{dc}$ , machine conditions). Finally, according to the reference values of torque  $T_m^*$  and speed  $\omega_m^*$  of the considered test point, the selected LUTs have been interpolated, getting the reference of the  $q$ -current  $i_q^*$  and stator flux  $\lambda_s^*$ . The interpolated value of  $q$ -axis current and stator flux represent the reference input  $i_q^*$ ,  $\lambda_s^*$  of the DFVC machine control.

The used validation approach brings the following advantage. The multi-three-phase IM's torque is controlled using the optimal references of the  $q$ -axis current and stator flux, thus maximizing the efficiency in each operating point since the validated mapping procedure considers all the IM's losses sources. Conversely, almost all the commercial torque controllers for IM drives perform the torque regulation using control schemes that, in the luckiest cases, minimize the stator Joule losses according to the voltage and current constraints imposed by the inverter feeding the machine, [125]. In contrast, in the worst cases, most commercial torque control solutions set the IM's rated flux below the base speed regardless of the load torque. Above the base speed, the flux level is reduced using several strategies proposed in the literature. The control scheme is implemented in rotating stator flux coordinates  $dqs$ . Therefore, the  $ds$ -axis position  $\theta_s$  corresponds with that of the stator flux vector. Since the  $dqs$  frame is adopted, the synchronous speed is defined as the angular speed of the stator flux vector to the stationary

Figure 4.62 Rotating stator flux frame  $dq_s$ .

$\alpha$ -axis. Finally, the machine load-angle  $\delta$  is defined as the  $ds$ -axis position to the rotor flux vector, where the latter determines the conventional  $d$ -axis, used until now. The control scheme implemented for the mapping validation can only manage a balanced operation among the healthy units. This means that the healthy units must operate with the same stator flux amplitude and torque values.

The proposed drive scheme regulates the machine torque by directly controlling the common-mode values of flux amplitude and torque-producing current. In parallel, the flux amplitude and  $qs$ -axis current of each differential-mode subspace are controlled at zero. The  $q$ -axis current  $i_q^*$  reference and stator flux reference  $\lambda_s^*$ , evaluated interpolating the efficiency mapping LUTs, are compared with the observed stator flux  $\hat{\lambda}_s$  and measured stator current. The latter reference values are transformed based on the adaptive decoupling matrix in the common-mode and differential-mode subspace reference values. Adaptive decoupling transformation means that the matrix is built in according to the active sets number  $n_{ON}$  Eq. (4.129) - Eq. (4.131), reported in Section 4.5.

These common-mode reference values  $\lambda_{cm-dqs}^*$ ,  $\lambda_{dm-dqs}^*$  and  $i_{cm-dqs}^*$ ,  $i_{dm-dqs}^*$  are compared with the observed stator flux and measured current evaluated in common-mode and differential-mode subspaces. Both the common- and differential-mode quantities are controlled using PI regulators. The outputs of these last correspond to the reference voltages of the machine in terms of common-mode  $v_{cm-dqs}^*$  and differential-mode  $v_{dm-dqsu}^*$ , where the subscript  $u$  represents the index of the differential-mode subspaces equal to the active

sets minus one ( $u = 1, \dots, n_{ON} - 1$ ). Remember that all values are referred to rotating stator flux reference frame  $dqs$ .

Based on the reference voltages in common- and differential-mode, the inverse adapting decoupling matrix is applied, obtaining the  $dq$  reference voltages of the healthy units in the active  $dqs$  frame  $v_{dq,s,k}$  ( $k = 1, \dots, n_{ON}$ ). Finally, after applying the inverse rotational transformation and the inverse Clarke transformations, the reference voltages of each active unit in phase-coordinates  $v_{abc,s,k}$  ( $k = 1, \dots, n_{ON}$ ) are computed, as shown in Fig. 4.63.

The DFVC implemented for the mapping algorithm validation needs a stator flux observer to estimate the stator flux vectors of all winding sets. In this way, the common- and differential- mode values of stator fluxes amplitudes can be computed, as well as the active stator frame  $dqs$  used to calculate the torque-producing currents of the machine as highlighted in Eq. (4.253).

$$T_{em} = \frac{3}{2} \cdot n_{ON} \cdot p \cdot \lambda_{cm-s} \cdot i_{cm-s} \quad (4.253)$$

Each three-phase set is observed combining two model-based estimators implemented in the stationary coordinates  $\alpha\beta$ . At low speed, the stator flux is estimated based on  $I\theta$  current model. The  $I\theta$  based estimator is immune

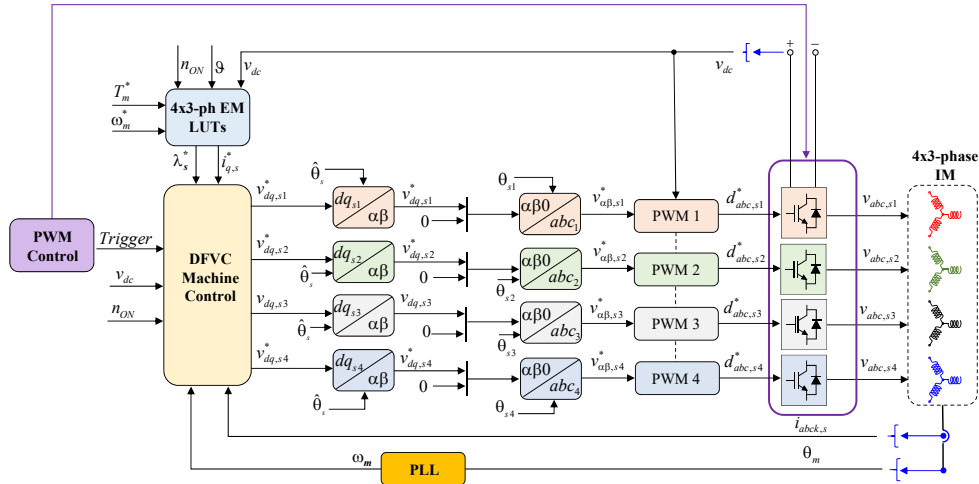


Figure 4.63 Drive configuration for the experimental validation of multi-three-phase IM mapping.

to the voltage errors introduced by the  $k$ -set inverter module since it implements the currents-to-flux relationships of the machine. This  $I\theta$  estimator gets a high observation accuracy in the low-speed range of the machine. For this reason, at the machine's medium/high-speed range, the stator flux estimator is based on  $VI$ -based estimator. The latter estimator relies on reconstructing the  $k$ -set phase-voltages from the  $k$ -set duty-cycles and inverter dc-link voltage. Indeed,  $VI$  observer is based on the time-integration of the machine's back-emf, thus requiring the accurate reconstruction of the IM's phase voltages from the estimated ones.

The crossover frequency (rad/s) between the  $I\theta$ -based estimator and the  $VI$ -based one is established through the observer's gain  $\omega_c$ , whose value in the validation stage has been set at 125 rad/s (near 20 Hz) for all three-phase units. Other details regarding the DFVC scheme are not reported since they are beyond the goal of this dissertation.

In summary, it is noted how the experimental mapping algorithm of multi-three-phase IMs is more challenging than the one performed for three-phase IM and synchronous motors. The proposed control approach for the mapping validation is an innovative control to perform the torque regulation of a multi-three-phase IM both in healthy and faulty operation. The control uses any of the control schemes commonly employed for three-phase drives. The application of the proposed control approach allowed to validation of the mapping algorithm having an arbitrary number of three-phase winding sets in any operating conditions and regardless of the stator winding configuration.

#### 4.11.2 Experimental results

The experimental efficiency maps have been evaluated considering the dc-link voltage value at 150 V for all possible machine conditions ( $n_{ON} = 4, 3, 2, 1$ ). The amplitude limit of the phase currents has been kept constant to the maximum value of the IM's overload current, i.e.,  $I_{max} = 24$  A, leading to the maximum extension of the efficiency maps for each value of the inverter's dc voltage. To properly reconstruct the IM's efficiency maps, these have been evaluated using speed and torque resolutions of 400 rpm and 2 Nm, respectively. The mapping algorithm validation has been performed



under a controlled ambient temperature equal to that in which the dc, no-load, and locked-rotor tests have been performed  $\vartheta_0 = 25$ . Moreover, an adequate pause time has been waited during the execution between one test point and the next. In detail, considering the overall active time in which one generic test point has been operated, e.g., 3 s, the pause time has been set equal to twenty times that time, i.e., 60 s referring to the example.

The experimental and computed efficiency maps obtained in the above-reported test conditions are shown in Fig. 4.64 - 4.67, where the white markers denote the operated test points. A slight distortion characterizes experimental efficiency maps since they are affected by the uncertainty of both electric and mechanical measurements. However, the experimental results are excellent, considering the complexity of both the test rig and the measurement system. The map reporting the error between the computed efficiency map and the experimental one is shown for each test condition, highlighting the accuracy of the proposed mapping procedure.

It is noted that the proposed mapping procedure estimates the multi-three-phase IM's efficiency in the whole torque-speed range with excellent accuracy in both healthy and faulty conditions. It is noted how the error is practically lower than 2 – 3 % in most of the torque-speed range, regardless of whether motoring or generator conditions are considered and regardless of the machine conditions (healthy or faulty). In detail, it is noted how the error becomes more significant for the test point near the MTPS at high speed and the test points in generation mode at low speed and high braking torque. The error near the MTPS profile is related to the observer implemented in DFVC machine control, which is troublesome due to the reconstruction of back-emf in the region characterized by the inverter nonlinearities and the resistive voltage drops. Instead, the efficiency is very low for the region at low speed with high torque braking, making the measurement difficult for the mechanical and electrical quantities. However, the trend is similar to the efficiency mapping results of three-phase IM.

Very interesting is the feasibility and robustness of the algorithm to evaluate every machine's conditions accurately. The reduced working area of the faulty machine is detected, changing the active sets number, and the error trend is confirmed yet. Note that the torque limits are invariant in

Fig. 4.64 - 4.66, highlighting the reduced torque capability, while in Fig. 4.67 the torque limits are adapted, and the error is more significant. However, the measured quantities in the worst faulty conditions (1 active set,  $n_{ON} = 1$ ) are meager and insignificant.

In summary, the comparison between computed and experimental efficiency maps confirms the accuracy of the proposed mapping procedure in estimating the multi-three-phase IM's efficiency in both healthy or open-winding faulty conditions. The algorithm is robust in wide torque-speed ranges and considers very different operating conditions like a significant variation of the active sets number.

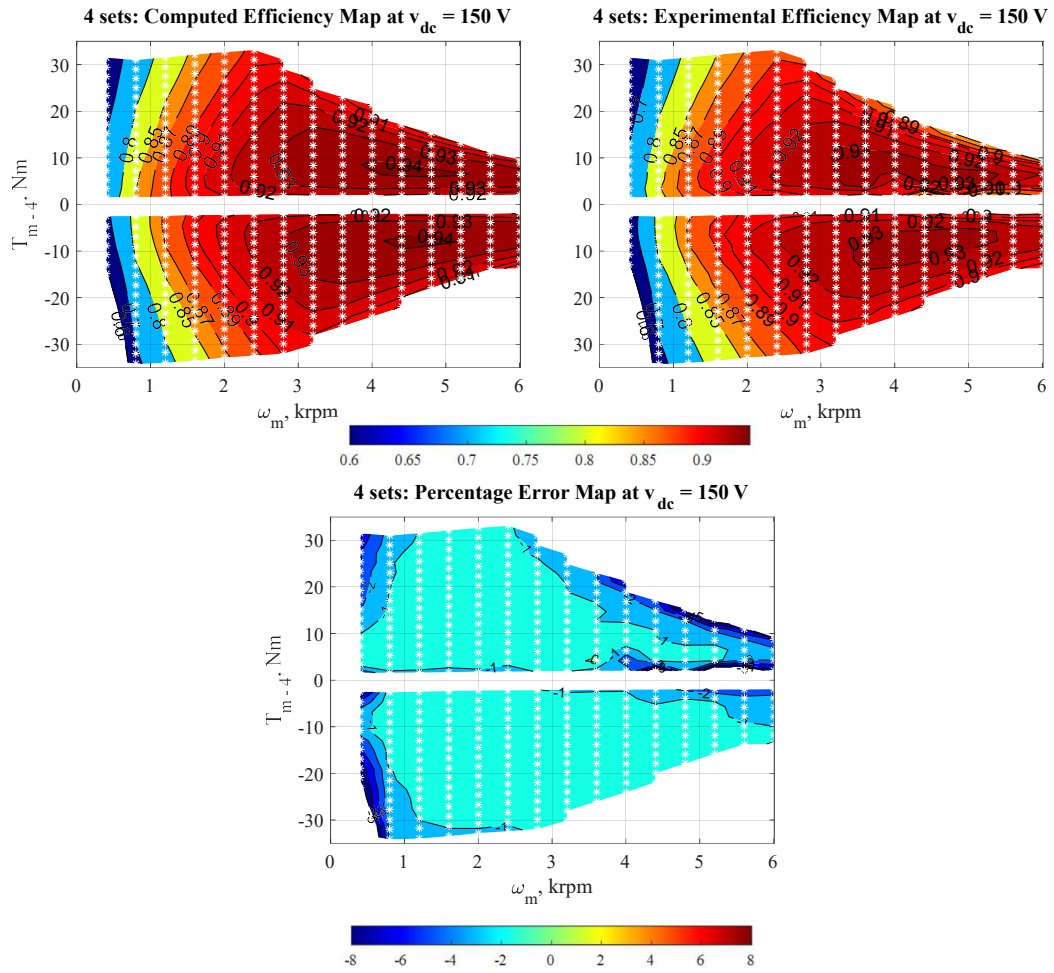


Figure 4.64 Computed and experimental efficiency maps at  $v_{dc} = 150$  V with the related percentual error map for healthy conditions ( $n_{ON} = 4$ ).

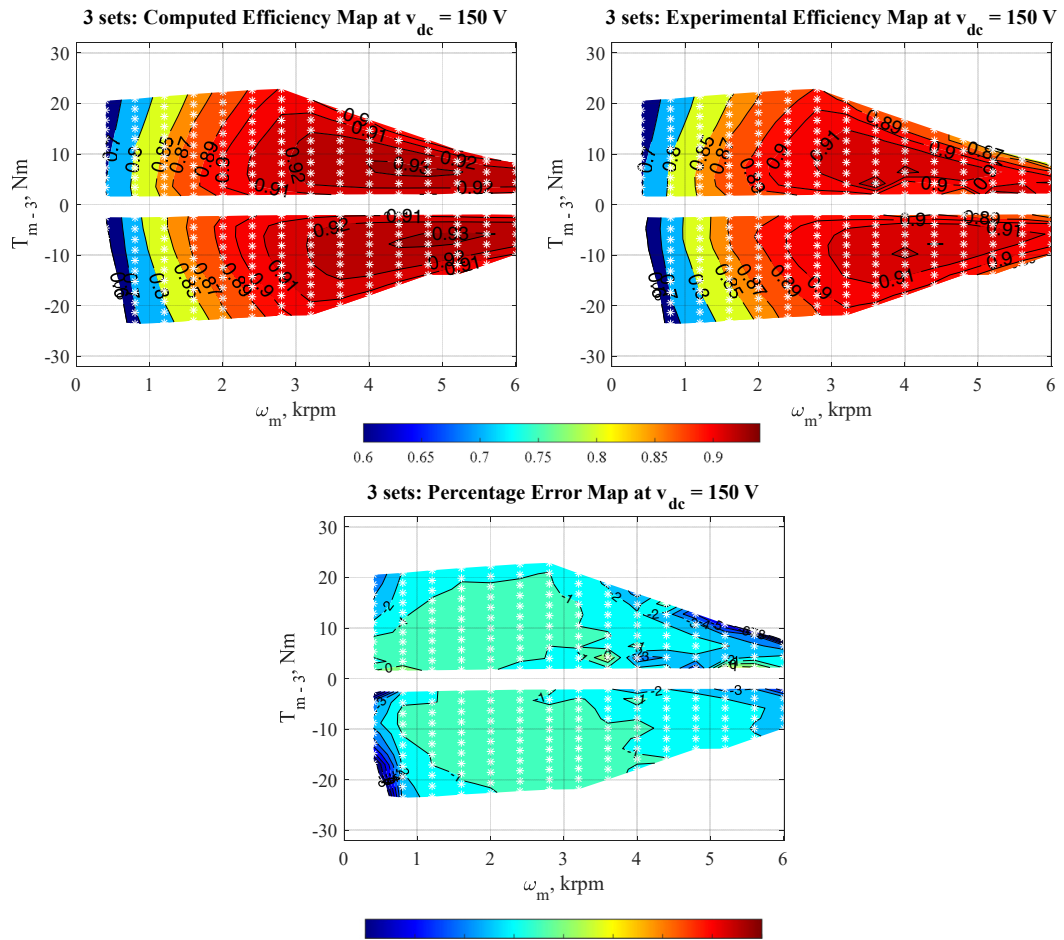


Figure 4.65 Computed and experimental efficiency maps at  $v_{dc} = 150$  V with the related percentual error map for faulty conditions ( $n_{ON} = 3$ ).

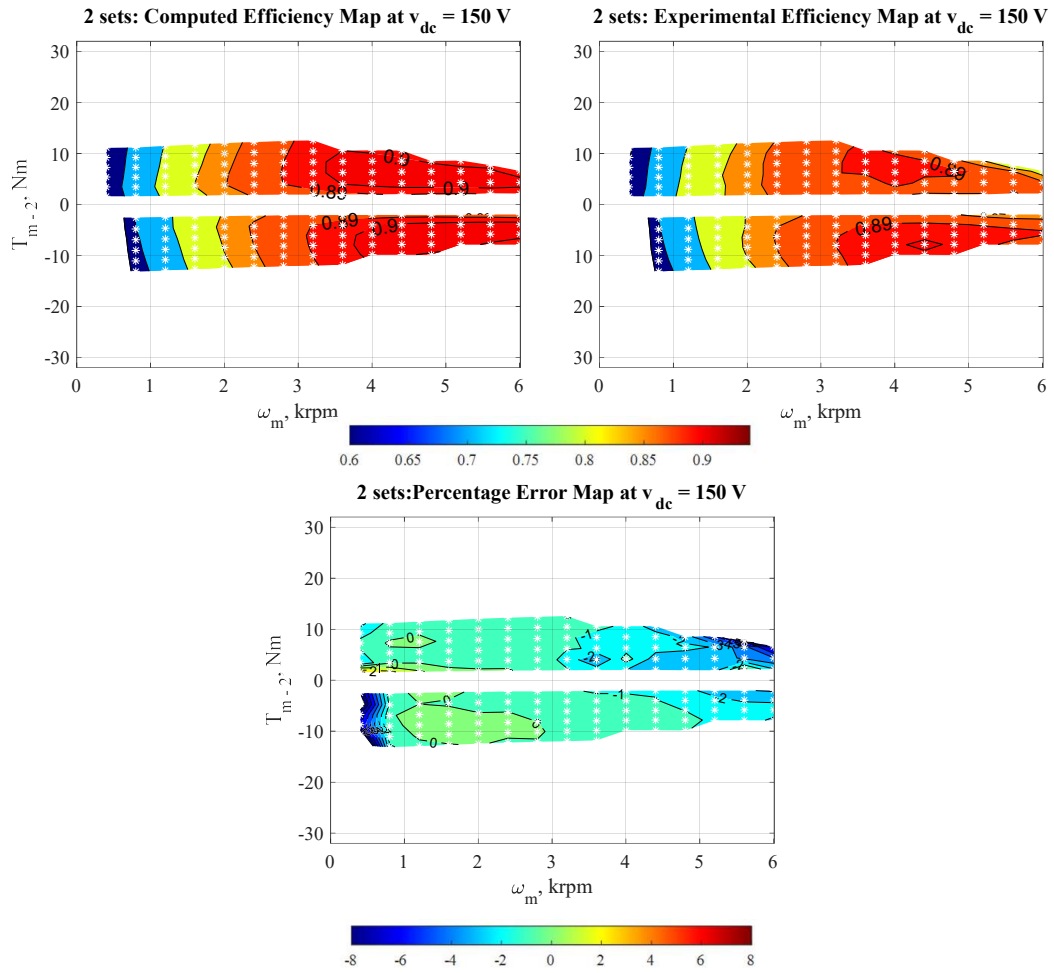


Figure 4.66 Computed and experimental efficiency maps at  $v_{dc} = 150$  V with the related percentual error map for faulty conditions ( $n_{ON} = 2$ ).

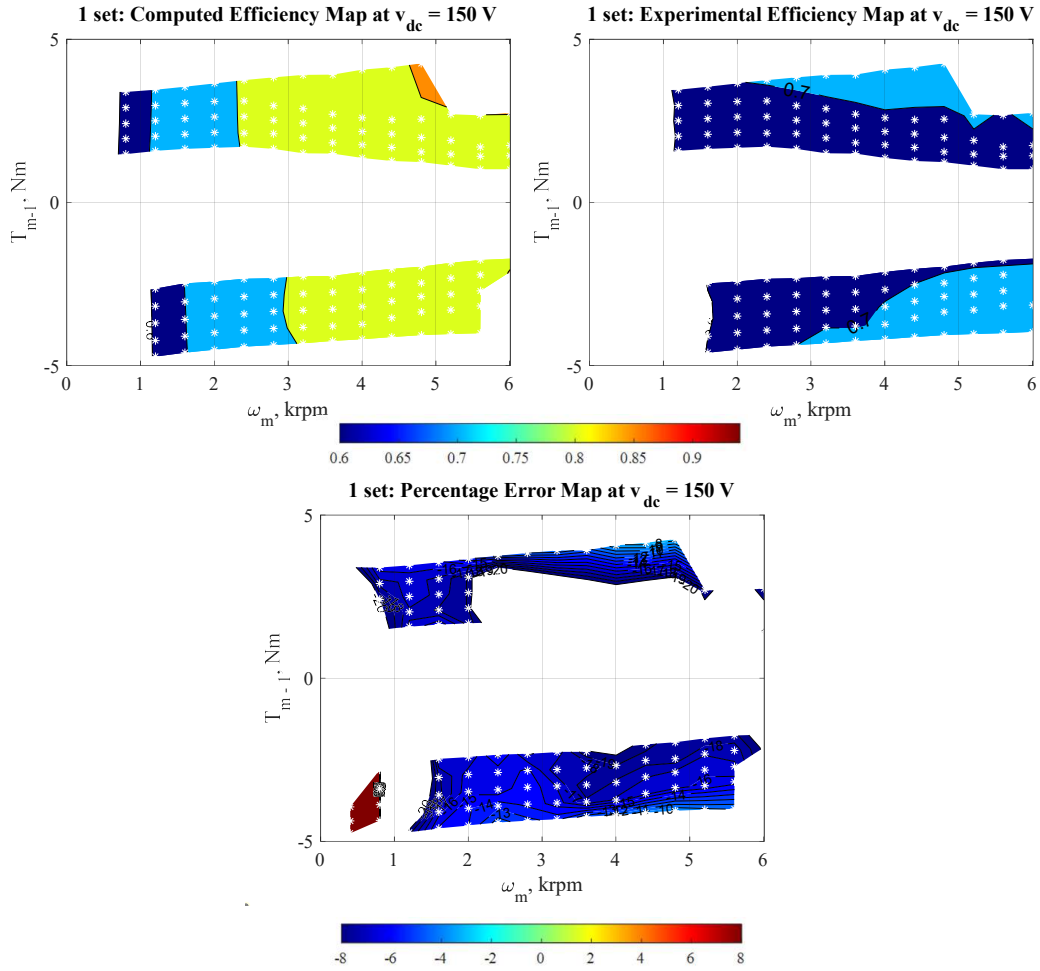


Figure 4.67 Computed and experimental efficiency maps at  $v_{dc} = 150$  V with the related percentual error map for faulty conditions ( $n_{ON} = 1$ ).

In Fig. 4.68, the shift of the maximum efficiency region is detected if changing the inverter's dc voltage, thus changing the extent of the region in which the flux-weakening is performed. Just the motoring operation has been experimentally validated for time reasons and laboratory facilities available, but these results are sufficient to confirm the algorithm's effectiveness.

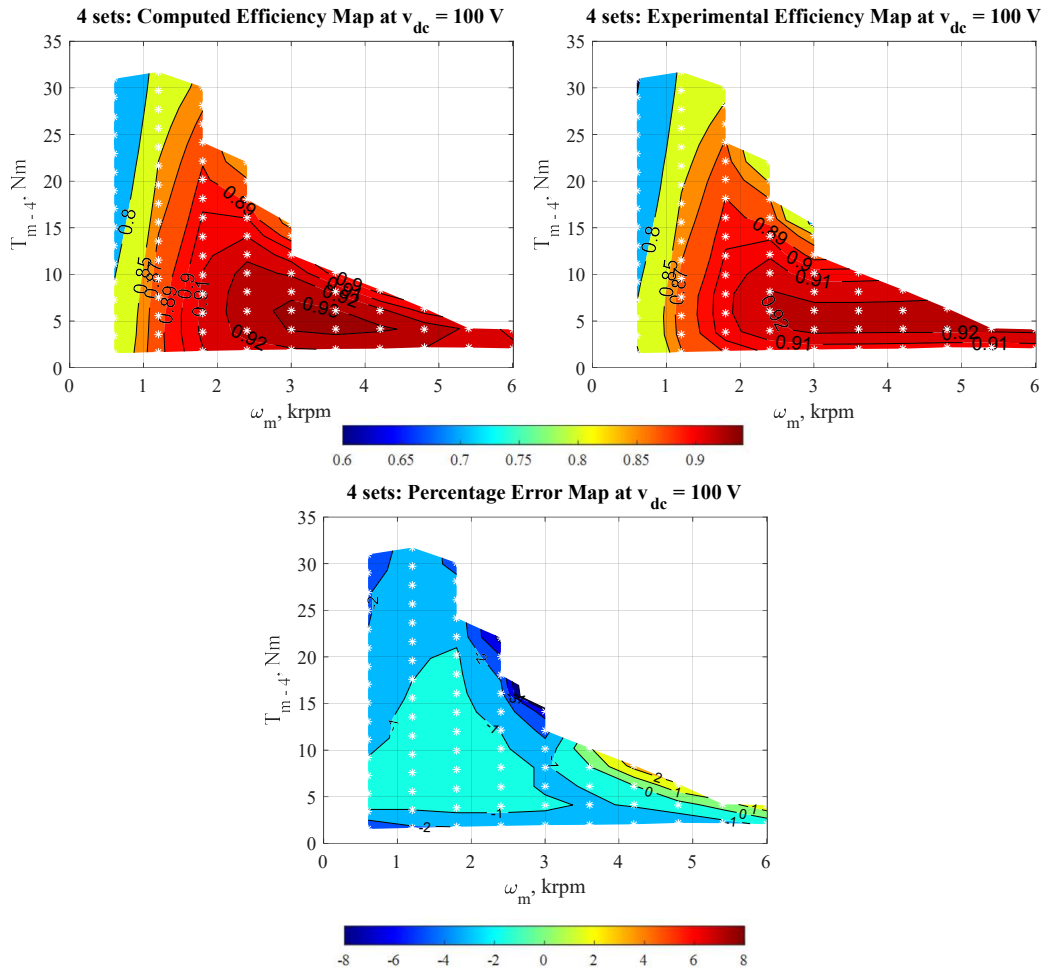


Figure 4.68 Computed and experimental efficiency maps at  $v_{dc} = 100 \text{ V}$  with the related percentual error map for normal conditions ( $n_{ON} = 4$ ).

In summary, the experimental validation confirms *i*) the possibility of performing the energy assessment of multi-three-phase IM in both machine conditions; *ii*) the machine virtualization will be performed using the maps of all electromechanical variables reconstructed by the algorithm given the algorithm reliability; *iii*) maximum efficiency strategy can be implemented as a machine control strategy. The multi-three-phase IM is usually controlled

using the optimal stator flux, following the MTPA strategy. However, the reference values to maximize the machine efficiency are known based on the algorithm's reconstructed variables. In the scenario of the electrification system, more efficient solutions are wanted, and accurate exploitation of the components plays a key factor, confirming a fundamental rule of what has been developed in this work.

## 4.12 Conclusion

The most relevant contributions to the development of multiphase machines have been published in the last three decades by covering many technical aspects [47, 49]. A literature survey providing the state-of-the-art in this field of research has been reported in Chapter 1. The multiphase solutions have been historically employed in both high-power and safety-critical applications. They represent a standard in marine applications for ship propulsion and onboard generation [47]. Today, multiphase machines represent an innovative and reliable solution [126] for fossil fuel emissions reduction [2]. This solution can be considered a competitive alternative to the conventional three-phase ones in the current scenario in which electrification covers a key role [114]. Nevertheless, among all the possible multiphase configurations, there is a strong interest in developing modular ones, known as multi-three-phase machines. Indeed the modularity of the drive topology leads to several advantages for the modular modeling approaches [121] to implement modular control techniques. The multiple solutions can use well-consolidated three-phase technologies, thus leading to a significant cost reduction [5].

About the modelling of a multiple three-phase IM Multi-Stator (MS), Vector Space Decomposition (VSD), Decoupling MS (DMS), and Adaptive DMS (A-DMS) approaches are reported for the mapping aim in healthy and faulty operating conditions. In detail, the most relevant contributions are analyzed:

- MS modeling of a multiple three-phase IM, considering an arbitrary number of three-phase winding. The machine stator is considered as multiple three-phase winding sets interacting with each other and with



an equivalent three-phase rotor. Each winding set's flux and torque contributions are highlighted. Therefore, the MS approach is suitable for modular approaches, and a simple model is required for the mapping in healthy conditions. All rotor and magnetizing parameters equal  $1/n$  of those computed using the VSD/DMS modeling. Magnetizing and rotor currents are much higher than the stator currents as they are computed from the sum of these last (see equivalent circuit). Iron losses are associated only to the active sets. There is only one subspace where the whole machine is considered. Indeed, the active sets' variables, i.e., voltage, current, and flux, coincide with the machine ones. The magnetic model (flux and torque maps) is computed using the MS equations, and the flux maps are representative of each active set. In faulty conditions, the current of the active sets must be opportunely adapted based on the active sets number  $n_{ON}$ , obtaining a machine model for mapping easily treated.

- VSD modeling of a multiple three-phase IM, considering an arbitrary number of three-phase winding sets, showing the VSD matrix for the benchmark machine. The VSD approach decomposes the multiphase machine model into multiple orthogonal subspaces. The main subspace performs the electromechanical energy conversion if a sinusoidal distribution of the stator windings is considered. Instead, the other subspaces have the meaning of time-harmonic and zero sequence patterns of the machine [12]. The main advantage of such an approach is evident since the torque control scheme should actively manage only the main subspace for healthy operation with balanced three-phase units. In faulty conditions, the harmonic subspaces are active and must be considered for loss calculation. The stator voltage of the main subspace doesn't define the stator voltage of the machine. Some precautions are necessary for the machine model for mapping to verify the voltage and current limits introduced by the power converter and IM. This approach involves a machine modeling not quickly treated, requiring additional precautions for mapping aim.
- DMS modeling of a multiple three-phase IM covers the limit of VSD modeling about the required symmetrical and asymmetrical config-

urations. The decoupling transformation is defined regardless of the stator winding configuration, and it is applied directly to the MS machine model. However, in balanced operation among the units under machine-healthy conditions, both the VSD- and DMS- based solutions, the currents appear in the secondary subspaces, i.e., the harmonic and the differential-mode subspaces for the VSD and DMS solutions, respectively. Consequently, the losses increase and the control system in these subspaces is required for torque production continuity. As for the VSD approach, the machine modeling for mapping in faulty conditions must be adapted, requiring the reconstruction of the machine stator voltage to verify the limit one.

Indeed, the common-mode/main subspace is active in healthy conditions, considering the DMS and VSD approaches. Differential/harmonic subspaces become active in faulty conditions. However, the parameters of common-mode/main subspace are always constant and do not depend on the number of active sets. Powers of common-mode/main subspace (stator Joule, iron, rotor Joule, etc.) correspond to the ones of the overall machine only in healthy conditions. In faulty conditions, the stator Joule losses are the sum of common-mode/main subspace plus differential/harmonic ones.

- A-DMS modeling covers the limit of DMS and VSD approaches. The DMS-based approach allows changing the decoupling transformation, i.e., adapting it to the post-fault configuration of the stator winding, defining A-DMS modeling. The faulty differential modes are removed in faulty conditions, and the common-mode subspace and the remaining differential-mode ones are adapted. In practical terms, the A-DMS machine model is obtained by considering only the healthy/active sets. The losses are related to the common and healthy differential-mode subspaces. Parameters of common-mode subspace depend on the number of active sets  $n_{ON}$ . Faulty differential-mode subspaces are not active, and the number of differential active subspace equals the number of active sets minus one ( $n_{ON}-1$ ). Powers of common-mode subspace (stator Joule, iron, rotor Joule, etc.) correspond to the overall machine's ones. This approach allows a simple and intelligent implementation of the mapping algorithm.

The developed mapping algorithm based on the MS and A-DMS approaches provides the same results. Indeed, based on the DMS/VSD approach, the mapping algorithm provides minimal differences in the efficiencies in faulty conditions. One possible reason could be the flux contribution in the differential/harmonic subspaces for the iron losses computation. However, the results are pretty consistent, and the results based on VSD/DMS approaches can be considered perfectly valid and in agreement with the ones based on MS and A-DMS approaches. For simplicity, the MS and A-DMS approaches are highly recommended for mapping analysis, independently by the adapted control strategy.

The algorithm's robustness has been experimentally validated through a 12-phase induction motor, rated 10 kW at 6000 rpm, using a quadruple-three-phase stator winding configuration.

# Bibliography

- [1] COP 21 Paris France Sustainable Innovation Forum 2015 working with UNEP.
- [2] European Environment Agency's home page — European Environment Agency.
- [3] Srdjan M. Lukic, Jian Cao, Ramesh C. Bansal, Fernando Rodriguez, and Ali Emadi. Energy Storage Systems for Automotive Applications. *IEEE Transactions on Industrial Electronics*, 55(6):2258–2267, June 2008. IEEE Transactions on Industrial Electronics.
- [4] J.A. Rosero, J.A. Ortega, E. Aldabas, and L. Romeral. Moving towards a more electric aircraft. *IEEE Aerospace and Electronic Systems Magazine*, 22(3):3–9, March 2007. IEEE Aerospace and Electronic Systems Magazine.
- [5] Wenping Cao, Barrie C. Mecrow, Glynn J. Atkinson, John W. Bennett, and David J. Atkinson. Overview of Electric Motor Technologies Used for More Electric Aircraft (MEA). *IEEE Transactions on Industrial Electronics*, 59(9):3523–3531, September 2012. IEEE Transactions on Industrial Electronics.
- [6] Ayman EL-Refaie. Toward a Sustainable More Electrified Future: The Role of Electrical Machines and Drives. *IEEE Electrification Magazine*, 7(1):49–59, March 2019. Conference Name: IEEE Electrification Magazine.
- [7] Phillip J. Ansell and Kiruba S. Haran. Electrified Airplanes: A Path to Zero-Emission Air Travel. *IEEE Electrification Magazine*, 8(2):18–26, June 2020. Conference Name: IEEE Electrification Magazine.
- [8] Noshin Omar, Mohamed Daowd, Omar Hegazy, Grietus Mulder, Jean-Marc Timmermans, Thierry Coosemans, Peter Van den Bossche, and Joeri Van Mierlo. Standardization Work for BEV and HEV Applications: Critical Appraisal of Recent Traction Battery Documents. *Energies*, 5(1):138–156, January 2012. Number: 1 Publisher: Molecular Diversity Preservation International.

- [9] A. Emadi, K. Rajashekara, S.S. Williamson, and S.M. Lukic. Topological overview of hybrid electric and fuel cell vehicular power system architectures and configurations. *IEEE Transactions on Vehicular Technology*, 54(3):763–770, May 2005. IEEE Transactions on Vehicular Technology.
- [10] Anton Rassõlkin, Viktor Rjabtšikov, Vladimir Kuts, Toomas Vaimann, Ants Kallaste, Bilal Asad, and Andriy Partyshev. Interface Development for Digital Twin of an Electric Motor Based on Empirical Performance Model. *IEEE Access*, 10:15635–15643, 2022. IEEE Access.
- [11] Mauro Bellone, Monica Lundh, Mattias Wahde, and Scott MacKinnon. Electrification and Automation in Maritime Applications: Employing AI Techniques for Energy Optimization and Efficiency. *IEEE Electrification Magazine*, 7(4):22–31, December 2019. IEEE Electrification Magazine.
- [12] Giuseppe Fabri, Antonio Ometto, Marco Villani, and Gino D’Ovidio. A Battery-Free Sustainable Powertrain Solution for Hydrogen Fuel Cell City Transit Bus Application. *Sustainability*, 14(9):5401, January 2022. Number: 9 Publisher: Multidisciplinary Digital Publishing Institute.
- [13] J.M. Apsley, E. Varrone, and N. Schofield. Hardware-in-the-loop evaluation of electric vehicle drives. In *5th IET International Conference on Power Electronics, Machines and Drives (PEMD 2010)*, pages 1–6, April 2010.
- [14] Kaibo Li, Shumei Cui, Alain Bouscayrol, and Michel Hecquet. Analytical Derivation of Efficiency Map of an Induction Machine for Electric Vehicle Applications. In *2018 IEEE Vehicle Power and Propulsion Conference (VPPC)*, pages 1–6, August 2018. ISSN: 1938-8756.
- [15] S. Williamson, M. Lukic, and A. Emadi. Comprehensive drive train efficiency analysis of hybrid electric and fuel cell vehicles based on motor-controller efficiency modeling. *IEEE Transactions on Power Electronics*, 21(3):730–740, May 2006. IEEE Transactions on Power Electronics.
- [16] Ezio Bassi, Francesco Vercesi, and Francesco Benzi. CAE Optimization of Synchronous Reluctance Motor and Vibro-Acoustic Analysis for Lift Systems. In *2021 International Conference on Electromechanical and Energy Systems (SIELMEN)*, pages 139–143, October 2021.
- [17] E.M. Freeman. CAE of electrical machines. *Electronics and Power*, 29(1):31–35, January 1983. Conference Name: Electronics and Power.
- [18] Qi Zhang, Naxin Cui, Ke Li, Yunlong Shang, and Chenghui Zhang. Co-simulation of energy management strategy for hybrid electric vehicle in AVL InMotion. In *2017 Chinese Automation Congress (CAC)*, pages 4932–4937, October 2017.

- [19] Dong-xu Zhang, Xiao-hua Zeng, Peng-yu Wang, and Qing-nian Wang. Co-simulation with AMESim and MATLAB for differential dynamic coupling of Hybrid Electric Vehicle. In *2009 IEEE Intelligent Vehicles Symposium*, pages 761–765, June 2009. ISSN: 1931-0587.
- [20] C. M. Apostoaia. AC machines and drives simulation platform. In *2013 International Electric Machines & Drives Conference*, pages 1295–1299, May 2013.
- [21] Amin Mahmoudi, Wen L. Soong, Gianmario Pellegrino, and Eric Armando. Loss Function Modeling of Efficiency Maps of Electrical Machines. *IEEE Transactions on Industry Applications*, 53(5):4221–4231, September 2017. IEEE Transactions on Industry Applications.
- [22] W. Q. Chu, Z. Q. Zhu, Jian Zhang, Xu Liu, D. A. Stone, and M. P. Foster. Investigation on Operational Envelops and Efficiency Maps of Electrically Excited Machines for Electrical Vehicle Applications. *IEEE Transactions on Magnetics*, 51(4):1–10, April 2015. Conference Name: IEEE Transactions on Magnetics.
- [23] Efficiency and loss mapping of AC motors using advanced testing tools | IEEE Conference Publication | IEEE Xplore.
- [24] Stjepan Stipetic and James Goss. Calculation of efficiency maps using scalable saturated flux-linkage and loss model of a synchronous motor. In *2016 XXII International Conference on Electrical Machines (ICEM)*, pages 1380–1386, September 2016.
- [25] C. López, T. Michalski, A. Espinosa, and L. Romeral. New SynRM design approach based on behaviour maps analysis. In *2016 XXII International Conference on Electrical Machines (ICEM)*, pages 1915–1921, September 2016.
- [26] Jingjuan Du, Xiaoyuan Wang, and Haiying Lv. Optimization of Magnet Shape Based on Efficiency Map of IPMSM for EVs. *IEEE Transactions on Applied Superconductivity*, 26(7):1–7, October 2016. Conference Name: IEEE Transactions on Applied Superconductivity.
- [27] E.B. Agamloh, A.K. Wallace, A. von Jouanne, K.J. Anderson, and J.A. Rooks. Assessment of nonintrusive motor efficiency estimators. *IEEE Transactions on Industry Applications*, 41(1):127–133, January 2005.
- [28] Solmaz Kahourzade, Amin Mahmoudi, Wen L. Soong, Simone Ferrari, and Gianmario Pellegrino. Correction of Finite-Element Calculated Efficiency Map using Experimental Measurements. In *2019 IEEE Energy Conversion Congress and Exposition (ECCE)*, pages 5629–5636, September 2019. ISSN: 2329-3748.

- [29] Matteo Carbonieri, Nicola Bianchi, and Luigi Alberti. Induction Motor Mapping Using Rotor Field-Oriented Analysis Technique. In *2019 IEEE Energy Conversion Congress and Exposition (ECCE)*, pages 2321–2328, September 2019. ISSN: 2329-3748.
- [30] Li Qi, Fan Tao, Wen Xuhui, Tai Xiang, Li Ye, and Zhang Guangzhen. Modeling of the efficiency MAP of surface permanent magnet machine for electrical vehicles. In *2013 International Conference on Electrical Machines and Systems (ICEMS)*, pages 1222–1225, October 2013.
- [31] H. Sano, K. Narita, N. Schneider, K. Semba, K. Tani, T. Yamada, and R. Akaki. Loss Analysis of a Permanent Magnet Traction Motor in a Finite Element Analysis based Efficiency Map. In *2020 International Conference on Electrical Machines (ICEM)*, volume 1, pages 2301–2306, August 2020. ISSN: 2381-4802.
- [32] Simone Ferrari, Paolo Ragazzo, Gaetano Dilevrano, and Gianmario Pellegrino. Flux-Map Based FEA Evaluation of Synchronous Machine Efficiency Maps. In *2021 IEEE Workshop on Electrical Machines Design, Control and Diagnosis (WEMDCD)*, pages 76–81, April 2021.
- [33] Liwei Song, Zijian Li, Zongze Cui, and Guoqing Yang. Efficiency map calculation for surface-mounted permanent-magnet in-wheel motor based on design parameters and control strategy. In *2014 IEEE Conference and Expo Transportation Electrification Asia-Pacific (ITEC Asia-Pacific)*, pages 1–6, August 2014.
- [34] Maher Al-Badri, Pragasen Pillay, and Pierre Angers. A Novel Algorithm for Estimating Refurbished Three-Phase Induction Motors Efficiency Using Only No-Load Tests. *IEEE Transactions on Energy Conversion*, 30(2):615–625, June 2015. IEEE Transactions on Energy Conversion.
- [35] Solmaz Kahourzade, Amin Mahmoudi, Wen L. Soong, and Gianmario Pellegrino. A Practical Method for Estimating Efficiency Maps for PM Machines Using a Reduced Number of Tests. In *2019 IEEE Vehicle Power and Propulsion Conference (VPPC)*, pages 1–6, October 2019. ISSN: 1938-8756.
- [36] R. Bojoi, E. Armando, M. Pastorelli, and K. Lang. Efficiency and loss mapping of AC motors using advanced testing tools. In *2016 XXII International Conference on Electrical Machines (ICEM)*, pages 1043–1049, September 2016.
- [37] Amin Mahmoudi, Wen L. Soong, Gianmario Pellegrino, and Eric Armando. Efficiency maps of electrical machines. In *2015 IEEE Energy Conversion Congress and Exposition (ECCE)*, pages 2791–2799, September 2015. ISSN: 2329-3748.

- [38] Emad Dlala, Mark Solveson, Scott Stanton, Zed Tang, Mark Christini, Raymond Ong, and Brian Peaslee. Efficiency map simulations for an interior PM motor with experimental comparison and investigation of magnet size reduction. In *2013 International Electric Machines & Drives Conference*, pages 23–29, May 2013.
- [39] Aldo Boglietti, Andrea Cavagnino, and Mario Lazzari. Fast Method for the Iron Loss Prediction in Inverter-Fed Induction Motors. *IEEE Transactions on Industry Applications*, 46(2):806–811, March 2010. IEEE Transactions on Industry Applications.
- [40] Luigi Alberti, Nicola Bianchi, and Silverio Bolognani. Variable-Speed Induction Machine Performance Computed Using Finite-Element. *IEEE Transactions on Industry Applications*, 47(2):789–797, March 2011. Conference Name: IEEE Transactions on Industry Applications.
- [41] Ornella Stiscia, Sandro Rubino, Silvio Vaschetto, Andrea Cavagnino, and Alberto Tenconi. Accurate Induction Machines Efficiency Mapping Computed by Standard Test Parameters. *IEEE Transactions on Industry Applications*, 58(3):3522–3532, May 2022. IEEE Transactions on Industry Applications.
- [42] Chetan S. Gajjar, Jamlick M. Kinyua, Mohamed A. Khan, and Paul S. Barendse. Analysis of a Nonintrusive Efficiency Estimation Technique for Induction Machines Compared to the IEEE 112B and IEC 34-2-1 Standards. *IEEE Transactions on Industry Applications*, 51(6):4541–4553, November 2015. IEEE Transactions on Industry Applications.
- [43] Maher Al-Badri, Pragasen Pillay, and Pierre Angers. Induction machine rapid performance tests. In *2017 IEEE Energy Conversion Congress and Exposition (ECCE)*, pages 782–785, October 2017.
- [44] Radu Bojoi, Andrea Cavagnino, Marco Cossale, and Alberto Tenconi. Multiphase Starter Generator for a 48-V Mini-Hybrid Powertrain: Design and Testing. *IEEE Transactions on Industry Applications*, 52(2):1750–1758, March 2016. Conference Name: IEEE Transactions on Industry Applications.
- [45] Ahmed Salem and Mehdi Narimani. A Review on Multiphase Drives for Automotive Traction Applications. *IEEE Transactions on Transportation Electrification*, 5(4):1329–1348, December 2019. IEEE Transactions on Transportation Electrification.
- [46] Mario J. Duran and Federico Barrero. Recent Advances in the Design, Modeling, and Control of Multiphase Machines—Part II. *IEEE Transactions on Industrial Electronics*, 63(1):459–468, January 2016. Conference Name: IEEE Transactions on Industrial Electronics.



- [47] Emil Levi. Multiphase Electric Machines for Variable-Speed Applications. *IEEE Transactions on Industrial Electronics*, 55(5):1893–1909, May 2008. Conference Name: IEEE Transactions on Industrial Electronics.
- [48] R. Bojoi, F. Farina, A. Tenconi, F. Profumi, and E. Levi. Dual three-phase induction motor drive with digital current control in the stationary reference frame. *Power Engineer*, 20(3):40–43, June 2006. Conference Name: Power Engineer.
- [49] Federico Barrero and Mario J. Duran. Recent Advances in the Design, Modeling, and Control of Multiphase Machines—Part I. *IEEE Transactions on Industrial Electronics*, 63(1):449–458, January 2016. IEEE Transactions on Industrial Electronics.
- [50] L. Parsa and H.A. Toliyat. Five-phase permanent magnet motor drives for ship propulsion applications. In *IEEE Electric Ship Technologies Symposium, 2005.*, pages 371–378, July 2005.
- [51] Timothy J. McCoy. Electric Ships Past, Present, and Future [Technology Leaders]. *IEEE Electrification Magazine*, 3(2):4–11, June 2015. Conference Name: IEEE Electrification Magazine.
- [52] Giorgio Sulligoi, Alberto Tassarolo, Varo Benucci, Andrea Millerani Trapani, Massimo Baret, and Fabio Luise. Shipboard Power Generation: Design and Development of a Medium-Voltage dc Generation System. *IEEE Industry Applications Magazine*, 19(4):47–55, July 2013. IEEE Industry Applications Magazine.
- [53] Siemens eMobility charging | Solutions | Siemens Global.
- [54] R. Bojoi, M. Lazzari, F. Profumo, and A. Tenconi. Digital field-oriented control for dual three-phase induction motor drives. *IEEE Transactions on Industry Applications*, 39(3):752–760, May 2003. IEEE Transactions on Industry Applications.
- [55] Y. Zhao and T.A. Lipo. Space vector PWM control of dual three phase induction machine using vector space decomposition. In *Proceedings of 1994 IEEE Industry Applications Society Annual Meeting*, volume 1, pages 742–749 vol.1, October 1994.
- [56] Marko Slunjski, Ornella Stiscia, Martin Jones, and Emil Levi. General Torque Enhancement Approach for a Nine-Phase Surface PMSM With Built-In Fault Tolerance. *IEEE Transactions on Industrial Electronics*, 68(8):6412–6423, August 2021. IEEE Transactions on Industrial Electronics.
- [57] Giacomo Sala, Michele Mengoni, Gabriele Rizzoli, Luca Zarri, and Angelo Tani. Decoupled d–q Axes Current-Sharing Control of Multi-Three-Phase Induction Machines. *IEEE Transactions on Industrial*

- Electronics*, 67(9):7124–7134, September 2020. IEEE Transactions on Industrial Electronics.
- [58] Emil Levi. Advances in Converter Control and Innovative Exploitation of Additional Degrees of Freedom for Multiphase Machines. *IEEE Transactions on Industrial Electronics*, 63(1):433–448, January 2016. IEEE Transactions on Industrial Electronics.
- [59] Ivan Zoric, Martin Jones, and Emil Levi. Vector space decomposition algorithm for asymmetrical multiphase machines. In *2017 International Symposium on Power Electronics (Ee)*, pages 1–6, October 2017.
- [60] R. H. Nelson and P. C. Krause. Induction Machine Analysis for Arbitrary Displacement Between Multiple Winding Sets. *IEEE Transactions on Power Apparatus and Systems*, PAS-93(3):841–848, May 1974. IEEE Transactions on Power Apparatus and Systems.
- [61] Sandro Rubino, Radu Bojoi, Fabio Mandrile, and Eric Armando. Modular Stator Flux and Torque Control of Multiphase Induction Motor Drives. In *2019 IEEE International Electric Machines & Drives Conference (IEMDC)*, pages 531–538, May 2019.
- [62] M. Zabaleta, E. Levi, and M. Jones. Modelling approaches for triple three-phase permanent magnet machines. In *2016 XXII International Conference on Electrical Machines (ICEM)*, pages 466–472, September 2016.
- [63] Sandro Rubino, Radu Bojoi, Davide Cittanti, and Luca Zarri. Decoupled and Modular Torque Control of Multi-Three-Phase Induction Motor Drives. *IEEE Transactions on Industry Applications*, 56(4):3831–3845, July 2020. IEEE Transactions on Industry Applications.
- [64] S. Williamson and S. Smith. Pulsating torque and losses in multiphase induction machines. In *Conference Record of the 2001 IEEE Industry Applications Conference. 36th IAS Annual Meeting (Cat. No.01CH37248)*, volume 2, pages 1155–1162 vol.2, September 2001. ISSN: 0197-2618.
- [65] J. M. Apsley, S. Williamson, A. C. Smith, and M. Barnes. Induction motor performance as a function of phase number. *IEE Proceedings: Electric Power Applications*, 153(6):898–904, 2006. Publisher: Institution of Engineering and Technology.
- [66] Aldo Boglietti, Radu Bojoi, Andrea Cavagnino, and Alberto Tenconi. Efficiency Analysis of PWM Inverter Fed Three-Phase and Dual Three-Phase High Frequency Induction Machines for Low/Medium Power Applications. *IEEE Transactions on Industrial Electronics*, 55(5):2015–2023, May 2008. IEEE Transactions on Industrial Electronics.

- [67] Nandor Bodo, Emil Levi, Ivan Subotic, Jordi Espina, Lee Empringham, and C. Mark Johnson. Efficiency Evaluation of Fully Integrated On-Board EV Battery Chargers With Nine-Phase Machines. *IEEE Transactions on Energy Conversion*, 32(1):257–266, March 2017. IEEE Transactions on Energy Conversion.
- [68] Ayman S. Abdel-Khalik, Shehab Ahmed, and Ahmed M. Massoud. A Nine-Phase Six-Terminal Concentrated Single-Layer Winding Layout for High-Power Medium-Voltage Induction Machines. *IEEE Transactions on Industrial Electronics*, 64(3):1796–1806, March 2017. Conference Name: IEEE Transactions on Industrial Electronics.
- [69] Masahiro Ikeda and Takashi Hiyama. Simulation Studies of the Transients of Squirrel-Cage Induction Motors. *IEEE Transactions on Energy Conversion*, 22(2):233–239, June 2007. Conference Name: IEEE Transactions on Energy Conversion.
- [70] M. Sokola and E. Levi. A Novel Induction Machine Model and its Application in the Development of an Advanced Vector Control Scheme. *The International Journal of Electrical Engineering & Education*, 37(3):233–248, July 2000. Publisher: SAGE Publications Ltd STM.
- [71] G.R. Slemon. Modelling of induction machines for electric drives. *IEEE Transactions on Industry Applications*, 25(6):1126–1131, November 1989. IEEE Transactions on Industry Applications.
- [72] M. Yu. Pustovetov. A mathematical model of the three-phase induction motor in three-phase stator reference frame describing electromagnetic and electromechanical processes. In *2016 Dynamics of Systems, Mechanisms and Machines (Dynamics)*, pages 1–5, November 2016.
- [73] Andres Diaz, Roger Saltares, Christian Rodriguez, Roberto F. Nunez, Eduardo I. Ortiz-Rivera, and Jesus Gonzalez-Llorente. Induction motor equivalent circuit for dynamic simulation. In *2009 IEEE International Electric Machines and Drives Conference*, pages 858–863, May 2009.
- [74] Ludmil STOYANOV, Vladimir LAZAROV, Zahari ZARKOV, and Encho POPOV. Influence of Skin Effect on Stator Windings Resistance of AC Machines for Electric Drives. In *2019 16th Conference on Electrical Machines, Drives and Power Systems (ELMA)*, pages 1–6, June 2019.
- [75] Nicola Bianchi and Grazia Berardi. Analytical Approach to Design Hairpin Windings in High Performance Electric Vehicle Motors. In *2018 IEEE Energy Conversion Congress and Exposition (ECCE)*, pages 4398–4405, September 2018. ISSN: 2329-3748.
- [76] Ignacio Lope, Claudio Carretero, Jesús Acero, Rafael Alonso, and José M. Burdío. AC Power Losses Model for Planar Windings With

- Rectangular Cross-Sectional Conductors. *IEEE Transactions on Power Electronics*, 29(1):23–28, January 2014. IEEE Transactions on Power Electronics.
- [77] D.M. Ionel, M.V. Cistelecan, T.J.E. Miller, and M.I. McGilp. A new analytical method for the computation of air-gap reactances in 3-phase induction motors. In *Conference Record of 1998 IEEE Industry Applications Conference. Thirty-Third IAS Annual Meeting (Cat. No.98CH36242)*, volume 1, pages 65–72 vol.1, October 1998. ISSN: 0197-2618.
  - [78] Ruilin Pei, Xiangjian Zhang, Lubin Zeng, and Shuhui Li. Studies of high-frequency iron core loss for synchronous electric machines used in electric vehicles. In *2017 20th International Conference on Electrical Machines and Systems (ICEMS)*, pages 1–4, August 2017.
  - [79] Aldo Boglietti, Andrea Cavagnino, and Mario Lazzari. Computational Algorithms for Induction Motor Equivalent Circuit Parameter Determination—Part II: Skin Effect and Magnetizing Characteristics. *IEEE Transactions on Industrial Electronics*, 58(9):3734–3740, September 2011. Conference Name: IEEE Transactions on Industrial Electronics.
  - [80] Aldo Boglietti, Andrea Cavagnino, Luca Ferraris, and Mario Lazzari. Skin effect experimental validations of induction motor squirrel cage parameters. In *2008 18th International Conference on Electrical Machines*, pages 1–4, September 2008.
  - [81] IEC 60034-2-1:2014 | IEC Webstore | energy efficiency, smart city.
  - [82] IEEE Standard Test Procedure for Polyphase Induction Motors and Generators. *IEEE Std 112-2017 (Revision of IEEE Std 112-2004)*, pages 1–115, February 2018. IEEE Std 112-2017 (Revision of IEEE Std 112-2004).
  - [83] Jiwon Yoo, Joon-Hee Lee, and Seung-Ki Sul. FEA-Assisted Experimental Parameter Identification of Induction Motor. In *2022 International Power Electronics Conference (IPEC-Himeji 2022- ECCE Asia)*, pages 789–794, May 2022.
  - [84] G. Bertotti, A. Boglietti, M. Chiampi, D. Chiarabaglio, F. Fiorillo, and M. Lazzari. An improved estimation of iron losses in rotating electrical machines. *IEEE Transactions on Magnetics*, 27(6):5007–5009, November 1991. IEEE Transactions on Magnetics.
  - [85] G. Bertotti. General properties of power losses in soft ferromagnetic materials. *IEEE Transactions on Magnetics*, 24(1):621–630, January 1988. Conference Name: IEEE Transactions on Magnetics.
  - [86] S.-H. Kim, S.-K. Sul, and M.-H. Park. Maximum torque control of an induction machine in the field weakening region. In *Conference Record*

- of the 1993 IEEE Industry Applications Conference Twenty-Eighth IAS Annual Meeting*, pages 401–407 vol.1, October 1993.
- [87] R. Bojoi, Z. Li, S. A. Odhano, G. Griva, and A. Tenconi. Unified direct-flux vector control of induction motor drives with maximum torque per ampere operation. In *2013 IEEE Energy Conversion Congress and Exposition*, pages 3888–3895, September 2013. ISSN: 2329-3748.
- [88] Jul-Ki Seok and Seung-Ki Sul. Optimal flux selection of an induction machine for maximum torque operation in flux-weakening region. *IEEE Transactions on Power Electronics*, 14(4):700–708, July 1999. Conference Name: IEEE Transactions on Power Electronics.
- [89] A.M. Hava, R.J. Kerkman, and T.A. Lipo. Simple analytical and graphical methods for carrier-based PWM-VSI drives. *IEEE Transactions on Power Electronics*, 14(1):49–61, January 1999. IEEE Transactions on Power Electronics.
- [90] Emmanuel B. Agamloh, Andrea Cavagnino, and Silvio Vaschetto. Standard Efficiency Determination of Induction Motors With a PWM Inverter Source. *IEEE Transactions on Industry Applications*, 55(1):398–406, January 2019. Conference Name: IEEE Transactions on Industry Applications.
- [91] W. Deprez, J. Lemmens, D. Vanhooydonck, Wim Symens, K. Stockman, S. Dereyne, and J. Driesen. Iso efficiency contours as a concept to characterize variable speed drive efficiency. pages 1–6, October 2010.
- [92] Dirk Vanhooydonck, Wim Symens, Wim Deprez, Joris Lemmens, K. Stockman, and Steve Dereyne. Calculating energy consumption of motor systems with varying load using iso efficiency contours. pages 1–6, October 2010.
- [93] Gabriele Rizzoli, Giovanni Serra, Paolo Maggiore, and Alberto Tenconi. Optimized design of a multiphase induction machine for an open rotor aero-engine shaft-line-embedded starter/generator. In *IECON 2013 - 39th Annual Conference of the IEEE Industrial Electronics Society*, pages 5203–5208, November 2013. ISSN: 1553-572X.
- [94] Induction Motor Drives. In Paul Krause, Oleg Wasynczuk, Scott Sudhoff, and Steven Pekarek, editors, *Analysis of Electric Machinery and Drive Systems*, pages 503–540. John Wiley & Sons, Inc., Hoboken, NJ, USA, July 2013.
- [95] X. Xu and D.W. Novotny. Selection of the flux reference for induction machine drives in the field weakening region. *IEEE Transactions on Industry Applications*, 28(6):1353–1358, November 1992. IEEE Transactions on Industry Applications.

- [96] P.L. Jansen and R.D. Lorenz. A physically insightful approach to the design and accuracy assessment of flux observers for field oriented induction machine drives. *IEEE Transactions on Industry Applications*, 30(1):101–110, January 1994. IEEE Transactions on Industry Applications.
- [97] I.R. Bojoi, E. Armando, G. Pellegrino, and S.G. Rosu. Self-commissioning of inverter nonlinear effects in AC drives. In *2012 IEEE International Energy Conference and Exhibition (ENERGYCON)*, pages 213–218, September 2012.
- [98] Stjepan Stipetic, James Goss, Damir Zarko, and Mircea Popescu. Calculation of Efficiency Maps Using a Scalable Saturated Model of Synchronous Permanent Magnet Machines. *IEEE Transactions on Industry Applications*, 54(5):4257–4267, September 2018. IEEE Transactions on Industry Applications.
- [99] Jorge O. Estima and Antonio J. Marques Cardoso. Efficiency Analysis of Drive Train Topologies Applied to Electric/Hybrid Vehicles. *IEEE Transactions on Vehicular Technology*, 61(3):1021–1031, March 2012. IEEE Transactions on Vehicular Technology.
- [100] Kundan Kumar and Subhendu Bikash Santra. Performance Analysis of a Three-Phase Propulsion Inverter for Electric Vehicles Using GaN Semiconductor Devices. *IEEE Transactions on Industry Applications*, 54(6):6247–6257, November 2018. IEEE Transactions on Industry Applications.
- [101] Yinye Yang, Sandra M. Castano, Rong Yang, Michael Kasprzak, Berker Bilgin, Anand Sathyan, Hossein Dadkhah, and Ali Emadi. Design and Comparison of Interior Permanent Magnet Motor Topologies for Traction Applications. *IEEE Transactions on Transportation Electrification*, 3(1):86–97, March 2017. Transactions on Transportation Electrification.
- [102] Chengyuan He and Thomas Wu. Analysis and design of surface permanent magnet synchronous motor and generator. *CES Transactions on Electrical Machines and Systems*, 3(1):94–100, March 2019. Conference Name: CES Transactions on Electrical Machines and Systems.
- [103] Gianmario Pellegrino, Alfredo Vagati, Paolo Guglielmi, and Barbara Boazzo. Performance Comparison Between Surface-Mounted and Interior PM Motor Drives for Electric Vehicle Application. *IEEE Transactions on Industrial Electronics*, 59(2):803–811, February 2012. IEEE Transactions on Industrial Electronics.
- [104] K.M. Rahman and S. Hiti. Identification of machine parameters of a synchronous motor. In *38th IAS Annual Meeting on Conference Record of the Industry Applications Conference, 2003.*, volume 1, pages 409–415 vol.1, October 2003.

- [105] K. Berringer, J. Marvin, and P. Perruchoud. Semiconductor power losses in AC inverters. In *IAS '95. Conference Record of the 1995 IEEE Industry Applications Conference Thirtieth IAS Annual Meeting*, volume 1, pages 882–888 vol.1, October 1995. ISSN: 0197-2618.
- [106] Massimo Barcaro, Mattia Morandin, Tomas Pradella, Nicola Bianchi, and Ivano Furlan. Iron Saturation Impact on High-Frequency Sensorless Control of Synchronous Permanent-Magnet Motor. *IEEE Transactions on Industry Applications*, 53(6):5470–5478, November 2017. IEEE Transactions on Industry Applications.
- [107] K. J. Meessen, P. Thelin, J. Soulard, and E. A. Lomonova. Inductance Calculations of Permanent-Magnet Synchronous Machines Including Flux Change and Self- and Cross-Saturations. *IEEE Transactions on Magnetics*, 44(10):2324–2331, October 2008. IEEE Transactions on Magnetics.
- [108] Gianmario Pellegrino, Barbara Boazzo, and Thomas M. Jahns. Plug-in Direct-Flux Vector Control of PM Synchronous Machine Drives. *IEEE Transactions on Industry Applications*, 51(5):3848–3857, September 2015. IEEE Transactions on Industry Applications.
- [109] Eric Armando, Radu Iustin Bojoi, Paolo Guglielmi, Gianmario Pellegrino, and Michele Pastorelli. Experimental Identification of the Magnetic Model of Synchronous Machines. *IEEE Transactions on Industry Applications*, 49(5):2116–2125, September 2013. IEEE Transactions on Industry Applications.
- [110] W. Zine, L. Idkhajine, E. Monmasson, P.A. Chauvenet, A. Bruyere, and B. Condamin. Investigation of saturation impact on an IPMSM saliency-based sensorless control for automotive applications. In *2016 International Symposium on Power Electronics, Electrical Drives, Automation and Motion (SPEEDAM)*, pages 1238–1243, June 2016.
- [111] Eric Armando, Paolo Guglielmi, Gianmario Pellegrino, and Radu Bojoi. Flux linkage maps identification of synchronous AC motors under controlled thermal conditions. In *2017 IEEE International Electric Machines and Drives Conference (IEMDC)*, pages 1–8, May 2017.
- [112] Gennadi Y. Sizov, Dan M. Ionel, and Nabeel A. O. Demerdash. Modeling and Parametric Design of Permanent-Magnet AC Machines Using Computationally Efficient Finite-Element Analysis. *IEEE Transactions on Industrial Electronics*, 59(6):2403–2413, June 2012. IEEE Transactions on Industrial Electronics.
- [113] W.N. Fu and Z.J. Liu. Estimation of eddy-current loss in permanent magnets of electric motors using network-field coupled multislice time-stepping finite-element method. *IEEE Transactions on Magnetics*, 38(2):1225–1228, March 2002. IEEE Transactions on Magnetics.

- [114] Sandro Rubino, Radu Bojoi, Andrea Cavagnino, and Silvio Vaschetto. Asymmetrical twelve-phase induction starter/generator for more electric engine in aircraft. In *2016 IEEE Energy Conversion Congress and Exposition (ECCE)*, pages 1–8, September 2016.
- [115] Ivan Zorić. MULTIPLE THREE-PHASE INDUCTION GENERATORS FOR WIND ENERGY CONVERSION SYSTEMS. page 171. PhD Thesis.
- [116] Sandro Rubino, Obrad Dordevic, Eric Armando, Iustin Radu Bojoi, and Emil Levi. A Novel Matrix Transformation for Decoupled Control of Modular Multiphase PMSM Drives. *IEEE Transactions on Power Electronics*, 36(7):8088–8101, July 2021. IEEE Transactions on Power Electronics.
- [117] Sandro Rubino, Eric Armando, Radu Bojoi, and Luca Zarri. Fault-Tolerant Torque Control Based on Common and Differential Mode Modeling for Multi-Three-Phase Induction Machines. In *2021 IEEE International Electric Machines & Drives Conference (IEMDC)*, pages 1–8, May 2021.
- [118] R. D. Begamudre. *Electromechanical Energy Conversion With Dynamics Of Machines*. New Age International, 2007. Google-Books-ID: osa7ldPgUpEC.
- [119] Analysis of Electric Machinery and Drive Systems, 3rd Edition | Wiley.
- [120] Yashan Hu, Z. Q. Zhu, and Milijana Odavic. Comparison of Two-Individual Current Control and Vector Space Decomposition Control for Dual Three-Phase PMSM. *IEEE Transactions on Industry Applications*, 53(5):4483–4492, September 2017. IEEE Transactions on Industry Applications.
- [121] Jussi Karttunen, Samuli Kallio, Pasi Peltoniemi, Pertti Silventoinen, and Olli Pyrhönen. Decoupled Vector Control Scheme for Dual Three-Phase Permanent Magnet Synchronous Machines. *IEEE Transactions on Industrial Electronics*, 61(5):2185–2196, May 2014. IEEE Transactions on Industrial Electronics.
- [122] Ornella Stiscia, Marco Biasion, Sandro Rubino, Silvio Vaschetto, Alberto Tenconi, and Andrea Cavagnino. Iron Losses and Parameters Investigation of Multi-Three-Phase Induction Motors in Normal and Open-Phase Fault Conditions. In *2022 International Conference on Electrical Machines (ICEM)*, pages 793–799, September 2022. ISSN: 2381-4802.
- [123] Sandro Rubino, Radu Bojoi, Michele Mengoni, and Luca Zarri. Optimal flux selection for multi three-phase machines in normal and fault conditions. In *2017 IEEE International Electric Machines and Drives Conference (IEMDC)*, pages 1–8, May 2017.



- [124] Felix Mariut, Stefan-George Rosu, and Radu Bojoi Alberto Tenconi. Multiphase modular power converter using the PEBB concept and FPGA-based direct high speed voltage measurement. In *2015 17th European Conference on Power Electronics and Applications (EPE'15 ECCE-Europe)*, pages 1–10, September 2015.
- [125] Sandro Rubino, Fabio Mandrile, Eric Armando, Radu Bojoi, and Luca Zarri. Fault-Tolerant Torque Controller Based on Adaptive Decoupled Multi-Stator Modeling for Multi-Three-Phase Induction Motor Drives. *IEEE Transactions on Industry Applications*, pages 1–16, 2022. Conference Name: IEEE Transactions on Industry Applications.
- [126] Radu Bojoi, Sandro Rubino, Alberto Tenconi, and Silvio Vaschetto. Multiphase electrical machines and drives: A viable solution for energy generation and transportation electrification. In *2016 International Conference and Exposition on Electrical and Power Engineering (EPE)*, pages 632–639, October 2016.